Anatoliy PAVLENKO – professor of Kielce University of Technology, Department of Building Physics and Renewable Energy. Scientific direction of work – thermophysics of dispersed media.
Scientific interest – mathematical modeling of thermophysical processes occurring in liquids in the metastable state.

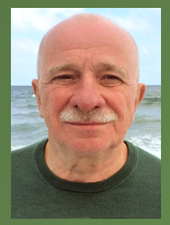

Borys BASOK – Corresponding Member of NAS of Ukraine, Professor, Doctor of Technical Science, Head of the Department of thermophysical basics of energy-saving technologies Institute of Engineering Thermophysics National Academy of Sciences of Ukraine

Borys DAVYDENKO – Doctor of Technical Science, Chief Research Scientist, Department of thermophysical basics of energy-saving technologies Institute of Engineering Thermophysics of National Academy of Sciences of Ukraine

ISSN 1897-2691
ISBN 9978-83-66678-01-9

ENERGY CONVERSION IN LOCAL VOLUMES OF DISPERSED MEDIA

MONOGRAFIE, STUDIA, ROZPRAWY

M138

Anatoliy Pavlenko
Borys Basok
Borys Davydenko

ENERGY CONVERSION IN LOCAL VOLUMES OF DISPERSED MEDIA

Politechnika Świętokrzyska
Kielce 2021

MONOGRAFIE, STUDIA, ROZPRAWY

M138

Anatoliy Pavlenko
Borys Basok
Borys Davydenko

ENERGY CONVERSION IN LOCAL VOLUMES OF DISPERSED MEDIA

Kielce 2021

MONOGRAFIE, STUDIA, ROZPRAWY NR M138

Redaktor Naukowy serii
INŻYNIERIA ŚRODOWISKA I ENERGETYKA
dr hab. Lidia DĄBEK, prof. PŚk

Recenzenci
Academician National Academy of Sciences of Ukraine, prof. Yurii MATSEVYTYI
Academician National Academy of Sciences of Ukraine, prof. Anatolii DOLINSKYI

Redakcja
Irena PRZEORSKA-IMIOŁEK

Projekt okładki
Tadeusz UBERMAN

Wydanie monografii finansowane w ramach projektu z programu Ministra Nauki i Szkolnictwa Wyższego pod nazwą „Regionalna Inicjatywa Doskonałości" w latach 2019-2022, nr projektu 025/RID/2018/19, kwota finansowania 12 000 000 zł

Ministerstwo Nauki
i Szkolnictwa Wyższego

ISSN 1897-2691
ISBN 978-83-66678-01-9

Wydawnictwo Politechniki Świętokrzyskiej
25-314 Kielce, al. Tysiąclecia Państwa Polskiego 7
tel./fax 41 34 24 581
e-mail: wydawca@tu.kielce.pl
www.wydawnictwo.tu.kielce.pl

Table of Contents

Preface 7

Part 1. THEORETICAL SUBSTANTIATION OF THERMODYNAMIC INITIATION OF HEAT AND MASS TRANSFER PROCESSES

List of conventions 11

CHAPTER 1. **Energy conversion in emulsification processes during thermal intensification** 13

1.1. Efficiency of energy input into a multiphase environment 15

1.2. Preconditions for the conversion of thermal energy into kinetic energy 17

1.3. Conversion of thermal energy into kinetic energy 24

1.4. Heat transfer with droplet surrounding medium 33

References 37

CHAPTER 2. **Dynamic effects of the homogenization process thermal initiation** . . . 41

2.1. Slow heating 41

2.2. Disturbance of metastable equilibrium with a sharp decrease in pressure 52

2.3. Comparison of obtained and experimental results 55

References 58

CHAPTER 3. **Dispersed phase breaking at emulsion boiling** 59

3.1. Mutual dynamic effects of neighbouring bubbles 59

3.2. Mutual effect of many neighbouring particles 71

3.3. Energy conversion in heat and mass transfer processes in boiling emulsions 84

3.4. Features of the energy conversion of the boiling phase of the emulsion 87

3.5. Results of research 93

3.5.1. Theoretical research 93

3.5.2. Field tests 98

3.6. Conclusions 102

References 103

Part 2. THEORETICAL SUBSTANTIATION OF MECHANICAL INITIATION OF HEAT AND MASS TRANSFER PROCESSES

List of conventions 109

CHAPTER 4. **Calculating methods for researching dynamics of liquid and heat and mass transfer in rotor-pulse apparatus** 113
4.1. Appointment, principle of operation and design features of rotary pulsation apparatus 113
4.2. Approximate hydrodynamic models for rotary pulsation apparatus 115
4.2.1. Numerical studies of fluid dynamics in cylindrical RPA obtained on the basis of approximate hydrodynamic models 116
4.2.2. An approximate hydrodynamic model for studying fluid dynamics in disk-type RPA 118
4.3. The problem of fluid dynamics in the working space of a cylindrical RPA 123
4.4. Features of numerical modeling of fluid dynamics and heat transfer in RPA working volume 128
References 131

CHAPTER 5. **Regularities of flow of liquid in RPA** 138
5.1. Velocity field in a fluid flow moving through the RPA working area 139
5.2. The flowrate of fluid passing through the working area of the apparatus 142
5.3. Stream function and vorticity of fluid flow in RPA working area 147
5.4. Pressure fields in the working area of RPA 149
5.5. The moment of hydrodynamic drag forces acting on the rotor from the side of a viscous fluid 158
5.6. Fluid flow in a rotary pulsation apparatus at the stage of its acceleration 160
5.7. The structure of the fluid flow in a vertical section of RPA 164
5.8. RPA dynamic characteristics at turbulent flow 169
References 177

CHAPTER 6. **Energy dissipation and heat transfer in the working area of a RPA** ... 179
6.1. The effect of the viscosity of processed medium on the level of heat dissipation in the working volume and on the degree of heating of processed medium 180
6.2. Statement and results of solving of conjugate heat transfer problem in the RPA working area 185
6.3. The results of solving the conjugate heat transfer problem in the RPA working area at turbulent flow of the fluid 190
6.4. Features of heat transfer in the working zone of RPA when processing non-Newtonian fluids 192

6.5. Numerical simulation of the mixing process of highly viscous fluids in a rotary pulsation apparatus 198
References 206

CHAPTER 7. **Effects of crushing dispersed particles of heterogeneous flows in RPA** 208
7.1. Deformation and fracture mechanisms of dispersed phase particles in a heterogeneous flow 208
7.1.1. The influence of inertial effects in a heterogeneous flow on the process of particle crushing 209
7.1.2. The effect of viscous stresses on the particle crushing process 212
7.1.3. Crushing of dispersed particles in a turbulent flow of a carrier medium 218
7.2. Calculation of the trajectories of dispersed particles in the working area of RPA 222
7.3. Evaluation of the dispersed composition of the emulsion after processing in RPA 226
7.4. The influence of structural and operational parameters of RPA on the average size of dispersed particles 235
7.5. The energy spent on crushing particles in RPA 239
7.6. The effect of crushing the dispersed phase of a highly viscous medium 240
References 247

CHAPTER 8. **Experimental researches of RPA hydraulic and thermal characteristics** 253
8.1. Experimental stand 253
8.2. The methodology of experimental research 254
8.3. RPA hydraulic characteristics studies 255
8.4. The study of the temperature characteristics of RPA 260
8.5. Experimental studies of the structural and mechanical characteristics of soybean paste 262
References 267

CHAPTER 9. **Influence of RPA construction and mode parameters on media characteristics** 268
9.1. Comparison of the hydrodynamic and thermal modes of operation of rotary-pulsating apparatuses with different arrangement of working bodies 268
9.2. The influence of the width of the gaps between the working elements of RPA on the dynamic characteristics of the fluid flow and heat transfer in the working area 279

9.3. The influence of the number of slots in the RPA working elements on the dynamic characteristics of the fluid flow in the working area of the apparatus 283
9.4. The effect of the angular velocity of the rotor on the dynamic and thermal characteristics of the fluid flow in the working area of RPA 286
References 288

CHAPTER 10. **Design and technical solutions when creating RPA** 289
10.1. RPA structural and operational parameters optimization 289
10.2. Rotary pulsation equipment for the production and processing of liquid dispersed media 297
References 302

CHAPTER 11. **Conclusion** 304

Preface

As a rule, to increase the efficiency of technological processes, they resort to their intensification, usually meaning use of various kinds of external physical effects; it makes it possible to change the system state and the rate of energy and mass transfer in the desired direction.

The search for methods of intensification and scientific substantiation of the optimal way to affect the system require a clear understanding of all physical phenomena, determining the studied process.

In traditional technologies, intensification, as a rule, is reduced to introduction of additional energy into the system, in some of its manifestations: thermal, kinetic, etc. However, physical processes are implemented in local (at the initial moment or throughout the entire process) volumes of the apparatus, for example, grinding, emulsification or homogenization processes.

In this case, it is obvious that only a small part of the energy introduced into the apparatus is spent on implementation of effective work, most of the energy is spent on accompanying processes and energy conversion (heating or mixing of the entire volume).

Energy efficiency can be increased by concentrating it in these local volumes.

The second task to be solved with such intensification is to achieve a sufficient level of energy concentration in local zones.

In this monograph, we will show how it can be achieved using the example of emulsification and homogenization problems.

We use two options for intensification – concentration of energy in local zones by supplying thermal energy and its local transformation in microvolumes and supplying kinetic energy to microvolumes.

On behalf of the authors, I would like to express my gratitude to the reviewers, renowned scientists who have developed the scientific foundations for technological process intensification: to ***Academician of the National Academy of Sciences of Ukraine Anatoly Andreevich Dolinsky and Academician of the National Academy of Sciences of Ukraine Yurii Mikhailovich Matsevyty*** for valuable comments and a positive assessment of this monograph.

Professor Anatoliy Pavlenko

Part 1

THEORETICAL SUBSTANTIATION OF THERMODYNAMIC INITIATION OF HEAT AND MASS TRANSFER PROCESSES

p_w, p_a – are the partial pressures of water vapor and the air, respectively, Pa
R – is the radius of a gas bubble, m
τ – is the time, s
p_B – is the pressure of a gas mixture inside a bubble, Pa
p_∞ – is the pressure in fluid, Pa
ρ_r – is the density of fluid, kg/m^3
μ_r – is the dynamic viscosity of fluid, Pa·s
σ_r – is the coefficient of surface tension of fluid, N/m
ρ_w, ρ_a – are the densities of vapor and the air, kg/m^3
ρ_w^* – is the densities of saturated water vapor, kg/m^3
R_μ – is the universal gas constant, J/(kmol·K)
μ_w – is the molecular mass of water, kg/kmol
μ_a – is the molecular mass of the air, kg/kmol
T – is the temperature of gas mixture in a bubble, K
a – is the Van der Waals constant, (N·m^4)/mol^2
b – is the Van der Waals constant, m^3/mol
I_w, I_a – are the mass of water vapor and air, that diffuse through a unit of the surface per unit of time, kg/(m^2·s)
I_{wr} – is the mass flow of water vapor that is condensed in gas medium of a bubble per unit of time, kg/(m^3·s)
s_w, s_a – are thermal capacity of water vapor of the air, J/(kg·°C)
q – is the specific thermal flow, directed from the wall to gas medium of a bubble, W/m^2
m_w – is the mass of water that evaporates from the surface of a bubble in the known time interval, kg
r_w – is the heat of the phase transition water–water vapor, J/kg
r_a – is the heat of air dissolution in water, J/kg
$\overline{v}_{(T)}$ – is the arithmetical mean velocity of gas molecules at temperature T, m/s
D_w, D_a – are the diffusion coefficients of water vapor in the air and of air in the water, respectively, m^2/s
Γ_a – is the Henry constant for the air above the water surface, (Pa·m^3)/kg

c_r – is the thermal capacity of fluid, J/(kg·°C)

T_r – is the fluid temperature, K

x – is the space coordinate, m

λ_r – is the effective coefficient of fluid thermal conductivity, W/(m·°C)

q_v – is the voluminous − power of sources or heat flows, W/m^3

T_0 – is the initial fluid temperature, K

P_0 – is the initial fluid pressure, Pa

A_P – is the amplitude of pressure fluctuations, Pa

d – is the diameter of a bubble, m

Π – is the oscillation period, s

Chapter 1

ENERGY CONVERSION IN EMULSIFICATION PROCESSES DURING THERMAL INTENSIFICATION

Typically, when choosing the physical effect on the technological process to intensify it, the general rule: physical effect shall be performed at that large-scale or energy level, at which the studied physical process occurs [1.1, 1.2].

Let us assume that we introduce energy into the system to intensify the technological process (increase the rate of mass or energy transfer), in other words, transform energy.

However, there are two obvious ways to increase its rate.

One of them is to achieve high power values (changes in energy over time) $W = \Delta E / \Delta \tau$. Another possibility to achieve high valuesis to reduce the energy conversion time $\Delta\tau$ at comparatively low level of ΔE. From ratio $\Delta E = W \cdot \Delta \tau$ it follows that at a given level of intensification W energy consumption is less, the shorter the effective exposure time $\Delta\tau$.

All technological processes are accompanied by a change in energy parameters of the medium, for example, temperature or relative velocity of phases, since we deal with energy conversion into its various forms, thermal, kinetic, etc.

Therefore, intensification of processes is directly related to the supply and transformation of any energy type in the system.

The process efficiency depends on energy supply and transformation intensity (parameter gradient).

In our opinion, it is this parameter that is decisive for intensification of technological processes.

So, it is possible to intensify energy transfer by increasing the power of supplied effect on the system. In this case, the duration of efficient work of the system $\Delta\tau$ will be the shorter, the higher the input power W, but only up to a certain limit. Energy consumption is determined from ratio $E = W \cdot \Delta \tau,$ but in this case $\Delta \tau = f(W)$. When a certain level of intensification is achieved, the subsequent increase in the apparatus power does not always contribute to further process acceleration.

Thus, with intensification of mass transfer processes, there is also a value of the maximum power.

A further increase in the input power will only cause an increase in inefficient energy consumption.

Therefore, the specific power level shall necessarily exceed value W_k, determined for these conditions, to ensure positive effect of the operation, but it shall not be much higher than W_k, to prevent unnecessary energy consumption. Considering that in modern technologies, increasing efficiency by reducing the time of the operation is a basic requirement, conditions $W \to W_k$ and, consequently, $\Delta\tau \to \Delta\tau_{\min}$ become evident.

Thus, a positive result cannot be achieved even at very high energy consumption, if the specific power in the apparatus working volume does not exceed a certain level (fig. 1.1).

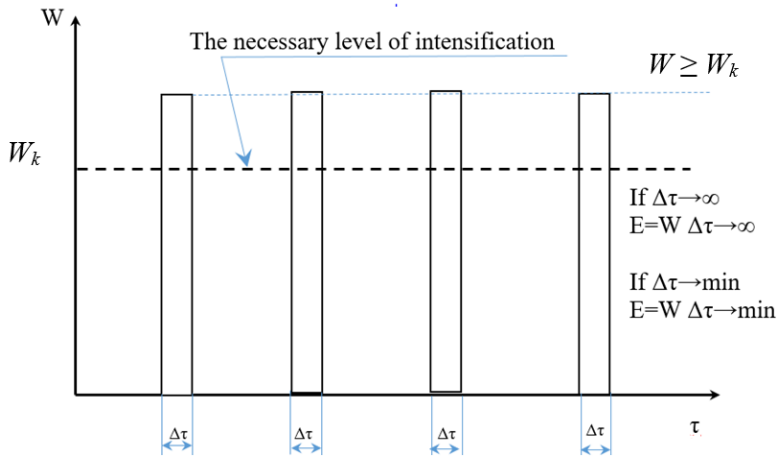

FIGURE 1.1. Schematic representation of the effective impact on the system

This figure schematically shows, that to obtain the required effect with minimal energy consumption, it is necessary to provide for a short time ($\Delta\tau \to \Delta\tau_{\min}$) a specified power level ($W \geq W_k$) or, in other words, convert the input energy into a short but powerful impulse. The more such impulses there are present in the system, the more efficiently the initiation of process transfer is implemented.

The next issue is how to realize such impulses in liquids or gases and how to ensure their distribution in the medium volume.

Use of multicomponent mixtures, for example, emulsions, in heat and mass transfer technologies may be one of the solutions to these problems.

Given the fact that practically all process media are multicomponent, this approach will be applicable to any medium.

Pulse energy input is most effective in the dispersed phase breaking processes, since the particle breaking is a one-stage act; to implement it, a sufficiently powerful effect is required within a very short time.

Similarly, when using the mechanism of shear stresses in narrow gaps, a high intensification level, determined by *dE/dy*, parameter, it is recommended to maintain not by the expense of to the power applied to the rotor shaft (thus providing high value ΔE), but by decreasing gap thickness *dy*.

Development of new methods for technological process intensification in heterogeneous media and creation of effective devices on this basis, the temporal and spatial discretization of the input energy is a necessary condition if the issues of energy and resource conservation attain the paramount importance.

1.1. Efficiency of energy input into a multiphase environment

The heat and mass transfer intensification and hydromechanical processes in a dispersed medium is determined by the acceleration value of the continuous liquid phase in the immediate vicinity of dispersed particles.

Therefore, one of the main efficiency conditions of this intensification is reaching the highest possible valuesof the local rate and acceleration, i.e. transformation of thermal energy into kinetic energy by supplying effective power W_k. In polydisperse liquid media, a temperature increase up to the level of a thermolabile liquid saturation causes vapor bubble formation.

This effect can also be achieved when thermodynamic equilibrium is disturbed in subcooled liquids (emulsions).

Let us consider a vapor bubble in an infinitely large volume of liquid being in a macro-quiescent state.

The accelerated liquid motion around the bubble is caused solely by a change in its volume during growth or compression.

The kinetic energy density at the liquid local point around the bubble is related to the local radial motion rate by w_r dependence $\varepsilon_k = \rho_l w_r^2 / 2$. The change rate of the kinetic energy density at the liquid local point is proportional to the radial flow rate and acceleration at this point $d\varepsilon_k / d\tau = \rho_l w_r \cdot dw_r / d\tau$.

The kinetic energy of the liquid radial motion around a single bubble can be calculated by recording the liquid kinetic energy for a thin layer with thickness of *dr*, located at a distance of *r* from the the bubble centre, and then integrating over the liquid volume.

$$E_k = \int_R^\infty 4\pi\rho_l r^2 \cdot \frac{w_l^2}{2} dr = 2\pi R^3 \rho_l w_R^2 \tag{1.1}$$

It is considered, that the liquid radial rate w_r at a distance *r* from the bubble centre is related to the liquid radial motion rate at the bubble surface interface w_R by ratio $w_r = w_R \cdot R^2/r^2$. The change rate of the kinetic energy of the liquid radial motion during bubble growth or compression can be written as

$$\frac{dE_k}{d\tau} = 4\pi R^2 \rho_l \left(R w_R \frac{dw_R}{d\tau} + \frac{3}{2} w_R^3 \right) \qquad (1.1^*)$$

The higher the liquid velocity and acceleration values at the bubble interface are, the faster energy is converted.

The change rate of the liquid kinetic energy at the local point at a distance of *r* from the bubble centre can be represented

$$\text{as} \frac{d\varepsilon_k}{d\tau} = \frac{\rho_l R^3}{r^4} \left(R w_R \frac{dw_R}{d\tau} + 2 w_R^3 \right) = \frac{1}{4\pi r^4} \left(R \frac{dE_k}{d\tau} + E_k w_R \right) \qquad (1.2)$$

As it follows from (1.2), the change rate in the density of kinetic energy $d\varepsilon_k/d\tau$, determining the dynamic effect of a bubble at the liquid local point, is directly related to the integral energy parameter E_k and kinematic parameters w_R and E_k and with kinematic parameters w_R and $dw_R/d\tau$, characterizing conditions at the bubble interface. Therefore, these parameters can be used for quantitative assessment of the bubble dynamic characteristics.

During destruction process of steam bubbles, mechanical energy is converted many times.

First, the potential energy due to pressure difference in both phases is gradually converted into kinetic energy, value of the latter goes up with increase of the bubble compression rate w_R. Right before the bubble reaches its minimum size, its compression rate and kinetic energy decrease rapidly.

At this, kinetic energy is converted into potential energy of compressed vapor and partially into the liquid potential energy E_{pot}, that at $w_R = 0$ is concentrated, in a very narrow zone ΔV directly at the surface of the extremely compressed bubble. It causes abnormally high pressure in this zone $p = \Delta E_{\text{pot}}/\Delta V$. In the process of the bubble re-expansion, this pressure pulse propagates in a liquid at the sound rate, and potential energy of the compressed vapor is converted into the liquid kinetic energy.

These mechanical energy conversions occur until the bubble disappears completely. Each stage of energy conversion is characterized by its transformation time $\Delta\tau_{tr}$.

1.2. Preconditions for the conversion of thermal energy into kinetic energy

Currently, there are many studies performed [1.1, 1.3-1.12], aimed to determine the optimal process modes of emulsification, dispersion and homogenization of mixtures of two and/or more mutually insoluble liquids.

Vapor bubbles and vapor cavities are especially important for these processes.

Therefore, models were proposed to describe the vapor bubble growth in a boiling liquid volume during liquid boiling under conditions of free convection on surfaces of unlimited size and on microsurfaces; a model of a vapor bubble growth located in a ensemble of the same bubbles is presented, considering their joint action on this bubble.

The droplet breaking processes during their extension and dynamic action of flows on the droplet, its behaviour under these conditions are described.

To describe the processes occurring with a vapor bubble during its growth or collapse, a model of the dynamics of a single vapor bubble, occurring in the continuous liquid volume, was developed [1.13, 1.14, 1.25].

The vapor bubble dynamics in the volume of its liquid is described by a system of equations of hydrodynamics and heat and mass transfer.

The calculation results, using this model for a bubble with initial radius $R_0 = 10$ μm, with 120°C, placed in a liquid with $t = 300$°C at normal pressure, demonstrate oscillations of the steam-water interface radius and high values of parameters at the moment of compression: $t \approx 1500$°C, $p \approx 12000$ atm. These calculations also demonstrate that in each of the subsequent oscillation periods of the collapsing vapor bubble, the amplitude decreases from 20% down to several percent.

Actually, emulsions consist of many droplets of one component distributed in another one, when one of the components boils up, a multitude of bubbles, distributed in the volume, will form.

To describe the vapor bubble behaviour under the effect of other bubbles in a liquid volume, a behaviour model of a vapor bubbles ensemble was proposed [1.13].

The individual bubble behaviour inside an ensemble with variations in external pressure is more complicated than it was presented in the mathematical model of a single bubble [1.14] in an infinite volume of liquid, since it is determined by the correlating effect of its nearest neighbours on the bubble evolution; during their development, they build their own pressure pattern in the vicinity of this bubble, this pattern is different from the external pressure, acting on the system at a given moment.

The bubble dynamics in an ensemble is solved in the approximation of a cell model, it is assumed that at a given moment of time geometric and dynamic parameters of all bubbles in the ensemble are identical, the distribution of rates and pressures near each bubble within the unit spherical cell is assumed as symmetric.

As it is seen from calculations [1.15] of the pressure distribution in the vicinity of a single bubble in the initial period of its growth in water with an instanteneous pressure relief; as the bubble grows, the pressure in a liquid at a certain distance from the centre gradually increases and even at a distance tenfold exceeding the current radius, the pressure in liquid is much higher than the applied pressure.

It proves that pressure patterns of the nearest neighbours shall mutually overlap and the pressure at any point in the inter-bubble area will exceed the external pressure, initiating the bubble growth or compression.

In [1.16], calculations were performed based on a cell model of a bubbles ensemble behaviour; it can be seen that an individual bubble behaviour inside the ensemble under identical effects and conditions differs from the behaviour of the same bubble in an infinite volume, the more the higher the concentration of bubbles in the ensemble.

A more noticeable effect of concentration is manifested during the bubbles collapse in the ensemble.

As it can be seen from model calculations, the pressure relief or liquid superheating degree have a minor effect on the bubble growth dynamics at the same temperature and concentrations; the size of bubbles at the beginning of their growth or collapse in a monodisperse two-phase system is also of little importance.

In the study on rate and pressure patterns [1.16], data were obtained, proving that in the ensemble inter-bubble area, even with monotonic bubble expansion, there are sharp jumps in pressure and rate characteristic of turbulent flow.

This flow character helps to intensify and stimulate heat and mass transfer and hydrodynamic processes in the liquid phase of the bubble system.

Condensation of superheated steam in subcooled liquid is used in many industrial installations, such as feed water heaters, jet pumps, etc. [1.17-1.22]. The collapse of vapor cavities and separate bubbles in a supercooled liquid is characterized by abnormally high pressure pulse values.

The initiation of such powerful dynamic effects with subsequent control of their effect can be used to intensify process operations of emulsification, dispersion and homogenization in liquid multicomponent media.

The study of vapor cavitation (collapse of bubbles filled with superheated vapor in an extremely subcooled liquid) was performed in [1.23] based the model of a single vapor bubble dynamics [1.24].

The study of vapor cavitation mechanisms is complicated by the fact that the influence of heat and mass transfer and hydrodynamic processes, determining a high level of dynamic effects, is most pronounced at the stage of maximum bubble compression, lasting within a nanosecond range.

In the same work, the effect of operating parameters on the bubble dynamics is studied; it was determined that the liquid subcooling degree has the greatest effect – at low subcooling, the process switches into a smooth condensation mode, when the bubble size decreases monotonically without noticeable pulsations.

A change in the external pressure does not affect dynamic characteristics of cavitation bubbles considerably – amplitude values of the characteristics decrease with external pressure decrease; with an increase in pressure, a more intense compression is compensated by a slowdown in the collapse rate due to a higher initial vapor content in a bubble.

With an increase in the initial bubble radius R_0, the energy transformation duration increases, and, consequently, amplitude values of the dynamic parameters decrease. The vapor superheating degree does not significantly affect the bubble dynamics.

In [1.25-1.27], experimental studies of a single vapor bubble dynamics in the volume of adiabatically boiling up water and adiabatically boiling up flow are presented.

It can be concluded that with adiabatic boiling up of dispersed multicomponent media, for example, oil-water emulsions, the explosive growth of vapor bubbles and resulting local medium turbulization can cause hydrodynamic breaking effects of the dispersed phase.

Thus, if a dispersed phase droplet is located on the line between two closely located and growing bubbles of a boiling up dispersed medium, then it will be affected by a hydrodynamic head, leading to the development of a Kelvin-Helmholtz-type instability for dispersed phase particles, cause their deformation and subsequent breaking.

Possible dispersion of such breaking can be estimated by Weber criterion

$$\delta = \frac{\sigma \cdot \mathrm{We}}{2\rho_c w^2} \tag{1.3}$$

High-frequency oscillations of a dispersed medium, caused by a pulse pressure change during destruction of vapor bubbles at the mirror water-air interface can cause Rayleigh-Taylor instability.

The size of broken particles can be determined based on Bond criterion

$$\delta = \sqrt{\frac{\sigma \cdot \mathrm{Bo}}{4g\rho_c}} \tag{1.4}$$

Mentioned reasons for hydrodynamic breaking of inclusions lead to the micron range of the obtained dispersed phase particles at: $g = 100$ m/s^2, $\delta = 1.3$ μm [1.28-1.30].

In flows with a liquid dispersed medium outflow, such as emulsions, rate non-equilibrium and tangential component difference of two phases $\Delta w = 13$ m/s can cause breaking of dispersed phase particles [1.31-1.33]. Based on Weber criterion $\delta = 0.2$ μm, i.e. micron dispersion range.

In [1.34], the phenomenon of adiabatic flow boiling up and main mechanisms of the dispersion destruction are studied and analysed based on a model, describing the evolution of the vapor bubbles ensemble during their intensive growth with a rapid external pressure decrease and a model of dispersed breaking in accelerated gas or liquid flows [1.35].

The study, performed for the liquid (water) outflow through a cylindrical channel $l = 0.1$ m long and $d = 0.01$ m in diameter, showed that for all outflow initial conditions, distribution curves of such parameters as liquid phase rate, pressure, as well as volumetric vapor content lengthwise the channel at a certain time moment, the dependences of these parameters in a certain section practically cease to depend on the ambient pressure. To analyse the mechanisms of foreign liquid droplet breaking in a boiling up flow, water was used as a continuous phase, benzene and carbon tetrachloride were used as a dispersed liquid phase.

The degree of droplet deformation increases with its size, large droplets begin to flatten in the channel zone, where flow acceleration is relatively low, breaking of all droplets with $R < 100$ μm occurs in a narrow zone at the very end of the channel, where acceleration increases sharply.

At the same time, it was determined that smaller droplets can be destructed earlier than large ones.

In [1.36-1.39], the experimental study results of boiling up of multicomponent mixtures, consisting of a continuous low-boiling component and a high-boiling component, uniformly distributed in the form of large droplets of a high-boiling component are presented to analyse laws of dispersion depending on the main process parameters. As a result, the main conditions for dispersion during adiabatic boiling up of multicomponent mixtures were formulated, as well as required device is for process implementation (vacuum homogenizer).

The advantage of the proposed method was demonstrated, consisting in energy consumption reduction by 2.5-3 times by reducing the cost of the entire liquid volume transfer in devices with stirrers.

Experimental data on a single vapor cavity dynamics, formed in an initially stationary water volume under normal conditions are presented in [1.27]. The parameters were measured with a high-rate camera at 4500 frames/s, as well as with a piezoceramic pulse pressure sensor and a microthermocouple.

Dynamic liquid parameters near the cavity, due to cumulative microjet motion and cavity collapse and breaking processes, can cause destruction of the multicomponent system dispersed phase.

The obtained data on the relative rate of diametrically opposite walls of the collapsing cavity (≈10 m/s) make it possible to use such breaking as a preliminary dispersion of a water and oil mixture, i.e. emulsification process implementation.

Destruction of thin liquid films of foam formations of the boiling up flow can also cause hydrodynamic breaking of inclusions.

In [1.27], an experiment is presented on the destruction of water solution liquid films using a high-molecular-weight surfactant, stretched over a circular wire frame. During filming, the dynamics of film destruction and breaking, the hole and resulting droplet size and growth rate were studied.

The forced and spontaneous destruction processes were studied. By the study results, the average destruction rate value was w = 1.9 m/s, while spontaneous destruction occurred at w = 12.5÷17.0 m/s.

The critical film thickness, i.e. the thickness at which, under the action of various oscillations, its spontaneous destruction occurs, can be determined by expression [1.13]

$$h^* = \left(\frac{A \cdot \lambda^2}{128\pi\sigma} \right)^{1/4} \tag{1.5}$$

where: A – Van der Waals-Hamaker constant; λ – the function, describing the film thickness change due to the propagation of fluctuations, determined by film size; σ – interfacial tension. Value $A = 5 \cdot 10^{-20}$ J and respectively h^* = 12.5÷17.0 μm.

Calculations of temperature patterns for the last stages of vapor cavity collapse show that temperatures of $10^3 \div 10^4$°C order can be reached [1.40-1.42]. Such high thermal modes can cause the effects of secondary local boiling up not only of the dispersed medium (water), but also of the dispersed phase (oil).

Boiling up results in vaporization of local oil inclusions and subsequent condensation of its vapors, i.e. to dispersion of particles [1.13].

It was determined in [1.21] that the model of a single bubble dynamics gives proper description of the vapor bubble dynamics in a liquid near its boiling point under the action of an acoustic field [1.21], as well as laws of vapor bubble cavitation in a cold liquid under the acoustic field action.

The laws, describing vapor bubble growth as a result of a liquid boiling up another liquid or flow volumes are presented above, the action of dynamic characteristics of this bubble growth or collapse on possible hydrodynamic breaking of inclusions

during the boiling up of multicomponent mixtures, consisting of two or more immiscible mixtures, was also considered.

However, vapor phase growth can also occur on solid surfaces. In [1.39], the mechanism of heat transfer during liquid boiling up as a result of vapor bubbles merging, formed from a micro-nucleus at the moment of liquid contact with the wall and during formed conglomerate growth are studied.

According to [1.1], the dynamics of vapor phase growth on a heated surface under free convection can be considered based on two models: bubble growth due to non-stationary thermal conductivity from the surrounding liquid and bubble growth due to heat supply by means of stationary thermal conductivity from the wall through the boundary thermal liquid microlayer.

It is preferable to consider a generalizing model based on these two models.

Based on heat balance, including: stationary heat, coming from the wedge-shaped layer, forms between the wall and the bubble; unsteady heat, coming from a superheated liquid layer, covering the bubble; dissipative component, arising due to friction during bubble growth with surrounding liquid; heat, taken by a vapor bubble; with introduction of geometric factors, the time dependence of the bubble radius is written [1.1, 1.2]

$$R = \gamma\sqrt{a\tau}\left[\frac{1+\sqrt{1+(1/\mathrm{Ja}+\varphi/\mathrm{Pr})\chi}}{1/\mathrm{Ja}+\varphi/\mathrm{Pr}}\right] = \sqrt{a\tau}\gamma\varepsilon \tag{1.6}$$

where: $\chi = 2\beta/\gamma^2$; γ, φ, β – are geometric factors.

As it is evident from (1.6) $R = f\left(\sqrt{a\tau}\right)$. In [1.1] the analysis of equation (1.6) for different values of Jacob Ja and Pranndtl Pr numbers, showing transformation of equation (1.6) into already known equations. It follows from the above experimental studies, that the bubble in its growth goes through the following stages: subcritical growth, accelerated growth, asymptotic and inertial-separating.

The growth rate of vapor bubbles during liquid boiling on microsurfaces was studied in [1.43].

When the bubble base radius before separation reaches the microsurface boundaries, the radius dependence on time has the following form

$$R = C_1\left(\frac{R_{mn}^2}{(1+\cos\theta)^2(2-\cos\theta)}\frac{\mathrm{Ja}}{\sqrt{\mathrm{Pr}}}\right)^{1/3}\cdot(a\tau)^{1/6} \tag{1.7}$$

when the base radius does not reach microsurface boundaries

$$R = C_2 \frac{\mathrm{Ja}}{\sqrt{\mathrm{Pr}}} \frac{\sin\theta}{(1+\cos\theta)^2(2-\cos\theta)} \sqrt{a\tau} \tag{1.8}$$

where C_1, C_2 – are coefficients; θ – is interfacial angle.

It was determined that the bubble contact time with heating surface depends on its size: the smaller the surface is, the earlier the bubble gets separated.

The droplet deformation and breaking processes during motion in a liquid were studied in [1.35], it was used as a basis for mathematical model of droplet deformation and breaking under the assumption that at all stages of droplet deformation retains the shape of an ellipsoid of rotation.

The droplet behaviour during its motion in a liquid or gas is depends on three factors – interfacial resistance forces, capillary forces, and viscous dissipative forces. A physical model, considering the role of all these factors, is the Voigt model [1.43], describing a viscoelastic medium behaviour.

Capillary forces are represented by spring action; dissipative viscous forces are represented by a friction piston. The droplet deformation is considered as the motion of mass centres of half-droplets in the direction of *x* axis under the action of three determining forces.

A spherical droplet is deformed into a flattened ellipsoid when mass centres of half-droplets move to the geometric droplet centre, otherwise it transforms into an oblong ellipsoid.

The droplet deformation is considered by the deviation of the mass centre of half-droplet from the hemisphere mass centre.

Calculations, using model [1.35] show that when CCl_4 droplet falls in pure water under gravity, this droplet oscillates with a constantly increasing amplitude, subsequently leading to its breaking.

Using this model, it is possible to predict the droplet behaviour with a sharp flow acceleration in nozzles or under action of centrifugal forces.

So, if the external effect is not intense enough, the droplet after small amplitude damped oscillations takes the stable shape of a flattened ellipsoid.

A more considerable effect causes more intense damped oscillations, bringing the droplet into the shape of an extremely flattened ellipsoid. With a further increase in the external effect, the droplet is destructed.

The droplet destruction process in a liquid flow is affected by various factors, including adsorption-desorption phenomena [1.34]. Thus, when analysing a liquid droplet, immersed in an infinite homogeneous liquid at rest, not mixing with the

first one, with dissolved substance, has surface-active properties to the interface, adsorption-desorption phenomena and chemical reactions are observed.

Reaction products do not possess surface-active properties and are rapidly (in comparison with surfactant adsorption) removed from the interface.

Analysing the interface surface dynamics, heat-capillary effects [1.44] are neglected in comparison with the concentration-capillary effects due to small thermal effects of interfacial reactions.

Concentration-capillary effects are conditioned by dependence of the surface tension on reagents concentration.

At this, the effects, associated with surface viscosity and inertia of adsorbed surfactants increase.

Actually, it is problematic to assess the droplet mass change under the action of surfactants; therefore, when droplets break up, the effect of surfactants is not considered in experimental studies.

1.3. Conversion of thermal energy into kinetic energy

To perform numerical calculations as an example, let us assume that a low boiling liquid is water in an oil-water emulsion.

We know thermophysical parameters of liquids.

For the computational model, we assume that there is a water droplet with R_3, radius, surrounded with vapor layer δ_n thick, present in the continuous oil volume. The entire system at the initial moment of time is at a certain pressure p and temperature T, corresponding to water saturation temperature at pressure p. At a certain moment of time, this system is in the medium with reduced pressure p_∞. To describe heat transfer processes between water and vapor, as well as vapor phase growth, we use the following equations:

$$\frac{dw_4}{d\tau} = \frac{p_n - p_\infty - 1.5\rho_m w_4^2 - \dfrac{2\sigma}{R_4} - \dfrac{4\mu_m w_4}{R_4}}{\rho_m R_4} \tag{1.9}$$

The heat flow equation can be written as follows:

$$Q = 4\pi\left(q \cdot R_3^2(\tau) + q_m \cdot R_4^2(\tau)\right) \tag{1.10}$$

where q_m is a specific heat flow from oil to vapor.

A specific heat flow from water side q is determined by expression

$$q = 0.25\rho_n \cdot c_n \cdot W_n\left(T_n\right) \cdot \left(T_3 - T_n\right) + j \cdot c_n \cdot T_3 \tag{1.11}$$

to determine q_m let us use the integral method used to solve non-stationary heat conductivity problems, first proposed by Landahl in the study of thermal physics problems [1.2] and developed in [1.45, 1.46].

From the continuity condition for a liquid it follows

$$\rho_m \cdot w(r) \cdot r^2 = \rho_m \cdot w_4 \cdot R_4^2 = \text{const}$$

Then the heat conductivity equation in spherical coordinates for an incompressible liquid, surrounding the vapor volume, looks as follows

$$\frac{\partial T_m}{\partial \tau} = \frac{1}{r^2} \cdot \frac{\partial}{\partial r}\left[a_m \cdot r^2 \cdot \frac{\partial T_m}{\partial r} - w_4 \cdot R_4^2 \cdot T_m \right] \tag{1.12}$$

To solve this equation, let us introduce parameter $\delta(\tau)$, called penetration depth [1.2], characterizing time-varying thickness of the liquid layer adjacent to the vapor volume, where the temperature gradient is non-zero.

This parameter cannot be identified with non-stationary thermal layer thickness [1.2, 1.47].

Assuming the temperature profile near vapor layer in the parabolic interpolation approximation and integrating (1.12) from R_4 to $R_4 + \delta$ we get

$$\frac{d}{d\tau}\left[\frac{1}{3}\pi\rho_m c_m \left(T_m - T_4\right)\left(4R_4^2\delta + R_4\delta^2\right)\right] = 4\pi\left(T_m - T_4\right)\lambda_m R_4^2\left(\frac{2}{\delta} + \frac{1}{R_4}\right) \tag{1.13}$$

Left side (1.13) represents the change in the amount of heat in oil within a layer δ thick due to heat transfer through the interface, and the right side characterizes the amount of heat flow, coming from oil to vapor. Assuming the condition at oil-vapor interface $T_4(\tau) = T_n(\tau)$, we get

$$q_m = \lambda_m\left(T_m - T_n\right)\left(\frac{2}{\delta} + \frac{1}{R_4}\right) \tag{1.14}$$

Equation (1.14) allows to determine the specific heat flow from oil to vapor if value $\delta(\tau)$ is known.

If we assume

$$\frac{dH_m}{d\tau} = \frac{d}{d\tau}\left[\frac{1}{3}\pi\rho_m c_m \left(T_m - T_4\right)\left(4R_4^2\delta + R_4\delta^2\right)\right] \tag{1.15}$$

it is evident that dependence $H_m = f(\delta)$ looks as follows

$$H_m(\tau) = \frac{1}{3}\pi\rho_m c_m \left(T_m - T_n\right)\left(4R_4^2\delta + R_4\delta^2\right) \tag{1.16}$$

Penetration depth is equal to

$$\delta = 2R_4\left[\left(1 + \frac{3H_m}{4\pi R_4^3 \rho_m c_m \left(T_m - T_n\right)}\right)^{0.5} - 1\right] \tag{1.17}$$

To determine function $H_m(\tau)$ we have to solve equation

$$\frac{dH_m}{d\tau} = 4\pi R_4^2 \lambda_m \left(T_m - T_n\right)\left(\frac{2}{\delta_0} + \frac{1}{R_4}\right) \tag{1.18}$$

where δ_0 is penetration depth value at the previous time interval at $\Delta\tau \to 0$.

By solving equation (1.18), using Euler method or by the finite difference method, we can write

$$\begin{aligned}&\frac{1}{3}\pi\rho_m c_m\left[\left(T_m - T_n\right)\left(4R_4^2\delta + R_4\delta^2\right) - \left(T_m - T_{n0}\right)\left(4R_{4_0}^2\delta_0 + R_{4_0}\delta_0^2\right)\right] = \\ &= 4\pi R_4^2 \lambda_m \left(T_m - T_n\right)\left(\frac{2}{\delta} + \frac{1}{R_4}\right)\cdot\Delta\tau, \quad \Delta\tau \to 0\end{aligned} \tag{1.19}$$

Solution of equation (1.19) will make it possible to determine target value $\delta(\tau)$ and q_m. The temperature field over the cross section of a water droplet is determined by equation

$$\frac{\partial T_w(r,\tau)}{\partial\tau} = a_w\left(\frac{\partial^2 T_w(r,\tau)}{\partial r^2} + \frac{2}{r}\cdot\frac{\partial T_w(r,\tau)}{\partial r}\right), \quad \tau > 0,\ 0 < r < R_3 \tag{1.20}$$

under the corresponding initial and boundary conditions

$$T(r,0) = T_0 = \text{const}; \qquad -\lambda_w \left.\frac{\partial T}{\partial r}\right|_{r=0} = 0; \qquad T_m(\tau) = T_{m0} \tag{1.21}$$

Temperature T_3 at each time interval is determined from equation

$$\frac{2\lambda_w}{R_3}\left(T_1 - T_3\right) = q + j\cdot L\left(T_3\right) \tag{1.22}$$

Thus, the thermal part of the problem consists in obtaining the temperature field over the water droplet section according to equation (1.20) according to changing temperature value T_3, and temperature distribution in oil layer, δ thick (in the form of parabolic interpolation), by obtaining value δ and q_m. The dynamic part consists in solving Rayleigh-Plesset equation.

The solution results without consideration of change in continuous medium temperature are shown in figures 1.2-1.6.

It was assumed that at the initial moment of time there is a water droplet with a radius of 100 μm, surrounded by a vapor layer, 1 μm thick, in a continuous medium – oil.

The entire system is at t_0 = 180°C and corresponding water saturation pressure.

At a certain moment of time relative to the initial one, the system enters the decreased pressure zone (p_∞ = 1 atm) resulting in water evaporation and vapor phase growth. The calculations were made using the finite difference method.

Figure 1.2a shows the behaviour of temperatures of water-vapor and oil-vapor interfaces, as well as the temperature of the water droplet centre.

This figure demonstrates that T_3 and T_n temperatures have an oscillatory dependence of change at the initial moment of the vapor phase growth ($\tau < 0.002$ s).

In this case, the vapor is even more superheated than during growth of vapor volume surrounded by an oil shell (fig. 1.3), its temperature will constantly increase, starting from the moment of practically equilibrium vapor pressure at level p_∞.

It is explained by the fact that the heat flow, coming from oil to vapor, will exceed the expansion effect of vapor volume throughout the entire period, as well as heat flow from vapor to water according to equation and mass flow heat.

$$\frac{dT_n}{d\tau} = \frac{1}{c_n m_n}\left[Q - c_n T_n j S_3 - p_n \frac{dV_n}{d\tau}\right], \quad S_3 = 4\pi R_3^2 \tag{1.23}$$

Decrease in Q_m according to figure 1.5a with radius increase R_4, can be attributed to a decrease in temperature differences $T_m - T_n$, shown in figure 1.2a, and joint effect of δ and R_4. Radius value R_4 value changes in time more intensively than with an increase in the vapor volume in oil shell, as it is shown in figure 1.3b, while no characteristic radius oscillations are observed, resulting from the fact that mass flow can compensate for vapor volume expansion (decrease in vapor density).

Water evaporation and vapor phase growth process is more intense than in the case of an oil shell, manifested by a noticeable decrease in radius R_3 in figure 1.4a and higher values of oil-vapor interface motion rate (fig. 1.6a). Curves of

specific mass flow changes (fig. 1.4b) and water-vapor interface motion rate (fig. 1.5b) have a similar behaviour in time.

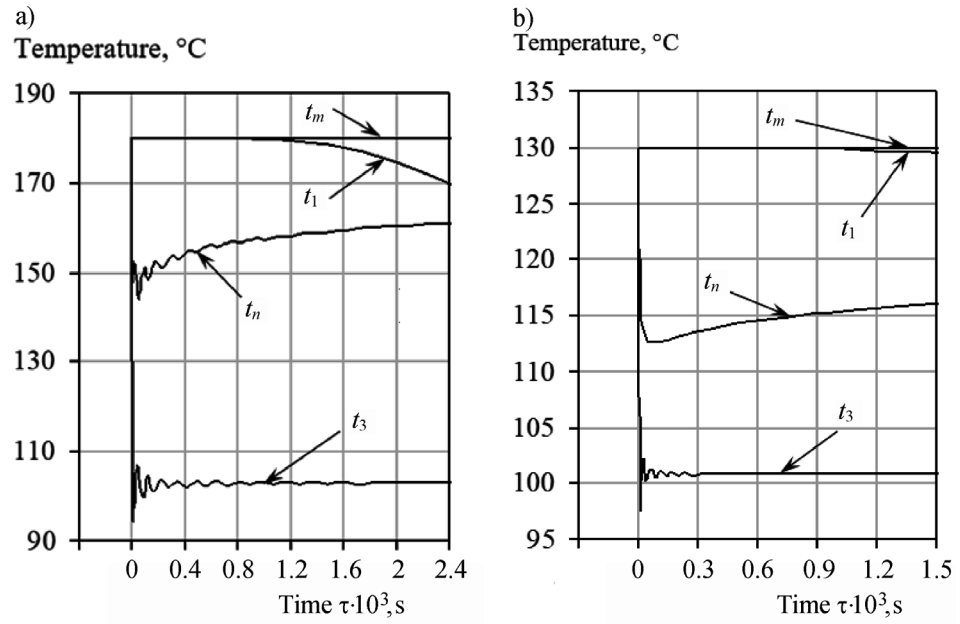

FIGURE 1.2. Behaviour of interfaces temperatures and the water droplet centre in time at initial temperature $t_0 = 180°C$ (a) and $t_0 = 130°C$ (b).

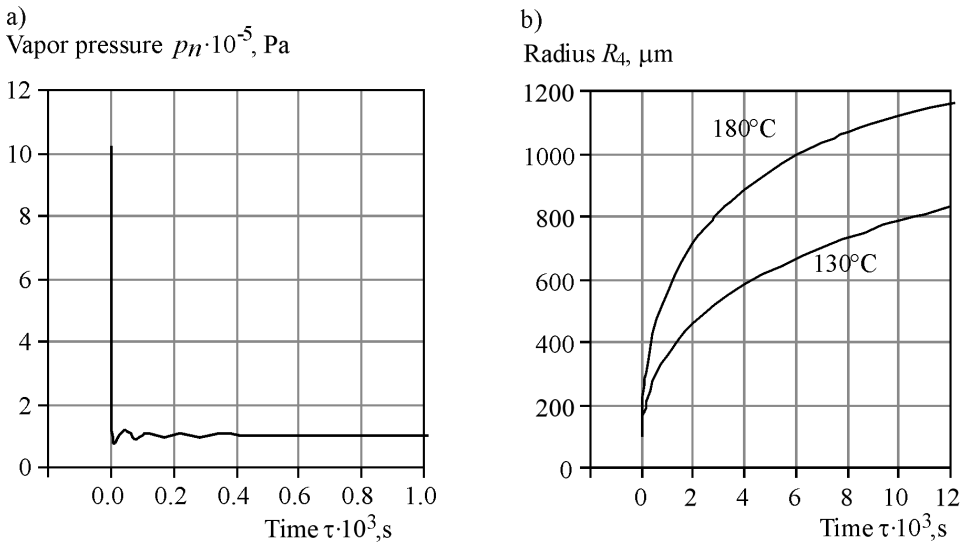

FIGURE 1.3. Vapor pressure change (a) at $t_0 = 180°C$ and oil-vapor interface radius (b) at different initial temperatures in time.

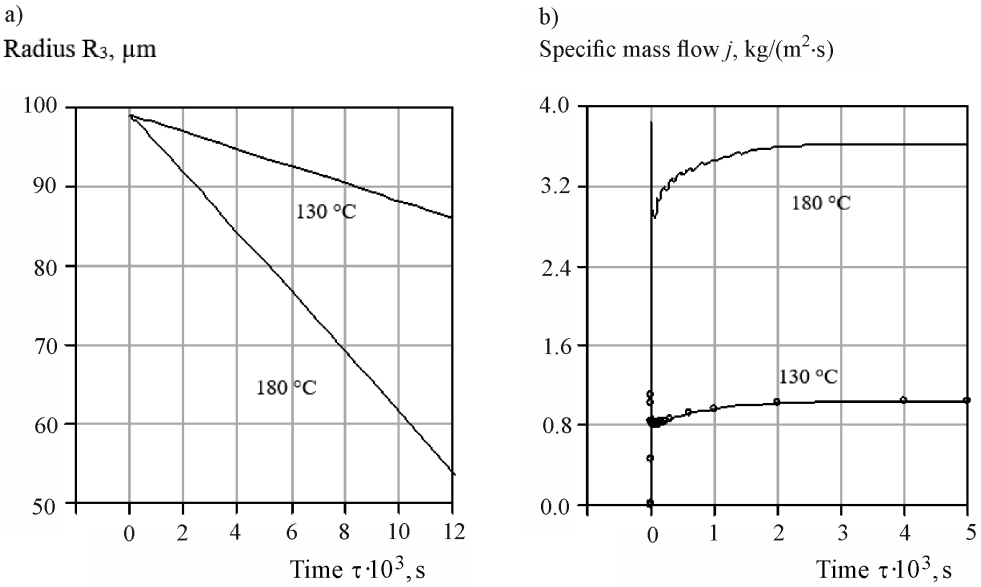

FIGURE 1.4. Change in water-vapor interface radius (a) and specific mass flow (b) in time.

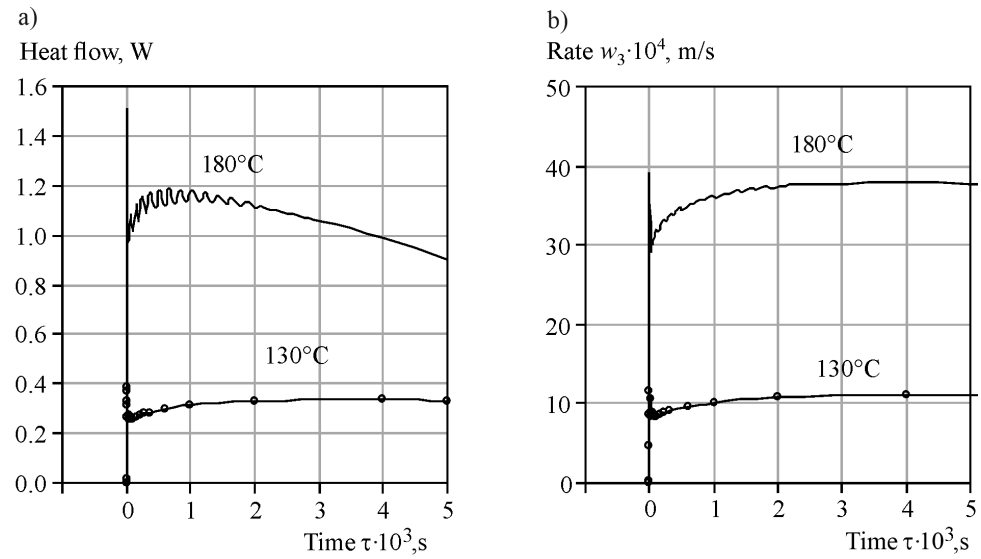

FIGURE 1.5. Change in heat flow from oil to vapor (a) and rate of water-vapor interface motion (b) in time.

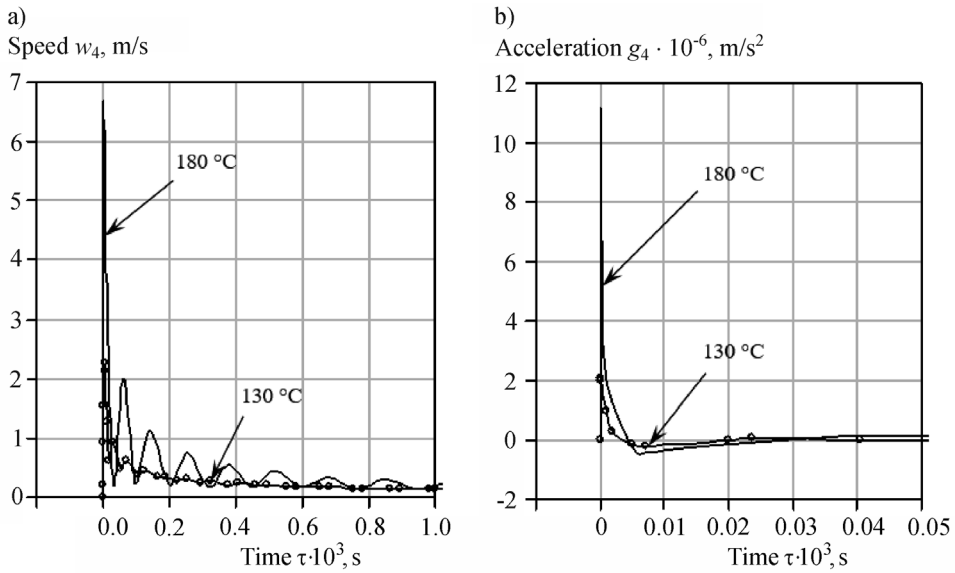

FIGURE 1.6. Dependence of rate (a) and acceleration (b) change of oil-vapor interface motion in time.

In this case, the initial surge in the mass flow and, as a consequence, water-vapor interface motion rate, result from a sharp decrease in temperature (fig. 1.2a) and vapor density, causing a decrease in vapor pressure (fig. 1.3a).

Further decrease of mass flow down to $\tau < 3 \cdot 10^{-5}$ s can be explained by the combined effect of temperature changes in vapor and water-vapor interface (fig. 1.2a), as well as by the vapor density according to equation:

$$j = 0.25\alpha_m \left[\rho_n \left(T_3 \right) \cdot W_3 \left(T_3 \right) - \rho_n \cdot W_n \left(T_n \right) \right] \tag{1.24}$$

A decrease in the vapor volume growth intensity, i.e. oil-vapor interface motion rate according to figure 1.6a, leads to accumulation (an increase in vapor density), as well as an increase in vapor temperature, resulting in decrease of incoming heat flow from oil to vapor (fig. 1.5a) and mass flow from water surface to vapor.

According to comparison of figures 1.2a and 1.6a, an increase in oil-vapor interface causes decrease in vapor temperature and vice versa. Oscillations of vapor pressure according to figure 1.3a result from combined action of temperature and vapor density, and if, in calculation, it is considered that vapor pressure is only a temperature function $\left(p_n = f\left(T_n \right) \right)$, then qualitatively incorrect results can be obtained. The vapor pressure, as in case with oil shell, has an oscillatory behaviour in time with constantly decaying amplitude, which ultimately leads to a certain equilibrium value of the vapor pressure.

An increase in the mass flow, starting from $\tau \approx 2 \cdot 10^{-5}$ s, results from the combined action of heat flows from the water droplet centre and from vapor to water-vapor interface.

In this case, a constant mass flow value for $\tau > 0.003$ s indicates compensation by heat flow from vapor to water-vapor interface for a decrease in heat flow from the water droplet centre due to temperature decrease T_1.

The calculated value of oil-vapor interface acceleration, shown in figure 1.6b, in the initial period of vapor volume expansion reaches a maximum equal to a million of gravity accelerations ($\approx 11.3 \cdot 10^6$ m/s^2).

Figures 1.2b, 1.3b-1.6 show the calculation results for initial temperature $t_0 = 130$°C. It is obvious that a temperature decrease down to this value results in a decrease in oscillations of measured parameters, or to complete disappearance of these oscillations.

According to figure 1.2b, vapor temperature initially decreases, then it begins to increase without significant oscillations, temperature T_3 more quickly equilibrates to equilibrium.

The behaviour of specific mass flow (fig. 1.4b) and water-vapor interface motion rate (fig. 1.5b) are consistent with the change in vapor temperature T_n, as well as at a temperature of 180°C. In general, the amplitude values of vapor volume growth (fig. 1.6a), water-vapor interface motion rate (fig. 1.5b), mass flow, heat flow from oil to vapor and acceleration of oil-vapor interface motion rate (figs. 1.4b, 1.5a, 1.6b) have lower valuesat lower valuesof oscillation periods. The general behaviour of calculated valuescurvesat 130°C is the same as at 180°C.

The vapor temperature change at $R_3 = 10$ μm, is characterized by the fact that it is more superheated relative to saturation pressure, than at $R_3 = 100$ μm, with an initial radius of 500 μm, the vapor is less superheated relative to p_s. At $R_3 = 10$ μm and $t_0 = 180$°C oscillations of oil-vapor interface radius appear, they do not exist at 130°C. The behaviour of measured valuesfor radii of 10 μm and 500 μm remains the same as at 100 μm, but the amplitude valuesincrease with radius decrease, except for the heat flow from oil to vapor, growing with an increase in the initial radius of oil-vapor interface. At low value of R_3 in curve $j = f(\tau)$ reflects a sharp decrease in mass flow caused by a heat input decrease from water, as a result of its intensive cooling (a rapid decrease in temperature T_1), mass flow growth at $R_3 = 500$ μm is due to effect of heat input from the water over a longer period of time. With a decrease in the emulsion droplet initial radius, significant oscillations of heat flow from oil to vapor are also observed. The change of vapor

pressure at $R_3 = 10$ μm and $t_0 = 130$°C is characterized by the fact that it does not fall lower than ambient pressure, it is always higher. It results from the fact that mass flow j and heat flow from oil to vapor Q_m can compensate for the effects of vapor volume expansion, resulting in vapor density and temperature decrease.

According to [1.2], pressure near vapor volume can be determined using the following equation

$$p(r) = p_\infty + \left[p_4 - p_\infty + 0.5\rho_m w_4^2 \left(1 - \frac{R_4^3}{r^3} \right) \right] \frac{R}{r} \qquad (1.25)$$

Calculations according to equations of the growth model of the vapor phase, boiling water droplet, located in an infinite oil volume, together with equation (1.25) for certain valuesof radius r we obtain the pressure distribution in the vicinity of the growing vapor volume. We get pressure distribution near the growing vapor volume. The calculation results are presented in figure 1.7.

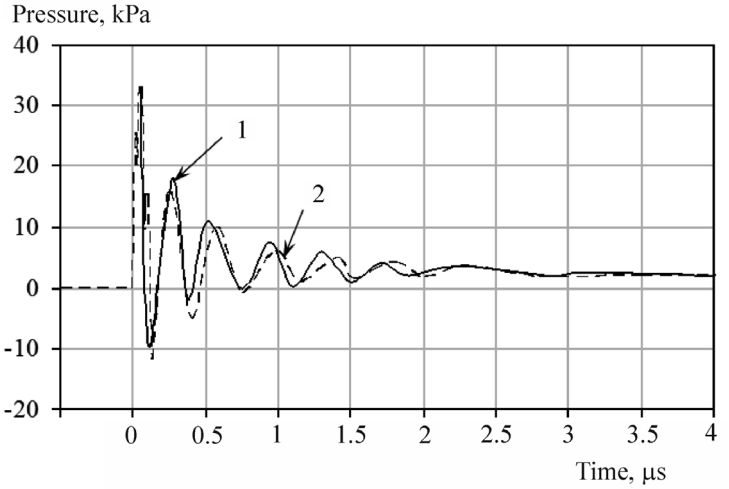

FIGURE 1.7. Comparison of calculated (curve 1) and experimental (curve 2) data on vapor phase growth upon boiling up of a water droplet, placed in superheated oil.

By comparing the calculated distribution in time of pressure with experimental data, one can see their consistency in the frequency of pressure change. The observed inconsistency in the amplitude of pressure change value is explained by the fact that in the calculation the considered droplet has a spherical shape, but even in view of the smallness of the surface wetting property, the real droplet did not have a perfect spherical shape.

In the calculation, it was assumed that a certain size of the vapor layer (1 μm) already exists, while it was experimentally determined that at first, separate

bubbles are formed, subsequently merging with each other; the initial vapor pressure is taken equal to the highest experimentally measured value.

As a consequence, the calculation did not consider a certain period of vapor phase formation, when pressure increased to the value, initially assumed for calculation.

But, as results from figure 1.7, formation of each individual bubble at the oil-water interface can be identified with vapor layer formation of a certain size.

The presence of a certain amount of surfactants also makes a special contribution, since the interfacial tension coefficient of oil-vapor interface was assumed by generalized data.

Comparing experimental and calculated data, it can be concluded that the relative error in determining the pressure pulses was ≈15.8%.

In general, we can conclude that the developed model of vapor phase growth provides a proper description of the processes, occurring during boiling up of superheated liquids, both in qualitative and quantitative aspects.

1.4. Heat transfer with droplet surrounding medium

During water evaporation, both water and oil consume energy, as a result, temperatures of the water oil volume will decrease, if no heat is supplied to the emulsion volume.

Change of oil volume temperature can be determined, knowing the total system volume, water and oil content, size of dispersed phase particles, as well as their number.

Let us take a certain volume V_Σ with 30% of water ($V_w = 0.3 \cdot V_\Sigma$) and 70% of oil ($V_m = 0.7 \cdot V_\Sigma$). To determine the number of dispersed phase particles, we can use histograms of particle size distribution [1.1, 1.2].

If we assume that the entire dispersed phase will be uniformly distributed in the volume with particles of the same size, then the number of dispersed phase particles (for example, water) is

$$N = \frac{3V_w}{4\pi R^3} \tag{1.26}$$

Then change of oil temperature in time is

$$\frac{dT_m}{d\tau} = 4\pi R_4^2 N \frac{q_m}{c_m m_m} \tag{1.27}$$

where m_m is carrier phase mass ($m_m = V_m \rho_m$).

For instance, for emulsion volume $V_\Sigma = 0.5 \cdot 10^{-3}$ m^3 with 30% of water (in combination with vapor) and for particles R = 100 μm in size, their number is equal to $N = 3.58 \cdot 10^7$ pcs. The calculation results, using the equations of vapor phase growth model, boiling water droplet with radius $R_4(0) = 100$ μm, present in infinite oil volume, combined with equations (1.26), (1.27), are shown in figures 1.8-1.10.

Figure 1.8a shows that oil temperature decrease is more intense than temperature decrease of the water droplet centre T_1, resulting from higher heat transfer from oil to vapor as compared to that from the water droplet centre to water-vapor interface. The difference in the vapor temperature change over time is its decrease, due to a decrease in T_m, as compared to calculation without considering the medium temperature decrease.

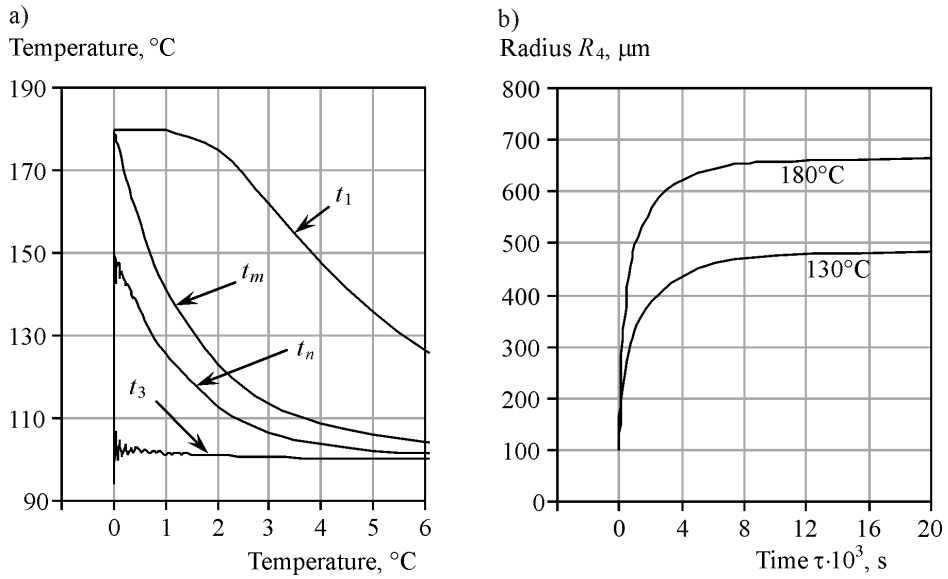

FIGURE 1.8. Behaviour of interface temperatures, the centre of a water and oil droplet in time at the initial temperature t_0 = 180°C (a), as well as the radius of the oil-vapor interface at different initial temperatures (b) in time.

In this case, amplitude valuesof growth rate, accelerations of motion, pressures, actually remain unchanged in comparison with the calculation without change of T_m. Heat flow from oil to vapor and mass flow (figs. 1.9b, 1.10a) in the initial period of time is equal to the same without considering $Q_m = f(T_m)$ (figs. 1.4b, 1.5a).

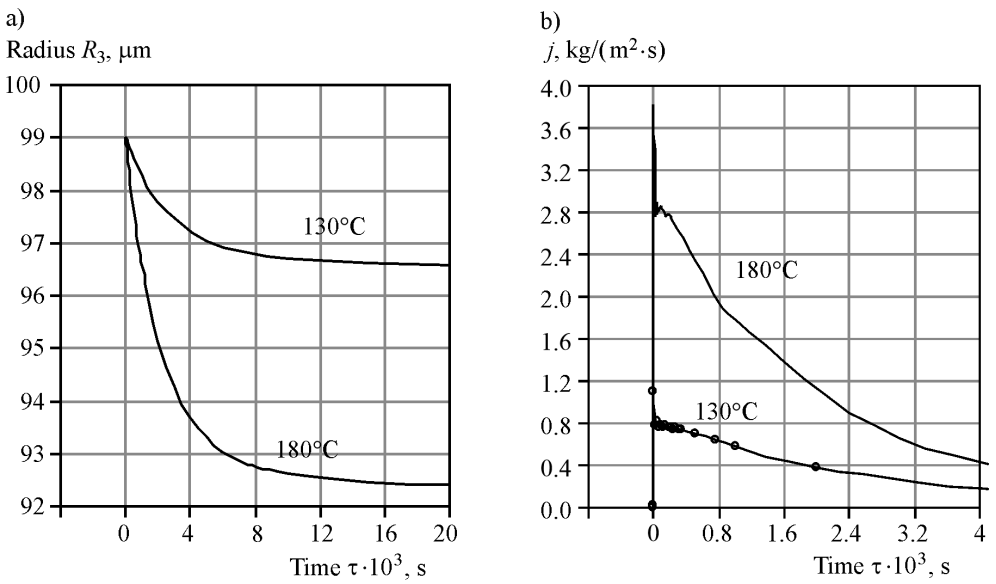

FIGURE 1.9. Change in water-vapor interface radius (a) and specific mass flow (b) in time.

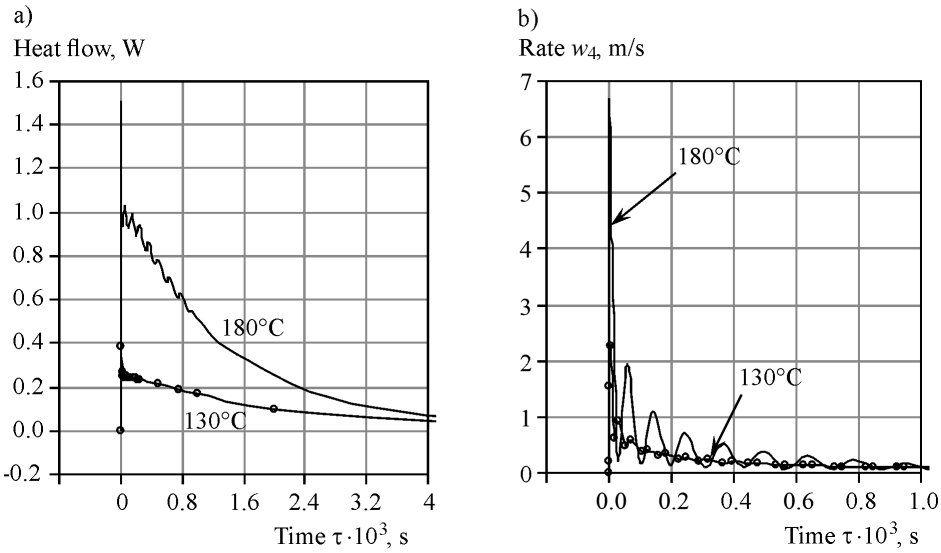

FIGURE 1.10. Change in heat flow from oil to vapor (a) and rate of water-vapor interface motion (b) in time.

But at considerable decrease of T_m further on, they begin to decrease, asymptotically approaching zero, indicationg the dominant role of the heat flow Q_m in heat transfer process.

Maximum calculated value Q_m reaches ≈1.5 W per one particle. Considering, that number of particles is equal to $N = 3.58 \cdot 10^7$, it can be concluded that the heat transfer process is highly intense, requiring an increased amount of heat.

Water-vapor interface radius (fig. 1.9a) first decreases rapidly, then the change curve $R_3(\tau)$ approaches a horizontal straight line.

The behaviour of oil-vapor interface radius R_4 (fig. 1.8b) is of the same character: rapid growth at first, but after reaching a certain value (for t_0 = 180°C, ≈680 μm), it increases slightly, at low rate ($w_4 \to 0$), resulting from reduced heat supply to the particle due to oil temperature decrease.

Similar patterns are observed at temperature t_0 = 130°C (figs. 1.8b-1.10). Changes in the temperatures of the water and oil droplet centre at smaller initial area characterized by the fact that in the initial period of time oil temperature decreases more intensively than water droplet temperature T_1. Further temperature decrease T_1 is faster than T_m, consequently, temperature T_m during the rest time period is always higher than T_1.

Such features, as increase or decrease in T_n depending on the initial droplet radius, appearance of radius oscillations R_4 at high temperature (180°C) and the initial droplet radius of 10 μm, and others, characteristic for the calculation, without considering the change in oil temperature, remain peculiar for the calculation with T_m = var.

According to figures 1.8-1.10, consideration of oil temperature decrease without any external heat sources results in qualitatively and quantitatively different results, demonstrating the need to consider this factor.

At this, typical characteristics of change in parameters, depending on initial R_0 and T_0 remain constant, as well as the initial amplitude values of growth rates, accelerations and other parameters, regardless of whether the change in oil temperature is considered or not.

Thus, the vapor phase growth model without considering change T_m results in the fact that vapor volume increases, as a result, the radius grows R_4 until the entire water evaporation.

This model makes it possible to describe in a more correct formulation the vapor phase growth in the presence of oil, as a surfactant, considering vapor phase formation at the water-oil interface.

The model of vapor phase growth, considering change in heat supply from oil with T_m = var allows us to consider and study the processes that occur when emulsions boil.

The problem of the effect of neighbouring vapor formations on the vapor phase growth dynamics, creating, in combination, a complex hydrodynamic situation in oil volume, require further study.

If the emulsion volume moves in the flow, then vapor volume deformations occur, resulting in its tearing off the water surface and water droplet breaking.

Dynamic parameters of oil-vapor interface in the presence of, for example, three particles, one of which being between two others, under conditions of their uneven boiling up, can result in Rayleigh-Taylor or Kelvin-Helmholtz instabilities, resulting in the vapor volume collapse and possible water droplet destruction. But the conditions, required for implementation of these phenomena, remain unclear.

References

[1.1] Dolinsky A.A., Pavlenko A.M., Basok B.I., Thermophysical Processes in Emulsions, Naukova Dumka, Kiev 2005, p. 265.

[1.2] Ivanitsky G.K., Modeling of the processes of deformation and droplets breakup when moving in liquid. *Heat-process engineering*. Vol. 19. No 1, 1997, pp. 9-16.

[1.3] Shima A., Tomita Y., Ohno T., Temperature effects on single bubble collapse and induced impulsive pressure. J.Fluid Eng., Vol. 110, No. 2, 1988, pp. 194-199.

[1.4] Teslenko V.S., Experimental investigation of bubble collapse at laser induced breakdown in liquids. Cavitation and Inhomogeneities in Underwater Acoustics (Ed. Lauterborn W.), NN.: Springer, 1980, pp. 30-34.

[1.5] Ivanitsky G.K., Destruction of emulsion droplets in adiabatically flashing flows. *Heat-process engineering,* Vol. 21, No. 4-5, 1999, pp.10-15.

[1.6] Reed R., Prausnitz J., Sherwood T., Properties of gases and liquids: Reference book. Leningrad: Khimiya, 1982, 592 p.

[1.7] Rayleigh L., On the pressure developed in a liquid during the collapse of a spherical cavity, Philos. Mag. 34, 2017, pp. 94-98.

[1.8] Hegedűs F., Stable bubble oscillations beyond Blake's critical threshold, Ultrasonics 54 (4), 2014, pp. 1113-1121.

[1.9] Avksentyuk B.P., Ovchinnikov V.V., The dynamics of explosion boiling of toluene under subatmospheric pressure, High Temp. 17 (4), 1999, pp. 606-613.

[1.10] Colonius T., Hagmeijer R., Ando K., Brennen C.E., Statistical equilibrium of bubble oscillations in dilute bubbly flows, Phys. Fluids 20 (4), 2008, pp. 40-52.

[1.11] Alhelfi A., Sunden B., Numerical investigation of an oscillating gas bubble in an ultrasonic field, 10th International Conference on Heat Transfer, Fluid Mechanics and Thermodynamics. Orlando, 2014, pp. 315-322. URL:https://repository.up.ac.za/bitstream/ handle/2263/44673/Alhelfi Numerical.pdf.

[1.12] Tsukamoto O., Uyemura T., Observation of bubble formation mechanism of liquid nitrogen subjected to transient heating, Adv. Cryog. Eng. 25, 1980, pp. 476-482.

[1.13] Dolinsky A.A., Ivanitsky G.K., Theoretical justification of the discrete-pulse energy input. 1. Model of the dynamics of a single vapor bubble. *Heat-process engineering*, Vol. 17, No. 5, 1995, pp. 3-29.

[1.14] Pavlenko A.M., Basok B.I., Laws of boiling of emulsified liquids. *Heat-process engineering*, Vol. 26, No. 1, 2004, pp. 21-25.

[1.15] Pavlenko A., Koshlak H., Słowak A., Stability of multiphase liquid media (2019) IOP Conf. Ser.: Earth Environ. Sci. 227 042032 https://doi.org/10.1088/1755-1315/227/4/042032.

[1.16] Pavlenko A., Koshlak H., Formation of the steam phase in superheated liquids in the state of metastable equilibrium, Eastern-European J. Enterprise Technol. 5 (589), 2017, pp. 35-42.

[1.17] Kumar S., Kumar R., Gandhi K.S., Alternative mechanism of drop breakage in stirred vessels. Chem. Engng. Sci., Vol. 46, No. 10, 1991, pp. 2493-2490.

[1.18] Hesketh R.P., Etchells A.W., Russell T.W., Bubble breakage in pipeline flow. Chem. Engng. Sci., Vol. 46, No. 1, 1991, pp. 1-10.

[1.19] Pavlenko A., Change of emulsion structure during heating and boiling. *International Journal of Energy for a Clean Environment*, 20(4), 2019, pp. 291-302. DOI: 10.1615/InterJEnerCleanEnv.2019032616.

[1.20] Clark N., Drop breakup in a turbulent flow. II. Experiments in a small mixing vessel. Chem. Engng. Sci., Vol. 43, No. 3, 1988, pp. 683-692.

[1.21] Pavlenko A.M., Thermodynamic Features of the Formation of Hydrocarbon Hydrates. Energies 2020, 13, 3396; doi:10.3390/en13133396.

[1.22] Pavlenko A.M., Basok B.I., Kinetics of water evaporation from emulsions. *Heat Transfer Research*, 36 (5), 2005, pp. 425-430.

[1.23] Pavlenko A.M., Dispersed phase breakup in boiling of emulsion, *Heat Transfer Research*, Volume 49, Issue 7, 2018, pp. 633-641. DOI: 10.1615/HeatTransRes. 2018020630.

[1.24] Pavlenko A., Energy conversion in heat and mass transfer processes in boiling emulsions. *Thermal Science and Engineering Progress,* Vol. 15, 1 March 2020, 100439. https://doi.org/10.1016/j.tsep.2019.100439.

[1.25] Brian P.L.T., Hales H.B., Sherwood T.K., Transport of heat and mass between liquids and spherical particles in an agitated tanks. A.I.Ch.E.Journ, Vol. 15, No. 5, 1969, pp. 727-732.

[1.26] Hesketh R.P., Etchells A.W., Russell T.W., Bubble breakage in pipeline flow. Chem. Engng. Sci., Vol. 46, No. 1, 1991, pp. 1-10.

[1.27] Roesle M.L., Kulacki F.A., An experimental study of boiling in dilute emulsions, part A: heat transfer, Int. J. Heat Mass Transf. 55 (7-8), 2012, pp. 2160-2165, https://doi. org/10.1016/j.ijheatmasstransfer.2011.12.020.

[1.28] Pavlenko A., Koshlak H., Usenko B., The processes of heat and mass exchange in the vortex devices Metallurgical and Mining Industry, 6(3), 2014, pp. 55-59.

[1.29] Pavlenko A.M., Basok B.I., Avramenko A.A., Heat Conduction of a Multi-Layer Disperse Particle of Emulsion. *Heat transfer research*, Vol. 36, Issue 1-2, 2005, pp. 55-61.

[1.30] Pavlenko A.M., Basok B.I., Regularities of Boiling-Up of Emulsified Liquids. *Heat transfer research,* Vol. 36, Issue 5, 2005, pp. 419-424.

[1.31] Mura E., Massoli P., Josset C., Loubar K., Bellettre J., Study of the micro-explosion temperature of water in oil emulsion droplets during the Leidenfrost effect, Exp. Therm Fluid Sci. 43, 2012, pp. 63-70, https://doi.org/10.1016/j.expthermflusci.2012. 03.027.

[1.32] Avksentyuk B.P., Ovchinnikov V.V., Plotnikov V.Ya., Dynamic effects on interphase surface during the disintegration of superheated near-wall liquid, Proc. Int. Cent. Heat Mass Transfer 33, 1991, pp. 583-598.

[1.33] Gasanov B.M., Bulanov N.V., Effect of the droplet size of an emulsion dispersion phase in nucleate boiling and emulsion boiling crisis, Int. J. Heat Mass Transf. 88, 2015, pp. 256-260, https://doi.org/10.1016/ j.ijheatmasstransfer.

[1.34] Dolinsky A.A., Basok B.I., Nakorchevsky A.I., Adiabatically boiling flows. Publishing house: Naukova Dumka, Kiev 2001, 208 p.

[1.35] Wang C.Y., Calabrese R.V., Drop breakup in turbulent stirred tank contactors. A.I.Ch.E.Journ., Vol. 32, No. 4, 1986, pp. 667-674.

[1.36] Pavlenko A.M., Basok B.I., Regularities of boiling-up of emulsified liquids. *Heat Transfer Research*. 36 (5), 2005, pp. 419-424.

[1.37] Rozentsvaig A.K., Strashinskii Ch.S., Regimes of heat transfer during boiling emulsions with low-temperature dispersed phase, Appl. Math. Sci. 9 (112), 2015, pp. 5593-5601, https://doi.org/10.12988/ams.2015.57474.

[1.38] Roesle M.L., Lunde D.L., Kulacki F.A., Boiling heat transfer to dilute emulsions from a vertical heated strip, J. Heat Transfer 137 (4), 2015, 8 p., https://doi.org/10.1115/1.4029456.

[1.39] Shilyaev M.I., Tolstykh A.V., Modelling of gas absorption processes in bubblers, Thermophys. Aeromech. 20 (5), 2013, pp. 565-576.

[1.40] Fauser J., Mitrovic J., Some features of boiling fronts on heated surfaces, Proc. 11th IHTC, Kyongju, August 23-28, vol. 2, 1998, pp. 377-382.

[1.41] Medvedev R.N., Chernov A.A., The calculation of thermal grows of the toroidal bubble on current concentrator in electrolyte, Modern Sci. 2 (10), 2012, pp. 50-56.

[1.42] Hegedűs F., Stable bubble oscillations beyond Blake's critical threshold, Ultrasonics 54 (4), 2014, pp. 1113-1121.

[1.43] Grace H.P., Dispersion phenomena in high viscosity immiscible fluid systems and application of static mixers as dispersion devices in such systems. Chem. Engng. Commun., Vol. 14, 1982, pp. 225-277.

[1.44] Sovova H., A model of dispersion hydrodynamics in a vibrating plate extractor. Chem. Engng. Sci., Vol. 38, No. 1, 1983, pp. 1863-1872.

[1.45] Konno M., Arai K., Saito S., The effect of stabilizer on coalescence of dispersed drops in suspension polymerization of system. J. Chem. Engng. Japan, Vol. 15, 1982, pp. 131-135.

[1.46] Dolinsky A.A., Ivanitsky G.K., Use of discrete-pulse energy input in various production processes. Proc. International Conf. on Transport Phenomena Science and Technology. Beijing (China), Higher Education Press, 1992, pp. 89-100.

[1.47] Kumar S., Kumar R., Gandhi K.S., Alternative mechanism of drop breakage in stirred vessels. Chem. Engng. Sci., Vol. 46, No. 10, 1991, pp. 2493-2490.

DYNAMIC EFFECTS OF THE HOMOGENIZATION PROCESS THERMAL INITIATION

2.1. Slow heating

The scheme of mathematical model of emulsion droplet heating is shown in figure 2.1.

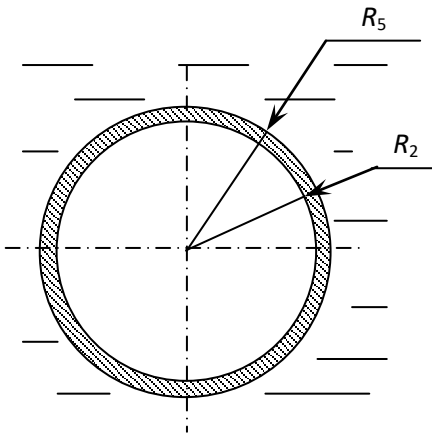

FIGURE 2.1. Heating model of a water droplet surrounded by oil layer (R_2 is water-oil interface radius; R_5 is oil-air interface radius).

The scheme shows a water droplet with radius R_2 and surrounded with oil layer δ_m thick. This typical droplet is spherical in shape, oil evenly surrounds water surface, the whole system is heated by heat transfer with the environment, for example, air with temperature T_{air}.

In the one dimension classical diffusion problems are written as

$$\frac{\partial T}{\partial \tau} = \frac{\lambda}{c\rho}\left(\frac{\partial^2 T}{\partial x^2} + \frac{i-1}{x}\cdot\frac{\partial T}{\partial x}\right) + \frac{q_V}{c\rho} \tag{2.1}$$

where: i = 1 – for plate; i = 2 – for cylinder; i = 3 – for sphere; $T = f(x,\tau)$ – temperature.

Equation (2.1) is linear as λ, c, ρ are not temperature functions.

For the model, shown in figure 2.1, the body shape is a sphere, there are no internal heat sources ($q_V = 0$), you can write down the differential equation of thermal conductivity:

– for water

$$\frac{\partial T_w(r,\tau)}{\partial \tau} = a_w \left(\frac{\partial^2 T_w(r,\tau)}{\partial r^2} + \frac{2}{r} \cdot \frac{\partial T_w(r,\tau)}{\partial r} \right); \quad \tau > 0, \quad 0 < r < R_2 \tag{2.2}$$

where $a_w = \dfrac{\lambda_w}{c_w \rho_w}$ is water temperature conductivity coefficient;

– for oil layer

$$\frac{\partial T_m(r,\tau)}{\partial \tau} = a_m \left(\frac{\partial^2 T_m(r,\tau)}{\partial r^2} + \frac{2}{r} \cdot \frac{\partial T_m(r,\tau)}{\partial r} \right); \quad \tau > 0, \quad R_2 < r < R_5 \tag{2.3}$$

Initially, water and oil have the same temperature value.

Then the initial condition will look as follows

$$T(r,0) = T_0 = \text{const} \tag{2.4}$$

At oil-air interface, at a known air temperature T_{air} and heat transfer coefficient α, the third type boundary condition is written

$$-\lambda_m \left. \frac{\partial T_m}{\partial r} \right|_{r=R_5} = \alpha \left(T_{air} - T_5 \right) \tag{2.5}$$

Assuming that the contact between water and oil is perfect, the fourth type boundary condition can be written at water-oil interface

$$-\lambda_m \left. \frac{\partial T_m}{\partial r} \right|_{r=R_2} = -\lambda_w \left. \frac{\partial T_w}{\partial r} \right|_{r=R_2} \tag{2.6}$$

We set thermal symmetry condition in the water droplet centre

$$-\lambda_w \left. \frac{\partial T_w}{\partial r} \right|_{r=0} = 0 \tag{2.7}$$

According to [2.1, 2.2], for spherical bodies in a flow, an equation can be written to determine the Nusselt number

$$\mathrm{Nu} = 2 \cdot \left(1 + \beta \cdot \mathrm{Re}^{0.5} \cdot \mathrm{Pr}^{0.33}\right) \tag{2.8}$$

where: $\mathrm{Re} = \frac{wd}{v}$ – Reynolds criterion; $\mathrm{Pr} = \frac{v}{a}$ – Prandtl criterion; β – coefficient ($\beta = 0.34$).

For stationary medium (Re = 0) and criterion Re << 1 the Nusselt number is equal to [2.3, 2.4]

$$\mathrm{Nu} = 2 \tag{2.9}$$

Heat transfer coefficient, derived from the Nusselt number

$$\alpha = \mathrm{Nu} \frac{\lambda_{air}}{d} \tag{2.10}$$

where d is characteristic size (for a sphere – diameter).

Substituting (2.9) into (2.10) and taking into account that the diameter is equal, we obtain

$$\alpha = \frac{\lambda_{air}}{R_5} \tag{2.11}$$

From equation (2.11) it is evident that at λ_{air} = const heat transfer coefficient α is inversely proportional to the emulsion droplet radius at oil-air interface, i.e. with increasing radius, the heat transfer coefficient decreases and vice versa.

It means that for smaller emulsion droplets, the heating process will proceed more intensively than for large droplets.

The emulsion droplet heating process continues until the temperature at water-oil interface reaches water boiling point.

We assume that boiling occurs under normal conditions, and then water boiling point is t_b =100°C (T_b = 373 K).

After the interface has reached temperature intensive evaporation begins from the water droplet surface (heating phase with boiling), resulting in vapor layer formation between the water droplet and oil layer, their thickness will increase over time.

The model of vapor layer growth is shown in figure 2.2.

In this case, water mass will decrease, the vapor volume will increase and, given that $\rho_n \ll \rho_w$, from one water volume during its boiling, a many times larger

vapor volume is formed; with vapor layer growth, oil-vapor interface radius will increase, thereby initiating oil layer stretching.

Assuming that oil layer volume remains constant, oil film thickness will decrease and, having reached its critical size, it will collapse.

The film critical size, when it breaks, is taken to be $\delta_m = 0.5$ μm [2.5].

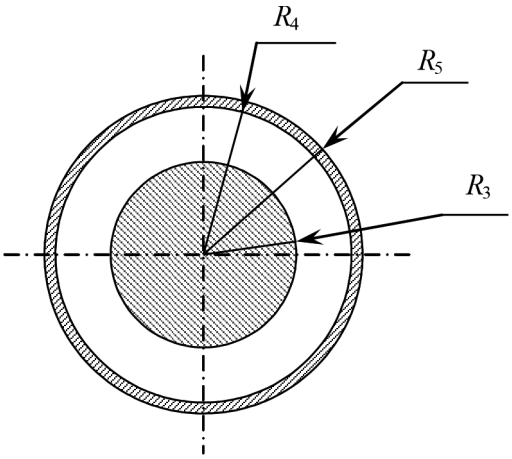

FIGURE 2.2. Model of vapor volume growth during water boiling when heated by air (R_3 is water-vapor interface radius; R_4 is vapor-oil interface radius; R_5 is oil-air interface radius).

For the model, shown in figure 2.2, differential equations of heat conductivity look as follows:

– for water

$$\frac{\partial T_w(r,\tau)}{\partial \tau} = a_w \left(\frac{\partial^2 T_w(r,\tau)}{\partial r^2} + \frac{2}{r} \cdot \frac{\partial T_w(r,\tau)}{\partial r} \right); \quad \tau > 0, \quad 0 < r < R_3 \qquad (2.12)$$

– for oil layer

$$\frac{\partial T_m(r,\tau)}{\partial \tau} = a_m \left(\frac{\partial^2 T_m(r,\tau)}{\partial r^2} + \frac{2}{r} \cdot \frac{\partial T_m(r,\tau)}{\partial r} \right); \quad \tau > 0, \quad R_r < r < R_5 \qquad (2.13)$$

The boundary condition at oil-air interface has the form of equation (2.5), but $\alpha = f(R_5, \tau)$.

We assume that water-vapor interface temperature during vapor volume growth will remain constant and equal to T_b, oil-vapor interface temperature in the process of intense heat transfer and vapor masses movement will not be much higher than T_b, thus, we assume that this temperature is equal to 373 K.

Then the boundary conditions at water-vapor and oil-vapor interfaces can be written as the first type boundary conditions

$$T_3(\tau) = T_b = 373 \text{ K} \tag{2.14}$$

$$T_4(\tau) = T_b = 373 \text{ K} \tag{2.15}$$

The central boundary condition for a water droplet is a symmetry condition and has the form of equation (2.7).

The criterion for destruction is a critical thickness of the oil film

$$\begin{aligned} \delta_m &= R_5 - R_4 \\ \delta_{m.cr} &\le 0.5 \text{ μm} \end{aligned} \tag{2.16}$$

Heat balance equation between oil film and water with vapor is as follows

$$Q_m = Q_n + Q_w + J \cdot L \tag{2.17}$$

where: Q_m – heat flow from oil layer; Q_n – heat flow for vapor layer heating; Q_w – heat flow for a water droplet heating.

Heat flow from oil level [2.6], is equal to

$$Q_m = \frac{4\pi\lambda_m \left(T_5 - T_4\right)}{\frac{1}{R_4} - \frac{1}{R_5}} \tag{2.18}$$

Under assumed boundary conditions (2.14) and (2.15), the temperature difference between oil wall and water surface is zero, therefore the heat flow, going for vapor layer heating is

$$Q_n = 0 \tag{2.19}$$

The heat, taken by a water droplet, is determined from the heat conductivity equation, which for spherical geometry looks as follows

$$q_V = \lambda_w \left[\frac{d^2 T_w}{dr^2} + \frac{2}{r} \frac{dT_w}{dr} \right] \tag{2.20}$$

Connection between Q_w and q_V looks as follows

$$q_V = \frac{Q_w}{V} = \frac{Q_w}{\pi d_3^3 / 6} \tag{2.21}$$

Equation (2.20) can be represented as

$$\frac{q_V}{\lambda_w} = \frac{1}{r^2}\frac{d}{dr}\left(r^2\frac{dT_w}{dr}\right) \tag{2.22}$$

By transforming equation (2.22) and integrating it, we get

$$r^2\frac{dT_w}{dr} = \frac{q_V}{\lambda_w}\frac{r^3}{3} + C_1 \tag{2.23}$$

By dividing (2.23) by r^2 and integrating again, we get

$$T_w(\tau) = \frac{q_V}{\lambda_w}\frac{r^2}{6} - \frac{C_1}{r} + C_2 \tag{2.24}$$

where C_1, C_2 are integrating constants.

Integrating constants are determined by boundary conditions.

At $r = 0$ (in the water droplet centre) $\frac{dT_w}{dr} = 0$ and as follows from equation (2.23), $C_1 = 0$. At $r = R_3$, temperature $T_w(r)$ is equal to water-vapor interface temperature. Then it follows from equation (2.24)

$$C_2 = T_3 - \frac{q_V}{\lambda_w}\frac{R_3^2}{6} \tag{2.25}$$

By inserting (2.25) into (2.24), we get

$$T_w(r) = \frac{q_V}{\lambda_w}\frac{r^2}{6} + T_3 - \frac{q_V}{\lambda_w}\frac{R_3^2}{6} \tag{2.26}$$

Equation (2.26) for the centre ($r = 0$) looks as follows

$$T_1 = T_3 - \frac{q_V}{\lambda_w}\frac{R_3^2}{6} \tag{2.27}$$

Considering (1.21), equation (2.27) will look as follows

$$Q_w = 8\pi R_3\lambda_w\left(T_3 - T_1\right) \tag{2.28}$$

Then equation (2.27) will be written as

$$\frac{4\pi\lambda_m\left(T_5-T_4\right)}{\frac{1}{R_4}-\frac{1}{R_5}}=8\pi R_3\lambda_w\left(T_3-T_1\right)+J\cdot L \tag{2.29}$$

From (2.29) vapor mass flow is equal to

$$J=\frac{1}{L}\left[\frac{4\pi\lambda_m\left(T_5-T_4\right)}{\frac{1}{R_4}-\frac{1}{R_5}}-8\pi R_3\lambda_w\left(T_3-T_1\right)\right] \tag{2.30}$$

The mass flow will change with the droplet growth, therefore, for a certain period of time $\Delta\tau$ the vapor mass, formed at water-vapor interface, can be calculated from equation

$$m_n=J\cdot\Delta\tau \tag{2.31}$$

Assuming that the heat transfer over the entire surface of the emulsion droplet will be the same, we assume that the amount of vapor, formed as a result of boiling on the water surface, will be evenly distributed over this surface.

The volume of water, transformed into vapor, and the volume of vapor, formed as a result of boiling are respectively equal to

$$V_w=\frac{m_n}{\rho_w};\qquad V_n=\frac{m_n}{\rho_n} \tag{2.32}$$

A change in water mass and volume results in a decrease in water-vapor interface radius to value

$$R_3^*=\left(R_3^3-\frac{3V_w}{4\pi}\right)^{1/3} \tag{2.33}$$

An increase in vapor volume as a result of water boiling causes an increase in oil-vapor phase interface radius and an increase in the vapor layer to values

$$R_4^*=\left(R_3^3+\frac{3V_n}{4\pi}\right)^{1/3};\qquad \gamma=R_4^*-R_3^* \tag{2.34}$$

Oil volume with a decrease in oil film thickness remains unchanged and is determined from equation

$$V_m=\frac{4}{3}\pi\left(R_5^3-R_4^3\right) \tag{2.35}$$

Then the oil-air interface radius will be equal to

$$R_5^* = \left(\left(R_4^* \right)^3 + \frac{3V_m}{4\pi} \right)^{1/3} \tag{2.36}$$

The growth rate of oil-vapor interface radius and decrease in the water-vapor interface radius can be determined from equations

$$w_4 = \frac{dR_4}{d\tau}; \qquad w_3 = \frac{dR_3}{d\tau} \tag{2.37}$$

We assume that at the initial moment of time, a droplet of emulsion, consisting of water, surrounded by a layer of MC-20 oil [2.1] has the same temperature over the entire section, equal to t_0 = 10°C. At a certain point in time, it is placed in air t_{air}, higher than t_0. We use the finite difference method for calculation.

Thermophysical properties of water, oil and vapor at the corresponding temperatures are determined from [2.6].

The calculation results are presented in figures 2.3-2.8.

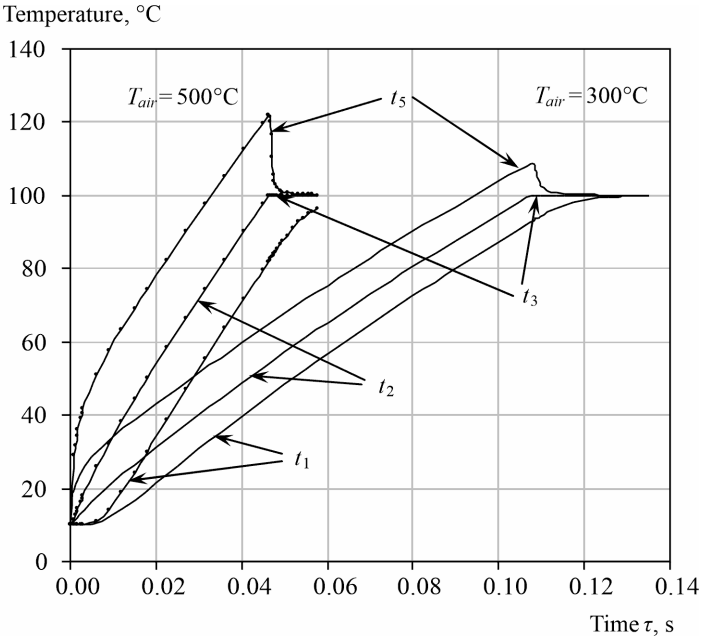

FIGURE 2.3. Diagram of emulsion droplet heating at different air temperatures (R_2 = 100 μm, δ_m = 15 μm, t_0 = 10°C).

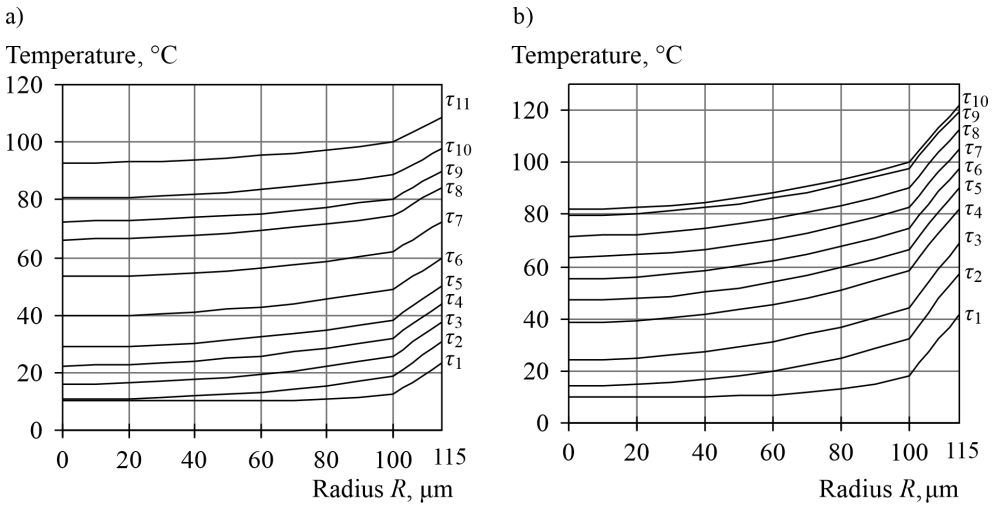

FIGURE 2.4. Temperature distribution over the emulsion droplet section at air temperatures t_{air} = 300°C (a) and 500°C (b) at different time moments τ_i (R_2 = 100 μm, δ_{M0} = 15 μm, t_0 = 10°C): a) τ_1 = 0.002 s; τ_2 = 0.007 s; τ_3 = 0.014 s; τ_4 = 0.021s; τ_5 = 0.028s; τ_6 = 0.04 s; τ_7 = 0.056 s; τ_8 = 0.072 s; τ_9 = 0.08 s; τ_{10} = 0.091 s; τ_{11} = 0.11 s; b) τ_1 = 0.003 s; τ_2 = 0.009 s; τ_3 = 0.015 s; τ_4 = 0.023 s; τ_5 = 0.027 s; τ_6 = 0.32 s; τ_7 = 0.036 s; τ_8 = 0.041s; τ_9 = 0.045 s; τ_{10} = 0.046 s.

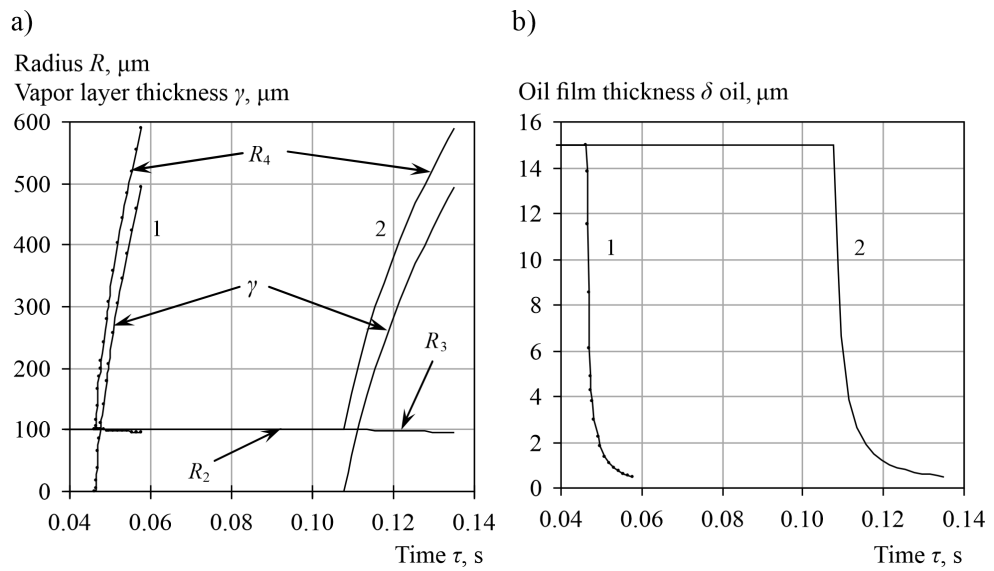

FIGURE 2.5. Change in the vapor layer interface radii and thickness in time (a), oil film thickness (b) at t_{air} : 1 – 500°C, 2 – 300°C.

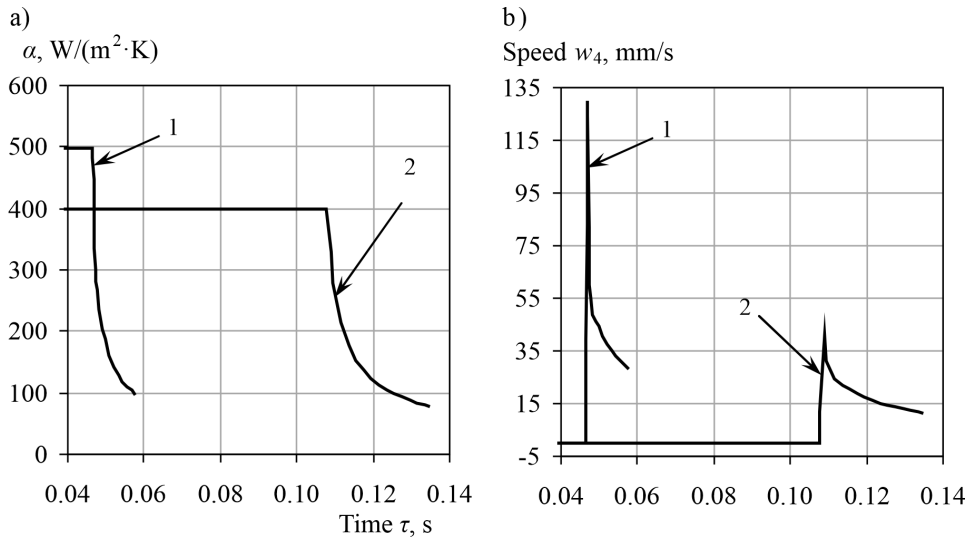

FIGURE 2.6. Time variation of the heat transfer coefficient from air to the water droplet surface, covered with oil layer (a) and the rate of oil-vapor interface motion (b) at different air temperatures: 1 – 500°C, 2 – 300°C.

Let us analyse presented graph curves for t_{air} = 300°C. Figure 2.3 shows the diagram of an emulsion droplet heating. This figure shows three heating phases.

The first one is the initial (inertial) phase, when a temperature of the water droplet centre remains constant and equal to the initial temperature. In this phase, the rate of temperature increase of oil-air interface is of the greatest importance.

The second one is a phase of regular heating; in this phase, rates of temperature changes t_1, t_2, t_5 remain constant, and the shape of temperature increase curves is almost a straight line.

The first and second heating phases are also seen in figure 2.4a, showing the temperature distribution over the emulsion droplet section.

In the second phase, temperature distribution curves for certain moments of time are equidistant.

In this case, the temperature difference over the oil layer section is higher than over water droplet section; it can be explained by lower oil temperature conductivity coefficient and the fact that oil is the first one to take up all the heat from the air, which it transfers it to water. It is true for a certain thickness value of oil layer.

These two phases take $\Delta\tau \approx 0.11$ s. The third phase is characterized by appearance of a vapor layer, while water-vapor interface radius R_3 decreases, oil-vapor interface radius R_4 increases, which can be seen from figure 2.5a, showing the change in radii of interfaces in time.

In this case, the growth rate of a vapor layer, i.e. rate of change in the oil-vapor interface radius w_4, will occur at the beginning of water boiling, increasing intensively, reaching its maximum, and then gradually decreasing, as shown in figure 2.6b. This figure shows that, for example, for an air temperature of 300°C, the maximum growth rate is $w_4^{\max} \approx 41$ mm/s. This maximum can be explained by the fact that from the initial moment of vapor volume growth, the processes of heat supply to water surface will play the main role, then "volumetric" factors will have a significant effect, i.e. to increase the oil-vapor interface radius by the same amount, when it becomes higher than the initial one, more vapor is already needed than it can be formed as a result of water boiling.

The effect of this factor can be shown in figure 2.5a. If this factor did not have its effect, then curves of changes R_4 and γ would be straight lines with the same amount of heat supplied.

This figure shows that the vapor layer increases almost to 500 μm, required breaking the oil film, while the oil-vapor interface radius increases by a factor of ≈5.

The change in oil layer thickness is shown in figure 2.5b, it can be seen that this thickness remains unchanged during emulsion droplet heating. During vapor volume growth, δ_m first, it abruptly decreases (curve $\delta_m = f(\tau)$ is practically vertical), then thickness decreases not so intensively; within its limit the presented curve approaches the horizontal line. Figure 2.6a shows the time variation of heat transfer coefficient α. Starting from the initial moment of time and until the moment of a vapor layer appearance, the heat transfer coefficient α has a constant value, equal to the maximum, and in the process of the oil-air interface radius, it decreases in inverse proportion to this radius.

The third phase takes about 0.025 s. At the same time, during this period, the temperature of a water droplet temperature is almost 100°C, the temperature of an oil-air interface during heating without boiling reaches a value of ≈109°C, from the moment of a vapor layer appearance, it increases by ≈0.1°C, then it sharply decreases and at the moment an oil film rupture is almost 100°C. It means that oil evaporation can be neglected, because most oils boil at a temperature of 200÷300°C, and evaporation at a temperature t_5 = 109°C will be negligibly low. Thus, the total temperature of the formed components will be equal to 100°C, and in the process of the vapor layer increase, the oil film will be cooled, even despite heating from high temperature air.

Figures 2.3-2.6 also show calculations of the same emulsion droplet, but at an air temperature of 500°C. As can be seen from these figures, heating and growth processes of the vapor phase until the oil film destruction is reduced in time by more than two times, compared with the process at t_{air} = 300°C, but the ratio between heating time and boiling time remains practically the same.

Figures 2.3 and 2.4 show that the temperature difference in the oil layer becomes even higher in comparison with the temperature difference over the water droplet section.

The oil-air interface temperature reaches ≈122°C, and during the vapor volume growth also reaches 100°C, while the temperature of the water droplet centre is equal to $t_1 \approx 97$°C. Thus, the water droplet centre, when the oil layer is destructed, does not even heat up to the boiling point, which can result in merging of oil with water and a new emulsion droplet formation, but with different sizes, i.e. the average water temperature after the oil film destruction is less than the boiling point under the given conditions.

The heat transfer coefficient from figure 2.6a, is equal at the beginning of ≈500 W/(m^2·K), which is more than when heated by air at a temperature of 300°C. It is affected by the air thermal conductivity coefficient, its value grows with temperature increase.

The vapor volume growth rate (oil-vapor interface) reaches a value of ≈130 mm/s, which is more than three times higher than the growth rate at temperature t_{air} = 300°C, the curve in figure 2.6b has the more expressed maximum. These results show that the pattern of the temperature difference changes qualitatively: the temperature difference over the water droplet section exceeds the difference over the oil layer section. The oil surface temperature reaches a value of ≈112.5°C, the temperature of the water droplet centre at the moment of oil film destruction is ≈80°C, i.e. subcooling to the boiling point becomes even higher. The ratio between boiling and heating times goes down.

The total droplet radius at the moment of oil film destruction is approximately four times higher than the initial one, in comparison with the similar radius at δ_0 = 15 μm. It is obvious that the total time of droplet heating and vapor phase growth until the oil film destruction decreases not so significantly with a decrease in the oil film thickness compared to an increase in the ambient temperature (in this case, air).

The behaviour of the interface radii, vapor layer size, oil film thickness and the heat transfer coefficient remains the same as for δ_0 = 15 μm, except that the heat transfer coefficient is initially of greater importance. The oil-vapor interface motion rate, as in the case of other ambient temperatures and oil film thickness, also has a pronounced maximum.

2.2. Disturbance of metastable equilibrium with a sharp decrease in pressure

Calculations of the vapor phase growth with a sharp drop in pressure will be performed for the model shown in figure 2.2 based on equations (2.12)-(2.37).

In this case, we assume that at the initial moment of time there is a water droplet covered with an oil layer, this system is heated up to 180°C at a certain pressure, excluding water boiling.

At some point in time, such an emulsion droplet is thrown into the atmospheric pressure zone, as a result, water becomes superheated relative to its saturation temperature at atmospheric pressure and, as a result, it begins to boil, forming a vapor layer, which, increasing in size will result in the oil layer destruction.

Calculation results for a water droplet with $R_3(0) = 100$ μm in radius and oil layer thickness $\delta_m(0) = 15$ μm, with initial temperature of 180°C, with a sharp drop in pressure to atmospheric and for ambient temperature (air) $t_{air} = 300$°C are shown in figure 2.7-2.9.

For the calculation, it was assumed that as a result of the pressure relief, the water-vapor and vapor-oil interface temperature will be equal to water boiling point of water at pressure p_a (100°C), the boiling process will occur only on the water surface (water-vapor interface).

The figures demonstrate that the vapor phase growth under pressure relief goes intensively than during simple heating at a certain ambient temperature.

Thus, time before oil film destruction t heating by ambient air is ≈0.025 s, with pressure relief ≈6 ms, that is nearly four times faster.

Figure 2.7a shows that the oil-air interface temperature at the beginning of the vapor phase growth slightly increases ($\Delta T_5 \approx 0.5$°C) and then rapidly goes down $t_0 \approx 100$°C.

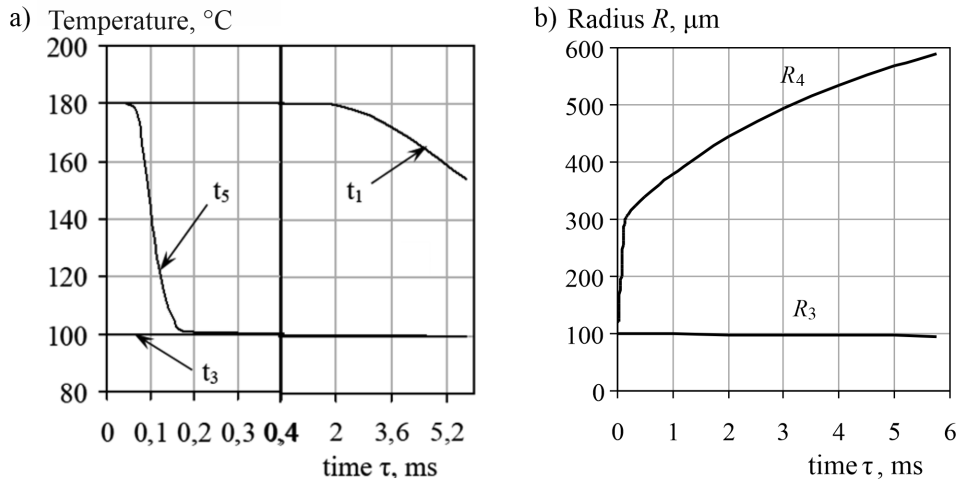

FIGURE 2.7. Changes in the phase interface temperatures and water droplet centre (a), water-vapor and oil-vapor interface radii (b) over time $R_3(0) = 100$ μm, $\delta_m(0) = 15$ μm, $t_0 = 10$°C.

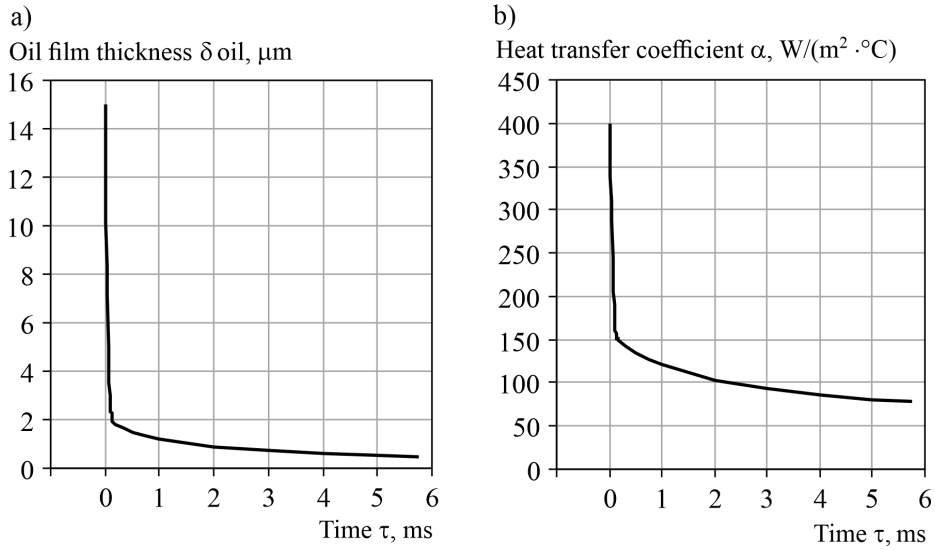

FIGURE 2.8. Change in time of the oil film thickness (a) and heat transfer coefficient from air to the water droplet surface, covered with an oil layer (b) under the conditions, shown in figure 2.7.

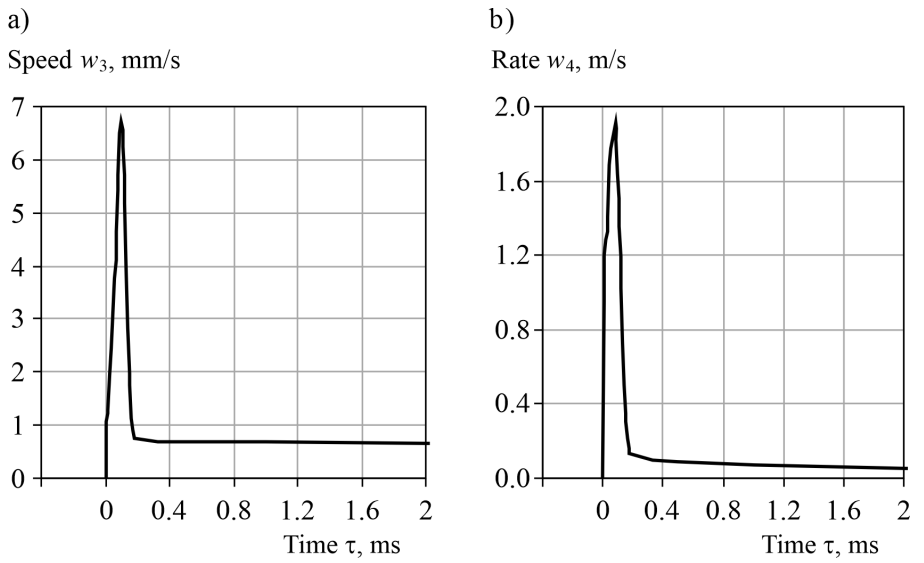

FIGURE 2.9. Change in time of water-vapor (a) and oil-vapor interface motion rate (b) under the conditions are shown in figure 2.7.

Unlike an almost identical temperature change curve t_5 (fig. 2.3) temperature in a shorter period of time decreases from a much higher initial value, i.e. the process is

much more intense. The water droplet centre temperature t_1 by the oil film destruction moment goes down $t_0 \approx 150$°C.

The characteristic difference between the graphs shown in figures 2.7-2.9 is a clear kink in comparison with figures 2.5, 2.6.

In this case, both a typical kink in curve dependences and decrease in time until the oil film destruction can be attributed to a qualitative change of heat flow direction with a pressure relief: all heat flows will be directed to a water-vapor interface and the entire amount of heat will go to vaporization (only a small part to oil film heating).

Oil temperature also significant in the initial period of time, subsequently determining the dominant role of oil in the heat transfer process.

By the curve behaviour in the oil-vapor interface radius growth interface R_4 (fig. 2.7b) it is obvious in the initial period of the vapor phase growth, a process proceeds most intensively, confirming the increase in the interface motion rate (fig. 2.9b) to $w_4 \approx 2$ m/s. Intense growth of the vapor phase results in a rapid temperature decrease t_5 (fig. 2.7a), due to heat transfer by the oil film for vaporization and its thinning (fig. 2.8a). The environment (air) even at 300°C cannot maintain temperature t_5 at constant level.

Further growth of the vapor phase occurs with a lower intensity than in the initial period, due to a decrease in oil film domination in the heat transfer process, confirmed by figures 2.7-2.9.

Figure 2.9a shows that the water-vapor interface motion rate also has a peak nature of its change, and subsequently acquires an almost constant value; it can be explained by the quantitative balance between the heat supplied to the water-vapor interface and the heat required to reduce radius R_3 by identical values.

2.3. Comparison of obtained and experimental results

There are no models that would consider the processes, occurring in emulsions, just as there were no experiments, and, consequently, no experimental data, characterizing the vapor phase growth during boiling of the emulsion aqueous phase.

Current data on vapor bubbles growth during boiling on heated surfaces, during boiling in a liquid volume, as well as as a result of pressure relief from the equilibrium value, can be compared with the presented model results only in terms of time scales, in the nature of curve changes, since the considered model takes into account the effect of the oil film heat and mass transfer processes.

Let us compare the experimental data, analysing vapor bubbles growth during liquid boiling as a result of heat supply from the surface [2.7] (fig. 2.10a) with

calculation results at heating by air. Comparing figure 2.10a and figure 2.5a, it can be seen that the behaviour of the curve of oil-vapor interface radius and the curve from [2.7] are identical.

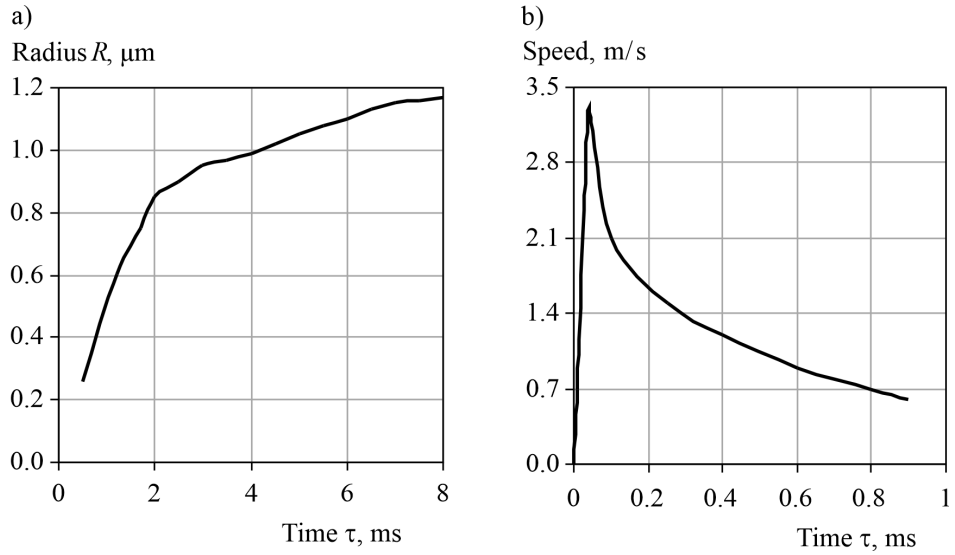

FIGURE 2.10. Experimental data on a vapor bubble growth on a microsurface (a) according to [2.7] and change in the vapor bubble growth rate in time (b) according to [2.8].

At the same time, with an increase in the ambient temperature and a decrease in the oil layer thickness, the time interval for the vapor phase growth decreases.

Comparing time intervals of the vapor phase growth, obtained by the model until the moment of oil film rupture, we can conclude that they will be higher than shown in figure 2.10a. It can be explained by the fact that the oil film generated thermal resistance, thereby reducing heat transfer between the environment and a water droplet, as well as by a certain inaccuracy in comparing heating from the surface and in air.

If we consider the graph in [2.9] of a vapor bubble growth rate during pressure relief (fig. 2.10b), we can compare it with similar graphs for the oil-vapor interface growth rate when heated by air (fig. 2.6b) and pressure relief (fig. 2.9b), and determine similar character of change in curves in figure 2.10b, especially curve $w_4(\tau)$ when heated by air at 300°C (fig. 2.6b), as well as the same peak in the change in these curves.

Comparing time intervals and peak values of the change in interface motion rates, it is observed that when heated without pressure relief, these rates are strikingly different, for example, ≈0.13 m/s in figure 2.10b.

Comparing the data in figure 2.10b with calculation results, using the model of the vapor phase growth when pressure is released to atmospheric pressure (fig. 2.9b), it can be seen that the behaviour in the oil-vapor interface growth rat differs from that in figure 2.10b, only peakedness remains. The maximum rate values are different, which is explained by the oil film presence and other conditions of the numerical study.

Figure 2.11 shows dependences of the change in a vapor bubble radius, when it grows in water as a result of pressure relief according to the model of a single vapor bubble dynamics and other models presented in [2.1].

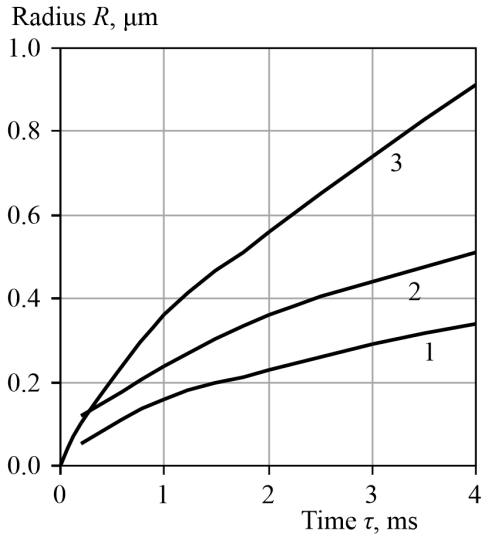

FIGURE 2.11. Time change of a vapor bubble radius according to: 1 – [2.1], 2 – [2.2], 3 – [2.9].

Comparing these graphs with pressure relief results in figure 2.7b, we can conclude that the time interval in all cases is within milliseconds range.

The behaviour of curves is also identical (disregarding the initial phase, shown in figure 2.7b).

The proposed model is idealized, it is based on certain assumptions.

It does not consider the action of capillary, dynamic and inertial forces.

For instance, this model disregards pressure effect on the vapor phase growth during its relief, a surface tension and viscosity effects (the oil film dynamic action when it is thinned).

The issue of increased temperature (overheating) of boiling water is not considered.

In practice, there are no such ideal processes, but, as a rule, they deal with flows in which turbulent flows arise, i.e. complex hydrodynamic environment.

But this model makes it possible to assess heat and mass transfer features in the presence of films, covering liquid droplets, as well as obtain graphical dependences of various parameters with a change in the heating medium temperature, film thickness, initial droplet radii, etc., which cannot be done using mathematical models of the above processes.

References

[2.1] Dolinsky A.A., Pavlenko A.M., Basok B.I., Thermophysical Processes in Emulsions, Naukova Dumka, Kiev, 2005, p. 265.

[2.2] Pavlenko A., Change of emulsion structure during heating and boiling. International *Journal of Energy for a Clean Environment*, 2019, 20(4), pp. 291-302. DOI: 10.1615/InterJEnerCleanEnv.2019032616.

[2.3] Pavlenko A.M., Dispersed phase breakup in boiling of emulsion, *Heat Transfer Research*, Vol. 49, Issue 7, 2018, pp. 633-641. DOI: 10.1615/HeatTransRes. 2018020630.

[2.4] Pavlenko A., Energy conversion in heat and mass transfer processes in boiling emulsions. *Thermal Science and Engineering Progress,* Vol. 15, March 2020, 100439. https://doi.org/10.1016/j.tsep.2019.100439.

[2.5] Pavlenko A., Melnyk V., Destruction of the Structure of Boiling Emulsions, *Rocznik Ochrona Środowiska*, 2020, Vol. 22, pp. 70-81.

[2.6] Pavlenko A., Koshlak H., Formation of the steam phase in superheated liquids in the state of metastable equilibrium, Eastern-European J. Enterprise Technol. 5 (589), 2017, pp 35-42.

[2.7] Avksentyuk B.P., Ovchinnikov V.V., The dynamics of explosion boiling of toluene under subatmospheric pressure, High Temp. 17 (4), 1999, pp. 606-613.

[2.8] Shima A., Tomita Y., Ohno T., Temperature effects on single bubble collapse and induced impulsive pressure. J.Fluid Eng. Vol. 110, No. 2, 1988, pp. 194-199.

[2.9] Pavlenko A., Koshlak H., Słowak A., Stability of multiphase liquid media. Earth and Environmental Science, Energy and Scientific Research, Vol. 227, No. 4, 2019, pp. 1-11.

DISPERSED PHASE BREAKING AT EMULSION BOILING

3.1. Mutual dynamic effects of neighbouring bubbles

The classical theory of deformation and destruction of droplets, depending on the flow turbulence degree, belongs to Kolmogorov [3.1], who considered this process as a manifestation result of a great number of random phenomena and, based on the theory of probability, obtained the logarithmic size distribution of droplets. When considering these processes, it is important to determine that the droplet is resistant to action of destructive forces. The main factors, causing droplet breaking in a liquid medium are as follows: the relative rate of the flow over a droplet, flow acceleration, dispersed and continuous phase density, surface tension, viscosity of both liquids and characteristic time of their interaction.

Types of hydrodynamic instability arising under the action of these factors will be as follows [3.2]:

1. Tolmien-Schlichting instability, resulting from the transition from laminar to turbulent flow.
2. Kelvin-Helmholtz instability, observed when two fluids move at different tangential velocities, relative to the interface. Surface rupture can be observed even at low rates when the flow is laminar.

   This type of instability is characterized by Weber criterion

$$\mathrm{We} = \frac{2R\rho w^2}{\sigma} \tag{3.1}$$

   Critical Weber criterion is assumed as equal to $\mathrm{We}_{cr} = 10$ [3.3, 3.4].

   The Rayleigh-Taylor instability, occurring, when the surface between two fluids is accelerated from a lighter fluid to a heavier one.

   This type of instability is characterized by Bond criterion

$$\mathrm{Bo} = \frac{4\rho g R^2}{\sigma} \tag{3.2}$$

   Critical Bond criterion is assumed as equal to $\mathrm{Bo}_{cr} = 40$ [3.3, 3.4].

3. Benard instability occurs as a result of density fluctuations, consisting in the fact that under the effect of various reasons (temperature gradient, concentration), heavier layers appear over lighter ones.

Tolmien-Schlichting and Benard instabilities are observed in both homogeneous and heterogeneous systems, while the Rayleigh-Taylor and Kelvin-Helmholtz instabilities are observed only in heterogeneous systems.

The calculations, presented in the literature, in most cases are based on Bond and Weber criteria [3.1-3.5], i.e. only instabilities of Rayleigh-Taylor and Kelvin-Helmholtz, which are most characteristic for emulsion media, are considered.

The processes of droplet deformation and breaking when moving in a liquid are described in [3.1, 3.2, 3.6, 3.7].

At the same time, no existing model considers the process of the dispersed phase breakage, taking into account the vapor layer formation at the interface of two phases and force interaction with respect to several simultaneously boiling particles of the dispersed phase. Basically, possible processes of deformation and breaking under the action of boil-off, growth of vapor bubbles, or under the action of vapor cavities, cavitation pockets at the moment of their collapse with possible maximum dynamic effect are described.

The formation of a vapor cavity (bubble) is assumed to be homogeneous and only the maximum dynamic effects are considered, while the dispersed phase destruction can occur at any other moment of time due to the fact that the hydrodynamic situation even near two growing bubbles is uncertain and, if the dispersed phase particle is at a certain distance from these bubbles (or between them at a certain distance), the effect of this particle breaking will manifest itself upon reaching the maximum force, which will exceed the critical one calculated by the Weber or Bond criteria, but will not necessarily be equal to the maximum, applied in this system. If we analyse the dispersed phase breaking, which itself boils up, the process becomes even more complicated and requires detailed study.

The above shows the main factors, determining the dispersed phase breaking.

According Weber and Bond criteria, the main factors, determining the dispersed phase breaking, respectively, will be: rate w, and acceleration g, acting on this particle. The rate at any point in space in the vicinity of a growing or collapsing vapor volume can be determined by the ratio

$$w(r) = \frac{w_4 R_4^2}{r^2} \tag{3.3}$$

It can be seen from this ratio that this rate is inversely proportional to the square of the radius (starting from the value of a vapor volume radius itself).

The acceleration distribution in the bubble vicinity is determined by the expression

$$g(r,\tau)=\frac{dw(r,\tau)}{d\tau}=\frac{\partial w(r,\tau)}{\partial\tau}+w(r,\tau)\frac{\partial w(r,\tau)}{\partial r} \tag{3.4}$$

Taking equation (3.2)

$$\frac{\partial w}{\partial\tau}=\frac{dw_4}{d\tau}\frac{R_4^2}{r^2}+2\frac{w_4^2R_4}{r^2};\qquad \frac{\partial w}{\partial r}=-\frac{2w_4R_4^2}{r^3} \tag{3.5}$$

By inserting (3.4) into (3.3), we get

$$g(r,\tau)=\frac{1}{r^2}\left[\frac{dw_4}{d\tau}R_4^2+2w_4^2R_4-\frac{2w_4^2R_4^4}{r^3}\right] \tag{3.6}$$

Then, using the Rayleigh-Plesset equation, we can write

$$g(r,\tau)=\left(p_4-p_\infty+0.5w_4^2\rho_m-\frac{2\rho_m w_4^2R_4^3}{r^3}\right)\frac{R_4}{\rho_m r^2} \tag{3.7}$$

Calculation results according to equation (3.7) are presented in figure 3.1.

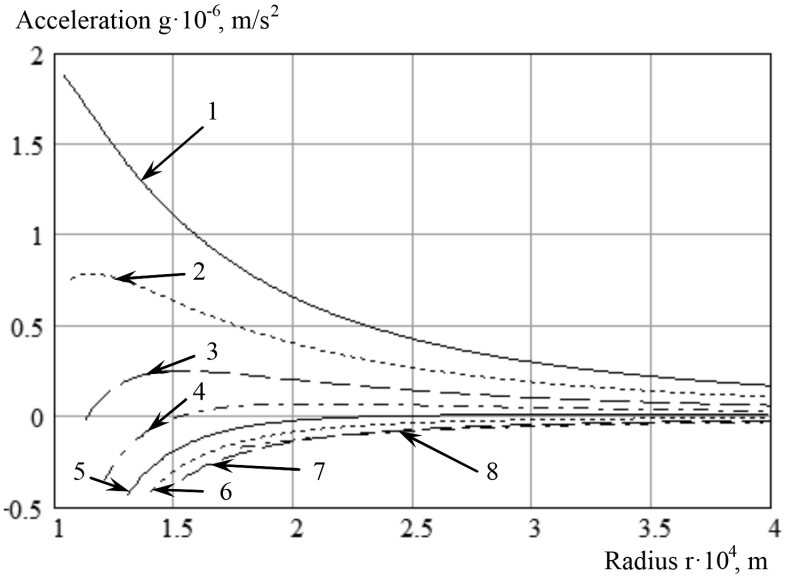

FIGURE 3.1. Acceleration distribution in the vicinity of a vapor layer during its growth for $R_4(0)=$ 100 μm, $t_0=$ 180°C resulting from pressure relief down to 1 atm at different time moments: 1 – 10^{-6} s; 2 – $1.5\cdot10^{-6}$ s; 3 – $2.4\cdot10^{-6}$ s; 4 – $3.6\cdot10^{-6}$ s; 5 – $5.2\cdot10^{-6}$ s; 6 – $7\cdot10^{-6}$ s; 7 – 10^{-5} s; 8 – $2\cdot10^{-5}$ s.

As this figure shows, acceleration at certain points in time ambiguously depends on distance r: it may have a negative value at oil-vapor interface, increase with growing r and, having reached the maximum, decrease; even at a distance four times the droplet radius, the acceleration is many times higher than the gravity acceleration.

Thus, it can be concluded that a dispersed phase droplet, located at a distance several times greater than the boiling particle radius, is subjected to the action of accelerations, resulting in a destabilizing effect of this droplet and at certain parameters (R, σ, g) they can destruct it.

Let us analyse a system consisting of two droplets of different sizes when they boil as a result of pressure relief located at a distance l from each other (fig. 3.2).

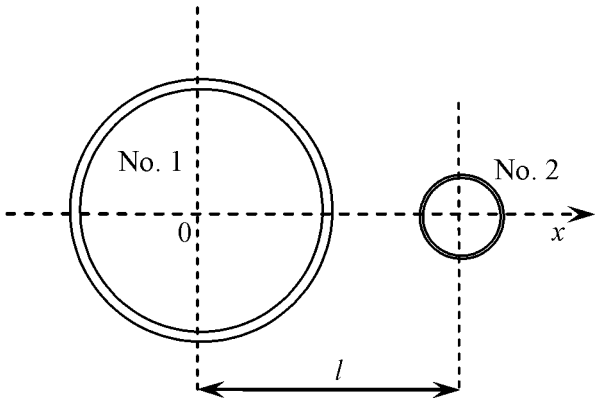

FIGURE 3.2. Calculated arrangement of droplets.

Then the resulting acceleration will be determined by the formula

$$g(x,\tau)=\sum_{i=1}^{2}\left(p_i-p_\infty+0.5\rho_m w_i^2-\frac{2\rho_m w_i^2 R_i^3}{d_i^3}\right)\frac{(x_i-x)R_i}{d_i^3} \tag{3.8}$$

where: x_i – initial coordinates of droplet centres; $d_i=|x_i-x|$ – radius vector; x – coordinate of acceleration calculation point; $w_i=w_{4i}$ – oil-vapor interface motion rate for the i-th droplet; $R_i=R_{4i}$ – radius of the oil-vapor interface of the i-th droplet.

Calculation results according to equation (3.8) are presented in figure 3.3.

The figure shows that the acceleration field can change dramatically depending on the distance between the particles, up to a complete change in the acceleration vector direction and, as a consequence, possible destruction of any of the particles.

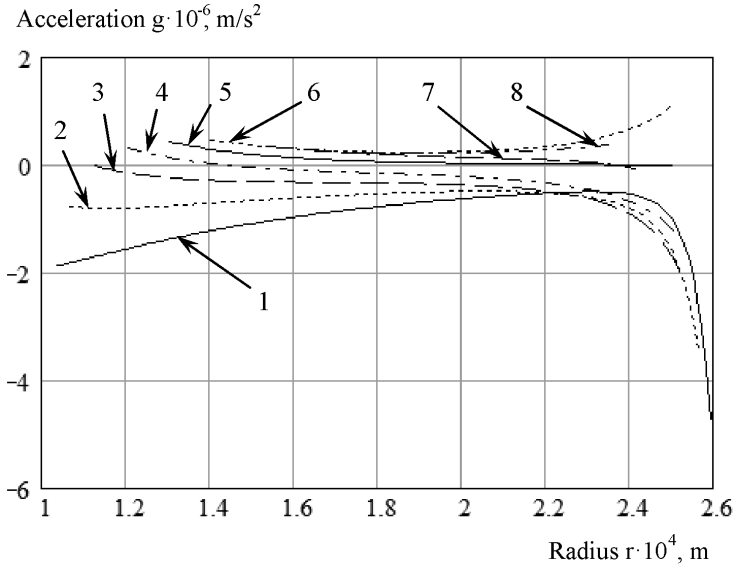

FIGURE 3.3. Distribution of acceleration between two growing vapor volumes: as a result of pressure relief down to 1 atm, at different points in time (designations from figure 3.1); $l = 3 \cdot 10^{-4}$ m, $R_1(0) = 100$ μm, $R_2(0) = 10$ μm, $t_0 = 180$°C.

It is evident that equation (3.8) does not consider turbulent flows, arising in the space between vapor volumes of droplets [3.8, 3.9], due to their complete uncertainty.

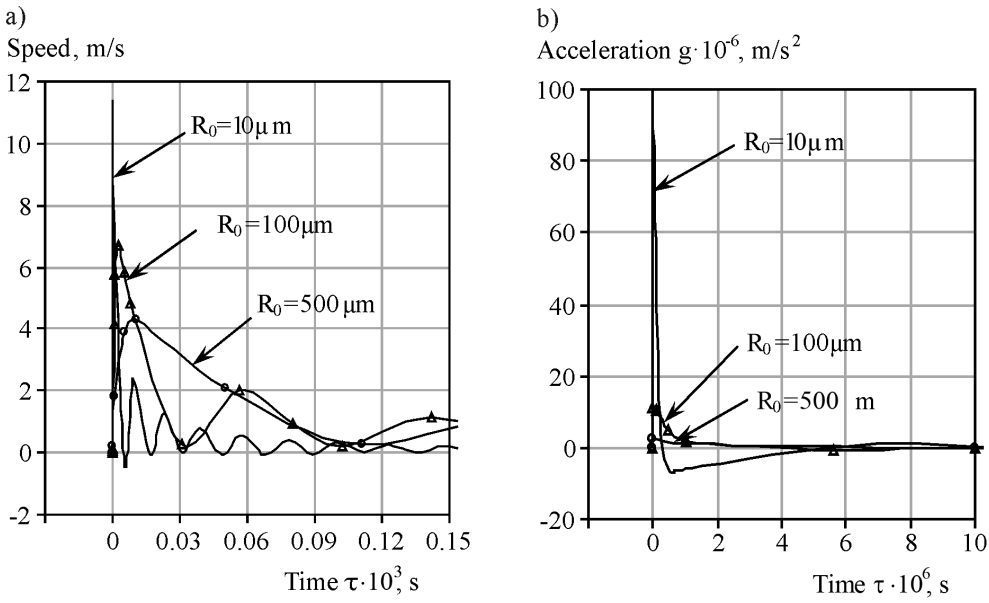

FIGURE 3.4. Dependence of rate (a) and acceleration (b) change of oil-vapor interface motion for different initial droplet radii.

Figure 3.4 shows joint graphs of the change in oil-vapor interface motion rate and its acceleration at the initial system temperature $t_0 =$ 180°C for different initial droplet radii according considering a vapor phase growth in the oil volume.

These graphs show that the smaller the initial droplet radius is, the more intensively the vapor phase grows, i.e. the interface rate and acceleration are higher.

At different droplet radii, both joint maximums (minimums) of the rate (acceleration) and significant differences in these rates (accelerations) can be observed. Then, considering that rates (accelerations) for different initial radii have different amplitudes and frequencies of variation in time, it can be assumed that at some point in time Kelvin-Helmholtz instability is possible, and for acceleration – Rayleigh-Taylor instability.

Let us define the force interaction that can result in a certain instability.

By joint analysis of the Bond and Weber criterion (3.1), (3.2), as well as their critical values, with the Rayleigh-Plesset equation, it follows that critical forces, resulting in Rayleigh-Taylor or Kelvin-Helmholtz instability, respectively, are as follows

$$F_{\mathrm{Bo}}^{cr} = 40\pi\sigma R_i \tag{3.9}$$

$$F_{\mathrm{We}}^{cr} = 30\pi\sigma R_i \tag{3.10}$$

Comparison of (3.9) and (3.10) shows that $F_{\mathrm{Bo}}^{cr} = 1.33 \cdot F_{\mathrm{We}}^{cr}$, but these forces are caused by various factors, and they cannot be identified.

Deformation and breaking of both the vapor layer and water droplets in water-oil emulsions can be caused by different directions of both the acceleration vector and rate vector.

Let us assume that deformation, breaking or displacement will occur only if the acceleration vector has a positive direction and, regardless of it, the rate vector is also positive.

We will assume that droplet No. 1 is at the origin of coordinates, and droplet No. 2 is at a distance of l from the first droplet centre, i.e. $x_1 = 0,\ \ x_2 = l.$ We make the following assumptions:

1. No matter how high the acceleration or rate of the particle boundary itself, the possible resulting instabilities cannot destruct the given particle boundary.
2. If the acceleration (rate) vector of the interface itself is unidirectional with the acceleration vector, acting on the particle boundary from the neighbouring side, then the resulting vector is equal to the one acting on the boundary from the neighbouring side.

Considering these assumptions, the acceleration tending to destruct the droplet No. 1 is equal to

$$g_{p_1} = \begin{cases} \sum_{i=1}^{2} g_i; & k_1 \geq 0, \quad k_2 \geq 0 \\ -\sum_{i=1}^{2} g_i; & k_1 \leq 0, \quad k_2 \leq 0 \\ g_2; & k_1 < 0, \quad k_2 > 0 \\ -g_2; & k_1 > 0, \quad k_2 < 0 \end{cases} \tag{3.11}$$

where:

$$g_i = \left(p_i - p_\infty + 0.5 w_i^2 \rho_m - \frac{2\rho_m w_i^2 R_i^3}{d_i^3} \right) \frac{R_i \left(x_i - R_1 \right)}{\rho_m d_i^3}$$

$$k_i = p_i - p_\infty + 0.5 w_i^2 \rho_m - \frac{2\rho_m w_i^2 R_i^3}{d_i^3}$$

$$d_i = \left| x_i - R_1 \right|$$

Then the force caused by the flow acceleration or deceleration is

$$F_{\mathrm{Bo}_1} = 4\pi\rho_m g_{p_1} R_1^3 \tag{3.12}$$

Similarly, it can be written for the rate

$$w_{p_1} = \begin{cases} \sum_{i=1}^{2} w_{r_i}; & w_1 \geq 0, \quad w_2 \geq 0 \\ -\sum_{i=1}^{2} w_{r_i}; & w_1 \leq 0, \quad w_2 \leq 0 \\ w_{r_2}; & w_1 < 0, \quad w_2 > 0 \\ -w_{r_2}; & w_1 > 0, \quad w_2 < 0 \end{cases} \tag{3.13}$$

Where $w_{r_i} = w_i R_i^2 \dfrac{\left(x_i - R_1 \right)}{d_i^3}$.

Then the dynamic head force is

$$F_{\mathrm{We}_1} = 6\pi\rho_m R_1^2 \left| w_{p_1} \right| w_{p_1} \tag{3.14}$$

As it is known, the capillary force F_σ regardless of a deformed droplet shape, is always directed so as to restore the spherical shape, i.e. in order for Gibbs free energy to be minimal [3.1].

Therefore, if a droplet is deformed in its motion direction into a flattened ellipsoid, capillary force opposes external force.

If it is deformed into an elongated ellipsoid, then capillary force coincides in direction with external force.

Hence it follows that in the deformation process, the shape of an elongated ellipsoid is unstable, while the shape of an oblate ellipsoid can be quasi-stable.

The minimum of a given capillary force is possible.

We will assume that this minimum is determined by Laplace force with corresponding force is

$$F_{\sigma_1} = 8\pi\sigma R_1 \tag{3.15}$$

Thus, if external force exceeds force F_σ, deformation of a given volume will occur, with equality of forces – equilibrium, and at $F_\sigma > F_{\text{Bo, We}}$ – repulsion of a given volume without deformation.

Differences between $F_{\text{Bo, We}}$ and F_σ are equal to

$$\Delta F_{\text{Bo}} = F_{\text{Bo}} - F_\sigma; \qquad \Delta F_{\text{We}} = F_{\text{We}} - F_\sigma \tag{3.16}$$

By the example of the force, resulting from flow acceleration or deceleration, the following conditions can be written: $F_{\text{Bo}} \geq F_{\text{Bo}}^{cr}$ – breaking; $\Delta F_{\text{Bo}} > 0$ – deformation; $\Delta F_{\text{Bo}} = 0$ – equilibrium; $\Delta F_{\text{Bo}} < 0$ – displacement.

The system of equations (3.11)-(3.16) for particle No. 2, located at a distance of *l* from the first particle will take the form

$$g_{p_2} = \begin{cases} -\sum_{i=1}^{2} g_i; & k_1 \geq 0, \quad k_2 \geq 0 \\ \sum_{i=1}^{2} g_i; & k_1 \leq 0, \quad k_2 \leq 0 \\ g_i; & k_1 < 0, \quad k_2 > 0 \\ -g_i & k_1 > 0, \quad k_2 < 0 \end{cases} \qquad w_{p_2} = \begin{cases} -\sum_{i=1}^{2} w_{r_i}; & w_1 \geq 0, \quad w_2 \geq 0 \\ \sum_{i=1}^{2} w_{r_i}; & w_1 \leq 0, \quad w_2 \leq 0 \\ w_{r_i} & w_1 < 0, \quad w_2 > 0 \\ -w_{r_i} & w_1 > 0, \quad w_2 < 0 \end{cases} \tag{3.17}$$

where: $g_i = k_i \dfrac{R_i (x_i - j)}{\rho_m d_i^3}$; $\quad w_{r_i} = w_i R_i^2 \dfrac{(x_i - j)}{d_i^3}$; $\quad d_i = |x_i - j|$; $\quad j = l - R_2$;

$$F_{\mathrm{Bo}_2} = 4\pi\rho_m g_{p_2} R_2^3 \tag{3.18}$$

$$F_{\mathrm{We}_2} = 6\pi\rho_m R_2^2 \left| w_{p_2} \right| w_{p_2} \tag{3.19}$$

$$F_{\sigma_2} = 8\pi\sigma R_2 \tag{3.20}$$

As an example, let us consider two emulsion droplets with radii of $R_1(0) = 100$ μm and $R_2(0) = 10$ μm, arranged at different distance l from each other, at an initial temperature of 180°C (130°C) and corresponding saturation pressure of the aqueous phase.

At a certain point in time, the pressure drops to atmospheric, thereby causing an intensive growth of vapor phase at the oil-water interface and further growth of the oil-vapor interface.

Let us study how the forces that cause displacement, deformation or breaking of the vapor volume change in time at different distances between droplets, on the surfaces of large and small droplets.

The calculation results are presented in figures 3.5-3.7.

These figures show that the greatest effect for droplet destruction is brought by Rayleigh-Taylor instability type.

In all the cases shown, it plays a decisive role, while Kelvin-Helmholtz instability type is also observed (fig. 3.22b), but on a small droplet surface and, as it is obvious from figure 3.22a, only after its dynamic effect has resulted in destruction of a large droplet after the maximum passes through the force F_{Bo} practically at the initial moment of time.

As a result, a small droplet will not get destructed. At small distances l the vapor volume destruction of a large droplet will occur almost right after the pressure is relieved (fig. 3.6a).

As a distance increases, the time until destruction also increases; it is expected, passing in the limit to infinity, if we do not consider the force interaction between droplets approaching and touching surfaces.

With a distance between droplets equal to 200÷250 μm, i.e. 2÷2.5 times larger than the initial radius of a large droplet, breaking will be observed at the first or second peak of force fluctuations F_{Bo} (figs. 3.5a, 3.6b), while at shorter distances this is the first peak.

At $\Delta F_{\mathrm{Bo,We}} > 0$, value $\Delta F_{\mathrm{Bo,We}}$ shows that at a certain moment in time, volume displacement or deformation is possible.

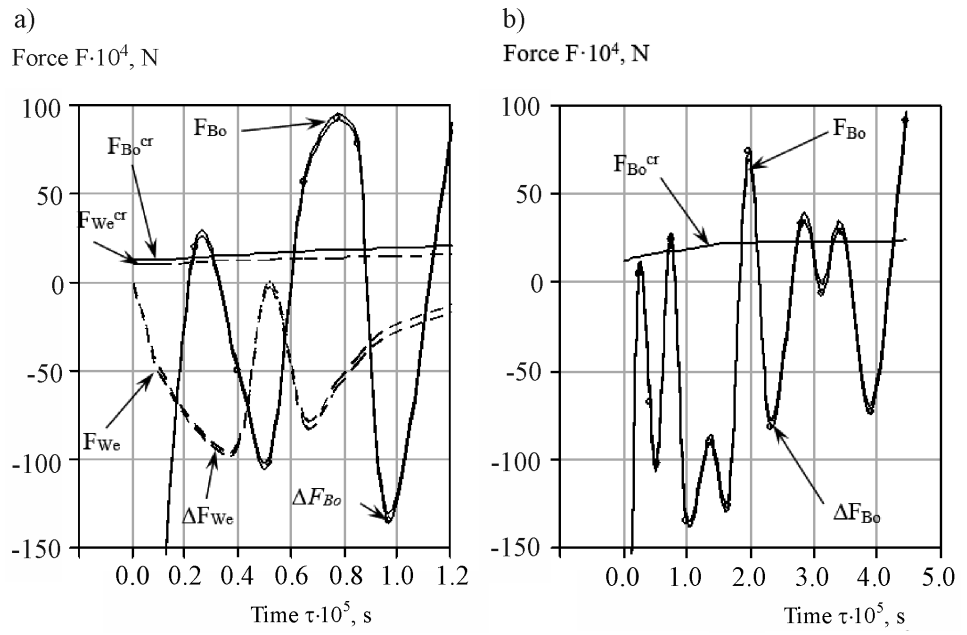

FIGURE 3.5. Change in forces, acting on droplet No. 1 (fig. 3.2) in time at $R_1(0) = 100$ μm, $R_2(0) = 10$ μm, $t = 180$°C, for $l = 200$ μm (a) and $l = 250$ μm (b).

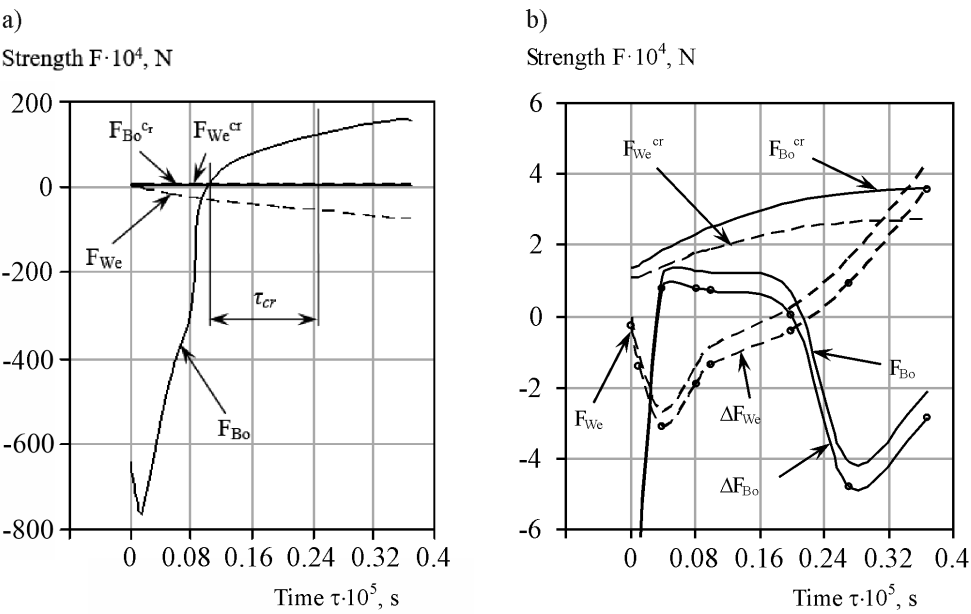

FIGURE 3.6. Change in forces, acting on droplet No. 1 (a) and droplet No. 2 (b) in time at $R_1(0) = 100$ μm, $R_2(0) = 10$ μm, $t = 180$°C, for $l = 150$ μm.

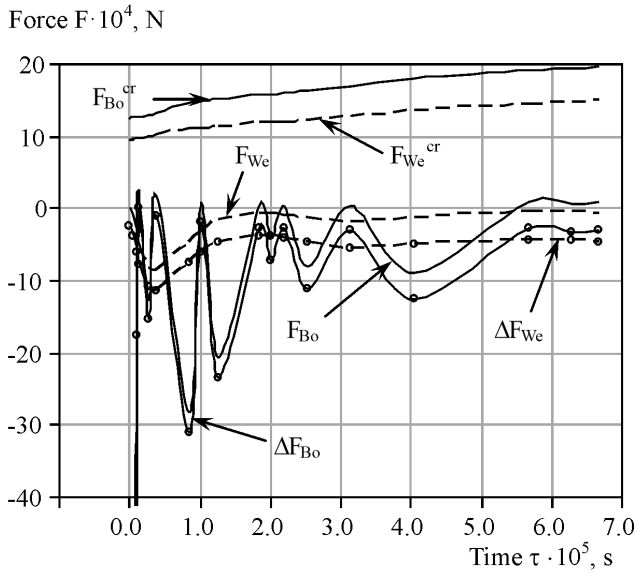

FIGURE 3.7. Change in forces, acting on droplet No. 1 (a) and droplet No. 2 (b) in time at $R_1(0) = 100$ μm, $R_2(0) = 10$ μm, $t = 130$°C, for $l = 150$ μm.

It is worth mentioning that at a distance of 150 μm (figs. 3.5a, 3.6b), a small droplet deforms before it breaks up a large one, while a large droplet will not even be deformed by this moment.

It can be explained by the fact that interface acceleration-deceleration at a small droplet proceed much faster, and this force peak of its deformation (fig. 3.6b) is caused by a sharp deceleration of its interface, while the oil-vapor interface of a large droplet is still accelerating.

It should be considered that a large surface area (larger droplet radius) creates a larger effect area.

For breaking process, it is required excess of the destructive force action period on the particle surface of the critical value, determined by equation

$$\tau_{cr} = R_0 \sqrt{\frac{\rho_m}{3k\left(p_0 + \frac{2\sigma}{R_0}\right)}} \tag{3.21}$$

This equation describes the period of a vapor bubble natural oscillations in an alternating pressure field.

In this case, the bubble surface oscillates, and its radius, increasing or decreasing, remains equal to a certain average value R_0. An alternating pressure acts on the

bubble, determined by the amplitude value from average pressure p_0. It is clear that this critical time shall depend to the greatest extent on the acting force level.

In the processes, studied in this work, an increase in the vapor volume results in a corresponding increase in the particle radius; it is constantly increasing.

In this case, the acting force change and, as a consequence, the oil-vapor interface pressure does not occur near some average value, but can vary significantly with different amplitudes.

Therefore, equation (3.21) can be used only indirectly to determine the critical exposure time.

Calculation for a droplet with a radius of 100 μm and an initial time period for temperature $t_0 = 180°C$, produces value $\tau_{cr} \approx 1.44 \cdot 10^{-6}$ s. Figure 3.6a shows a geometric interpretation of the critical time.

This figure shows that the particle will be broken, because time of a force action, exceeding critical value $F_{\text{Bo}} > F_{\text{Bo}}^{cr}$ is higher than τ_{cr}.

As shown in figure 3.7, with a decrease in the initial temperature to 130°C, even at a distance of 150 μm, breaking or deformation effects are not observed at all.

Presented in [3.4] and shown in figure 3.8 photographs of industrial emulsions show the standard size and distance between dispersed particles.

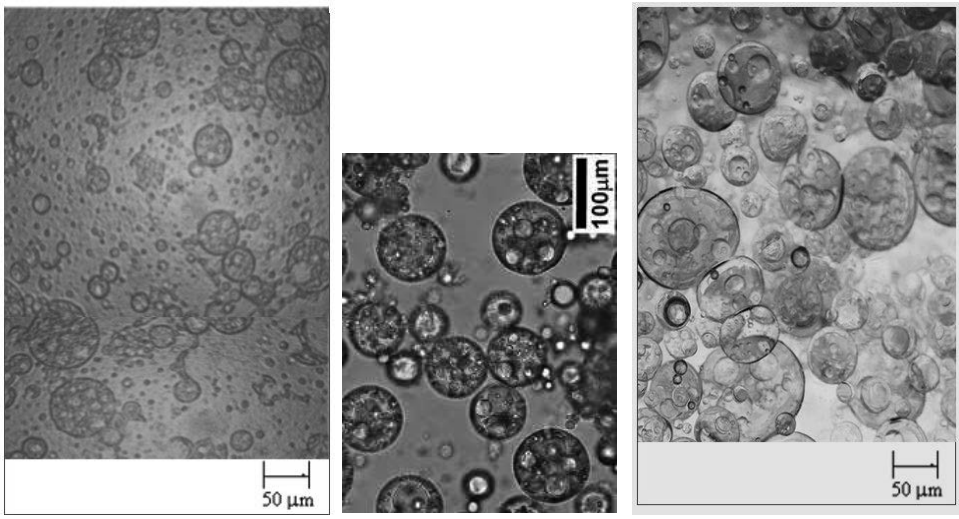

FIGURE 3.8. Photos of emulsion.

These photos demonstrate that large and small emulsion droplets are almost always closely spaced.

Considering a standard relative size of the droplets and their distance between themselves, it can be concluded that at temperatures of 180°C and 130°C, they will be broken unambiguously.

Certainly, for this type of emulsion, it is necessary to consider the effects that occur in the inverse emulsion inside the straight one (fig. 3.8).

The question of these droplets motion remains open, since it results in mutual displacement of a water and vapor droplet, with possible breaking off of a vapor layer.

Clearly, the greatest dynamic effect for the calculated droplets can be at their closest approach.

While at large distances only vapor breaking off is possible, at small distances and high initial temperatures, a water droplet breaking is also possible.

Considering that boiling up at different droplet areas does not occur at the same time, even more intense processes of the emulsion dispersed phase breaking can be predicted.

In general, this model makes it possible, in a fairly simple formulation, to consider breaking processes of large dispersed phase droplets by neighbouring small droplets at different initial temperatures and distances between them.

3.2. Mutual effect of many neighbouring particles

In this part, we will study breaking processes of dispersed phase droplets, surrounded by other droplets during their boiling up. We take the emulsion shown in figure 3.9.

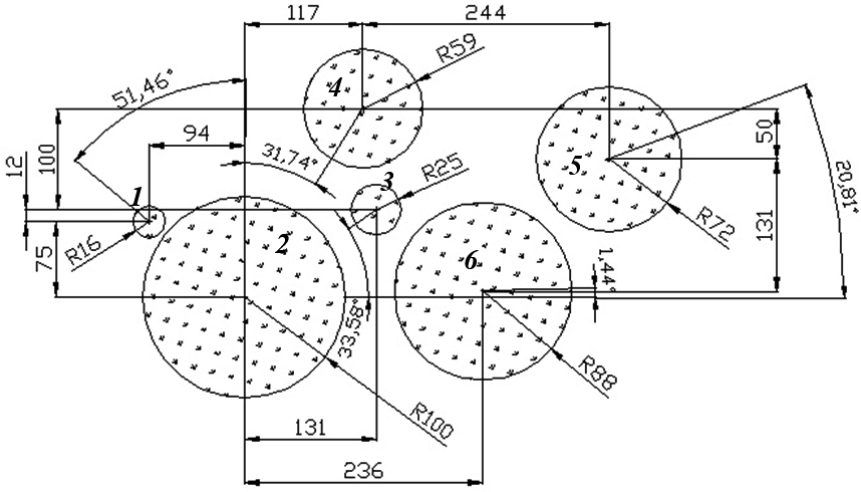

FIGURE 3.9. To the calculation model of the dispersed phase droplet breaking of the emulsion (typical dimensions in micrometers).

This figure shows that there are “small” droplets between “large” droplets, the former serve as sources of increased dynamic forces at boiling up, thus, initiating breaking processes of larger droplets due to significant difference in accelerations and/or growth rates between them.

The main types of instability will be considered Kelvin-Helmholtz instability caused by the difference in rates and Rayleigh-Taylor instability, resulting from difference in accelerations.

Considering the emulsion droplet, it can be concluded that the main role will be played by the forces, acting along normal component to the droplet surface, i.e. forces directed either towards the droplet centre or away from it.

Thus, the acceleration and rate, acting on the particle surface and directed towards its centre (from the centre) can be determined from equations

$$g_{nr}\left(x_0, y_0\right) = g\left(x_0, y_0\right) \cdot k_{nr} \tag{3.22}$$

$$w_{nr}\left(x_0, y_0\right) = w\left(x_0, y_0\right) \cdot k_{nr} \tag{3.23}$$

where: x_0, y_0 – coordinates of the droplet surface point; g – acceleration at the required point, acting from any source and determined by expression (3.7); w – the rate, acting at a given point from the source is determined by expression (3.3); k_{nr} – correction for the normal component.

Correction k_{nr} can be determined by figure 3.10

$$k_{nr} = \cos\gamma = \frac{d_{y'_i}}{d_i} = \frac{\left(x_i - x_0\right)\sin\beta + \left(y_i - y_0\right)\cos\beta}{d_i\left(x_0, y_0\right)} \tag{3.24}$$

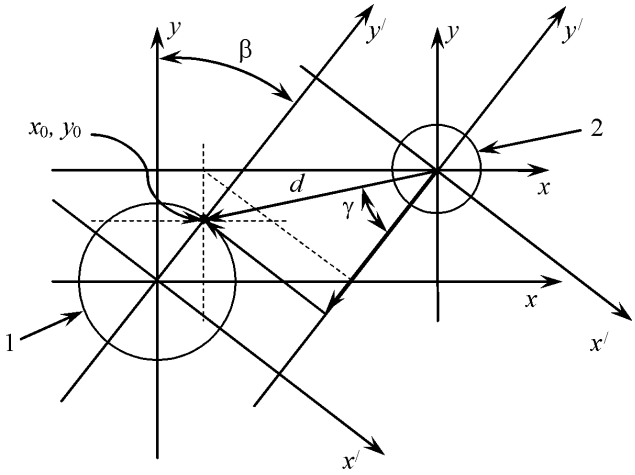

FIGURE 3.10. Determination of correction for the normal component.

We assume that acceleration and its resulting force are positive, if they are directed towards the let centre and negative if they are directed away from the centre.

Similarly, we assume rate and its resulting force. In this case, the rate (acceleration) vector of the oil-vapor interface of the considered boiling up particle is considered positive, if it is directed from the droplet centre and negative, if it is directed to the centre.

Acceleration and rate, acting on the droplet surface from several sources are determined by expressions

$$g_{nr}\left(x_0, y_0\right) = \sum_{i=1}^{N-1} g_i\left(x_0, y_0\right) \cdot k_{nr_i} \tag{3.25}$$

$$w_{nr}\left(x_0, y_0\right) = \sum_{i=1}^{N-1} w_i\left(x_0, y_0\right) \cdot k_{nr_i} \tag{3.26}$$

where N is the total number of boiling up dispersed phase droplets.

It is important to analyse forces, acting on inclusion opposite sides. Taking as alternate angle β (Fig. 3.10), we can determine coordinates of target opposite points of the particle surface

$$\begin{aligned} &x_{s1} = x + \Delta x; \qquad y_{s1} = y + \Delta x \\ &x_{s2} = x - \Delta x; \qquad y_{s2} = y - \Delta x \\ &\Delta x = R_4 \sin\beta; \qquad \Delta y = R_4 \cos\beta; \qquad 0 \le \beta < 180° \end{aligned} \tag{3.27}$$

where: x, y – coordinates of this particle; x_{s1}, y_{s1} – coordinates of droplet side surface ($0 \le \alpha < 180°$) as in figure 3.11; x_{s2}, y_{s2} – coordinates of opposite side ($180° \le \alpha < 360°$).

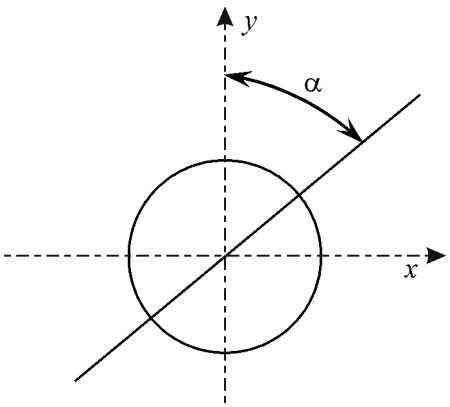

FIGURE 3.11. Determination of angle α.

Then determination of k_{nr} will be determined by expressions

$$k_{nr} = \frac{(x_i - x_{s1})\sin\beta + (y_i - y_{s1})\cos\beta}{d_i(x_{s1}, y_{s1})}; \qquad 0 \le \beta < 180° \qquad (3.28)$$

$$k_{nr} = \frac{(x_i - x_{s2})\sin\beta + (y_i - y_{s2})\cos\beta}{d_i(x_{s2}, y_{s2})}; \qquad 180° \le \beta < 360° \qquad (3.29)$$

In equation (3.29) x_{s2}, y_{s2} are calculated at $0 \le \beta < 180°$, k_{nr} at $\beta = \beta + 180°$.

Let us study how the value and direction of the force, acting on the droplet surface (fig. 3.9) changes, determined by the acceleration arising in the inter-bubble area at the initial moment of pressure relief from the value, determined by pressure at aqueous phase saturation temperature at the initial moment of time ($t_0 \approx 105°C$), to atmospheric pressure, equal to 10^5 Pa. For all droplets, existence of the same vapor layer equal to 1 μm is assumed from the initial moment of time.

In this case, behaviour in acceleration on the particle surface shows in which direction and how the force will change.

The change in acceleration is shown depending on angle β. Calculation results for water-oil emulsion according to equations (3.24)-(3.28) are shown in figures 3.12 and 3.13.

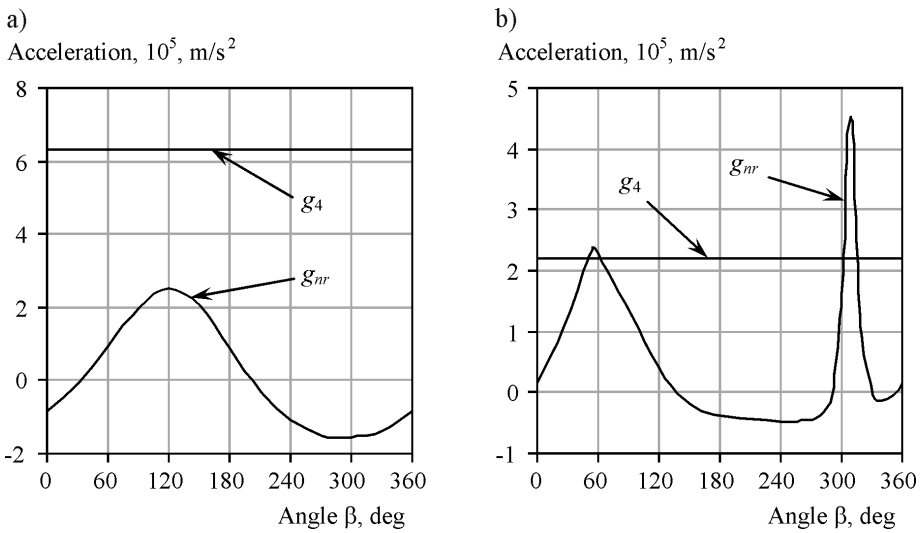

FIGURE 3.12. The pattern of acceleration, acting on droplet surface No. 1 (a) and droplet No. 2 (b) (fig. 3.9) from neighbouring boiling up particles (g_{nr}) and acceleration of the counteraction of growing oil-vapor interface of the particle itself (g_4) at initial pressure relief from 0.121 MPa to 0.1 MPa.

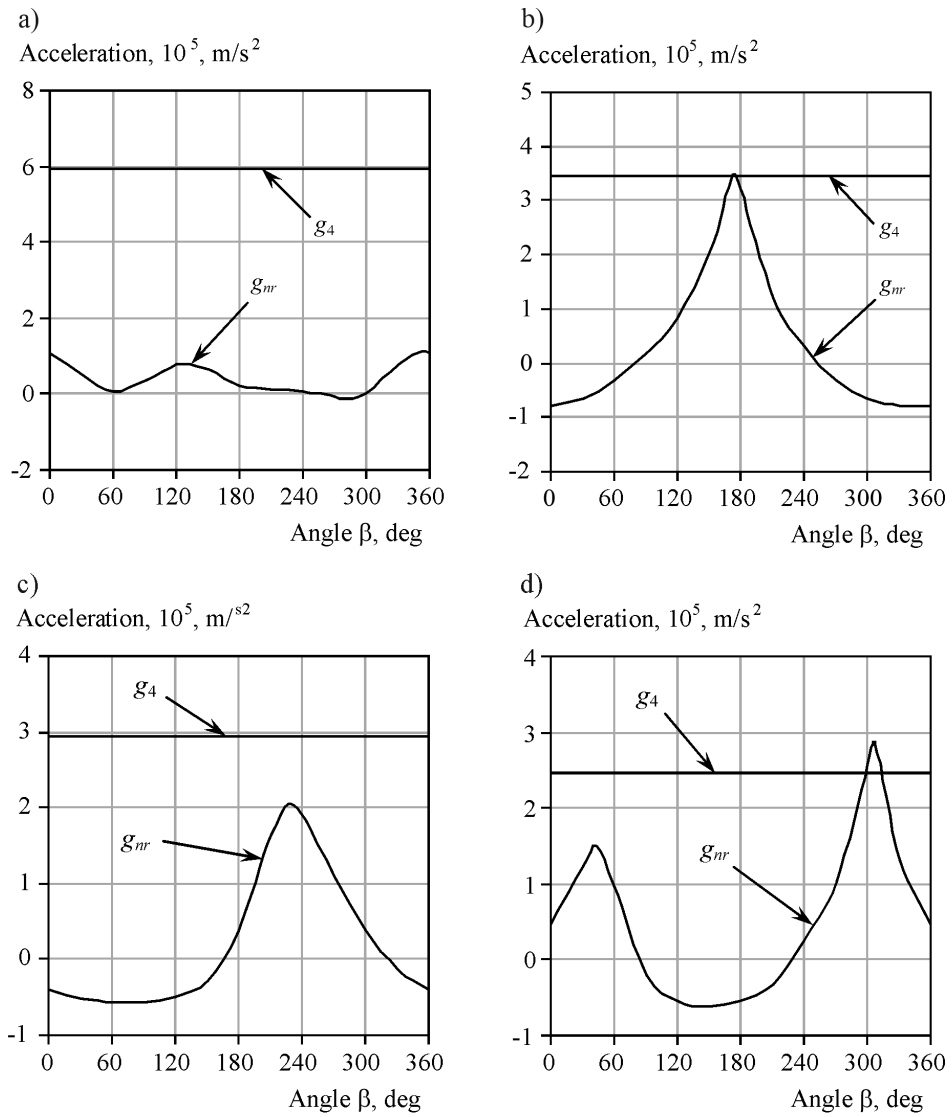

FIGURE 3.13. The pattern of acceleration, acting on droplet surface No. 3 (a), No. 4 (b), No. 5 (c), No. 6 (d) according to figure 3.9 at the initial moment of pressure relief (conditions are given in figure 3.12).

Figures 3.12, 3.13 show a change in the acceleration, acting on each droplet, shown in figure 3.9. The graphs show a clearly traceable relationship between angles of droplet arrangement relative to the analysed one and acceleration value. Thus, for example, for droplet No. 2 (fig. 3.12b) there are two acceleration maximums at once – angle $\beta \approx 55°$ and $\beta \approx 310°$, corresponding to angles of the nearest neighbouring droplet No. 1 and No. 3 (fig. 3.13) arrangement respectively.

These figures show that there are always several maximums of acting acceleration (force).

It is clear that the greatest effect of the force from all the maximums, taking into account the effect of the force, acting on the opposite inclusion side.

For instance, calculation of acceleration and its resulting force on one side and opposite droplet side, we will assume that if two opposite forces are directed towards the droplet centre, then the total force, acting on the droplet is equal to the sum of these two forces. If both forces are directed from the droplet centre, then the total force is also equal to the sum of two vector forces.

If both forces act in opposite directions relative to the droplet centre, i.e. unidirectional in space, we will consider the determining force that has a greater value of two acting forces.

Thus, a dispersed phase inclusion, which does not boil up, i.e. does not generate any opposition to acting forces, the determining effect, resulting in possible destruction, will be a maximum of two forces that act on opposite sides, under the conditions described above.

When an emulsion droplet begins to boil up, it has its own force, resisting external action from other sources. In this case, the opposing force is positive if it acts from the droplet centre and negative, if it acts towards the centre, as was assumed above.

Then the determining force can be one, acting on one side of the inclusion and exceeding the opposing force. It can be explained based on the following conclusions.

Let us analyse a boiling emulsion droplet (fig. 3.14), affected by external forces.

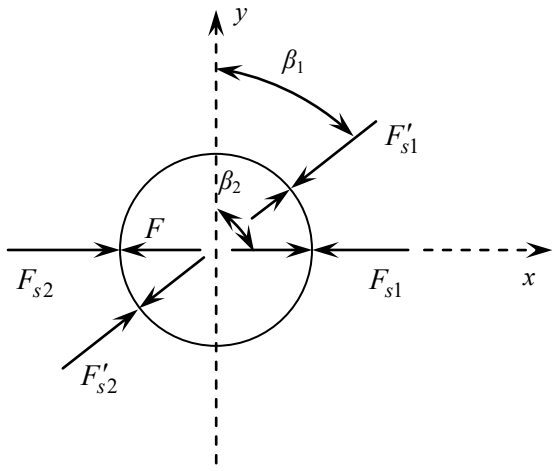

FIGURE 3.14. Forces acting on emulsion droplet (designations in the text).

Let the maximum of two forces, acting on opposite sides, be equal $F_{\Sigma}^{'} = F_{s1}^{'} + F_{s2}^{'}$ and locate at β_1 to axis *y*. The maximum force, acting on one side is and is located at angle β_2 from axis *y*. It is clear that $F_{\Sigma}^{'} > F_{\Sigma}$, where it is clear that *F*, with $F > F_{s1}^{'}$, $F > F_{s2}^{'}$, $F > F_{s2}$, $F < F_{s1}$. Therefore, only one difference will determine the force, which can result in either deformation or breaking.

This force is equal to $\Delta F = F_{s1} - F$.

Thus, it is obvious that though the maximum of two opposing forces is at angle β_1 to axis *y*, but the determining maximum is the one caused by force F_{s1} (angle β_2). It is the main difference in forces, acting on a boiling up droplet, as opposed to a non-boiling droplet.

This means that two given maximums shall be accounted for to determine the main one. Clearly, a coincidence in the existence of these force maximums is possible, i.e. $\beta_1 = \beta_2$.

Then, for a non-boiling droplet, the force acting on its surface, considering assumed conditions, is determined by acceleration

$$\Delta g = \begin{cases} g_{s1} + g_{s2}; & Z > 0 \\ g_{s1}; & Z < 0, \quad |g_{s1}| > |g_{s2}| \\ g_{s2}; & Z < 0, \quad |g_{s2}| > |g_{s1}| \end{cases} \tag{3.30}$$

where: $Z = g_{s1} / g_{s2}$ – a coefficient, considering the direction of acceleration action; g_{s1} – the acceleration acting on the inclusion surface at $0 \le \alpha < 180°$ and determined by the equation (3.25); g_{s2} – acceleration, acting on inclusion surface at $180° \le \alpha < 360°$, and determined by equation (3.25).

The force that can result in breaking of a non-boiling inclusion of a dispersed phase is determined by the maximum effective acceleration

$$g_d = \max\left(|\Delta g|\right), \qquad 0 \le \beta < 180° \tag{3.31}$$

For a boiling up particle, two force maximums are determined due to accelerations, acting on one side of the inclusion

$$g_{d1} = \max\left(|g_{si}|\right), \qquad g_{si} = \begin{cases} g_{s1}; & |g_{s1}| > |g_{s2}| \\ g_{s2}; & |g_{s1}| < |g_{s2}| \end{cases} \qquad 0 \le \beta < 180° \tag{3.32}$$

on opposite inclusion sides

$$g_{d2} = \max\left(\left|g_{s1,s2}\right|\right), \qquad g_{s1,s2} = \begin{cases} g_{s1} + g_{s2}; & Z > 0 \\ g_{s1}; & Z < 0, \quad |g_{s1}| > |g_{s2}| \\ g_{s2}; & Z < 0, \quad |g_{s2}| > |g_{s1}| \end{cases} \qquad 0 \le \beta < 180° \tag{3.33}$$

Each of given acceleration maximums g_{d1} and g_{d2} correspond to accelerations, acting on different sides of analysed particle g_{d1} and g_{d2}.

Considering the fact, that the action force of a droplet itself cannot destruct itself, we can write equations to determine accelerations and rates, acting on the boiling up inclusion of a dispersed phase and resulting in its destruction.

Assuming, that if the resulting acceleration or rate is positive, then they result in instability, and if they are negative, then there is no destabilizing effect, we can write

$$g_{p1} = \begin{cases} g_{s1} - g_4; & g_4 \ge 0, \quad g_{s1} \ge 0 \\ -g_{s1}; & g_4 > 0, \quad g_{s1} < 0 \\ g_{s1}; & g_4 < 0, \quad g_{s1} > 0 \\ g_4 - g_{s1}; & g_4 \le 0, \quad g_{s1} \le 0 \end{cases} \tag{3.34}$$

where: g_{s1} – the resulting acceleration, acting on one side of inclusion; g_4 – acceleration of the oil-vapor inclusion interface.

For the opposite side, you can write an equation similar to (3.34), but instead of g_{p1} and g_{s1}, by inserting g_{p2} and g_{s2}, respectively.

Then, the general acceleration, acting on the droplet, is determined by the equation

$$\Delta g_d = g_{p1} + g_{p2} \tag{3.35}$$

with required conditions

$$g_{p1} = \begin{cases} 0; & Z < 0, \quad |g_{s1}| - |g_{s2}| < 0 \\ 0; & Z > 0: \quad g_4 > 0, g_{s1} > 0, g_{s2} > 0, g_{s1} - g_4 < 0, g_{s2} - g_4 > 0 \\ & \quad\;\; g_4 < 0, g_{s1} < 0, g_{s2} < 0, g_{s1} - g_4 > 0, g_{s2} - g_4 < 0 \end{cases}$$

$$g_{p2} = \begin{cases} 0; & Z < 0, \quad |g_{s1}| - |g_{s2}| > 0 \\ 0; & Z > 0: \quad g_4 > 0, g_{s1} > 0, g_{s2} > 0, g_{s1} - g_4 > 0, g_{s2} - g_4 < 0 \\ & \quad\;\; g_4 < 0, g_{s1} < 0, g_{s2} < 0, g_{s1} - g_4 < 0, g_{s2} - g_4 > 0 \end{cases} \tag{3.36}$$

If the force maximums (accelerations, rates) do not coincide, acting on inclusion opposite sides and on the one hand, we consider that the total force that is of greater importance is determined

$$g_d = \begin{cases} \Delta g_{d1}; & \Delta g_{d1} > \Delta g_{d2} \\ \Delta g_{d2}; & \Delta g_{d1} < \Delta g_{d2} \end{cases} \tag{3.37}$$

where Δg_{d1}, Δg_{d2} are general accelerations, acting on the droplet, calculated from the maximums, acting, respectively, on one side and on opposite sides, at values g_{s1} and g_{s2}.

Similarly, we can get equation for the rate.

In this case, equation (3.35) will look as follows

$$\Delta w = k\sqrt{|w_p|} \tag{3.38}$$

where $k = \begin{cases} +1, & w_p \geq 0; \\ -1, & w_p > 0; \end{cases}$ $w_p = w_{p1}|w_{p1}| + w_{p2}|w_2|$.

Studies were performed to determine how forces, acting on a droplet, change over time, as well as how the angle of force maximum action changes.

Considering that Kelvin-Helmholtz instability plays a secondary role in comparison with Rayleigh-Taylor instability, we will consider the force action caused by acceleration to be decisive.

Based on equations (3.30)-(3.38), for these conditions the force acting at $0 \leq \alpha < 180°$ is equal to

$$F_{g1} = 4\pi R_4^3 \rho_m g_{s1} \tag{3.39}$$

For $180° \leq \alpha < 360°$

$$F_{g2} = 4\pi R_4^3 \rho_m g_{s2} \tag{3.40}$$

Opposing force from the oil-vapor interface of the droplet itself

$$F_g = 4\pi R_4^3 \rho_m g_4 \tag{3.41}$$

Total force, acting on a droplet

$$F_{\text{Bo}} = 4\pi R_4^3 \rho_m g_d \tag{3.42}$$

Critical force, resulting in Bond instability

$$F_{\mathrm{Bo}}^{cr} = 40\pi\sigma R_4 \tag{3.43}$$

Force, determining a droplet deformation or displacement

$$\Delta F_{\mathrm{Bo}} = F_{\mathrm{Bo}} - 8\pi\sigma R_4 \tag{3.44}$$

For each of the analysed droplets, the calculation is performed either until the condition

$$F_{\mathrm{Bo}} \geq F_{\mathrm{Bo}}^{cr} \tag{3.45}$$

is met, or until mutual meeting of droplets, determined by condition

$$\Delta R_{i,j} \leq 0 \tag{3.46}$$

where $\Delta R_{i,j} = d_{i,j} - \left(R_{4i} + R_{4j}\right)$, $d_{i,j} = \sqrt{\left(x_i - x_j\right)^2 + \left(y_i - y_j\right)^2}$; $i = 1,2,\ldots,N$; $j = i+1$, $i+2,\ldots,N$; i, j are droplet numbers with corresponding coordinates $x_i, y_i; x_j, y_j$.

The calculation results using equations (3.26)-(3.46) together with the equations of the vapor phase growth model in an infinite volume of oil are shown in figure 3.15-3.18. Calculations for initial temperature $t_0 = 105°\mathrm{C}$ showed that only one droplet No. 2 would be broken at the initial moment of pressure relief, due to the relatively close location of droplet No. 1, and, as a consequence, the maximum peak of acceleration at an angle of relative position of the two given droplets. Figures 3.15-3.17a show that critical force F_{Bo}^{cr} increases over time due to increase in radius R_4 of analysed droplet, values of the force, acting on the droplet, approach zero in time.

Therefore, we can conclude that if we do not consider further interaction of droplets with each other when they come into contact, then at $t_0 = 105°\mathrm{C}$, if at the initial moments of pressure relief, breaking of large droplets does not occur, then until the contact moment they will no longer be destructed.

Change curves F_{g1}, F_{g2}, the force maximum, acting at the given moment of time.

These curves determine the predominance of these forces over opposing force F_g, or their smallness over this force. They also do not determine the force, acting at the same angle since to a large extent they depend on a given angle, which is shown in figure 3.18a.

But their analysis in combination makes it possible to calculate the force F_{Bo}, playing, in its turn, the main role in this process.

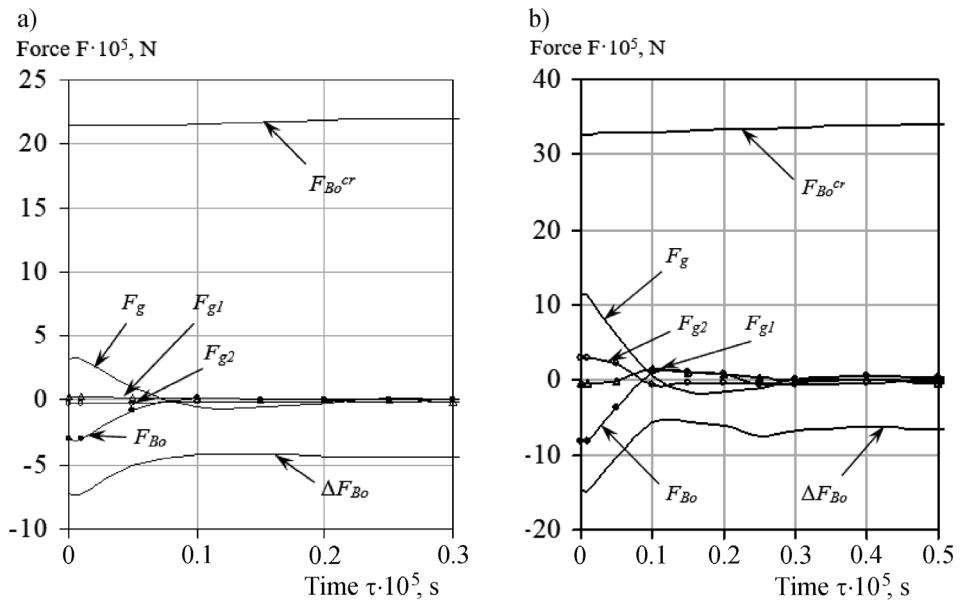

FIGURE 3.15. Changes in the forces acting on droplets No. 1 (a) and No. 3 (b) surfaces (fig. 3.9) in time under the conditions in figure 3.12.

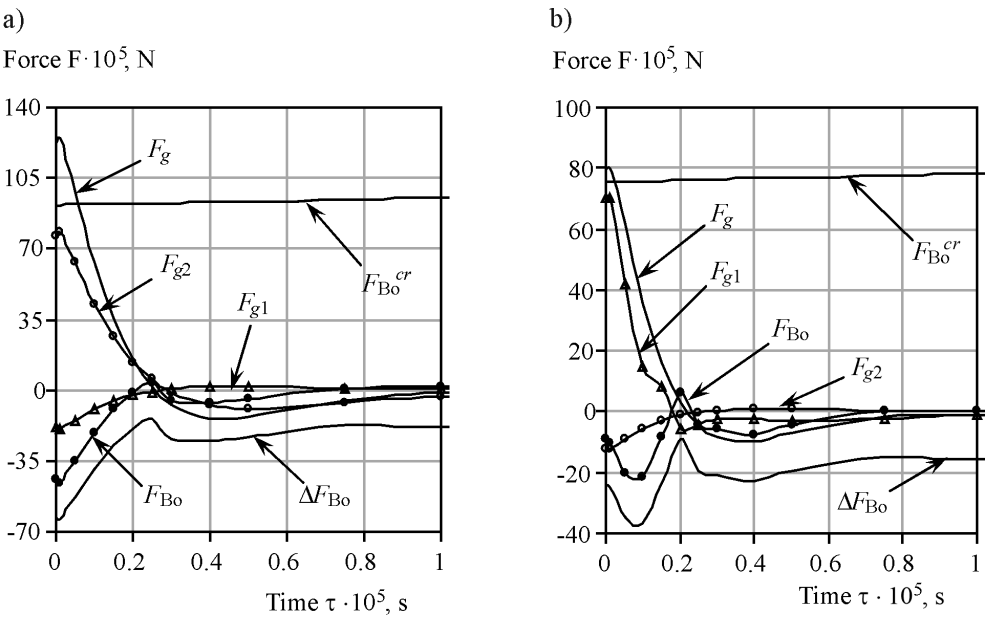

FIGURE 3.16. Changes in the forces acting on droplets No. 4 (a) and No. 5 (b) surfaces (fig. 3.9) in time under the conditions in figure 3.12.

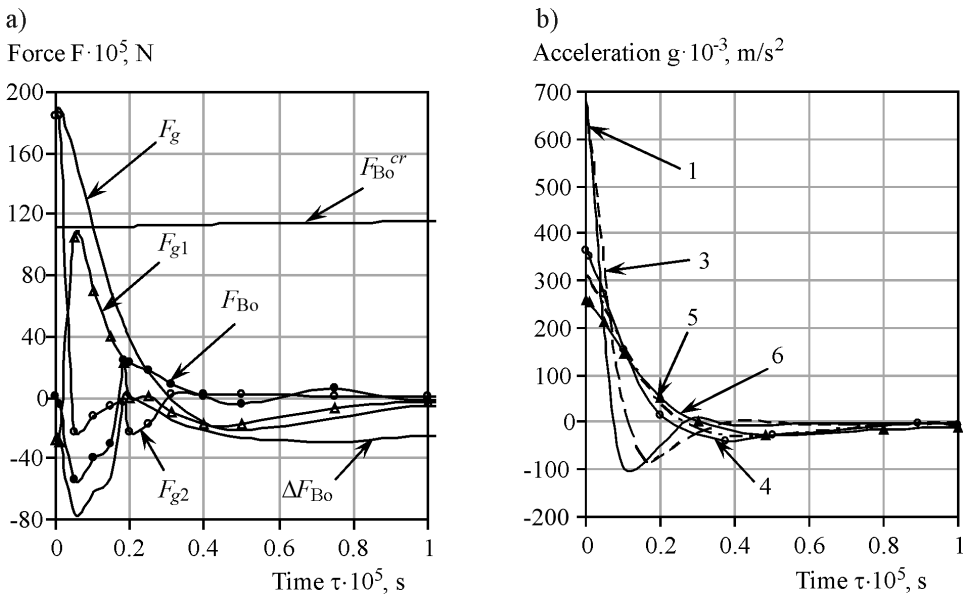

FIGURE 3.17. Change in the, forces acting on droplet No. 6 surface (a), and change of oil-vapor interface acceleration (b) of analysed droplets (fig. 3.9) in time (conditions in figure 3.12).

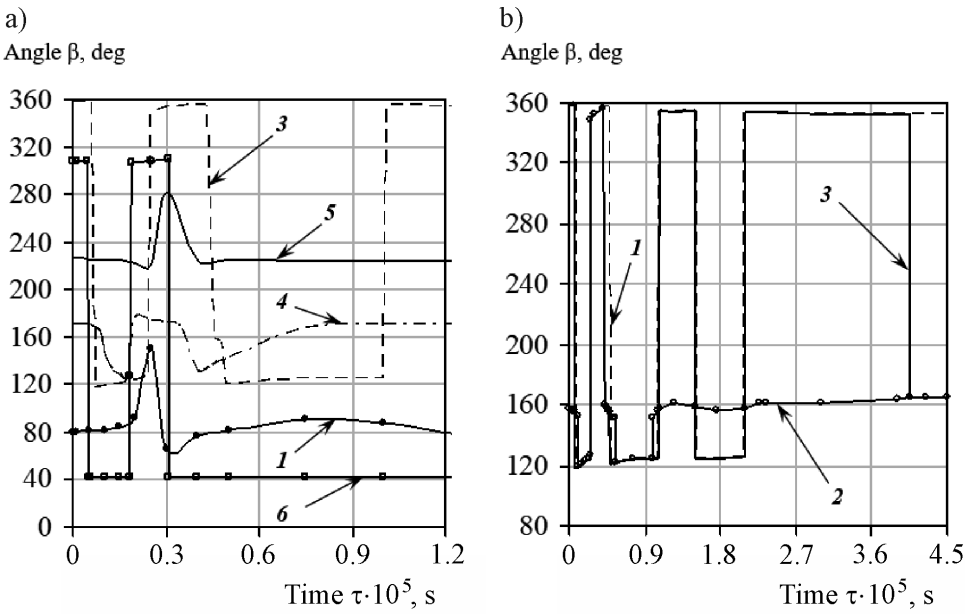

FIGURE 3.18. Change in time of the angle of the maximum force action for particles 1, 3-6 (a) and the angle of the maximum force action for particle No. 3 (b), acting on one side (1) and on opposite sides of the inclusion (2), as well as the angle of determining force action for calculation (3) from figure 3.9.

It is clear that for droplets No. 1, 3, 4, 5 (figs. 3.15, 3.16) with a positive value of force F_{Bo}, only their mutual movement is possible, as designated by negative sign while for droplet No. 6 (fig. 3.17a), a slight deformation can be observed at $\tau \approx 2 \cdot 10^{-6}$ s.

The most dramatic change in the angle of the maximum force action is also observed, especially for droplets No. 3 and No. 6 (fig. 3.18a).

Let us analyse droplet No. 6 as an example. As it is seen in figure 3.18a, with a change in the angle of the maximum force action, the dominant effect of either the fifth droplet ($\beta \approx 40°$), or the third ($\beta \approx 300°$) together with the fourth one, changes.

The first peak of angle change β at $\tau \approx 5 \cdot 10^{-7}$ s can be explained by a sharp decrease in the boundary acceleration of droplet No. 3 (fig. 3.18b) and further predominant action from particle No. 5, then at $\tau \approx 1.8 \cdot 10^{-6}$ s the third particle exerts the greatest force. It is also shown in figure 3.18a as sharp decrease in force F_{g2} and resulting surge of acting force F_{Bo} due to F_{g2} and F_g turn out to be unidirectional and force F_{g2} dominates. Similarly, there is a redistribution of maximum forces in time $\tau \approx 3 \cdot 10^{-6}$ s, when acceleration from droplet No. 5, taking into account the distance to surface of droplet No. 6, exceeds the acceleration effect from droplet No. 3.

The predominance of force from the fifth droplet continues until the moment of time $\tau \approx 2.8 \cdot 10^{-5}$ s, that can also be explained by the greatest force effect F_{g1} according to figure 3.18a.

At the same time, despite sharp change of angle β actions of the maximum force for particles No. 3 and 6, for No. 5 this angle changes quite smoothly (fig. 3.18a), most of the time is ≈230°, that is, in the area of the maximum force from droplet No. 6.

Angle surge β at $\tau \approx 3 \cdot 10^{-6}$ s can be explained by the fact that the acceleration in figure 3.17b, and, consequently, the acting force from droplet No. 6, are equal to zero.

At the same time, there are forces from droplets No. 3 and No. 4, which is indicated by the non-zero value of force F_{g2} (fig. 3.16b).

We may conclude that angle β can change sharply only for those droplets that are surrounded by others, while droplets located on the "margin area" will change the angle of the maximum force action by a small value.

It is explained by the fact that for droplets inside the emulsion, the force maximum can change quite rapidly, both in value and direction, due to a quite close arrangement of neighbouring droplets, changing their dominant effect on a given particle.

At the same time, the droplets in the outer layers have neighbours on a small fraction of their circumference, thus predetermining a small change in the angle of the maximum force action.

Figure 3.18b shows behaviour of the maximum force angle action, acting on one side of the inclusion changes $F_{\Delta g_{d1}}$, and opposite sides $F_{\Delta g_{d2}}$. It is obvious that there is no clear relationship between the angles of these forces action; they can both coincide and be strikingly different.

Therefore, it is necessary to consider the highest maximum force and its action angle.

Performed calculations for temperatures $t_0 = 180°C$ and $t_0 = 130°C$ showed, that at the moment of instantaneous pressure release nearly all large droplets will be broken up, while at $t_0 = 105°C$ only the largest droplet will be broken up due to the smallest particle maximum approximation.

Thus, a breaking model of dispersed phase large inclusions of an emulsion at different initial temperatures was studied.

The angles of the maximum forces action were calculated; breaking processes of boiling up inclusions proceeds at different force maximums (different angles β) in comparison with non-boiling particles.

It proves the need to determine at least two maximum forces, that can coincide in terms of their action angle on a droplet, or differ significantly in this angle of action.

Clearly, it is necessary to consider both the surface deformation of inclusions and their movement, as well as variation during the boiling of droplets different in size.

Surfactants also play an important role; they make it possible to break a particle with much smaller forces, applied from other boiling up inclusions.

The issue of behaviour of two or more droplets, approaching each other, as well as the effect of neighbours on a given droplet growth still needs to be studied.

Analysis of these phenomena will make it possible to study growth and breaking processes of a dispersed phase in detail.

3.3. Energy conversion in heat and mass transfer processes in boiling emulsions

In many works [3.10-3.13], the authors pay due attention to the study of heat and mass transfer processes in boiling emulsions and describe effects of intensification of these processes.

But in cited works, the authors do not pay attention to kinetic energy conversion of the vapour region growing volume (vapour bubbles) into other types of energy.

In our studies, we recorded abnormally high valuesof accelerations of the vapour-fluid interface and, accordingly, dynamic effects, contributing to breaking up of dispersed drops of the secondary emulsion fluid.

And, what is more important, these phenomena are accompanied by a powerful acoustic effect.

Therefore, of course, the question arises as to whether it is possible to solve the inverse problem, that is, to induce or enhance these dynamic effects by achieving acoustic resonance but at lower temperatures.

At this, intensity of heat and mass transfer processes, as well as in boiling ones (superheated relative to thermolabile component), will increase.

Thermodynamic processes that occur on the surface of gas-vapor bubbles, such as absorption [3.14], aeration [3.15], bubbling [3.16], and vacuum distillation [3.17], are at the heart of many advanced industrial technologies. Thermal and mass exchange processes, which are the basis of degassing [3.18], boiling [3.19], cavitation [3.20], obtaining gas hydrates [3.21] and many others also occur on the interphase surface of bubbles. Active research into the influence of bubbles on sound oscillations was carried out to optimize the operation of hydrolocators. In the available literature [3.22], the issue of damping of oscillations with frequencies from 4 kHz to 150 kHz in sea water at different depths was highlighted. Another direction of research was caused by the necessity of application of cavitation [3.23]. Studies of fluid degassing by the cavitation method were carried out starting with 10 kHz to 1 MHz frequency.

Bubble oscillations have a damping character in most cases. However, the most intense heat and mass exchange processes on the surface of bubbles were observed during these oscillations. A very quick change of thermodynamic parameters of the "gas bubble–fluid" system occurs during oscillation. The relevance of the study into dynamics of mass exchange processes on the surface of an oscillating gas bubble is explained by the necessity for optimization of various technological processes.

The Rayleigh-Plesset equation is often used for analysis of the dynamics of oscillations of vapor bubbles. The analysis of fluid flow with lots of bubbles of different dimensions, considered in [3.24], is also based on the solution of this equation. Given the large amount of calculation of a three-dimensional model, the authors did not consider the phase transition processes either on the surface of the fluid, nor in the middle of bubbles. The Clapeyron-Clausius equation was applied for determining pressure under conditions of constant boiling [3.25]. However, due to oscillatory pressure changes, it is necessary to consider that boiling periods alternate with diffusive mass transfer periods. Moreover, such problem statement does not consider partial pressure of gases that do not participate in phase transitions.

Quite often, in order to determine pressure inside cavitation bubbles, the process is considered to be adiabatic [3.26]. However, this assumption is only possible for separate stages in the development of a cavitation bubble when the wall velocity exceeds one hundred meters per second. In the work [3.23], mathematical problem statement considers phase transition and heat transfer near the surface of an oscillating bubble. However, this model is designed for the bubbles that are formed as a result of cavitation and inside of which there is greatly rarified gas. The mathematical model, considered in [3.18], contains a model of the source of harmonic oscillations but pressure of saturated vapor inside a bubble is accepted as constant, and only bubbles of critical dimensions are considered. Hegedűs in [3.28] considered a single spherical gas bubble that contains both non-condensed gas and vapor, but did not take into consideration phase transition processes on the surface of a bubble.

Comparison of three mathematical models of motion of a cavitation bubble in the acoustic field was performed in paper [3.23]: a polytropic model, a model ideal gas and radially distributed thermodynamic parameters inside a bubble. A description of mass transfer and phase transition processes is also missing in these models, the frequency of acoustic oscillations, assigned by the author, is significantly lower than the resonance one. Paper [3.14] presents a physical- mathematical model of heat and mass transfer and gas absorption on the bubble surface. The obtained results of calculation show a considerable influence of gas dissolution on the temperature mode of the gas phase of a bubble, but do not consider oscillatory character of a bubble's motion velocity.

Analysis of the scientific literature shows that the study of resonance oscillations of bubbles in terms of acoustic impact should be not only interesting from the scientific point of view, but are also of great practical importance, since it is a way of intensification of heat and mass transfer processes for a variety of industrial technologies.

The formation of the vapor phase as a means of energy conversion in boiling emulsion

Vapor bubbles can form when the emulsion is heated or when the pressure in the superheated emulsion decreases.

The problem of technological processes intensification is solved by use of various external physical effects on the system, thus, allowing to change speed of the energy and mass transfer processes in the required direction.

Vapour bubbles in a boiling emulsion can be such points, or it is better to call them discrete volumes. Phase transition makes it possible to transfer more energy and thereby intensify heat transfer process. Vaporization will contribute to the fluid flow turbulence, which also increases the heat transfer intensity.

3.4. Features of the energy conversion of the boiling phase of the emulsion

To initiate local transfer mechanisms, the system, for example, the liquid-vapour bubbles, shall be disturbed from equilibrium state by producing pressure difference in vapour and liquid phases.

It provides a reserve of potential energy, which, during system transition in its equilibrium state, is converted into kinetic energy of the fluid radial motion around the separate bubble.

On reaching its maximum value, kinetic energy is converted into the compressed gas potential energy inside the bubble and partially into the compressible fluid potential energy, represented as a high pressure zone around the bubble, then it propagates in the fluid at the sound speed in the acoustic wave form.

During these conversions, a certain part of the mechanical energy is converted into thermal energy and vice versa.

Let us consider a vapour bubble in an infinitely large volume of fluid being in a macro-quiescent state (fig. 3.19). The accelerated fluid motion around the bubble is caused solely by a change in its volume during growth or compression. The kinetic energy density at the fluid local point around the bubble is related to the local radial motion speed w_r by dependence $\varepsilon_k = 0.5\rho_l w_r^2$. The change rate of the kinetic energy density at the fluid local point is proportional to the radial flow speed and acceleration at this point $d\varepsilon_k / d\tau = \rho_l w_r^2 \cdot dw_r / d\tau$.

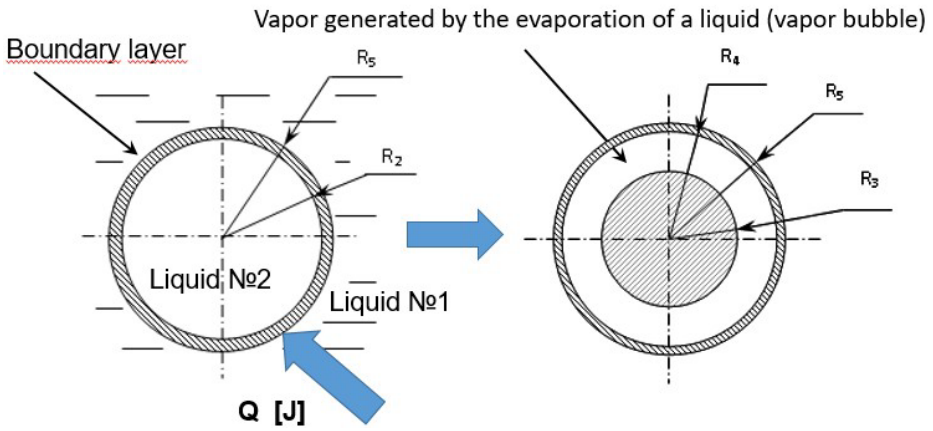

FIGURE 3.19. Steam generation process diagram: R_2, R_5 – internal and external radii of the interface of emulsion liquids; R_3, R_4 – inner and outer radii of the steam region.

The kinetic energy of the fluid radial motion around a single bubble can be calculated by recording the fluid kinetic energy for a thin layer with thickness of *dr*, located at a distance of *r* from the bubble centre, and then integrating over the fluid volume.

$$E_k = \int_R^\infty 2\pi\rho_l r^2 w_l^2 = 2\pi\rho_l R^3 w_R^2 \tag{3.47}$$

It is considered, that the fluid radial speed w_r at a distance of *r* from the bubble centre is related to the fluid radial motion speed at the bubble surface interface w_R by ratio $w_r = w_R R^2 / r^2$.

The change rate of the kinetic energy of the fluid radial motion during bubble growth or compression of a bubble can be written as

$$\frac{dE_k}{d\tau} = 4\pi\rho_l R^2 \left[R w_R \frac{dw_R}{d\tau} + \frac{3w_R^3}{2} \right] \tag{3.48}$$

The higher the fluid velocity and acceleration values at the bubble interface are, the faster energy is converted. The change rate of the fluid kinetic energy at the local point at a distance of *r* from the bubble centre can be represented as

$$\frac{d\varepsilon_k}{d\tau} = \frac{\rho_l R^3}{r^4} \left[R w_R \frac{dw_R}{d\tau} + 2w_R^3 \right] = \frac{1}{4\pi r^4} \left[R \frac{dE_k}{d\tau} + E_k w_R \right] \tag{3.49}$$

As it follows from (3.49), the change rate in the density of kinetic energy $d\varepsilon_k / d\tau$, determining the dynamic effect of a bubble at the fluid local point, is directly related to the integral energy parameter E_k and kinematic parameters w_R and $dw_R / d\tau$, characterizing conditions at the bubble interface. Therefore, these parameters can be used for quantitative assessment of the bubble dynamic characteristics.

During destruction process of steam bubbles, mechanical energy is converted many times.

First, the potential energy due to pressure difference in both phases is gradually converted into kinetic energy, value of the latter goes up with increase of the bubble compression speed w_R.

Right before the bubble reaches its minimum size, its compression speed and kinetic energy decrease rapidly.

At this, kinetic energy is converted into potential energy of compressed vapour and partially into the fluid potential energy E_{pot}, which, at $w_R = 0$ is concentrated, in a very narrow zone ΔV directly at the surface of the extremely compressed bubble.

It causes abnormally high pressure in this zone $p = \Delta E_{pot} / \Delta V$. In the process of the bubble re-expansion, this pressure pulse propagates in a fluid at the sound speed, and potential energy of the compressed vapour is converted into the fluid kinetic energy.

These mechanical energy conversions occur until the bubble disappears completely. Each stage of energy conversion is characterized by its transformation time $\Delta\tau_{tr}$.

Figure 3.20 shows the specific capacity value change pattern $\breve{W} = d\varepsilon_k / d\tau$ around an oscillating bubble during two periods of oscillations.

During one period, four power pulses are registered, at the final compression stage and at the initial expansion stage, pulse amplitudes are equally large. Thus, the analysed bubble medium is a thermodynamic heterogeneous system, where, in case of disequilibrium, interrelated heat-mass exchange, hydrodynamic and other processes initiate, determining the subsequent system evolution.

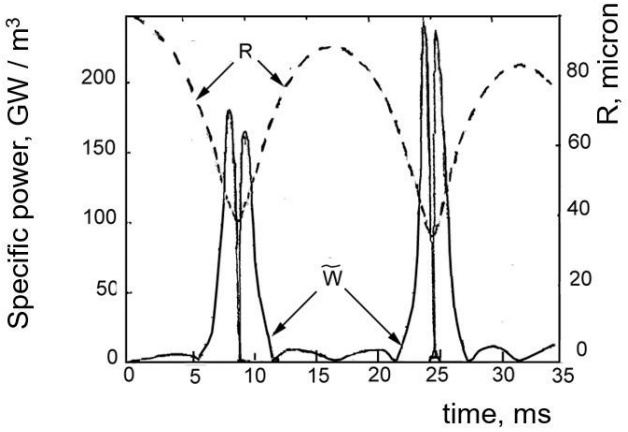

FIGURE 3.20. Dependence of specific capacity in the fluid at the vapour bubble interface and bubble radius on time for the first two periods of the vapour bubble oscillation. The calculation has been performer for the following conditions: T = 363 K; R_5 = 100 μm; pressure above the surface of the emulsion 70 kPa [3.1, 3.7].

Let us consider in more detail the equilibrium bubble evolution, when pressure in the fluid suddenly drops from p_{l0} to $p_l > p_{l0}$. The amount of potential energy, which in this case is no longer accumulated in the fluid, but inside the bubble, is still determined by expression

$$E_{pot} = 1.3\pi R^3 \left(p_l + \frac{2\sigma}{R_0} - p_{sat}\left(T_{l0}\right) \right) \tag{3.50}$$

The bubble evolution is determined by three non-equilibrium processes. Due to pressure difference, the bubble begins to expand rapidly and vapour pressure in the bubble drops quickly to external pressure value. At this point, the vapour potential energy is completely converted into the kinetic energy of fluid motion. Energy is not concentrated in the local area, but is distributed within the fluid volume.

According to equation (3.47), as the bubble radius increases, its growth rate w_R shall decrease. Vapour pressure decrease is compensated for by rapid evaporation inside the bubble. This leads to a decrease in surface temperature until the vapour pressure in the bubble pv becomes equal to the saturated vapour pressure at surface temperature of $p_{sat}(T_s)$ and fluid pressure at the same time p_l. If this condition is met, a short stage of a bubble inertial growth is completed, when a rapid transformation of vapour accumulated energy into kinetic energy of fluid motion occurs.

The further evolution of a growing bubble is controlled by only one non-equilibrium process with potential $T_l - T_s > 0$, wherein the fluid thermal energy is converted into kinetic energy of the fluid radial motion.

The steam bubble acts as a transformer of such conversion. Figure 3.21 shows how the value of fluid specific capacity at interface with the bubble changes as it grows.

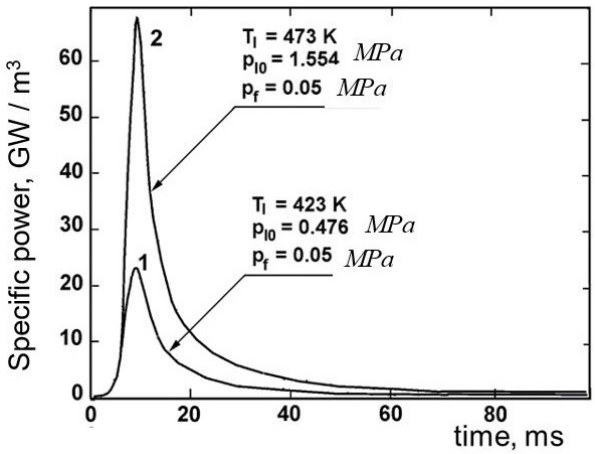

FIGURE 3.21. Value of fluid specific capacity at interface with the bubble: 1 – $R_5 = 100$ μm; 2 – $R_5 = 300$ μm; p_f – pressure above the surface of the emulsion; p_{l0} – vapor pressure [3.1, 3.7].

Temporal variation of the fluid specific power in the fluid at the bubble interface during its expansion due to instantaneous pressure release from initial equilibrium value $p_{l0} = p_{sat}(T_{l0})$ to the final value $p_f << p_{l0}$ at two values of fluid temperature. Inertial expansion stage is $\Delta\tau \approx 20$ μs.

Mechanical energy conversion duration $\Delta\tau_{tr}$ shall be very short to perform the accumulated energy as the maximum power pulse $W = E_{acc} / \Delta_{tr}$.

Energy in a pulse form shall be released simultaneously in many local zones, uniformly distributed within the device operating volume. Simultaneous compliance with these basic conditions ensures generation of maximum power.

When solving specific practical problems, these conditions are represented as necessary criteria to be met when choosing the most effective and rational method of local energy conversion.

The method, developed by us, has been implemented in several projects, wherein processes of creating homogeneous fluid media, homogeneous fuels, explosive substances, combustion processes, explosions and intensive cooling of surfaces were considered. Such results can be obtained with a sharp decrease in the pressure of the overheated emulsion.

To obtain similar results in the case of heating the emulsion at atmospheric pressure, it is necessary to use additional energy, for example, acoustic.

To account for the additional source of energy, the following tasks are defined:

- to supplement the mathematical model of a gas bubble in fluid with the source of sound oscillation, consider phase transition processes in the fluid, on the surface of a bubble and in the gas-vapor medium;
- to perform calculations of transient thermodynamic processes inside oscillating gas bubbles of different dimensions in terms of acoustic impact on the fluid;
- to analyze the effect of temperature on thermal-physical parameters of oscillating bubbles;
- to conduct field tests to prove the calculated resonance frequencies and observation of the phenomenon of bubbles resonance, to evaluate the effect of surfactants on bubble oscillatory processes.

The mathematical model [3.25, 3.29, 3.30] was accepted as the basis for studying the influence of acoustic oscillations of the resonance frequency on the thermobaric characteristics of a gas-vapor bubble). This model is based on Rayleigh equation [3.31], which is applied in a new form in these articles.

In this article, the equations are modified to the general case when the vapour region may also contain other gas.

The dependence of thermophysical characteristics of vapour on pressure and temperature is known and can be determined, e.g, as in literary reference [3.32].

Equation (3.55) was changed in order to take into account mass transfer processes at condensation/evaporation of water vapor inside a bubble. Equation (3.63) was used for description of a source of harmonic pressure oscillations (acoustic oscillations). The model contains the following simplifying assumptions:

– a gas bubble is of spherical shape;
– a fluid is viscous and non-compressed;
– inside a gas bubble, there is a mixture of gases (air and water vapor), the weight of which may vary as a result of mass exchange processes both on the boundary of a bubble, and in its volume;
– gases inside a bubble are considered as actual gas (taking into account the van der Waals forces).

Let us consider the equations describing thermodynamic characteristics of a gas-vapor bubble during transition to a new state of thermodynamic equilibrium [3.25, 3.29, 3.30]:

$$\frac{dR}{d\tau} = \frac{p_{B(\tau)} - p_\infty}{\rho_r R} - \frac{3R^2}{2R} - \frac{4\mu_r R}{\rho_r R^2} - \frac{2\sigma_r}{\rho_r R^2} \tag{3.51}$$

$$\frac{dR}{d\tau} = R + \frac{I_w}{\rho_r} \tag{3.52}$$

$$p_B = p_w + p_a \tag{3.53}$$

$$p_w = \frac{R_\mu T \rho_w}{\mu_w - b_w \rho_w} - \rho_w^2 \frac{a_w}{\mu_w^2}, \qquad p_a = \frac{R_\mu T \rho_a}{\mu_a - b_a \rho_a} - \rho_a^2 \frac{a_a}{\mu_a^1} \tag{3.54}$$

$$\frac{d\rho_w}{d\tau} = 3R^{-1}\left(I_w - \frac{\rho_w dR}{d\tau}\right), \qquad \frac{d\rho_a}{d\tau} = 3R^{-1}\left(I_a - \frac{\rho_a dR}{d\tau}\right) \tag{3.55}$$

$$\frac{dT}{d\tau} = \frac{3R^{-1}}{c_w\rho_w - c_a\rho_a}\left(q - \frac{p_B dR}{d\tau}\right) \tag{3.56}$$

$$q = \left\{\left(\rho_w \overline{v}_{w(T)} + 6I_w\right)c_w + \left(\rho_a \overline{v}_{a(T)} + 6I_a\right)c_a\right\}\left(T_{r(R,\tau)} - T\right) \tag{3.57}$$

$$\overline{v}_{w(T)} = \left(8R_\mu T / \pi\mu_w\right)^{0.5} \text{ and } \overline{v}_{a(T)} = \left(8R_\mu T / \pi\mu_a\right)^{0.5} \tag{3.58}$$

$$I_w = -D_w P_w \left(R\Gamma_w\right)^{-1} \quad \text{and} \quad I_a = -D_a P_a \left(R\Gamma_a\right)^{-1} \tag{3.59}$$

$$\frac{\partial\left(\rho_r c_r T_{(x,\tau)}\right)}{\partial\tau} = \frac{\partial}{x^2\partial x}\left(\lambda_r x^2 \frac{\partial T_{(x,\tau)}}{\partial x}\right) - \frac{\partial\left(\rho_r c_r T_{(x,\tau)}\right)}{\partial x} + q_{v(x,T)} \tag{3.60}$$

$$-\frac{\partial\left(\lambda_r, T\right)}{\partial x}\bigg|_{(x=R,\tau)} = -q - \frac{r_w}{4\pi R^2}\frac{dm_r}{d\tau} + I_a r_m \tag{3.61}$$

$$-\left.\frac{\partial(\lambda_r, T)}{\partial x}\right|_{(x=\infty,\tau)} = 0 \qquad (3.61^*)$$

$$T_{(x,\tau=0)} = T_0 \qquad (3.62)$$

$$p_\infty = p_0 + A_p \sin\left(2\pi\tau\Pi^{-1}\right) \qquad (3.63)$$

Conditions for the occurrence of phase transitions

In the gas-vapor medium:

- if $T < T_s$, water vapor condensate occurs;
- if $T < T_s$ and $m_{wr} > 0$, evaporation of water vapor condensate occurs.

Hereinafter, T_s is the dew point temperature, K; m_{wr} is the mass of condensed water vapor in the gas-vapor medium in a bubble, kg.

At the boundary of a bubble (water surface):

- if $T_r > T_s$, water boils;
- if $T_r < T_s$, condensation of water vapor occurs;
- if $P_w^* > P_w$, diffusion of water vapor from the surface of a bubble to its gas-and-vapor medium;
- if $P_w^* < P_w$, diffusion of water vapor from the gas-vapor medium of a bubble to its surface.

3.5. Results of research

3.5.1. Theoretical research

Calculations of oscillation of air bubbles of different dimensions in water were performed according to the proposed mathematical model (3.51)-(3.63). Water temperature was accepted as 10°C at atmospheric pressure; the amplitude of sound oscillation pressure 5 kPa. Results of mathematical modelling of parameters of bubbles of different dimensions are shown in figures 3.22-3.25.

Figure 3.22 shows that every size of a bubble corresponds to its resonance frequency, which depends on thermodynamic parameters of gas-vapor mixture inside a bubble and surrounding layers of fluid. For the assigned resonance conditions, the frequency of bubbles can be determined from the approximation formula, Hz

$$f_R = \frac{5.465}{d}$$

After the bubbles enter the resonance, the amplitude of oscillation is stabilized at the level of 30-50% of the radius. This is due to alignment of energy balance: the number of fed energy of sound vibrations is equal energy losses to friction in water, heat and mass exchange near the surface of a bubble.

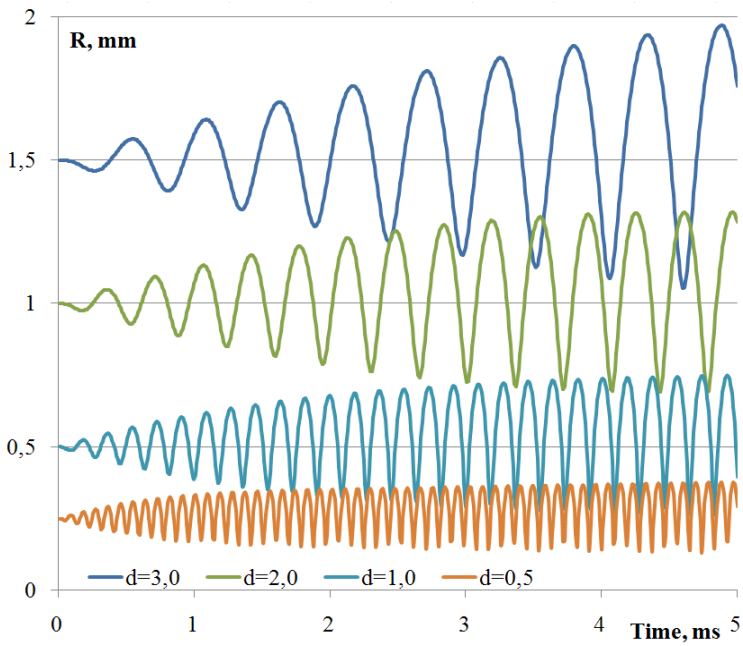

FIGURE 3.22. Change of the radius of bubbles (R, mm) of various dimensions (d, mm) under resonance conditions.

Analysis of motion velocity of the walls of a bubble (fig. 3.23) shows that it may exceed 6 m/s.

This is about a thousand times as much as velocity of a wall during damping oscillations of a bubble. Higher velocities are observed only in cavitation bubbles in the period of maximum compression.

At the same time, there is a change of internal pressure in the anti-phase to the motion of the wall of a bubble (fig. 3.24). Calculations show that in half-periods of compression, the inner pressure of a bubble may exceed the ambient pressure as much as by three times. In half-periods of expansion, pressure of the gas-vapor medium decreases compared to ambient pressure of by more than two times. Such pressure fluctuations create preconditions for intensification of heat and mass exchange near the surface of a bubble.

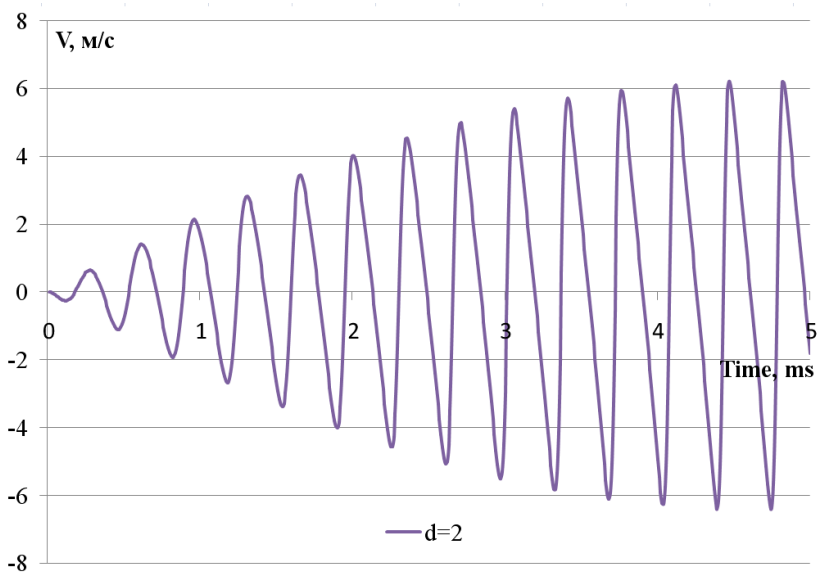

FIGURE 3.23. Rate of change in the radius of a bubble (diameter d = 2 mm).

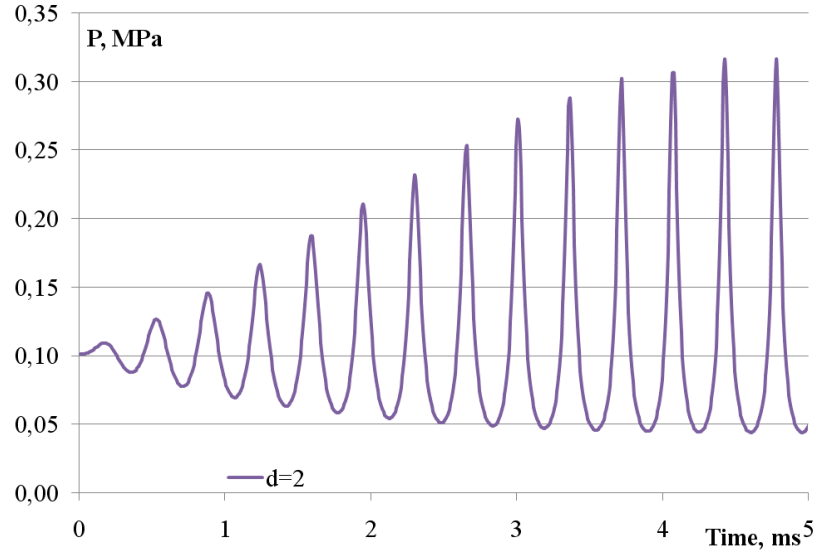

FIGURE 3.24. Diagram of gas pressure in a resonance bubble (diameter d = 2 mm).

Figure 3.25 shows the temperature mode of the gas-vapor medium of a resonance bubble. Temperature fluctuations occur within from +13°C to −7°C relative to the initial value. Fluctuations in temperature on the surface of a bubble are shown in figure 3.26. In spite of the simultaneous nature of the fluctuations of gas temperature in a bubble, the temperature mode of water surface differs

significantly. The temperature increases by 7.4°C and decreases only by 1°C relative to the initial value.

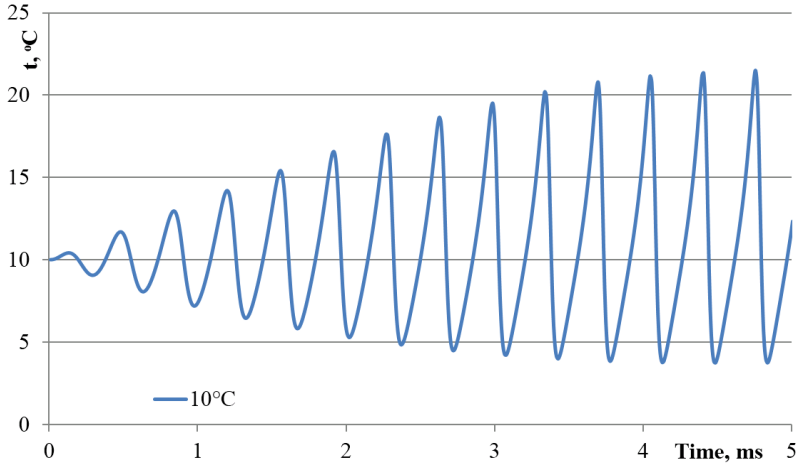

FIGURE 3.25. Diagram of gas temperature in a resonance bubble.

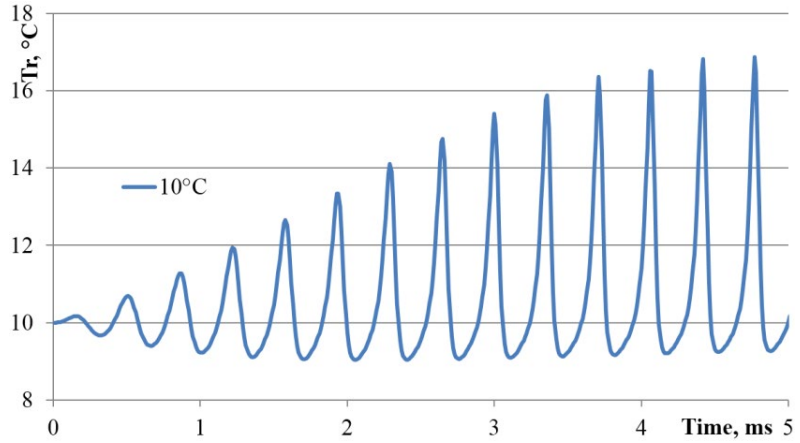

FIGURE 3.26. Temperature of the surface of a resonance air bubble in water.

A number of calculations, the results of which are shown in figure 3.27, were carried out to analyze the influence of the gas-vapor medium on the amplitude and resonance frequency oscillations. The absence of harmonics at changing the temperature indicates independence of resonance frequency on the temperature of a bubble. A decrease in the amplitude of oscillations at an increase in temperature of gas-vapor medium is an evident fact. The reason for this is intensification of mass transfer processes both near the surface of a bubble and in its gas-vapor medium at an increase in temperature.

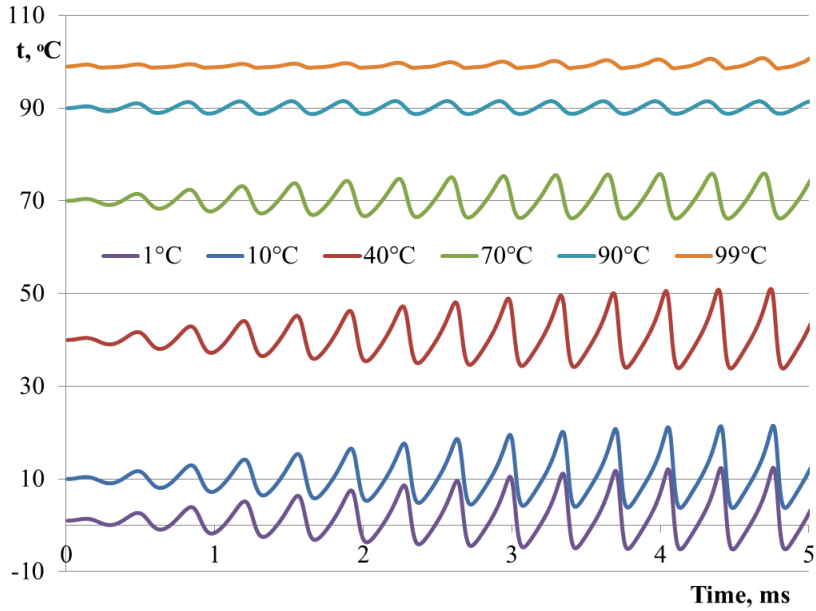

FIGURE 3.27. Influence of fluid temperature on amplitude of resonance oscillations of temperature of gas-vapor medium of a bubble.

It is important to analyze the chronological order to understand the processes, taking place in an oscillating bubble. For this purpose, we will follow the deployment of various processes in time, which will be divided into 5 stages.

STAGE 1. Let us start with the maximum dimensions of a bubble. The pressure in a bubble is minimal. Temperatures of gas and water are approximately equal to each other, so there is practically no heat exchange. There is no condensed water vapor inside a bubble. As a result of the great difference of partial pressures of water vapor near the surface of a bubble and the gas-vapor medium, specific mass flow of water vapor near the surface of a bubble is almost maximum and directed inside a bubble. Low gas pressure initiates the process of compression of a bubble, a gradual increase in pressure begins. We observe an increase in the temperature of the gas medium and the surface of a bubble. Diffusion of water vapor from the surface of a bubble to the gas medium gradually decreases and reaches zero, when gas pressure becomes equal to atmospheric.

STAGE 2. The pressure inside a bubble becomes excessive, the diameter of a bubble decreases and the temperature of its gas-vapor medium increases. Diffusion of water vapor from the gas medium to the wall of a bubble increases. The temperature of water on the surface of a bubble increases. The temperature of the gas-vapor medium of a bubble reaches its maximum. The temperature peak is ahead of the pressure peak of a bubble due to intense heat exchange near its surface.

STAGE 3. As a result of an increase in internal pressure, a bubble's compression begins to slow down, and the temperature of its gas-vapor medium starts to decrease. At this time, the temperature on the surface of a bubble reaches a maximum. The mass flow of diffusing water vapor to the wall of a bubble continues to grow and reaches a maximum at the moment of maximum pressure inside a bubble. The dimensions of a bubble at this moment are minimal.

STAGE 4. The dimensions of a bubble increase, while pressure and temperature decrease. Due to a rapid decrease in gas temperature and a pressure decrease in a bubble, condensation of water vapor in the volume of a bubble begins and abruptly increases – fog formation occurs. The condensate mass reaches the maximum under conditions of medium pressure and the minimum temperature inside a bubble. At low temperatures, condensation of water vapor inside a bubble almost does not influence the temperature mode, since the mass of condensed water vapor is negligible. When approaching the water boiling temperature, condensation and evaporation of water vapor in the volume of a bubble begins to play a key role in an increase in the amplitude of oscillations.

STAGE 5. During subsequent extension of a bubble, gas pressure decreases to the level that is below atmospheric. Due to intense heat exchange from the surface, gas is heated inside a bubble. At the same time, condensation (fog) gradually evaporates. Evaporation of water vapor from the surface of a bubble reaches its maximum and then begins to decrease gradually. Stage 5 ends when a bubble reaches the maximum dimensions.

After that the whole cycle of thermodynamic processes repeats.

3.5.2. Field tests

The scheme of a measuring set is shown in figure 3.28.

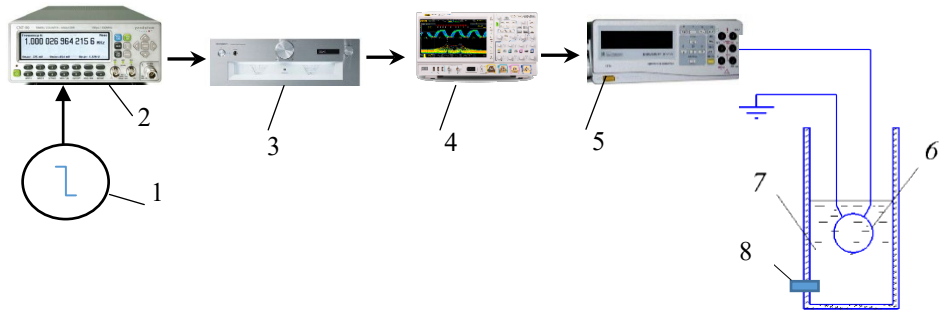

FIGURE 3.28. Scheme of a facility for research of bubbles in the resonance acoustic field: 1 – master multivibrator; 2 – frequency meter; 3 – two-step amplifier; 4 – oscilloscope; 5 – voltmeter; 6 – piezoceramic resonator; 7 – fluid; 8 – hydrophone.

Harmonic oscillations in the water were created using piezoceramic resonator with the diameter of 27 mm. It was powered by the multi-vibrator of alternating frequency with an amplifying output cascade. In general, the multi-vibrator covers the frequency range from 280 Hz to 500 kHz. In the experiments, the frequency of the output signal was determined by the electronic frequency meter F 5311, and the shape was determined by the oscilloscope N313.

By the experimental data, the power, connected to the emitter in the frequency range of 2÷5 kHz, was approximately 0.6 W. The specific power of the resonator is 1047 W/m^2, which corresponds to the sound pressure in water P = 5.404 kPa. This sound pressure is equivalent to the sound volume of 168.6 dB. Water was fed to the capacity under pressure in order to obtain bubbles. In case there are bubbles of resonance dimensions in the water oscillations begin to be observed and overall sound increases by ten times. The fragment of a sound track recording during a bubble entering resonance is shown in figure 3.29.

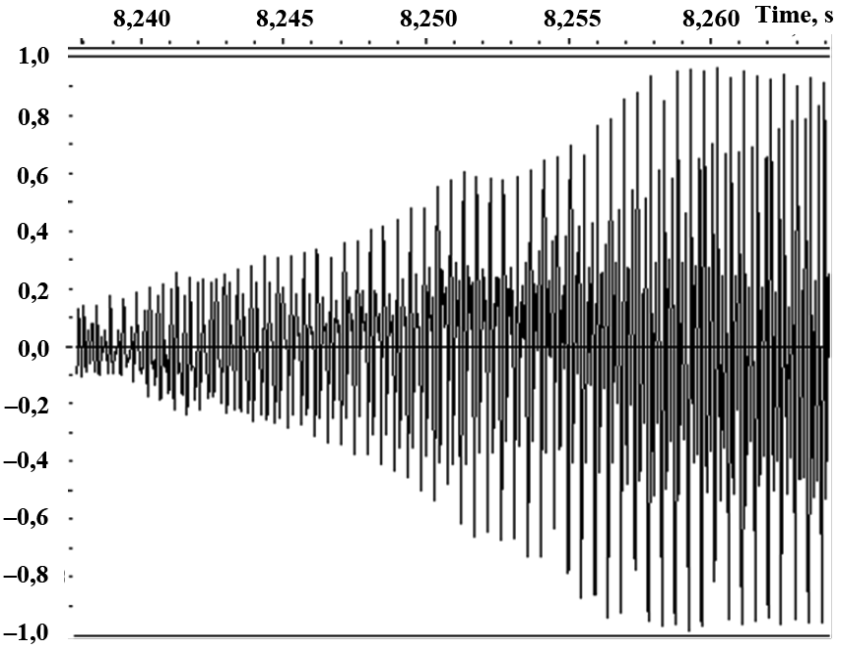

FIGURE 3.29. Fragment of sound track recording during a bubble entering resonance.

In distilled water, multi-bubbles begin to be formed at frequency of above 2 kHz and cease to be formed at frequencies of above 3 kHz. Maximum activity is observed at 2.5 kHz, which corresponds to the diameter of bubbles of 2.3 mm. Upon reaching the maximum size (3.6-4.1 mm), a multi-bubble can be divided into smaller ones (fig. 3.30) or can explode with formation of a cloud of small bubbles.

In other cases, a large bubble can be a source of small ones, which constantly "break away" from a large one and start an "independent" life in fluid.

Addition of surfactants (SAS) to water immediately extends the range of formation of multi-bubbles. These structures begin to appear at frequency of 830 Hz and finish their formation at frequencies above 5 kHz. The most active formation of multi-bubbles is observed at frequency of 2.5 kHz. When using SAS, the number of small bubbles in a large one increases significantly. An "explosion" of such multi-bubble with formation of a cloud of microscopic bubbles is seen in the image (fig. 3.31c).

By using surfactants of various kinds, it is possible to significantly change the strength of the surface tension on the gas bubble surface.

In these studies, the effect of surfactants on frequency and amplitude of the vapour bubble fluctuations was analysed.

Emulsions use surfactants to stabilize the structure, so the objective was to study how these parameters change at different concentrations of surfactants.

The following mixture of surfactants was used: sodium lauryl ether sulphate ($CH_3(CH_2)10CH_2(OCH_2CH_2)nOSO_3Na$) and lauramine oxide ($C14H_31NO$).

Decrease of surface tension magnitude simplifies breaking up of emulsion droplets, since the deformation resistance force decreases by $2\sigma/R$.

Besides, surfactants stabilize the formation of small bubbles.

Therefore, as the surface tension decreases, using surfactants, and as temperature rises, an increase in the amplitude and frequency of oscillations at the vapour-fluid interface boundary, shown in figure 3.30.

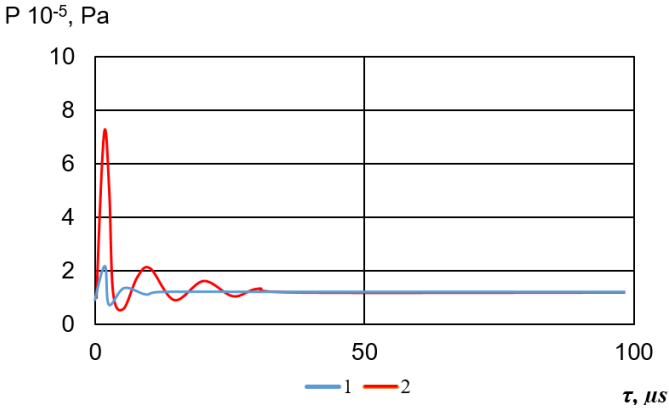

FIGURE 3.30. Bubble pressure of different sizes with and without use of surfactants: 1 – d = 1 mm without SAS; 2 – d = 1 mm with SAS.

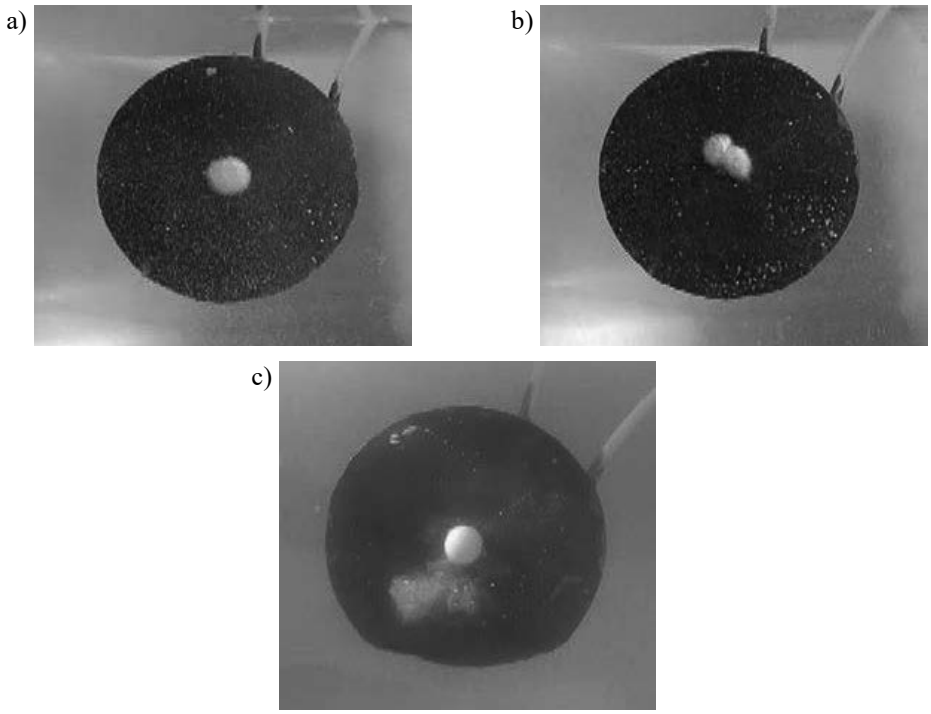

FIGURE 3.31. Division of a large multi-bubble into two ones of smaller dimensions: a) initial moment; b) in 0.03 s; c) explosion (burst) of a multi-bubble with formation of small bubbles after 0.06 s.

It appeared, that if bubbles are greater than 1 mm in diameter, use of surfactants has little effect on the bubble internal pressure.

For small-sized bubbles, addition of surfactants results in a decrease of the bubble internal pressure by the surface tension decrease. In general, experimental studies proved existence of resonance of gas bubbles in water at calculation frequencies. In addition, it was possible to obtain multi-bubbles and a large number of bubbles of dimensions less than 0.1 mm.

Theoretical and experimental studies of resonance oscillations of gas-vapor bubbles in water is a continuation of a series of papers [3.25, 3.29, 3.30], devoted to thermodynamic processes at the fluid-gas boundary. The obtained results are caused by taking into account heat and mass exchange that occur on the surface and inside an oscillating gas-vapor bubble. The merit of this study is a good match of calculation data with the results of the field test, which was achieved thanks to the improvement of the mathematical model and compliance of the output data of mathematical modeling with the conditions of the field test. The results of field tests not only proved the theoretically calculated resonance frequencies, but also made it possible to identify an interesting phenomenon of formation of multi-

bubbles. When oscillations reach certain amplitude, a large bubble is divided into a very large number of small ones, which are retained inside a large bubble by the forces of surface tension. The obvious consequence of formation of such a structure is a sharp increase in heat and mass exchange surface at the boundary of the contact of phases. Calculations and field tests were conducted for bubbles in water under conditions of atmospheric pressure. Development of such research could be analysis of the influence of pressure on resonance characteristics of bubbles, experimental evaluation of mass transfer processes on the inter-phase surface, check of formation of multi-bubbles in other fluids and many others.

The results of the conducted studies can have a wide range of applications in various industrial processes, based on heat and mass exchange at the boundary of the gas-fluid contact. The consequence of the use of resonant sound oscillations for bubbling plants, aeration, vacuum distillation, absorption and others may be a decreasing power capacity and increasing rate of technological processes.

Figure 3.32 shows how the structure of the emulsion changes during thermal intensification of the homogenization process.

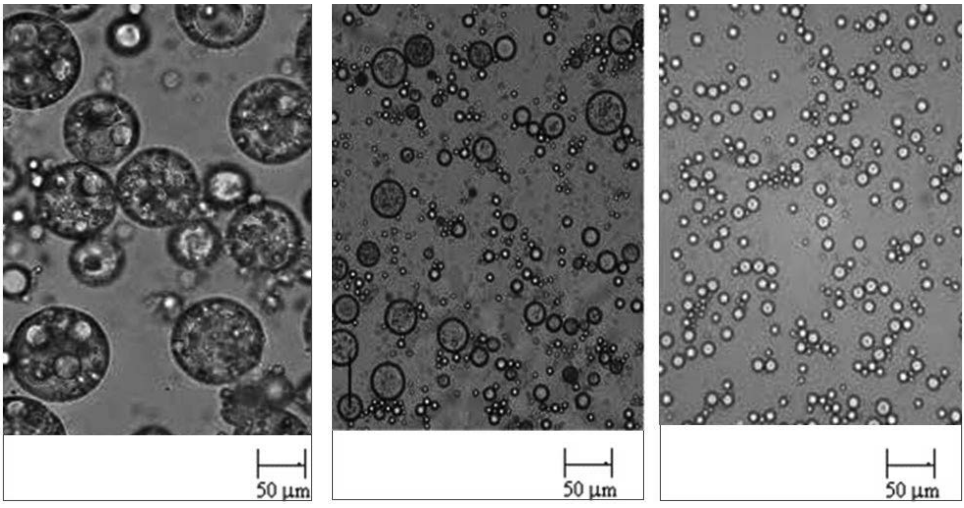

FIGURE 3.32. Change in the structure of the emulsion during thermal intensification of the homogenization proces.

3.6. Conclusions

1. As a result of research, the possibility of resonance in vapor-gas bubbles in water in the frequency range 0.5-5 kHz was established. Quantitative indicators of thermodynamic parameters of a bubble under conditions of resonance are determined.

2. Performed calculations showed that temperature of gas-vapor medium of a bubble does not affect its resonance frequency, however, has a significant impact on the amplitude of oscillations. When fluid temperature approaches its boiling temperature, an abrupt increase in amplitude of oscillations of a bubble occurs. For example, amplitude of oscillations of the wall of a bubble decreases by six times at an increase in water temperature from +10°C to +99°C.
3. The existence of resonance bubbles on calculated frequencies was experimentally proved. The field observations showed that resonance oscillations of bubbles are accompanied by formation, growth and destruction of multi-bubbles. Long-term effect of sound waves at resonance frequencies leads to formation of a very large number of bubbles of dimensions of less than 0.1 mm in fluid volume. It was established experimentally that application of SAS considerably expands the frequency range of formation of multi-bubbles and increases the number of small bubbles inside a large one. This makes it possible to increase the area of heat exchange and mass exchange surface of bubbles. Application of the resonance of bubbles has great prospects for intensification of many technological processes, based on heat and mass exchange processes at the fluid-gas boundary.
4. A significant increase in the intensity of heat and mass transfer processes at any temperature can be achieved through the use of a liquid-bubble structure. At the same time, such a structure can be created by disrupting the thermodynamic equilibrium of a liquid by a sharp decrease in pressure. A similar effect can be achieved by applying an acoustic field with resonant frequencies. The proposed method allows to determine the main operating characteristics. Besides, using the obtained results, it is possible to determine conditions for the emulsion breaking-up (homogenization) by increasing its temperature, acoustic action, or a combination of these methods.

References

[3.1] Dolinsky A.A., Ivanitsky G.K., Use of discrete-pulse energy input in various production processes . Proc. International Conf. on Transport Phenomena Science and Technology. Beijing (China): Higher Education Press, 1992, pp. 89-100.

[3.2] Dolinsky A.A. Pavlenko A.M., Basok B.I., Thermophysical Processes in Emulsions, Naukova Dumka, Kiev 2005, p. 265.

[3.3] Pavlenko A.M., Dispersed phase breakup in boiling of emulsion, *Heat Transfer Research*, Volume 49, Issue 7, 2018, pp. 633-641. DOI: 10.1615/HeatTransRes. 2018020630.

[3.4] Pavlenko A., Change of emulsion structure during heating and boiling. International *Journal of Energy for a Clean Environment*, 20(4), 2019, pp. 291-302. DOI: 10.1615/InterJEnerCleanEnv.2019032616.

[3.5] Pavlenko A., Energy conversion in heat and mass transfer processes in boiling emulsions, *Thermal Science and Engineering Progress*, Volume 15, 1 March 2020, 100439. https://doi.org/10.1016/j.tsep.2019.100439.

[3.6] Dolinsky A.A., Ivanitsky G.K., The principle of discrete-pulse energy input – new approach to the development of efficient power-saving technologies. Ann.Review of Heat Transfer. Vol. XIII, 2003. N.-Y, Wallingford (UK): Begell House Inc, pp. 47-83.

[3.7] Dolinsky A.A., Ivanitsky G.K., Vapor-Gas Bubble Dynamics at Discrete-Pulse Energy Injection. Proc. International Seminar on Transient Phenomena in Multiphase Flow. Dubrovnik (Jugoslavia), 1987, Part 4, pp. 86-92.

[3.8] Dolinsky A.A., Ivanitsky G.K., Collective effects of the behavior of a vapor bubble ensemble in superheated or supercooled liquids. Proc. International Conf on Transport Phenomena Science and Technology. Beijing (China): Higher Education Press, 1996, pp. 225-233.

[3.9] Taleyarkhan R.P., West C.D., Cho J.S., Lahey jr. R.T., Nigmatulin R.I., Block R.C. Evidence for Nuclear Emissions During Acoustic Cavitation. Science, Vol. 295, March 2002, pp. 1868-1873.

[3.10] Roesle M.L., Kulacki F.A., An experimental study of boiling in dilute emulsions, part A: Heat transfer. International Journal of Heat and Mass Transfer, 55(7-8), 2012, pp. 2160-2165, https://doi.org/10.1016/j. ijheatmasstransfer.2011.12.020.

[3.11] Rozentsvaig A.K., Strashinskii Ch.S., Regimes of Heat Transfer During Boiling Emulsions with Low-Temperature Dispersed Phase Applied Mathematical Sciences 9(112), 2015, pp. 5593-5601, DOI: 10.12988/ams.2015.57474.

[3.12] Roesle M.L., Lunde D.L., Kulacki F.A., Boiling Heat Transfer to Dilute Emulsions From a Vertical Heated Strip. J. Heat Transfer, Vol. 137(4), 2015, p. 8 https://doi.org/10.1115/1.4029456.

[3.13] Mura E., Massoli P., Josset C., Loubar K., Bellettre J., Study of the micro-explosion temperature of water in oil emulsion droplets during the Leidenfrost effect. Exp. Therm. Fluid Sci., 43, 2012, pp. 63-70, 10.1016/j.expthermflusci.2012.03.027.

[3.14] Shilyaev M.I., Tolstykh A.V., Modelling of gas absorption processes in bubblers. Thermophysics and Aeromechanics, Vol. 20, No. 5, 2013, pp. 565-576.

[3.15] Gasanov B.M., Bulanov N.V., Effect of the droplet size of an emulsion dispersion phase in nucleate boiling and emulsion boiling crisis International. Journal of Heat and Mass Transfer, Volume 88, 2015, pp. 256-260 https://doi.org/10.1016/j.ijheatmasstransfer.

[3.16] Ramamurthi K., Sumil Kumar S., Collapse of vapor locks by condensation over moving subcooled liquid. Int. J. Heat Mass Transfer, Vol. 44, No. 6, 2001, pp. 2983-2994.

[3.17] Fauser J., Mitrovic J., Some features of boiling fronts on heated surfaces, Proc. 11th IHTC, Vol. 2, Kyongju, August 23-28, 1998, pp. 377-382.

[3.18] Tsukamoto O., Uyemura T., Observation of bubble formation mechanism of liquid nitrogen subjected to transient heating, Advances in Cryogenic Engineering, Vol. 25, 1980, pp. 476-482.

[3.19] Medvedev R.N., Chernov A.A., The calculation of thermal grows of the toroidal bubble on current concentrator in electrolyte Modern Science, Issue 2 (10), 2012, pp. 50-56.

[3.20] Hegedűs F., Stable bubble oscillations beyond Blake's critical threshold. Ultrasonics. Vol. 54, Issue 4, 2014, pp. 1113-1121.

[3.21] Pavlenko A., Koshlak H., Usenko B., The processes of heat and mass exchange in the vortex devices Metallurgical and Mining Industry, 6(3), 2014, pp. 55-59.

[3.22] Bulanov V.A., Korskov I.V., Popov P.N., Measurements of the nonlinear acoustic parameter of sea water via a device using reflected pulses. Instruments and Experimental Techniques. Volume 60, Issue 3, 2017, pp. 414-417.

[3.23] Alhelfi A., Sunden B., Numerical investigation of an oscillating gas bubble in an ultrasonic field, 10th International Conference on Heat Transfer, Fluid Mechanics and Thermodynamics. Orlando 2014, pp. 315-322, URL: https://repository.up.ac.za/bitstream/ handle/2263/44673/Alhelfi Numerical.pdf.

[3.24] Colonius T., Hagmeijer R., Ando K., Brennen C.E., Statistical equilibrium of bubble oscillations in dilute bubbly flows. Physics of Fluids, Volumen. 20, Issue 4, 2008, pp. 40-52.

[3.25] Pavlenko A.M., Thermodynamic Features of the Formation of Hydrocarbon Hydrates. Energies 2020, 13, 3396; doi:10.3390/en13133396.

[3.26] Avksentyuk B.P., Ovchinnikov V.V., Plotnikov V.Ya., Dynamic effects on interphase surface during the disintegration of superheated near-wall liquid. Proc. Int. Cent. Heat Mass Transfer, Vol. 33, 1991, pp. 583-598.

[3.27] Avksentyuk B.P., Ovchinnikov V.V., The Dynamics of Explosion Boiling of Toluene under Subatmospheric Pressure, High Temperature, Vol. 17, No. 4, 1999 pp. 606-613.

[3.28] Hegedűs F., Stable bubble oscillations beyond Blake's critical threshold Ultrasonics, Vol. 54, Issue 4, 2014, pp. 1113-1121.

[3.29] Pavlenko A., Koshlak H., Słowak A., Stability of multiphase liquid media. Earth and Environmental Science, Volume 227, 4, 2019, pp. 1-11.

[3.30] Pavlenko A., Koshlak H., Formation of the steam phase in superheated liquids in the state of metastable equilibrium. Eastern-European Journal of Enterprise Technologies, Vol. 5, No. 5 (89), 2017, pp. 35-42.

[3.31] Rayleigh, On the pressure developed in a liquid during the collapse of a spherical cavity. Phil. Mag, Vol. 34, 2017, pp. 94-98.

[3.32] Reed R., Prausnitz J., Sherwood T., Properties of gases and liquids: Reference book. Leningrad: Khimiya 1982, 592 p.

Part 2

THEORETICAL SUBSTANTIATION OF MECHANICAL INITIATION OF HEAT AND MASS TRANSFER PROCESSES

List of conventions

a – coefficient of thermal diffusivity, m^2/s

B – volume, m^3

C_D – is the coefficient of hydrodynamic drag of a drop

C_p – heat capacity at constant pressure, J/(kg·K)

C – is mass concentration

D – is the coefficient of mutual diffusion of the components, m^2/s

D – is the diameter of the dispersed particles, mm (μm)

D_{32} – the average diameter of the dispersed particles, microns(μm)

d – is the differential

F – resistance force, N

g – acceleration of gravity, m/s^2

G – volumetric flow rate, m^3/s

H – is the dimensionless time

h – height of working elements, m

i, j – are the numbers of the steps of the difference grid

k – kinetic energy of turbulence, m^2/s^2

M – moment of resistance forces, N·m

M, N – the number of steps of the difference grid along the longitudinal and transverse coordinates

n – number of revolutions per second, rev/s

p – pressure, Pa

Δp – pressure drop, Pa

P – is the dimensionless pressure

r – radius, radial coordinate, m (mm)

r_0 – internal radius of the RPA internal stator, mm

R – is the dimensionless radial coordinate

Q – heat dissipation power; electric power, W;

t – temperature, °C

ΔT – temperature difference, °C

u, v, w – projections of the velocity vector on the axis of a rectangular coordinate system, m/s

v_r – radial velocity, m/s

v_θ – tangential velocity, m/s
V_r – the average radial velocity over the cross section, m/s
V, U – dimensionless radial and tangential velocities
$x; y; z$ – transverse, longitudinal and vertical rectangular coordinates, m
z – number of slots in the RPA working elements
α – heat transfer coefficient, W/(m^2·K)
α – surface tension coefficient, N/m
δ – the width of the cylinder gap, mm
Δ – is the difference
ε – is the dissipation rate of the kinetic energy of turbulence, m^2/s^3
κ – Karman constant
θ – is the angular coordinate
ϑ – dimensionless temperature
λ – thermal conductivity coefficient, W/(m·K)
μ – dynamic coefficient of viscosity, Pa·s
ν – kinematic viscosity coefficient, m^2/s
ρ – density, kg/m^3
τ – time, s
$\Delta\tau$ – period, s
ω – angular velocity, s^{-1}
ω_0 – the angular velocity of rotation, s^{-1}
$\Omega = \omega / \omega_0$ – is the dimensionless angular velocity

Index superscript

$\overline{\ }$ – is the average value (for the period)
rel – relative

Index subscript

b – destruction
bo – to the border
c – is the critical value of the parameter
con – is construction elements
D – is a drop
in – input
f – is fluid
max – is the maximum

min – is the minimum
out – output
r – is the radial coordinate
s – is stable
t – is turbulent
θ – is the tangential coordinate
opt – optimal
ev – is the average value
ef – effective
0 – dispersion (carrier) medium
1 – dispersed medium

Similarity numbers

Bo – is the Bond number
Ca – is the capillary number
Lp – is the Laplace number
Nu – is the Nusselt number
Pr – is the Prandtl number
Re – is the Reynolds number constructed by the initial parameters
Re_{ex} – Reynolds number based on current speed
Ta – is the Taylor number
We – is the Weber number constructed by the initial parameters
We_{ex} – is the Weber number constructed by current parameters

Abbreviations

DIVE – discrete-pulse input of energy
RPA – rotary pulsation apparatus
IETF NASU – Institute of Engineering Thermophysics National Academy of Sciences of Ukraine

Chapter 4

CALCULATING METHODS FOR RESEARCHING DYNAMICS OF LIQUID AND HEAT AND MASS TRANSFER IN ROTOR-PULSE APPARATUS

4.1. Appointment, principle of operation and design features of rotary pulsation apparatus

Rotary pulsation apparatuses are devices intended for the processing of mechanical mixtures of dissimilar mutually insoluble liquids into chalk-dispersed emulsions. These devices are widely used in food, chemical, pharmaceutical and other industries. Based on design features, distinguish RPA disk [4.1-4.3] or cylindrical types. The operating experience of cylindrical rotary pulsation apparatuses in various technological processes indicates their high efficiency when used as mixers and homogenizers [4.4-4.23].

The cylindrical-type RPA working elements are hollow coaxial cylindrical bodies separated by narrow gaps and provided with radial slots (fig. 4.1). One part of the working elements is rigidly fixed (stators), and the other part (rotors) rotates with a high angular velocity [4.24, 4.25]. Rotors and stators are arranged in series. The medium being processed, entering the working zone of the apparatus through the internal sections of the slots of the internal stator, flows in the radial direction due to the pressure differential between the inlet and outlet sections of the working zone, as well as due to the action of centrifugal forces caused by the rotation of the rotor. Due to the rotation of the rotors in the flow of a heterogeneous medium passing through radial slots and gaps, high flow strain rates, significant pressure gradients, normal and tangential stresses arise, which rapidly change in time and have the nature of pulsations. These pulsations are capable of causing deformation and destruction of dispersed inclusions in the carrier fluid flow. The higher the values of the indicated values characterizing the dynamic effect of the apparatus on the heterogeneous flow, the smaller the dispersed particles can be crushed. In addition to these crushing factors, turbulent pulsations, as well as cavitation processes that are likely to occur in the RPA working area due to periodic pressure drops, should also be mentioned.

Important performance indicators of cylindrical RPA are their finished product performance, processing time of the initial mixture to the required size of dispersed inclusions, energy consumption, dimensions, and also the dispersed composition

itself, i.e. the prevailing particle size of the dispersed component of the mixture. The last indicator characterizing the required quality of the resulting product should be considered the main one.

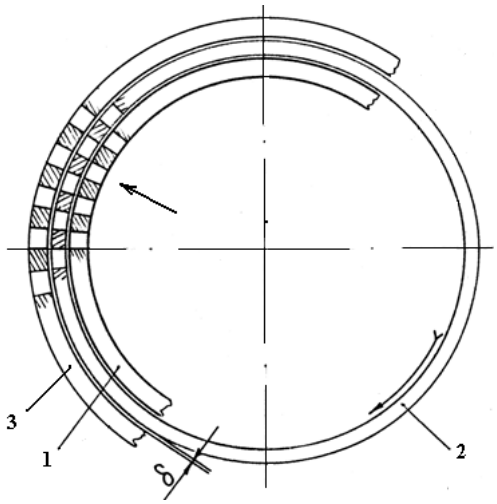

FIGURE 4.1. The scheme of the working bodies of RPA cylindrical type: 1 – internal stator; 2 – rotor; 3 – external stator, δ – gaps between cylinders.

To create optimal designs of these devices, to set the required operational parameters of their work, it is necessary to find their relationship with the dispersed composition of the finished product, i.e. it is necessary to answer the question under what operating parameters of the apparatus the resulting product meets the requirements for its quality. Currently, this issue remains the most problematic. The answer to it can be obtained by analyzing the kinematic and dynamic characteristics of the flow of the carrier dispersion medium, i.e. based on data on the mentioned pressure gradients, stresses, velocities, accelerations, the intensity of their pulsations in time, etc.

An important problem for the devices under consideration is also the dissipation of the mechanical energy of the fluid flow due to friction. As a result of the transfer of mechanical energy into heat, the processed product is heated, which can lead both to changes in the required properties of the product itself and to failure of the apparatus elements. Moreover, as will be shown below, dissipative heat releases do not occur uniformly throughout the volume, but most often locally, i.e. in limited areas adjacent to the working bodies. When locally heating mixtures of organic substances, including, for example, protein, its thermocoagulation can occur, which is usually unacceptable according to the technological instructions for the preparation of food products. In these cases, one must either organize some kind of heat removal system from the apparatus, or reduce the rotor velocity.

Thus, to solve the problem of crushing dispersed particles in the RPA working area, establishing their average size after processing a heterogeneous medium in RPA, and also about possible energy costs for this process, a detailed study of the dynamic and temperature characteristics of the fluid flow in RPA is necessary. To solve these problems, both experimental and theoretical research methods are used.

4.2. Approximate hydrodynamic models for rotary pulsation apparatus

In theoretical studies, the main attention was paid to methods for calculating flow characteristics, mass-average velocities, pressure pulsations, and volumes of energy costs [4.3, 4.26-4.37]. The results of theoretical calculations were compared with experimental data [4.5, 4.19, 4.37-4.41]. Based on the obtained theoretical solutions to problems and experimental data, the mechanisms of crushing of dispersed inclusions in the RPA working area were studied. Among them, the most common were the acoustic [4.42-4.45] and cavitation [4.5, 4.33, 4.46-4.51] mechanisms, as well as the mechanism of particle crushing by turbulent pulsations generated in the carrier flow [4.5, 4.23, 4.52, 4.55, 4.61]. On this basis, methods were also built for predicting the dispersion of the resulting emulsions, i.e. methods for calculating the average size of dispersed inclusions [4.29, 4.30, 4.53-4.62]. A detailed analysis of the literature in which these issues were addressed is presented in the monograph [4.5].

The problems of fluid flow in the RPA working area were considered mainly in a one-dimensional formulation [4.5, 4.17, 4.27-4.33, 4.37, 4.46, 4.47, 4.63-4.71]. An attempt to obtain closed analytical solutions led to the need for a significant simplification of the problem statement. In [4.64], for example, to use the conformal mapping method for modeling the flow in the slots of the rotor and stator, the ideal fluid model was used. To study fluid dynamics in the gaps between the working elements, the Couette flow model between rotating and stationary cylinders was usually used [4.27, 4.63]. To calculate the fluid flow in the slots, the Bernoulli equation was used [4.5, 4.31-4.33, 4.37, 4.46, 4.47, 4.63, 4.65-4.71]. For studies of velocity and pressure pulsations, this equation was considered as unsteady. Losses of pressure on friction and on local resistances were considered proportional to the pressure head. The hydrodynamic drag coefficients were considered as complex functions of the flow regime, Reynolds number, and geometry of the computational domain [4.31-4.33, 4.67, 4.68, 4.70]. In [4.33, 4.63, 4.69], the equations of dynamics were compiled taking into account the action of centrifugal forces.

In [4.31, 4.32], attempts were made to construct analytical solutions of the approximate unsteady equations of fluid dynamics in RPA. However, due to the need for significant simplifications in the statement of the problem, the results of

such solutions can be used only for a qualitative assessment of hydrodynamic phenomena in the RPA working area.

One-dimensional solutions to the problems of fluid dynamics were also used to study the dissipation of mechanical energy in a stream passing through the working volume of the RPA. The main conclusions about the levels of energy dissipation and the degree of heating of the medium being processed, based on theoretical and experimental results, are presented in [4.16, 4.23, 4.26, 4.38, 4.40, 4.41, 4.63, 4.72-4.75]. On the basis of one-dimensional solutions, approximate methods for optimizing RPA structural and operational parameters were also constructed [4.5, 4.34, 4.35].

4.2.1. Numerical studies of fluid dynamics in cylindrical RPA obtained on the basis of approximate hydrodynamic models

The use of numerical methods to solve fluid dynamics problems in RPA significantly expands the possibilities of both qualitative and quantitative analysis of the laws of such flows. The characteristic features of the pulsating fluid flow in the RPA, obtained on the basis of the numerical solution of the simplified non-stationary hydrodynamic problem, are considered in [4.67]. As a model of the fluid flow in the slot of the RPA internal stator, the flow in the channel is considered with the area of the channel exit section periodically changing in time (with a period $\Delta\tau$). The fluid flow is described by an equation of the form:

$$\left(1+\zeta_M+\zeta_T\right)\cdot\frac{\rho w^2}{2}+\rho l\frac{\partial w}{\partial\tau}\cdot K=\Delta p_l$$

where: w – velocity; l – channel length; Δp_l – pressure difference between inlet and outlet sections; ζ_M – coefficient of pressure loss at local resistances; ζ_T – coefficient of friction losses, the value of which depends on the flow regime of the liquid; K – is a value characterizing the degree of overlap of the output section of the channel.

Losses at local resistances consist of losses in the input and output sections of the channels and losses when the fluid flows through an obstacle of variable cross-section ("gate valve"). In the developed turbulent regime, such losses are independent of the number Re, and the drag coefficient of the "valve" ζ_M depends only on the degree of overlap of the channel, i.e. from the coefficient of living cross-section $\overline{f}=F_{\text{o}}/F_{\text{1}}$, where F_{1} is the total cross-section of the channel, and F_{o} is the bore in the current position of the rotor. To determine this dependence, an approximation of a number of consistent literature data [4.76, 4.77] was performed using the drag coefficients of a rectangular gate, grating, and aperture. At the same time, it was taken into account that in a real rotary-pulsating apparatus, due to the presence of gaps, $\overline{f}$ it never becomes equal to zero, i.e. ζ_M in the closed state, the

"valve" has not some infinite, but some finite value. Given these circumstances, a function was proposed to calculate the loss coefficient at local resistances

$$\zeta_M = \left(\frac{4}{0.01 + \sin^2\left(\pi\tau / \Delta\tau\right)} - 1.96 \right)$$

the values of the coefficients in which characterize the influence of the gaps on the value ζ_M at $\overline{f} = 0$ and $\overline{f} = 1$.

For the coefficient of overlap of the channel cross section *K*, the relation

$$K = 0.5\left[1 + \sin\left(2\pi\tau / \Delta\tau - \frac{\pi}{2}\right)\right] + \chi$$

in which the term χ reflects the influence of the gap and shows that even when the output channel cross section completely overlaps, there is some minimal liquid transit flow.

The results of a numerical solution of the fluid dynamics equation are presented in figure 4.2 in the form of time dependences of the fluid velocity in the channel *w*, as well as the acceleration of the flow $dw/d\tau$. The case of fluid flow with a density $\rho = 10^3$ kg/m^3 with a viscosity coefficient $\nu = 3 \cdot 10^{-5}$ m^2/s in a channel of length $l = 10^{-2}$ m with an equivalent diameter of $d_{equ} = 5 \cdot 10^{-3}$ m at a pressure drop is considered $\Delta p_l = 16$ Pa and a period of $\Delta\tau = 0.33 \cdot 10^{-3}$ s.

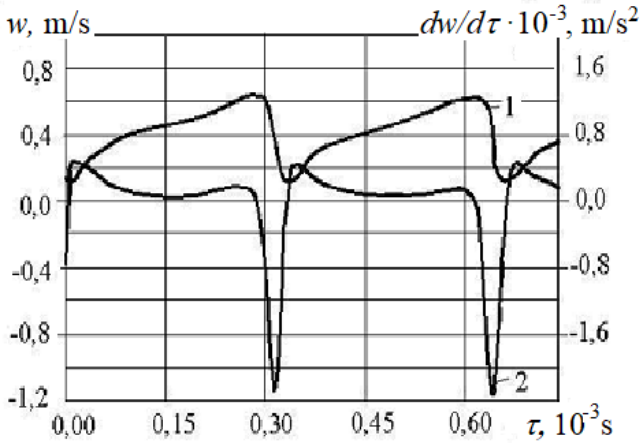

FIGURE 4.2. The character of the pulsating fluid motion in channels of RPA of a cylindrical type: 1 – $w(\tau)$, m/s; 2 – dw/dτ, m/s^2.

As can be seen from figure 4.2, the dependence of velocity on time has the form of a periodic function with a smooth increase and a sharp decline within one period, and the time of the decrease in velocity from the maximum value to the minimum is approximately $0.13\Delta\tau$. In the indicated time interval, the acceleration of the flow reaches a minimum, which is $dw/d\tau \approx -2.3\cdot10^3$ m/s^2.

4.2.2. An approximate hydrodynamic model for studying fluid dynamics in disk-type RPA

Disk rotary pulsation apparatuses are similar to cylindrical ones according to the principle of operation and basic characteristics. The specific features of these RPA are that the disk rotor 2, located between the stators 1 and 3, rotates in a plane perpendicular to the direction of fluid movement (fig. 4.3). In this case, the fluid flow in the working area is provided only due to the applied external pressure drop. In comparison with a cylindrical apparatus, which is characterized by slotted slits of rectangular cross section, it is advisable to use round cuts in the disk apparatus along with rectangular slots. The lengths of the slots of the stators and the rotor can be significantly different. Features of an approximate solution to the problem of pulsating fluid flow in a RPA slot of a disk type are considered in [4.1]. The solution is based on the same principles as in [4.67]. If the slots in the disks have a rectangular shape, the problem of the pulsating fluid flow in the slots of the disk RPA is solved in the same way as in the case of a cylindrical RPA. In the case of circular channels, the dependence of the passage area f_0 on the dimensionless time has a more complex form:

$$f_0 = r^2(\alpha - \sin\alpha)$$

where $\alpha = 2\arcsin\sqrt{1-\left(1-2\left|\tau/\Delta\tau - 0.5\right|\right)^2}$.

In [4.1], the results of a numerical solution of the one-dimensional differential equation of fluid motion in a disk RPA obtained by the Runge-Kutta method are presented. The calculation options were performed for the geometric and operational parameters characteristic of disk RPA: equivalent channel diameter $d_e = 5\cdot10^{-3}$ m; density $\rho = 10^3$ kg/m^3; the number of slots z = 60, the rotor velocity n = 50 s^{-1}, the period $\Delta\tau = 1/z/n = 0.33\cdot10^{-3}$ s, the viscosity of the medium $\nu = 1\cdot10^{-5}$ m^2/s and $3\cdot10^{-5}$ m^2/s; ranges of differential pressure Δp = (4...20) kPa; channel lengths l = (13...123) 10^{-3} m. The results of calculations of the velocity and acceleration of the fluid flow ($\nu = 3\cdot10^{-5}$ m^2/s) in the rectangular channel of the disk RPA ($l = l_1 + l_0 + l_2 = 0.043$ m) at Δp = 12 kPa are presented in figure 4.4.

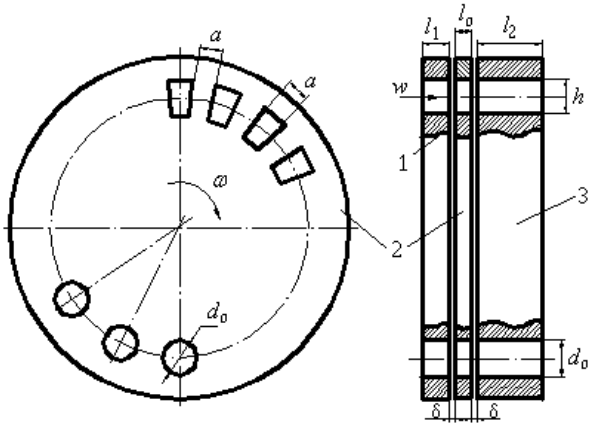

FIGURE 4.3. The working bodies of the disk rotary pulsation apparatus.

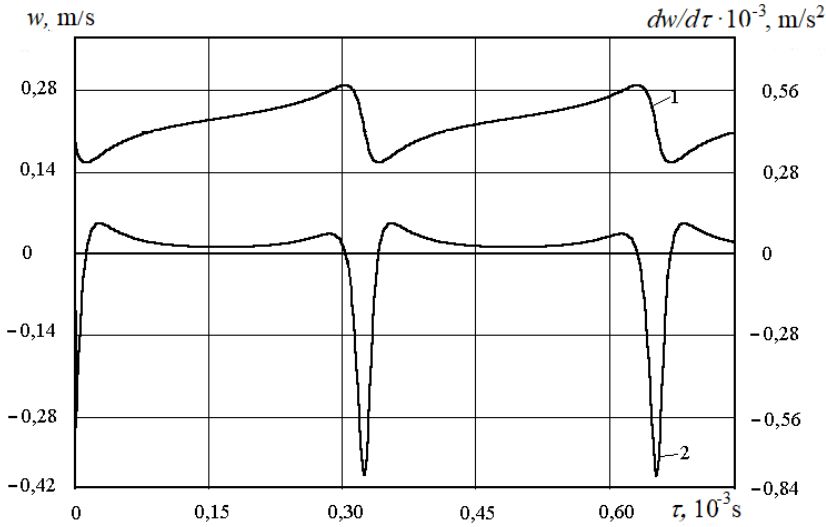

FIGURE 4.4. The character of the pulsating fluid motion in the RPA channels of the disk type: 1 – $w(\tau)$, m/s; 2 – $dw/d\tau$, m/s^2.

As can be seen from the figure, the law of variation of the velocity w in the channel for one period $\Delta\tau$ is characterized, as in the case of a cylindrical RPA, by a smooth increase and a sharp drop. From the results obtained for channels of various lengths l, it follows that the period of time at which a sharp drop in velocity is observed slightly decreases with increasing channel length and is approximately 0.15...0.1 of the period $\Delta\tau$. The negative impulses of acceleration $dw/d\tau$, caused by the sharp deceleration of the flow at the moment of mutual overlapping of the slots of the rotor and stators, result in pressure pulses positive in front of the rotor and negative

behind it. Based on the shape of the acceleration pulse (fig. 4.5), it can be assumed that the current (average over the time of falling velocity) acceleration value is 0.4 of its amplitude value. Then the level (average value for a specified period of time) of pressure pulsations can be approximately estimated as

$$\Delta p_{\text{pulse},\, i} = 0.4 \cdot \rho \cdot l_i \cdot \left(\frac{dw}{d\tau} \right)_{\max}$$

where l_i is the channel length of the corresponding working *i*-element.

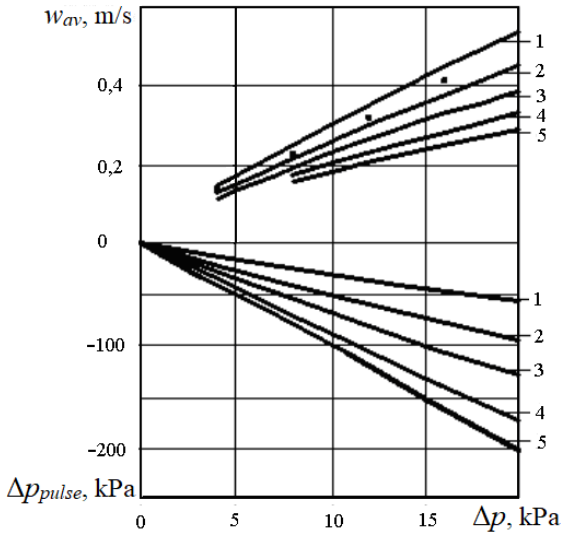

FIGURE 4.5. The dependence of the average hydrodynamic characteristics of the disk RPA on the difference in external pressure at *l*, m: 1 – 0.013; 2 – 0.018; 3 – 0.023; 4 – 0.043; 5 – 0.123.

It should be noted that such pressure pulses cannot directly be effective for the implementation of dispersive phase dispersion or emulsification processes in heterogeneous systems. In these processes, normal and tangential viscous stresses, as well as sufficient pressure gradients, are productive. Therefore, positive pressure pulsations in the zone up to the rotor are generally not of interest in this sense. Negative pulsations behind the rotor can be effective through the mechanism of excitation of adiabatic boiling under conditions when the total pressure in the considered zone of the apparatus reaches, at certain points in time, less than the saturation pressure of the liquid at the considered temperature. In this regard, it is advisable to further consider only the zone of the medium flow behind the rotor. Here the level of pressure pulsations depends on the length of the channel of the second stator.

In figure 4.5 the calculated dependences of the average fluid velocity w_{av} for the period $\Delta\tau$ and pressure pulsation level Δp_{pulse} versus the total pressure drop Δp in the RPA working area and the total channel length for the case when they have a rectangular cross section are presented. Here, for comparison, the dots show the results of calculating w_{av} for channels of circular cross section in the case when l = 0.013 m. When setting the total length of the channels, it is assumed that l_0 = 0.003 m; l_1 = 0.005 m, and the total length of the channels l changes only by increasing the length of the second stator l_2.

A comparison of the calculation results shows that the values of the average current velocity in round channels with the same value of equivalent diameter turn out to be only 8-10% lower than in rectangular channels. This fact makes it possible to use data obtained for rectangular channels with a correction factor of 0.9 to evaluate the pressure-flow characteristics of a disk-type RPA. The decrease in velocity in the round channels is explained by the fact that the average integral over the period $\Delta\tau$ area of the cross section of the system with round channels is 15% less than the same area of the system with rectangular channels. The influence of the shape of the channels on the values of accelerations and pressure pulsations is somewhat more pronounced. The dependence of pressure pulsations on the channel length of the second stator l_2 is shown in figure 4.6 (the scale for l_2 is logarithmic). From an analysis of the results in figure 4.6, it follows that the dependence of the pressure fluctuation levels on the channel length has a maximum. The length value l_2 corresponding to the indicated maximum weakly depends on the applied pressure drop.

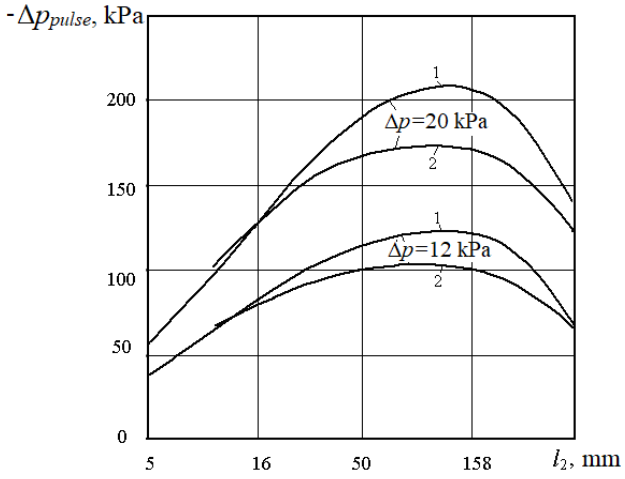

FIGURE 4.6. Dependence of pressure pulsations on the channel length of the second stator l_2: 1 – rectangular channels; 2 – round channels.

From an analysis of the presented results of a numerical study of the hydrodynamic regimes of disk-type RPA, it follows that with an increase in the channel length of the second stator, the value of negative pressure pulses in the maximum zone exceeds 100 kPa, i.e. the beginning of the process of adiabatic boiling in this zone is possible already at an average pressure in the apparatus close to atmospheric. With a pressure drop Δp = 12...20 kPa between the input and output sections of the RPA working area, the maximum level of pressure pulsations is 120...200 kPa, i.e. there is a tenfold increase in the energy potential, which is a typical sign of the process of discrete-pulse energy input.

The influence of the shape of the channels on the levels of pressure pulsations in general is insignificant. The maximum values of Δp_{pulse} for channels of rectangular cross section exceed similar indicators for channels of circular cross section by approximately 20% (fig. 4.6).

Strictly speaking, these results have physical meaning only under the condition that the pressure at the inlet to the working zone of the apparatus substantially exceeds 200 kPa, otherwise it is impossible to use the model of the flow of a single-phase medium. At the same time, from the above results, based on the use of an approximate hydrodynamic model, one can draw qualitative conclusions that negative pressure pulses of high amplitude with a frequency measured in thousands of Hertz and duration measured in tens of microseconds can be generated in the area of the working zone located behind the rotor. These conditions can cause adiabatic boiling of the treated heterogeneous medium behind the rotor.

In general, it should be noted that the current approaches to solving problems of fluid dynamics and heat transfer in RPA, based on approximate hydrodynamic models, do not allow to fully evaluate the complex structure of the flow of the medium being processed and to find out its characteristic features associated with the influence of structural and operating parameters of the device.

As the development of computer facilities and software designed to solve the problems of hydrodynamics, the formulation of problems on the fluid flow in RPA was refined and complicated. Currently, these problems are already being solved in a three-dimensional formulation [4.78-4.80]. However, in this case, problems arise, mainly related to the rate of convergence of the numerical solution of problems and the significant amount of computer time needed to find it, which makes it difficult to obtain a sufficient amount of data for a generalized analysis of the characteristic features of dynamics and heat transfer in RPA.

As a result of this, there is a need to develop such numerical models that will allow for a real period of time to study in detail the dynamic and thermal characteristics of RPA, on the basis of which both methods for assessing the degree of dispersion of the heterogeneous medium being processed and methods for calculating the optimal structural and operational parameters of the apparatus can be created.

4.3. The problem of fluid dynamics in the working space of a cylindrical RPA

Let us consider a method for constructing a numerical solution to the two-dimensional problem of hydrodynamics and heat transfer in the working zone of a cylindrical RPA. The solution is constructed for the case of two resting (external and internal stators) and one rotating (rotor) cylinders. Since the slots in the rotor and stators are periodically repeated with a constant angular step, it is advisable to consider only one of these periodically repeating fragments (fig. 4.7).

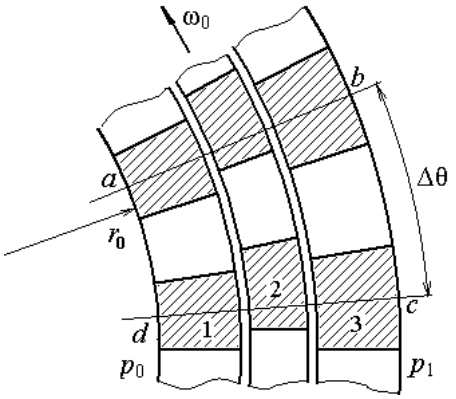

FIGURE 4.7. The design scheme of a fragment of the working space of a cylindrical rotary pulsation apparatus: 1, 3 – stators; 2 – rotor.

The considered period of *abcd* includes one slot and two halves of the side walls of the stators. The slot of the rotor due to its rotation will periodically align with the slots of the stators, and will also periodically overlap the walls of the stators. Since the main working elements of the apparatus are coaxial cylindrical bodies, it is advisable to present the system of equations of fluid dynamics and heat transfer in a cylindrical coordinate system (z, r, θ), the origin of which lies on the common axis of the working elements. The system of equations of dynamics, compiled in stresses, has the form:

$$\frac{\partial(v_r r)}{\partial r}+\frac{\partial v_\theta}{\partial \theta}+r\frac{\partial v_z}{\partial z}=0 \tag{4.1}$$

$$\rho\left(\frac{\partial v_r}{\partial \tau}+\frac{1}{r}\frac{\partial\left(v_r^2 r\right)}{\partial r}+\frac{1}{r}\frac{\partial\left(v_r v_\theta\right)}{\partial \theta}+\frac{\partial\left(v_r v_z\right)}{\partial z}-\frac{v_\theta^2}{r}\right)= \tag{4.2}$$

$$=-\frac{\partial p}{\partial r}+\frac{1}{r}\frac{\partial}{\partial r}\left(r\sigma_{rr}\right)-\frac{\sigma_{\theta\theta}}{r}+\frac{1}{r}\frac{\partial \sigma_{r\theta}}{\partial \theta}+\frac{\partial \sigma_{rz}}{\partial z}$$

$$\rho\left(\frac{\partial v_\theta}{\partial \tau}+\frac{1}{r}\frac{\partial\left(v_\theta v_r r\right)}{\partial r}+\frac{1}{r}\frac{\partial v_\theta^2}{\partial \theta}+\frac{\partial\left(v_\theta v_z\right)}{\partial z}+\frac{v_\theta v_r}{r}\right)= \\ =\frac{1}{r}\frac{\partial}{\partial \theta}\left(-p+\sigma_{\theta\theta}\right)+\frac{1}{r^2}\frac{\partial}{\partial r}\left(r^2\sigma_{\theta r}\right)+\frac{\partial \sigma_{\theta z}}{\partial z} \tag{4.3}$$

$$\rho\left(\frac{\partial v_z}{\partial \tau}+\frac{1}{r}\frac{\partial(v_r v_z r)}{\partial r}+\frac{1}{r}\frac{\partial(v_z v_\theta)}{\partial \theta}+\frac{\partial v_z^2}{\partial z}\right)=\frac{\partial}{\partial z}\left(-p+\sigma_{zz}\right)+\frac{1}{r}\frac{\partial \sigma_{z\theta}}{\partial \theta}+\frac{1}{r}\frac{\partial(\sigma_{zr} r)}{\partial r} \tag{4.4}$$

These equations of motion include the components of the stress tensor, which are calculated by the formulas:

$$\sigma_{rr}=2\mu_{ef}\frac{\partial v_r}{\partial r};\quad \sigma_{\theta\theta}=\frac{2\mu_{ef}}{r}\left(\frac{\partial v_\theta}{\partial \theta}+v_r\right);\quad \sigma_{zz}=2\mu_{ef}\frac{\partial v_z}{\partial z};$$

$$\sigma_{r\theta}=\sigma_{\theta r}=\mu_{ef}\left[\frac{1}{r}\frac{\partial v_r}{\partial \theta}+r\frac{\partial}{\partial r}\left(\frac{v_\theta}{r}\right)\right];$$

$$\sigma_{\theta z}=\sigma_{z\theta}=\mu_{ef}\left[\frac{1}{r}\frac{\partial v_z}{\partial \theta}+\frac{\partial v_\theta}{\partial z}\right];\quad \sigma_{zr}=\sigma_{rz}=\mu_{ef}\left[\frac{\partial v_z}{\partial r}+\frac{\partial v_r}{\partial z}\right]$$

where: v_r, v_q, v_z – the radial, tangent, and vertical components of the velocity, μ_{ef} – the effective viscosity coefficient of the processed medium.

The system of equations of dynamics (4.1)-(4.4) is usually considered in conjunction with the energy equation

$$C_p\rho\left[\frac{\partial T}{\partial \tau}+\frac{1}{r}\frac{\partial(r\cdot v_r T)}{\partial r}+\frac{1}{r}\frac{\partial(v_\theta T)}{\partial \theta}+\frac{\partial(v_z T)}{\partial z}\right]= \\ =\frac{1}{r}\frac{\partial}{\partial r}\left(r\lambda_{ef}\frac{\partial T}{\partial r}\right)+\frac{1}{r^2}\frac{\partial}{\partial \theta}\left(\lambda_{ef}\frac{\partial T}{\partial \theta}\right)+\frac{\partial}{\partial z}\left(\lambda_{ef}\frac{\partial T}{\partial z}\right)+\mu_{ef}S^2 \tag{4.5}$$

where

$$S=\left[2\left(\frac{\partial v_r}{\partial r}\right)^2+2\left(\frac{1}{r}\frac{\partial v_\theta}{\partial \theta}+\frac{v_r}{r}\right)^2+2\left(\frac{\partial v_z}{\partial z}\right)^2+\right. \\ \left.+\left(\frac{1}{r}\frac{\partial v_r}{\partial \theta}+r\frac{\partial}{\partial r}\left(\frac{v_\theta}{r}\right)\right)^2+\left(\frac{1}{r}\frac{\partial v_z}{\partial \theta}+\frac{\partial v_\theta}{\partial z}\right)^2+\left(\frac{\partial v_z}{\partial r}+\frac{\partial v_r}{\partial z}\right)^2\right]^{1/2}$$

Equation (4.5) describes the heat transfer by the flow, taking into account the dissipation of mechanical energy due to friction.

With such a formulation of the problem, the dispersion medium is considered as homogeneous, having physical properties corresponding to the effective properties of a heterogeneous medium. In the laminar flow of a Newtonian fluid, the effective transport coefficients μ_{ef} and λ_{ef} will correspond to its coefficients of molecular viscosity and molecular thermal conductivity. If equations (4.1)-(4.5) are considered as time-averaged equations of turbulent momentum and energy transfer, the coefficient μ_{ef} should be considered the sum of the coefficients of molecular μ and turbulent viscosity μ_t. In this case, the effective thermal conductivity coefficient is represented as $\lambda_{ef} = \lambda + \lambda_t$. If the dispersion medium is a non-Newtonian fluid, then, according to [4.81-4.83], its dynamics and heat transfer are described by the system of equations (4.1)-(4.5), for which

$$\mu_{ef} = \left(\frac{\sigma_o^{1/n}}{S^{1/m}} + \mu^{1/m} \right)^n S^{n/m-1} \tag{4.6}$$

where n, m, σ_o, μ are the experimentally found parameters of the rheological model. For n = 1, m = 1, model (4.6) describes a Newtonian fluid with shear viscosity μ.

If we assume that the fluid flow in the direction of the rotational axis of the OZ rotor practically does not occur, and that the fluid moves only in the plane of the horizontal section perpendicular to the OZ axis, the hydrodynamic problem can be considered as two-dimensional. For such a problem, it is advisable to present the system of equations of dynamics and heat transfer in the polar (r, θ) coordinate system. The numerical solution of the system of equations (4.1)-(4.5) is conveniently performed by representing the tangential velocity component in the form $v_\theta = \omega \cdot r$, where ω is the angular velocity. It is also convenient to use the angular velocity ω instead of the tangential v_θ because on the rotor surface the quantity ω is, by the condition of the problem, a known given quantity ω_0. The system of equations of fluid dynamics and heat transfer should also be unmeasured. After the transition from v_θ to the angular velocity ω and dimensionless, the system of equations will take the form:

$$\frac{1}{R}\frac{\partial(RV)}{\partial R} + \frac{\partial \Omega}{\partial \theta} = 0 \tag{4.7}$$

$$\frac{\partial V}{\partial H}+\frac{1}{R}\frac{\partial\left(RV^2\right)}{\partial R}+\frac{\partial(V\Omega)}{\partial\theta}-\Omega^2R=-\frac{\partial P}{\partial R}+\frac{2}{\mathrm{Re}\,R}\frac{\partial}{\partial R}\left(R\zeta\frac{\partial V}{\partial R}\right)-$$
$$-\frac{2}{\mathrm{Re}\,R}\zeta\left(\frac{\partial\Omega}{\partial\theta}+\frac{V}{R}\right)+\frac{1}{\mathrm{Re}\,R^2}\frac{\partial}{\partial\theta}\left(\zeta\frac{\partial V}{\partial\theta}\right)+\frac{1}{\mathrm{Re}}\frac{\partial}{\partial\theta}\left(\zeta\frac{\partial\Omega}{\partial R}\right) \tag{4.8}$$

$$\frac{\partial\Omega}{\partial H}+\frac{1}{R^2}\frac{\partial\left(R^2\Omega V\right)}{\partial R}+\frac{\partial\Omega^2}{\partial\theta}+\frac{\Omega V}{R}=-\frac{1}{R^2}\frac{\partial P}{\partial\theta}+\frac{2}{\mathrm{Re}\,R^2}\frac{\partial}{\partial\theta}\left[\zeta\left(\frac{\partial\Omega}{\partial\theta}+\frac{V}{R}\right)\right]+$$
$$+\frac{1}{\mathrm{Re}\,R^3}\frac{\partial}{\partial R}\left[R\zeta\left(R^2\frac{\partial\Omega}{\partial R}+\frac{\partial V}{\partial\theta}\right)\right] \tag{4.9}$$

$$\frac{\partial\vartheta}{\partial H}+\frac{1}{R}\frac{\partial(R\vartheta V)}{\partial R}+\frac{\partial\vartheta\Omega}{\partial\theta}=\frac{1}{\mathrm{Re}\,\mathrm{Pr}}\left[\frac{1}{R}\frac{\partial}{\partial R}\left(\Lambda R\frac{\partial\vartheta}{\partial R}\right)+\frac{1}{R^2}\frac{\partial}{\partial\theta}\left(\Lambda\frac{\partial\vartheta}{\partial\theta}\right)\right]+$$
$$+2\varsigma\left[\left(\frac{\partial V}{\partial R}\right)^2+\left(\frac{\partial\Omega}{\partial\theta}+\frac{V}{R}\right)^2+0.5\cdot\left(\frac{1}{R}\frac{\partial V}{\partial\theta}+R\frac{\partial\Omega}{\partial R}\right)^2\right] \tag{4.10}$$

where: $V=v_r/\left(\omega_0r_0\right)$; $\Omega=\omega/\omega_0$; $H=\tau\omega_0$; $R=r/r_0$; $P=\left(p-p_0\right)/\left(\rho\omega_0^2r_0^2\right)$; $\mathrm{Re}=\rho_0\omega_0r_0^2/\mu_0$; $\vartheta=\left(T-T_0\right)\rho_0C_{p0}/\left(\omega_0\mu_0\right)$; $\mathrm{Pr}=C_{p0}\mu_0/\lambda_0$; $\zeta=\mu_{ef}/\mu_0$; $\Lambda=\lambda_{ef}/\lambda_0$; p_0,T_0 – pressure and temperature of the medium at the entrance to the RPA working zone; r_0 – is the radius of the inner surface of the inner stator; μ_0 – is the conditional viscosity scale; λ_0 – is the conditional scale of thermal conductivity. In the case of a Newtonian fluid, flow, μ_0 and λ_0 correspond to its molecular viscosity and thermal conductivity coefficients.

As boundary conditions in the input and output sections of the working area, it is advisable to take the pressure drop $\Delta p=p_0-p_1$ between them and set the tangential velocity component to zero. This pressure drop is considered uniformly distributed over the corner. Due to the rotation of the rotor and the presence of friction between the rotor and the liquid, its particles also begin to rotate with the rotor. This results in centrifugal forces arising in the flow, forcing the fluid to move in the radial direction. Thus, the radial fluid flow in cylindrical RPA is provided both by the presence of a pressure differential between the inlet and outlet sections, and by the action of centrifugal forces. Therefore, radial movement can take place not only with a positive pressure drop Δp, but also at zero, and even (up to a certain value) with a negative Δp (i.e. against pressure forces).

Since there is a geometric periodicity of the considered fragments of the working elements, it is logical to assume that the physical processes in them also proceed

the same way. The consequence of this will be the periodic (in space) character of the change in the functions included in the system of equations of fluid dynamics and heat transfer. Therefore, on the radial planes *ab* and *cd* separating geometrically similar fragments, it is advisable to set the periodicity conditions in the angular coordinate for all the functions under study.

In view of the foregoing, the boundary conditions for the dimensionless system of equations (4.5)-(4.8) are presented in the form:

– conditions at the entrance to the working area:

for $0 < \theta < \Delta\theta$ and $R = R_{in}$: $\Omega(R_{in},\theta) = 0;\ P(R_{in},\theta) = 0$

$$\vartheta(1,\theta) = 0 \tag{4.11}$$

– conditions at the exit from the working area:

for $0 < \theta < \Delta\theta$ and $R = R_{out}$: $\Omega(R_{out},\theta) = 0;\ P(R_{out},\theta) = P_1$

$$\frac{\partial\vartheta(R_{out},\theta)}{\partial R} = 0 \tag{4.12}$$

– conditions for the periodicity of functions with respect to angle θ:

for $R_{in} < R < R_{out}$: $\Omega(R,0) = \Omega(R,\Delta\theta)$

$$\frac{\partial\Omega(R,0)}{\partial\theta} = \frac{\partial\Omega(R,\Delta\theta)}{\partial\theta} \tag{4.13}$$

$$V(R,0) = V(R,\Delta\theta);\quad \frac{\partial V(R,0)}{\partial\theta} = \frac{\partial V(R,\Delta\theta)}{\partial\theta} \tag{4.14}$$

$$P(R,0) = P(R,\Delta\theta);\quad \frac{\partial P(R,0)}{\partial\theta} = \frac{\partial P(R,\Delta\theta)}{\partial\theta} \tag{4.15}$$

$$\vartheta(R,0) = \vartheta(R,\Delta\theta);\quad \frac{\partial\vartheta(R,0)}{\partial\theta} = \frac{\partial\vartheta(R,\Delta\theta)}{\partial\theta} \tag{4.16}$$

– on the surfaces of stators:

$$\Omega(R,\theta) = 0;\quad V(R,\theta) = 0;\quad \frac{\partial\vartheta(R,\theta)}{\partial n} = 0 \tag{4.17}$$

– on the surfaces of the rotor:

$$\Omega(R,\theta) = 1;\quad V(R,\theta) = 0;\quad \frac{\partial\vartheta(R,\theta)}{\partial n} = 0 \tag{4.18}$$

where: n – the normal to the surfaces of the working elements; R_{in}, R_{out} – dimensionless radii of the input and output sections of the working area.

The indicated temperature conditions on the surfaces of the working elements of the apparatus mean that these elements are considered thermally insulated. If thermal conductivity through the working elements cannot be neglected, conditions of the fourth kind (conjugation conditions) must be set on their surface.

4.4. Features of numerical modeling of fluid dynamics and heat transfer in RPA working volume

To carry out numerical modeling of fluid dynamics and heat transfer in the working volume of RPA, the finite-difference method for solving the system of differential equations is used. To discretize the system of equations (4.7)-(4.10), as well as the boundary conditions (4.11)-(4.18), an implicit time approximation scheme and a spaced difference grid are used to approximate the derivatives with respect to spatial coordinates. A feature of the spaced grid is that at the centers of discrete elements, nodes are specified for the grid functions of pressure and temperature, and nodes on the lateral faces of the elements are set for components of the velocity vector [4.84]. For the inertial terms on the left-hand sides of the transport equations, a simplified linearization form and a counter-flow scheme for approximating the first derivatives by finite differences are used.

The computational domain can be conditionally divided into five subregions: a slot in the inner stator, a gap between the inner stator and the rotor, a slot in the rotor, a gap between the rotor and the outer stator, a slot in the outer stator. The specificity of this computational domain is that, in addition to the areas occupied by the liquid, it also includes moving and stationary elements of the apparatus. If the entire computational domain is covered with a difference grid rigidly connected with fixed elements, then part of the grid cells corresponding to the rotor slot will periodically be completely or partially blocked by the moving rotor, while the other part will be freed from the rotor sections and "filled" with liquid. In this regard, it is advisable to solve the considered problem simultaneously in two coordinate systems: in a fixed one, connected with the stators, and in a rotating one, connected with the rotor. In a stationary system, it is convenient to consider the flow in the slots of the stators and in the gaps, and in a rotating system – flow in the slots of the rotor.

The system of equations is solved by the tridiagonal matrix method, a detailed description of the procedure of which is presented in [4.85].

If only the steady-state periodic mode of operation of the apparatus is of interest, the dynamic problem and the heat transfer problem can be considered as problems without specific initial conditions. In other words, the initial conditions can be arbitrary. In this case, it is assumed that no matter what the real initial conditions are, the transfer processes will eventually come to a certain periodic mode. Of course, these processes, due to their periodicity, will be unsteady.

It is easiest to choose the following as initial conditions: for $H = 0$ we have $\Omega = 0$; $V = 0$; $\vartheta = 0$; $\Omega_0 = 1$.

They reflect a situation in which at the initial moment of time the rotor is already accelerated to the required angular velocity of rotation, and the liquid is still stationary. More realistic, however, is the following condition: for $H = 0$, the angular velocity of the rotor is $\Omega_0 = 0$. The last condition must be set when solving the problem of acceleration of the rotor from a state of rest.

As mentioned above, the parameters of the problem that determine the characteristics of the process of fluid flow in the RPA will be: geometry of the computational domain, rotor velocity, pressure drop between the inlet and outlet sections of the computational domain, physical properties of the processed fluid. Physical properties in this case include its density ρ_0, viscosity μ_0 (for Newtonian fluids) or rheological law (for non-Newtonian fluids), thermal conductivity λ_0 and heat capacity C_{p0}. If we consider the problem in dimensionless variables, the number of determining parameters decreases to the dimensionless geometric characteristics of the RPA, Reynolds number, dimensionless pressure drop, and Prandtl number. For non-Newtonian media, a rheological law is also written down in a dimensionless form.

To solve the problem in the stated formulation, the most problematic is the task of the pressure differential between the input and output sections of the working area. This value depends both on the design of the apparatus and on the processes themselves occurring in the working area, which is only one of the sections of the fluid flow in the RPA. The value that largely determines the specified pressure drop is the difference in liquid levels in the RPA loading tank and in the outlet section of the outlet pipe. Since the indicated level difference can be arbitrary, it is advisable to obtain a solution to the problem in this formulation for various values of pressure drops: positive, zero, and (up to a certain value) negative.

A very important question is the regime of fluid flow in RPA. Thus, the authors of [4.5, 4.23, 4.52] believe that the flow regime in the working space of the apparatus is turbulent. Moreover, they believe that the crushing of dispersed particles is caused mainly by their collision with turbulent vortices of a certain scale and energy. Reliable experimental data indicating the presence of laminar or turbulent flows in the working area of the apparatus are currently missing. Carrying out such experiments is very difficult. As is known, the possibility of establishing a developed turbulent flow regime in a stream depends on many factors and conditions. Among them, we should mention the class and nature of the flow, the geometry of the flow region, a linear geometric scale, levels of flow rates, fluid viscosity, the presence or absence of external mass forces, the presence of moving solid elements that form the flow, the initial regime of fluid flow before entering the considered region, and etc. In rotary devices, these conditions can be implemented to one degree or another,

since their geometric, operational and technological parameters vary in a rather wide range depending on the purpose of a particular device. It is also very likely that in different sections of the fluid flow in the RPA, simultaneously laminar, transitional and developed turbulent flow regimes can exist. Moreover, in principle, both a transition from a laminar flow regime to a turbulent one is possible, as well as relaminarization of the flow. The case may also be probable if the flow regime changes periodically in time in the local area of space, depending on the relative position of the RPA working elements.

These circumstances necessitate the consideration of both modes of fluid flow and heat transfer in the RPA working area. The numerical modeling procedure discussed above was applied to the cases of laminar flow of the medium being treated. In cases of turbulent flow, the system of equations of dynamics and heat transfer (4.1)-(4.5) must be supplemented by the conditions of its closure in terms of determining the effective turbulent transfer coefficients μ_{ef} and λ_{ef}. For this purpose, equations describing some model of turbulence adequate to this class of flows are also added to the indicated system of equations. Among the numerous two-parameter turbulence models, the RNG *k*-ε model obtained theoretically without attracting additional empirical information regarding a specific class of the medium flow has certain advantages [4.86]. In this regard, it is advisable to use it for numerical simulation of turbulent flow in RPA.

Since the system of equations (4.1)-(4.5) is written in polar coordinates, the RNG *k*-ε equations of the turbulence model should also be represented in the indicated coordinate system. After dimensioning, the system of equations of the RNG model is represented in the form:

$$\frac{\partial K}{\partial H}+\frac{1}{R}\frac{\partial (RVK)}{\partial R}+\frac{\partial (\Omega K)}{\partial \theta}=\frac{1}{\mathrm{Re}}\left[\frac{1}{R}\frac{\partial}{\partial R}\left(\frac{R\zeta}{\sigma_k}\frac{\partial K}{\partial R}\right)+\frac{1}{R^2}\frac{\partial}{\partial \theta}\left(\frac{\zeta}{\sigma_k}\frac{\partial K}{\partial \theta}\right)\right]+\frac{\overline{S}^2}{\mathrm{Re}}\xi-E \tag{4.19}$$

$$\begin{aligned}&\frac{\partial E}{\partial H}+\frac{1}{R}\frac{\partial (RVE)}{\partial R}+\frac{\partial (\Omega E)}{\partial \theta}=\frac{1}{\mathrm{Re}}\left[\frac{1}{R}\frac{\partial}{\partial R}\left(\frac{R\zeta}{\sigma_\varepsilon}\frac{\partial E}{\partial R}\right)+\frac{1}{R^2}\frac{\partial}{\partial \theta}\left(\frac{\zeta}{\sigma_\varepsilon}\frac{\partial E}{\partial \theta}\right)\right]+\\&+\left[C_1-\frac{\eta_\varepsilon}{1+\beta_\varepsilon\eta_\varepsilon^3}\left(1-\frac{\eta_\varepsilon}{\eta_{\varepsilon_0}}\right)\right]\frac{\overline{S}^2}{\mathrm{Re}}\xi\frac{E}{K}-C_2\frac{E^2}{K}\end{aligned} \tag{4.20}$$

where: $K=k/\left(\omega_0 r_0\right)^2$; $E=\varepsilon/\left(\omega_0^3 r_0^2\right)$; $\xi=\frac{\nu_t}{\nu}=C_\mu\,\mathrm{Re}\frac{K^2}{E}$; $\zeta=\mu_{ef}/\mu$;

$$\eta_\varepsilon=K\overline{S}/E;\quad \overline{S}=\left[2\left(\frac{\partial V}{\partial R}\right)^2+2\left(\frac{\partial \Omega}{\partial \theta}+\frac{V}{R}\right)^2+\left(\frac{1}{R}\frac{\partial V}{\partial \theta}+R\frac{\partial \Omega}{\partial R}\right)^2\right]^{0.5}.$$

The constants for this model have the following meanings:

$$C_\mu = 0.0847; \quad C_1 = 1.42; \quad C_2 = 1.68; \quad \beta_\varepsilon = 0.012; \quad \eta_{\varepsilon_0} = 4.38$$

The number σ_k is determined from the solution of the transcendental equation:

$$\left|\frac{\sigma_k^{-1} - 1.3929}{0.3929}\right|^{0.6321} \left|\frac{\sigma_k^{-1} + 2.3929}{3.3929}\right|^{0.3679} = \frac{\nu}{\nu_t}$$

and the number σ_ε is taken equal σ_k. The turbulent Prandtl number σ_t for the energy equation is also calculated from the transcendental equation

$$\left|\frac{\sigma_T^{-1} - 1.3929}{\sigma^{-1} - 1.3929}\right|^{0.6321} \left|\frac{\sigma_T^{-1} + 2.3929}{\sigma^{-1} + 2.3929}\right|^{0.3679} = \frac{\nu}{\nu_t}$$

The system of equations (4.19), (4.20) is also solved by the finite difference method. The approximation of data by finite differences is performed similarly to the approximation of the energy equation (4.10). The solution of the system of difference equations is also performed using the tridiagonal matrix method. Since in the general case the degree of flow turbulization at the entrance to the RPA working area is unknown, it is advisable to take the zero value of derivatives of *K* and *E* with respect to the radial coordinate as boundary conditions in its input and output sections. On the lateral faces of the computational domain, for the functions *K* and *E*, as well as for other unknown functions, the conditions for their periodicity in the angular coordinate θ are accepted. On the surfaces of the working elements, the value of *K* is zero. The values of *E* are determined in the nodes of the computational grid adjacent to solid surfaces from the expression

$$E_{\Delta n} = C_\mu^{3/4} K^{3/2} / (\kappa \cdot \Delta n)$$

where Δn is the dimensionless distance from the node to the wall, $\kappa = 0.4...0.42$ is the Karman constant.

References

[4.1] Basok B.I., Davydenko B.V., Kravchenko Yu.S. [et al.], Features of hydrodynamics of rotor-pulsation apparatuses of disk type. Industrial heat engineering. Vol. 25, No. 3, 2003, pp. 21-25 (rus.).

[4.2] Basok B.I., Shetankov O.K., Chaika A.I., Hydrodynamic and mass transfer characteristics of rotor-disk pulsation apparatus. Bulletin of the National Technical University of Ukraine "KPI", series of "Mechanical Engineering". Vol. 40, 2001, pp. 417-425 (rus.).

[4.3] Evstigneeva T.I., Kolesnik V.N., Kravchenko Yu.S. [et al.], On the mechanism of generating pressure pulsations in rotary pulsation devices. Industrial heat engineering. Vol. 13, No. 2, 1997, pp. 63-67 (rus.).

[4.4] Basok B.I., Hartwig A.P., Koba A.R. [et al.], Equipment for obtaining and processing highly viscous dispersed media. Industrial heat engineering. Vol. 18, No. 1, 1996, pp. 50-56.

[4.5] Promtov M.A., Rotary-type pulsation apparatus: theory and practice. M.: Mechanical Engineering, 2001, 260 p. (rus.).

[4.6] Granovsky V.Ya., Comparative evaluation of dispersing devices. M.: Dairy industry. No. 11, 1999, pp. 37-38 (rus.).

[4.7] Basok B.I., Sharkova N.A., Avdeeva L.Yu. [et al.], Energy Saving in Soya Paste Production Technology. Sat. materials of the international scientific-practical conference "Regional problems of energy conservation in decentralized heat power engineering", 2000, pp. 4-6 (rus.).

[4.8] Basok B.I., Obodovich A.N., Martynenko M.P. [et al.], Intensification of the technology for the production of condensed milk with sugar through rotary pulsation apparatus. Industrial heat engineering. Vol. 27, No. 1, 2005, pp. 36-39 (rus.).

[4.9] Basok B.I., Obodovich A.N., Pirozhenko I.A. [et al.], Intensification of alcoholic fermentation by DIVE method. Abstracts of the international science-methodical conference: “Strategic steps for developing the business of the business and trade”. Kharkiv 2002, pp. 79-81.

[4.10] Basok B.I., Obodovich A.N., Kashurin A.N. [et al.], Discrete-pulse energy input in fermentation technology. Industrial heat engineering. Vol. 25, No. 4, 2003, pp. 94-96 (rus.).

[4.11] Basok B., Hartvig A., Koba A. [et al.], Energy and resource saving for the testing of heterogeneous secondary media. News of the National University “Lviv Polytechnic”. L.: Vidavnitsvo of the National University “Lviv Polytechnic”. No. 452, 2002, pp. 119-122 (rus.).

[4.12] Basok B.I., Obodovich A.N., Pirozhenko I.A. [et al.], Energy-saving waste-free technology for the homogenization of fruits and vegetables and citrus raw materials. Industrial heat engineering. Vol. 25, No. 4, 2003, pp. 90-93 (rus.).

[4.13] Nakorchevsky A.I., Basok B.I., Features of the processing of pasty media in rotary-pulse apparatuses. Industrial Heat Engineering. Vol. 23, No. 1-2, 2001, pp. 41-46 (rus.)

[4.14] Dolinsky A.A., Basok B.I., Shurchkova Yu.A., Analysis of the effectiveness of emulsion homogenization by various dispersing devices. Ecotechnologies and Resource Saving. Vol. 18, No. 1, 1995, pp. 50-56 (rus.).

[4.15] Dolinsky A.A., Basok B.I., Koba A.R. [et al.], Rotary-pulse installation for mixing and homogenization of liquid dispersed seafood. Collection of reports of the

international conference “Problems of energy conservation and the environment in shipbuilding”. Nikolaev 1996, pp. 22-23 (rus.).

[4.16] Dolinsky A.A., Shurchkova Yu.A., Basok B.I. [et al.], Experimental studies of thermal effects during sterilization of disperse systems. Collection of reports of the II Russian National Conference on Heat Transfer. Moscow 1998, pp. 50-52 (rus.).

[4.17] Balabudkin M.A., Rotary pulsation apparatus in the pharmaceutical industry. M.: Medicine, 1983, 160 p. (rus.).

[4.18] Balabyshko A.M., Zimin A.I., Ruzhitsky V.P., Hydromechanical dispersion. M.: Nauka, 1998, 331 p. (rus.).

[4.19] Balabyshko A.M., Yudaev V.F., Flow modulating rotary apparatus and their application in industry. M.: Nedra, 1992, 176 p. (rus.).

[4.20] Zimin A.I., Intensification of the preparation of dispersed media in rotary-pulse apparatuses in the pharmaceutical industry. Chemical and Pharmaceutical Journal. No. 8, 1997, pp. 50-53 (rus.).

[4.21] Ledova T.M., Balabudkin M.A., Plyushkin S.A., Patterns of preparation of emulsion systems in a rotary pulsation apparatus. Chemical and Pharmaceutical Journal. Vol. 14, No. 5, 1980, pp. 96-99 (rus.).

[4.22] Pavlov B.P., Batuev S.P., Schevelev K.V., Preparation of water-fuel oil emulsions for combustion in furnace devices. Improving the efficiency of using gaseous and liquid fuels in furnaces and heating boilers. L.: Nedra, 1983, 216 p. (rus.).

[4.23] Balabudkin M.A., Goloborodkin S.I., Shulaev N.S., On the effectiveness of RPA in the processing of emulsion systems. Theoretical Foundations of Chemical Technology. Vol. 24, No. 4, 1990, pp. 502-508.

[4.24] Pat. 65406 A. Ukraine. MKI 7 V01F7/00. Rotor homogenizer. Dolinsky A.A., Basok B.I., Kravchenko Yu.S., Gartvig A.P., Koba A.R., Pirozhenko I.A., Claim 08/04/2003; Publ. March 15, 2004, Bull. No. 3, 5 p. (rus.).

[4.25] Pat. 64606 A. Ukraine. IPC 7 V01F7/28. Rotary-pulsating apparatus. Basok B.I., Davydenko B.V., Kremnyov V.O., Kravchenko Yu.S., Vasilchenko L.O., Pirozhenko I.A., Claim 07/15/2003; Publ. 02.16.2004, Bull. No. 2, 4 p. (rus.).

[4.26] Nakorchevsky A.I., Basok B.I., Pirozhenko I.A., Kinematic, dynamic and thermal characteristics of rotary pulsation apparatuses. Bulletin of the National Technical University of Ukraine "KPI", series of "Mechanical Engineering". Vol. 40, 2001, pp. 400-405 (rus.).

[4.27] Balabudkin M.A., On the laws of hydromechanical phenomena in rotary pulsation apparatus. Theoretical Foundations of Chemical Technology. Vol. 9, No. 5, 1975, pp. 783-788 (rus.).

[4.28] Derko P.P., Baram A.A., Kogan V.B., On the hydromechanical laws of operation of a rotary pulsation apparatus. Theoretical Foundations of Chemical Technology. Vol. 7, No. 1, 1973, pp. 123-124 (rus.).

[4.29] Balabudkin M.A., Baram A.A., Investigation of the frequency-amplitude spectrum of dynamic pressure in rotary-pulsation apparatus. Theoretical Foundations of Chemical Technology. Vol. 2, No. 4, 1968, pp. 609-614 (rus.).

[4.30] Balabudkin M.A., Loshakova O.A., Baram A.A., The dependence of the frequency characteristics of the rotary pulsation apparatus on the number of slots. Collection of scientific papers of the Leningrad Technological Institute of the Pulp and Paper Industry. Issue 31, 1973, pp. 127-130 (rus.).

[4.31] Yudaev V.F., Zimin A.I., Bazadze L.G., Methods for calculating the hydraulic and dynamic characteristics of a modulator of a rotary apparatus. News of universities. Mechanical Engineering. No. 1, 1985, pp. 65-70 (rus.).

[4.32] Yudaev V.F., Zimin A.I., Bazadze L.G., On methods for calculating the hydraulic and dynamic characteristics of a modulator of a rotary apparatus. News of Universities. Mechanical Engineering. No. 11, 1987, pp. 63-65 (rus.).

[4.33] Zimin A.I., Applied mechanics of intermittent flows. M.: Folio, 1997, 308 p. (rus.).

[4.34] Yudaev V.F., Kokorev D.T., Sopin A.I., To the question of calculating the geometric parameters of devices like a hydromechanical siren. News of Universities. Mechanical Engineering. No. 6, 1972, pp. 80-85 (rus.).

[4.35] Zimin A.I., Zvezdin A.K., Optimization of design parameters and operating modes of rotor-pulsation devices. Optimal design in the problems of chemical engineering: Collection of scientific. Labor. M.: MIHM, 1983, pp. 31-34 (rus.).

[4.36] Chervyakov V.M., Yudaev V.F., Hydrodynamic and cavitation phenomena in rotary devices. M.: "Publishing House Engineering-1", 2007, 128 p. (rus.).

[4.37] Fomin V.M., Fedorov A.V., Hops T.A. [et al.], Theoretical and experimental study of the characteristics of a rotary pulsation apparatus. Engineering Physics Journal. Vol. 81, No. 5, 2008, pp. 817-825 (rus.).

[4.38] Basok B.I., Nakorchevsky A.I., Ryzhkova T.S. [et al.], Experimental studies of the hydraulic and thermal characteristics of the flow in rotary pulsation devices. Industrial heat engineering. Vol. 23, No. 6, 2001, pp. 73-76 (rus.).

[4.39] Basok B.I., Pirozhenko I.A., Nezhuta V.P. [et al.], Hydraulic characteristics of the rotary pulsation apparatus TF-2. Bulletin of the National Technical University of Ukraine "KPI", series of "Mechanical Engineering". Vol. 43, 2002, pp. 160-162 (rus.).

[4.40] Pirozhenko I.A., Experimental studies of the hydrodynamic and thermal characteristics of a fluid in a rotary pulsation apparatus. Industrial Heat Engineering. Vol. 26, No. 6, 2004, pp. 21-25 (rus.).

[4.41] Pirozhenko I.A., Dissipative effect in a rotary pulsation apparatus. Industrial Heat Engineering. Vol. 25, No. 4, 2003, pp. 336-338 (rus.).

[4.42] Neduzhiy S.A., Investigation of the process of formation of emulsions caused by the action of sound and ultrasonic vibrations. Acoustic Journal. Vol. 7, Issue 3, 1961, pp. 275-294 (rus.).

[4.43] Baram A.A., On the mechanism of emulsification in an acoustic field. Acoustic Journal. Vol. 10, Issue 4, 1964, pp. 398-402.

[4.44] Neduzhiy S.A., On the state of the dispersed phase of an emulsion in an acoustic field. Acoustic Journal. Vol. 8, Isue 4, 1962, pp. 481-482 (rus.).

[4.45] Neduzhiy S.A., On the nature of disturbances causing the formation of a dispersed phase of an emulsion in an acoustic field. Acoustic Journal. Vol. 10, Issue 4, 1964, pp. 458-464 (rus.).

[4.46] Promtov M.A., Fundamentals of the method of calculating rotary pulse-cavitation apparatus. Bulletin of the Tambov State Technical University. Vol. 10, No. 1A, 2004, pp. 149-153 (rus.).

[4.47] Dolinsky A.A., Basok B.I., Impulse rotary apparatus. 1. The pulsed effects of local adiabatic boiling and cavitation of the liquid. Industrial heat engineering. Vol. 20, No. 6, 1998, pp. 7-10 (rus.).

[4.48] Yudaev V.F., Hydromechanical processes in rotary devices with modulation of the flow cross section of the processed medium. Theoretical Foundations of Chemical Technology. Vol. 28, No. 6, 1994, pp. 581-590 (rus.).

[4.49] Yudaev V.F., Calculation methods for rotary devices with flow modulation. Development, research and calculation of machines and apparatus for chemical production: Interuniversity collection of scientific. labor. M.: MIHM, 1984, pp. 139-143 (rus.).

[4.50] Kurochkin A.K., Smorodov E.A., An experimental study of cavitation in rotary hydrodynamic emitters. Acoustic Journal. Vol. 33, No. 4, 1987, pp. 707-711.

[4.51] Tal-Figiel B., Wpływ ultradźwięków na wtórny rozpad kropel fazy rozproszonej w układach ciesz-ciesz. Inżynieria Chemiczna i Procesowa. Vol. 8, No. 4, 1987, pp. 617-633 (pol.).

[4.52] Romankov P.G., Kurochkin M.I., Hydromechanical processes of chemical technology. Leningrad: Chemistry, 1982, 287 p. (rus.).

[4.53] Karpenko L.A., Troshkin O.A., Karpenko I.A., Study of the dispersion characteristics of emulsions obtained by dispersing liquids with a rotary pulsation apparatus. Theoretical Foundations of Chemical Technology. Vol. 12, No. 5, 1978, pp. 780-783 (rus.).

[4.54] Reusova L.A., Lykov M.V., The study of the dispersion of viscous emulsions obtained in a rotary-pulsation type apparatus. Theoretical Foundations of Chemical Technology. Vol. 18, No. 3, 1984, pp. 405-409 (rus.).

[4.55] Baram A.A., Dispersion in a liquid-liquid system in a rotary-pulsation type apparatus. Theoretical Foundations of Chemical Technology. Vol. 22, No. 5, 1988, pp. 655-660 (rus.).

[4.56] Kokushkin O.A., Baram A.A., Pavlushenko I.S., On the calculation of the power of rotary apparatus. Journal of Applied Chemistry. No. 8, 1969, pp. 1793-1795 (rus.).

[4.57] Levich V.G., Physicochemical hydrodynamics. M.: Fizmatgiz, 1959, 455 p. (rus.).

[4.58] Averbukh Yu.I., Nikiforov A.O., Kostin N.M. [et al.], The calculation of the dispersion of emulsions formed in the rotor-stator apparatus. Journal of Applied Chemistry. No. 2, 1988, pp. 433-434 (rus.).

[4.59] Dolinsky A.A., Basok B.I., Impulse rotary apparatus. 3. Crushing of inclusions of the dispersed phase. Industrial heat engineering. Vol. 21, No. 2-3, 1999, pp. 5-6 (rus.).

[4.60] Balabudkin M.A., The scaling of rotary pulsation apparatus. Chemical and Pharmaceutical Journal. No. 1, 1981, pp. 100-105 (rus.).

[4.61] Kolesnikov G.E., Dispersion characteristics of a two-phase system. Kolesnikov G.E., Troshkin O.A., Makarov Yu.I. [et al.], Theoretical Foundations of Chemical Technology. Vol. 23, No. 4, 1989, pp. 542-545 (rus.).

[4.62] Basok B.I., Pirozhenko I.A., Bulavka A.V., Dispersion analysis of soybean paste obtained by rotor-pulsation homogenization. Industrial heat engineering. Vol. 25, No. 4, 2003, pp. 88-92 (rus.).

[4.63] Nakorchevsky A.I., Basok B.I., Hydrodynamics and heat and mass transfer in heterogeneous systems and pulsating flows. K.: Naukova Dumka, 2001, 348 p. (rus.).

[4.64] Baram A.A., Loshakova O.A., Hydrodynamic patterns of operation of rotary-pulsation-type apparatus. Theoretical Foundations of Chemical Technology. Vol. 12, No. 2, 1978, pp. 231-240 (rus.).

[4.65] Promtov M.A., Zimin A.I., Monastyrsky M.V., A model of fluid flow through a chopper of a single-stage rotary pulsation apparatus. Industrial Heat Engineering. Vol. 23, No. 1-2, 2001, pp. 129-133 (rus.).

[4.66] Nakorchevsky A.I., Basok B.I., Ryzhkova T.S., Hydrodynamics of rotor-pulsation apparatus. Engineering Physics Journal. Vol. 75, No. 2, 2002, pp. 58-68 (rus.).

[4.67] Basok B.I., Davydenko B.V., KravchenkoYu.S. [et al.], Experimental and analytical model of fluid dynamics in a rotary pulsation apparatus. Reports of the National Academy of Sciences of Ukraine. No. 10, 2003, pp. 90-96 (rus.).

[4.68] Yudaev V.F., The outflow of gas-liquid mixture through the holes of the rotor and stator of the siren. News of universities. Engineering. No. 12, 1985, pp. 60-66 (rus.).

[4.69] Karepanov S.K., Mathematical model of the fluid flow in the channels of the rotor and stator of a hydromechanical dispersant. Application of rotary hydromechanical dispersants in the mining industry: theory, practice: Minsk 1998, pp. 57-67 (rus.).

[4.70] Bigler V.I., Yudaev V.F., Unsteady outflow of real liquid through the holes of a hydrodynamic siren. Acoustic Journal. Vol. 24, No. 2, 1978, pp. 289-291 (rus.).

[4.71] Dolinsky A.A., Pavlenko A.M., Basok B.I., Thermophysical processes in emulsions. K.: Naukova Dumka, 2005, 264 p. (rus.).

[4.72] Promtov M.A., Monastyrsky M.V., Calculation of changes in liquid temperature during energy dissipation in the gap of a rotary-pulse apparatus. Industrial Heat Engineering. Vol. 26, No. 4, 2004, pp. 28-32 (rus.).

[4.73] Dolinsky A.A., Basok B.I., Impulse rotary apparatus. 2. Local pulse heating of the liquid. Industrial heat engineering. Vol. 21, No. 1, 1999, pp. 3-5.

[4.74] Baram A.A., Derko P.P., Klotsung B.A., Calculation of the power of rotary-pulsation type devices. Chemical and Petrochemical Engineering. No. 4, 1978, pp. 4-6 (rus.).

[4.75] Pavlov I.G., Litkin V.P., Glukhov V.P. [et al.], On the calculation of the power for mixing fluid in rotary devices. Journal of Applied Chemistry. Vol. 45, No. 8, 1972, p. 1782 (rus.).

[4.76] Idelchik I.E., Handbook of hydraulic resistance. M.L.: Gosenergoizdat, 1960, 462 p. (rus.).

[4.77] Kutateladze S.S., Borishansky V.M., Heat Transfer Reference. M.L.: SEI, 1959, 416 p. (rus.).

[4.78] Krukovsky P.G., Grabov L.N., Yurchenko D.D., Grabova T.L., Three-dimensional CFD model of hydrodynamic processes in a reactor apparatus. Industrial heat engineering, Vol. 26, No. 4, 2004, pp. 5-12 (rus.).

[4.79] Krukovsky P.G., Grabov L.N., Yurchenko D.D., Grabova T.L., CFD analysis of hydrodynamic processes in a rotary pulsation apparatus. Proceedings of the 4th conference of users of software SAV-REM OMVN. M., 2004, pp. 272-278 (rus.).

[4.80] Grabova T.L., Dispersion of heterogeneous systems in rotary-pulsating apparatuses of a disk-cylindrical type: Abstract. dis. candidate techn. Science. K., 2007, 23 p. (rus.).

[4.81] Shulman Z.P., Convective heat and mass transfer of rheologically complex liquids. M.: Energy, 1975, 352 p. (rus.).

[4.82] Rheophysics and rheodynamics of fluid systems. Ed. Lykov A.V., Shulman Z.P., Minsk: Science and Technology, 1970, 172 p. (rus.).

[4.83] Lykov A.V., Berkovsky B.M., Heat and mass transfer in non-Newtonian fluids. Transfer laws in non-Newtonian fluids. M.: Energy, 1968, pp. 5-14 (rus.).

[4.84] Peyre R., Taylor T.D., Computational methods in problems of fluid mechanics. L.: Gidrometeoizdat, 1986, 352 p. (rus.).

[4.85] Davydenko B.V., The tridiagonal matrix method for solving the grid equations of hydrodynamics. East European Journal of Advanced Technologies. No. 5/5(35), 2008, pp. 7-11 (rus.).

[4.86] Avramenko A.A., Basok B.I., Kuznetsov A.V., Group methods in thermophysics. K.: Naukova Dumka, 2003, 484 p. (rus.).

REGULARITIES OF FLOW OF LIQUID IN RPA

The patterns of fluid flow in the RPA working area were studied by numerical simulation, which was carried out according to the algorithm considered in chapter 4. This section presents the results of studies of the fields of velocity, acceleration, pressure, normal and tangential stresses depending on the viscosity of the liquid and the pressure drop between the input and output sections of the working area. The laminar and turbulent flow regimes of Newtonian fluids with constant thermophysical properties are considered. The results of these studies are also presented in [5.1-5.7].

To study the patterns of fluid dynamics and heat transfer in RPA, a basic model of this apparatus is considering. This model has the following geometric characteristics of working elements: $r_0 =$ 43.3 mm (internal radius of the inner stator); $r_1 =$ 48.3 mm (outer radius of the inner stator); $r_2 =$ 48.5 mm (inner radius of the rotor); $r_3 =$ 51.5 mm (outer radius of the rotor); $r_4 =$ 51.7 mm (inner radius of the external stator); $r_5 =$ 56.7 mm (outer radius of the external stator). Thus, the width of the inner and outer stators is 5 mm, and the width of the rotor is 3 mm. The width of the gaps between the rotor and the stators is $\delta = 0.2$ mm. The number of slots at the rotor and stators is the same – $z = 60$. The opening angles of all slots in the working elements are also the same and equal $\Delta\theta_s = \pi / z$. At that $\Delta\theta_w = \Delta\theta_s$. The angular velocity of rotation of the rotor is taken equal to $\omega_0 = 100\pi \text{ s}^{-1}$ (3000 turns per minute). The height of the rotor and stators is $h = 20$ mm.

The solution of the fluid dynamics problem in the RPA working zone was obtained on a difference grid with $N = 48$ steps along the angle and with $M = 142$ steps along the radius R. Along the variable R an irregular grid step is used. The step of grid decreases in the areas of entry and exit from the slots, as well as in the areas of gaps. From the condition of the formal equality of dimensionless time steps and the angular coordinate steps follows that the dimensional time step is $6.944 \cdot 10^{-6}$ s, and the time period for the functions V, Ω, P and ϑ is respectively $\Delta\tau = 0.33 \cdot 10^{-3}$ s.

5.1. Velocity field in a fluid flow moving through the RPA working area

The velocity fields were calculated at pressure drops Δp = +10 kPa; 0; and –10 kPa for Newtonian fluids having viscosities μ = 0.01; 0.1; and 1.0 Pa·s. The density of the liquid for all cases is ρ = 1000 kg/m^3. As the results of calculations showed, the structure of the fluid flow in the working area of the RPA is very complex. Over a period of time $\Delta\tau$, during which the relative position of the slots of the rotor and stators is repeated, the flow pattern in individual sections of the working zone can change significantly. The maximum fluid velocity is on the outer surface of the rotor, as well as in areas directly adjacent to it. For the indicated values of the outer radius of the rotor and the angular velocity of its rotation, this velocity is 16.18 m/s. In the areas adjacent to the rotor, the velocity modulus is slightly higher because of the presence of the radial component of the velocity due to vortex formation.

In figure 5.1, which relates to the case Δp = +10 kPa; μ = 0.01 Pa·s, the velocity fields are presented in such a way that in the slot of the rotor their values are considered with respect to the rotating rotor (movable reference frame), and in the rest of the flow region, with respect to the stationary stator. The flow patterns are presented in coordinates R, θ.

As can be seen from figure 5.1, the velocity field in the initial section of the slot of the internal stator is almost radial. Vortex formation begins in the region where the flow exits from this slot. This is due to the high speed rotation of the rotor. In the gaps between the rotor and the stators, the fluid flow is somewhat similar to the Couette flow. However, this takes place only at the moments of coincidence of the slots of the rotor and stators. In subsequent time instants, reverse flows arise near the outer surface of the inner stator, which are the consequences of displacement of the liquid into the gaps from the slots at the moments of mutual overlapping of the slots of the rotor and stators.

In cases of relatively low values of the viscosity of the medium (which corresponds to high Reynolds numbers), which include the considered example, a circulation flow forms in the slot of the rotor, which is superimposed on the rotational motion of the fluid in the reference frame, which connected with the rotor. The direction of the formed single vortex coincides with the direction of rotation of the rotor. The formation of a vortex is associated with high values of shear stresses arising between the fluid layers rotating together with the rotor and the flows moving in the stators slots. Due to the presence of a vortex, the radial component of the velocity in the slot of the rotor takes both positive and negative values. On the whole, the average radial velocity over the cross section of the rotor slot is positive.

The fluid flow in the slots of the external stator is predominantly circulating. In the region of the entrance to the slot of the external stator, a vortex is formed with a center approximately located on the axis of symmetry of the stator slot. The direction

of the vortex is opposite to the direction of rotation of the rotor. Its occurrence, as well as a vortex in the rotor, is associated with shear stresses due to the rotation of the rotor. In the region of the outlet cross section of the slot of the external stator, there is also a vortex, but its direction is opposite to the direction of first vortex. The movement in the positive radial direction (outflow) occurs near the left wall of the channel, and the inflow occurs near the right wall. As in the rotor slot, the mass-average fluid velocity in the slot of the external stator is positive.

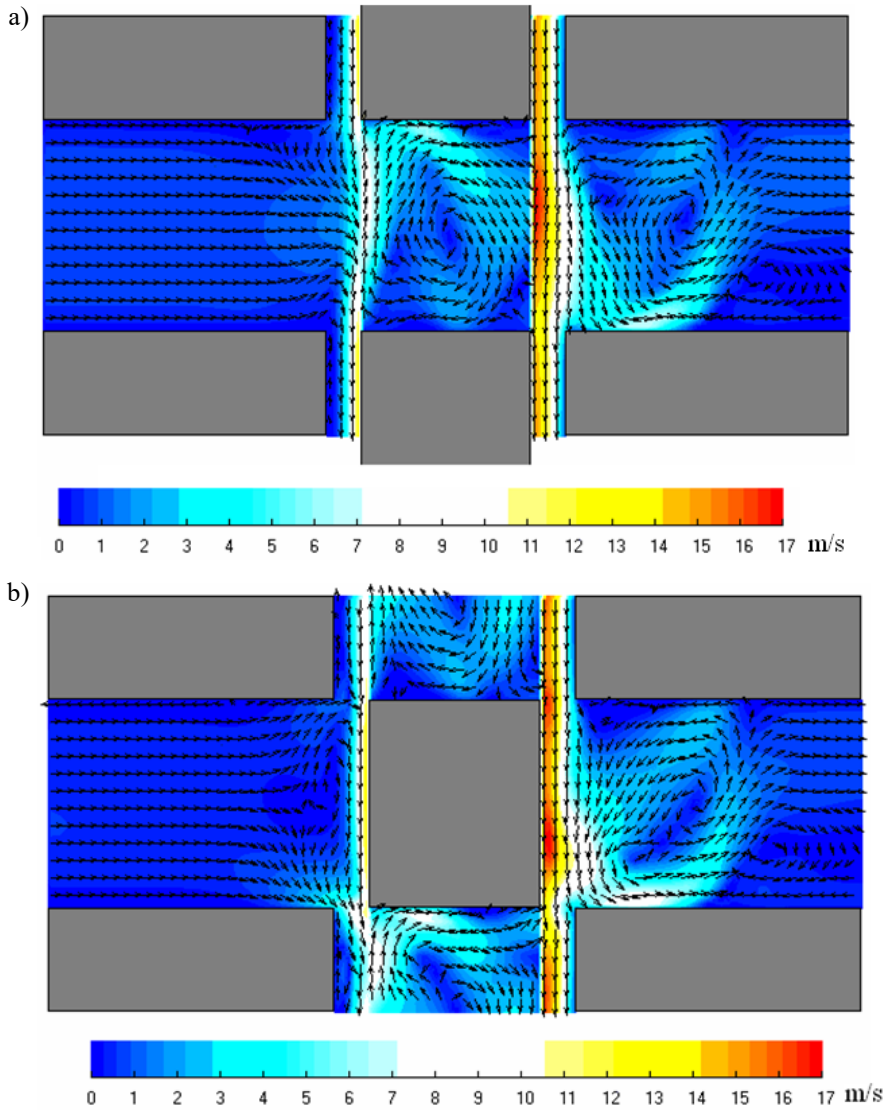

FIGURE 5.1. The velocity field of the fluid flow in the RPA working area at Δp = +10 kPa; μ = 0.01 Pa·s: a) $\tau/\Delta\tau = 0$; b) $\tau/\Delta\tau = 1/2$.

With a change in pressure drops and viscosities of the processed media, the picture of the fluid flow changes noticeably. Due to the centrifugal force caused by the rotation of the rotor, the radial flow rate of the liquid can be positive both at zero value and up to a certain value of negative pressure difference (when the pressure at the inlet to the working area is lower than the pressure at the outlet). At zero pressure difference, the intensity of the vortex movement in the rotor slot is somewhat weaker compared with the case of a positive pressure difference. The region occupied by the vortex in the input section of the slot of the external stator decreases somewhat, and the vortex at the output section of the slot of the external stator disappears, i.e. the flow at the outlet section of this slot is almost radial. The reverse flow in the gap between the rotor and the internal stator also disappears. At the same time, the vortex formation at the output section of the slot of the internal stator is intensified.

At negative values of the external pressure difference, the flow pattern in the stator slots becomes close to symmetric with respect to the average section of the rotor slot. The noted features of the flow behavior with a decrease in the pressure drop are associated with a significant decrease in the intensity of the radial fluid flow.

With a constant pressure difference and an increase in the viscosity of the medium, there is a decrease in the number of vortices in the slot of the external stator and the vortex in the slot outlet of external rotor is absent. At $\mu = 0.1$ Pa·s, the vortex in the rotor slot is not the only one. In addition to one large vortex, another smaller vortex is formed at the exit of the rotor slot. At $\mu = 1.0$ Pa·s, two almost symmetric vortices already exist in the rotor slot. With an increase in the viscosity of the liquid, the tendency toward vortex formation at the exit from the slot of the internal stator is significantly enhanced. If at $\mu = 0.1$ Pa·s this vortex is localized near the right outer edge of the slot of the inner stator, then at $\mu = 1.0$ Pa·s its center is already located almost on the axis of the slot. At $\mu = 1.0$ Pa·s, the flow in the RPA working zone is close to symmetric with respect to the midline of the rotor slot (as in the case of negative pressure drops at $\mu = 0.01$ Pa·s).

The features of the effect of viscosity growth on the flow structure are mainly associated with a decrease in the intensity of the radial fluid flow. Noteworthy is the fact that at the entrance to the slot of the external stator the fluid flow is predominantly tangential, even at the moment of coincidence of the slots of the rotor and stators. However, the width of the layer in which this tendency is most manifest is substantially dependent on the viscosity of the medium. At low viscosities, the width of this layer is minimal, and the values of the tangential velocity in this layer are maximum. At large values of viscosity, the width of the region increases due to the involvement of neighboring fluid layers in the rotational motion. The tangential velocity itself decreases.

5.2. The flowrate of fluid passing through the working area of the apparatus

An important indicator of the operation of the rotary pulsation apparatus is the flowrate of the fluid passing through the working area in the radial direction. This value can be obtained from the data on the distribution of the radial velocity at the entrance to the slots of stators at various points in time. Fluid flow in the radial direction is proportional to the average velocity of the radial flow $V_r(\tau) = \frac{1}{\Delta\theta}\int_0^{\Delta\theta} v_r(\tau, r_0, \theta)\, d\theta$. Calculations of this value were performed for the external pressure drops Δp = +10 kPa; Δp = 0; and Δp = -10 kPa. The time dependences of the average velocity V_r at the inlet to the slot of the internal stator at an external pressure drop Δp = +10 kPa for media with different viscosities are shown in figure 5.2.

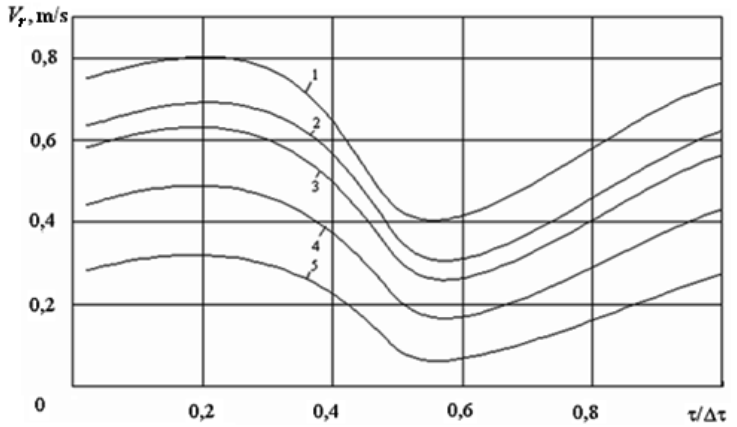

FIGURE 5.2. The change in time of the average fluid velocity in the inlet section of the slot of the internal stator at Δp = +10 kPa: 1 – μ = 0.01 Pa·s; 2 – 0.03 Pa·s; 3 – 0.1 Pa·s; 4 – 0.3 Pa·s; 5 – 1 Pa·s.

The time scale in the figure (ordinate axis) is presented so that the values $\tau/\Delta\tau = 0$ and $\tau/\Delta\tau = 1$ correspond to the moments of coincidence of the rotor slots with the stators, and $\tau/\Delta\tau = 0.5$ – to moment of complete mutual overlapping of the slots of the rotor and stators. As can be seen from the figure, the curves $V_r(\tau)$ in shape resemble raised sinusoids above the time axis with maxima and minima shifted to the right. For almost all values of μ, the maximum values of $V_r(\tau)$ correspond to the values of the dimensionless time $\tau/\Delta\tau \approx 0.2...0.23$, and the minimum values correspond to the values of $\tau/\Delta\tau \approx 0.58$. In other words, the maximum speed corresponds to that moment in time at which the slots of the stators are overlapped

by the walls of the rotor by 40...46%. The minimum speed is observed somewhat later than the complete mutual overlap of the slots of the rotor and stators. The nature of the increase in speed from its minimum value to the maximum is smoother than the character of decrease from the maximum value to the minimum. At the same time, the time interval corresponding to a decrease in speed is about 0.35 of the duration of the entire period $\Delta\tau$.

It follows from the calculations that, at $\Delta p \geq 0$, the values of the velocity $V_r(\tau)$ decrease with increasing viscosity of the medium μ, which is the result of an increase in friction resistance to the fluid flow in the slots. For $\Delta p < 0$, when the fluid moves in the radial direction only due to the action of centrifugal forces, a decrease in $V_r(\tau)$ with an increase in μ is clearly observed only for $\mu > 0.1$ Pa·s. For lower values of viscosity, the velocities $V_r(\tau)$ practically cease to depend on it.

The indicated feature is more clearly visible from those presented in figures 5.3, 5.4 graphs of the dependence of the mass average radial velocity on μ and Δp, which is calculated by the formula $\overline{V}_r = \frac{1}{\Delta\tau}\int_0^{\Delta\tau} V_r(\tau)d\tau$. The mass-average velocity is the average value for the period $\Delta\tau$ of the velocity $V_r(\tau)$ and characterizes the volumetric productivity of the apparatus. For the dependencies presented in figure 5.3, the argument is μ, and the parameter is Δp. As can be seen from this figure, in the interval ($0.01 < \mu < 0.1$) Pa·s at Δp = -10 kPa, the dependence $\overline{V}_r(\mu)$ has even a weakly expressed maximum corresponding to the value of $\mu \approx 0.03$ Pa·s. The dependencies shown in figure 5.4, for which the argument is Δp, and the parameters are the viscosity of the media, this feature appears in the fact that with a negative pressure drop of Δp = -10 kPa, the values $\overline{V}_r(\Delta p)$ almost the same for μ = 0.1; 0.03 and 0.01 Pa·s.

The indicated character of the effect of viscosity on the mass-average velocity $\overline{V}_r(\Delta p, \mu)$ is explained as follows. Since the shear stress on the walls of the slots of the rotor and stators is proportional to the viscosity, it is obvious that the hydrodynamic resistance to the translational motion of the liquid in the slots should increase with increasing viscosity, and the velocity $V_r(\tau)$ should accordingly decrease. However, due to the fact that the liquid in the apparatus performs rotational motion in addition to the translational motion, the centrifugal force acting on the flow also turns out to be dependent on viscosity. The rotation of the liquid occurs due to the transfer of the momentum from the rotating rotor to it due to the presence of shear stress on its cylindrical walls. Therefore, the centrifugal forces acting on the liquid should increase with an increase in its viscosity. It follows from this that at negative pressure drops, when only the centrifugal force is

the driving force of the translational radial motion, small viscosity values cannot sufficiently provide the momentum transfer from the rotating rotor to the liquid.

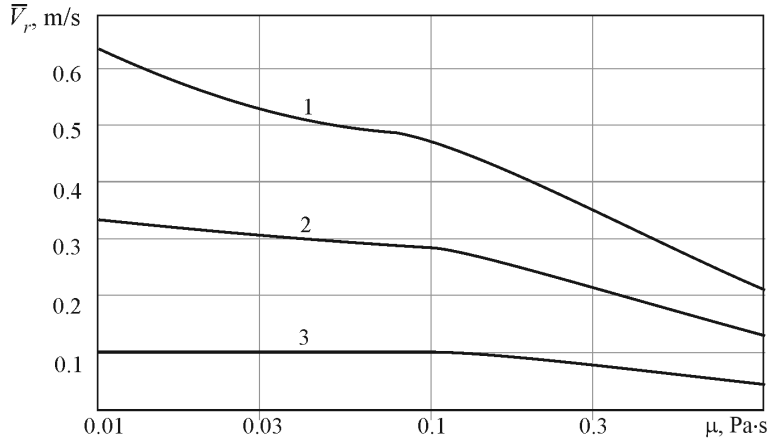

FIGURE 5.3. The dependence of the time-averaged fluid velocity in the inlet section of the internal stator slot on the viscosity: 1 – Δp = +10 kPa; 2 – Δp = 0; 3 – Δp = -10 kPa.

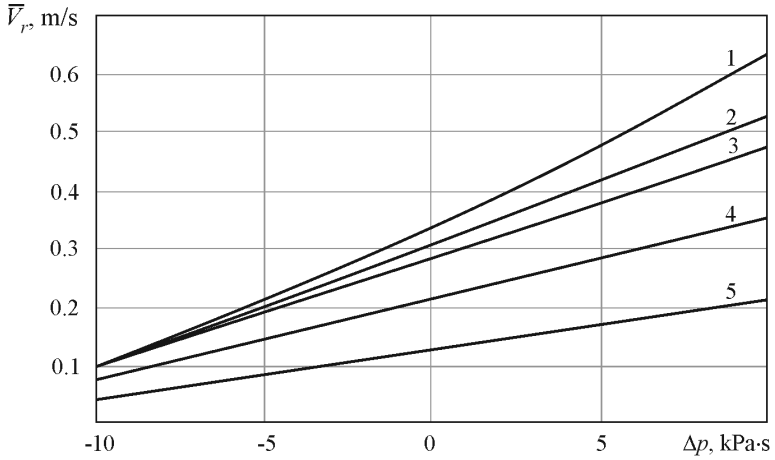

FIGURE 5.4. The dependence of the time-averaged fluid velocity in the inlet section of the slot of the internal stator on the pressure drop: 1 – μ = 0.01 Pa·s; 2 – 0.03 Pa·s; 3 – 0.1 Pa·s; 4 – 0.3 Pa·s; 5 – 1 Pa·s.

Since the results discussed above were obtained from solving the problem in dimensionless variables, presented in figures 5.3, 5.4, the dependences of the mass-average radial velocity on μ and Δp can also be interpreted as the dependences of the dimensionless quantity $\frac{r_0 \overline{V}_r \rho}{\mu}$ on the numbers $\mathrm{Re} = \frac{\rho \omega_0 r_0^2}{\mu}$ and on the

dimensionless pressure drop $\Delta P = \dfrac{\Delta p}{\rho\omega_0^2 r_0^2}$. The graphs rebuilt in the indicated variables are shown in figure 5.5. The considered dependencies can be generalized using the expression:

$$\log_{10}\left(\frac{r_0\overline{V}_r\rho}{\mu}\right) = \sum_{i=0}^{i=2}\left\{\left[\log_{10}\left(\frac{\rho\omega_0 r_0^2}{\mu}\right)\right]^i \cdot \sum_{j=0}^{j=2} C_{i,j}\left(\frac{\Delta p}{\rho\omega_0^2 r_0^2}\right)^j\right\} \qquad (5.1)$$

where: $C_{22} = -6.08$; $C_{12} = 49.59$; $C_{02} = -139.6$; $C_{21} = 0.734$; $C_{11} = -5.13$; $C_{01} = 15.2$; $C_{20} = -0.135$; $C_{10} = 2.23$; $C_{00} = -4.40$.

Expression (5.1) can be used for an approximate estimate of the average mass velocity of a fluid $\overline{V}_r(\Delta p, \mu)$ through the working zone, depending on its viscosity and pressure drop for RPA, geometrically similar to the considered one, in the intervals ($5.9\cdot10^2 < \mathrm{Re} < 5.9\cdot10^4$) and ($-0.054 < \Delta P < +0.054$).

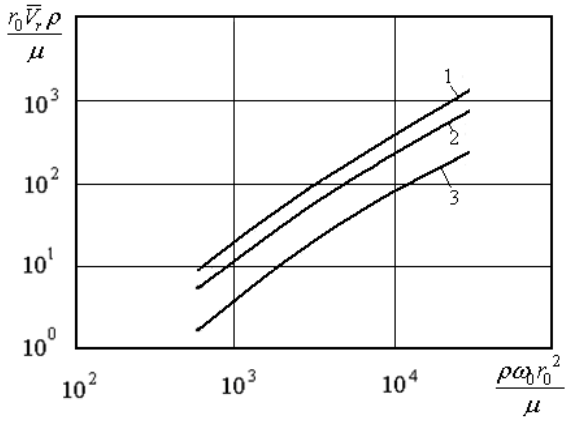

FIGURE 5.5. The dependence of the dimensionless average fluid velocity in the inlet section of the internal stator slot on the number Re: 1 – ΔP = +0.054; 2 – ΔP = 0; 3 – ΔP = -0.054.

As already mentioned, the fluid in the working area of the RPA performs both translational motion in the radial direction and rotational motion. The fluid flow in the radial direction is determined by the above-considered mass-average radial velocity $\overline{V}_r$. Its values calculated depending on the viscosity of the medium and the pressure differences are presented in figures 5.3, 5.4. The volumetric flowrate of fluid in the radial direction G_r can be found by multiplying $\overline{V}_r$ by the area of the inlet section of the slot of the inner stator. The dependence of the flowrate G_r on the viscosity of the medium μ at Δp = 0 for the apparatus of the considered

geometry with the angular velocity of rotation of the rotor indicated above is represented by curve 1 in figure 5.6. The fluid flowrate in the tangential direction $G_{\theta,g}$ can be calculated by integrating the tangential velocity v_θ over the cross sections of two gaps. Since the flow in the gaps is largely similar to the Couette flow, the law of variation of v_θ along the radius weakly depends on the viscosity of the medium and is determined mainly by the angular velocity of rotation of the rotor and the width of gaps. For the case under consideration, the dependence of $G_{\theta,g}$ on the viscosity of the medium is represented by curve 3 in figure 5.6.

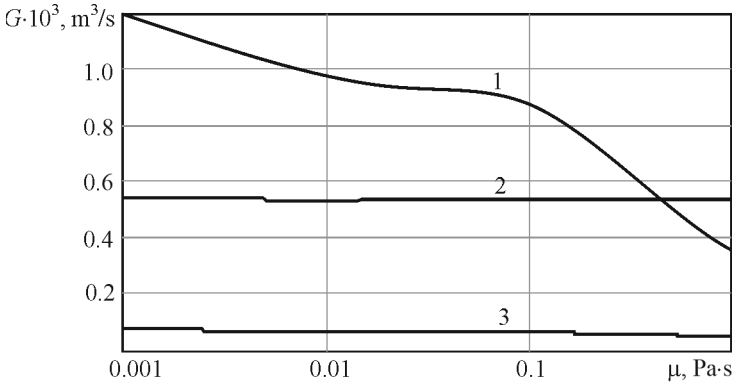

FIGURE 5.6. Dependences of the radial (1) and tangential (2, 3) fluid flowrates in the RPA working area on viscosity at $\Delta p = 0$.

However, it should be noted that since the fluid located in the slot of the rotor rotates together with the rotor, its flowrate in the tangential direction $G_{\theta,r}$ is determined only by the total volume of the slot of the rotor and the angular velocity of its rotation. The sum of the two tangential expenses $G_{\theta,g} + G_{\theta,r}$ is presented in figure 5.6 of curve 2. The data, on the basis of which the graphs on figure 5.6 are building, are given in table 5.1. As can be seen from the figure and table, the total tangential fluid flow rate can prevail over the radial flow rate only in cases of very viscous fluids or with negative pressure drops Δp.

TABLE 5.1. Changes in fluid flowrates in RPA depending on the viscosity of the medium.

μ, Pa s	$(G_{\theta,g} + G_{\theta,r}) \cdot 10^3$, m³/s	$G_{\theta,g} \cdot 10^3$, m³/s	$G_r \cdot 10^3$, m³/s
0.001	0.535	0.0656	1.1949
0.01	0.534	0.0620	0.9782
0.1	0.535	0.0610	0.8797
1.0	0.535	0.0534	0.3548

5.3. Stream function and vorticity of fluid flow in RPA working area

Studying the structure of the fluid flow in the RPA working zone, it is appropriate to recall such important characteristics of it as the stream function and vorticity. The stream function characterizes the flow of fluid through a certain section of the flow region. Its connection with velocity is represented by the expression $v_r = \frac{1}{r}\frac{\partial \varphi}{\partial \theta}$ from which it follows that $\varphi = \int_0^{\theta} v_r r d\theta$. According to the results of calculating the velocity fields by numerical integration, one can find the distribution of φ in the flow region. The isolines of the stream function thus found for the cases μ = 0.001 Pa·s and μ = 1.0 Pa·s at Δp = 0 are presented in figures 5.7 and 5.8.

From figures it is show how different are the characters of the flow of liquids with low viscosity from the flows of highly viscous liquids in the working area of RPA. At μ = 0.001 Pa·s (fig. 5.7), the flow has a very complex structure. In the slot of the internal stator, the flow is almost radial, with the exception of the output section. In the slot of the rotor, there is one large vortex and several small vortices. In the slot of the external stator, the flow is also predominantly circulating. The flow structure at μ = 0.001 Pa·s varies significantly over time. Depending on the relative position of the slots of the rotor and stators, new vortex structures periodically appear and disappear in them.

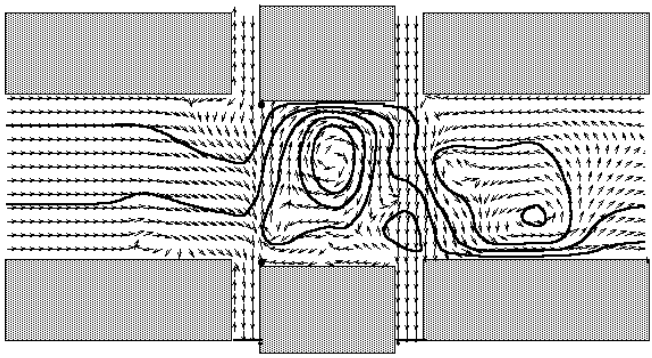

FIGURE 5.7. Isolines of the flow function in the RPA working area at μ = 0.001 Pa·s and Δp = 0.

In the case μ = 1.0 Pa·s (fig. 5.8), in the output section of the slot of the internal stator and in the input section of the slot of the external stator there are multidirectional, almost symmetrical circulation flows. Two practically symmetric vortices are also present in the slot of the rotor. At the entrance to the slot of the internal stator and at the exit of the slot of the external stator, the fluid flow is almost radial. Moreover, this flow structure is quite stable in time.

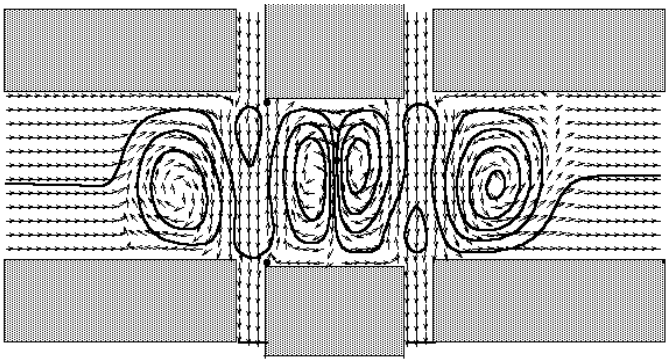

FIGURE 5.8. Isolines of the flow function in the RPA working area at μ = 1.0 Pa·s and Δp = 0.

Another important characteristic of the flow structure is its vorticity. In a polar coordinate system, a vorticity is defined as $\Omega_z = -\frac{1}{2}\left(\frac{1}{r}\frac{\partial v_r}{\partial \theta} - r\frac{\partial \omega}{\partial r}\right) + \omega.$

The flow vorticity fields in the RPA working area for liquids with viscosities μ = 0.001 and 1.0 Pa·s at Δp = 0 are presented in figures 5.9, 5.10. As can be seen from the figures, the vorticity acquires the greatest values in the gaps between the rotor and the stators. At μ = 0.001 Pa·s, its values reach in the gaps Ω_Z = ±50000 1/s. In the inlet section of the slot of the external stator and in outlet section of the slot of the internal stator, the vorticity values decrease to the values Ω_Z = ±10000 1/s. In approximately the same range also changes the values of the vorticity in the slot of the rotor.

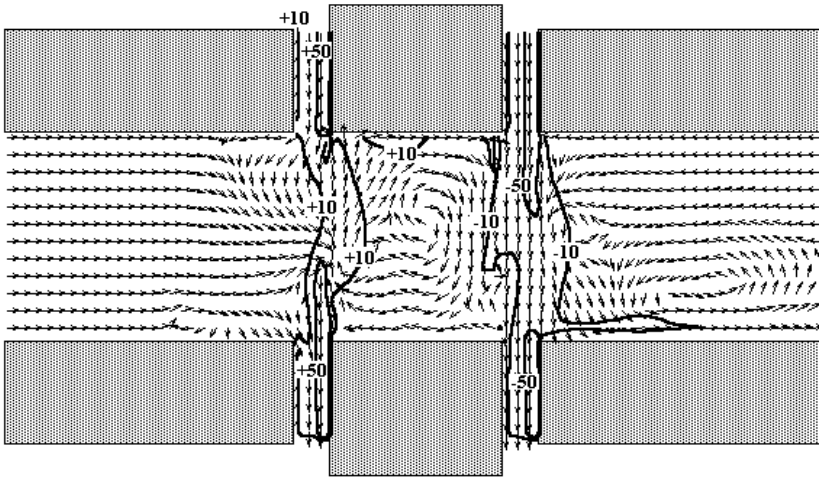

FIGURE 5.9. Isolines of the flow vorticity ($\Omega_z \cdot 10^{-3}$, s^{-1}) in the RPA working zone at μ = 0.001 Pa·s and Δp = 0.

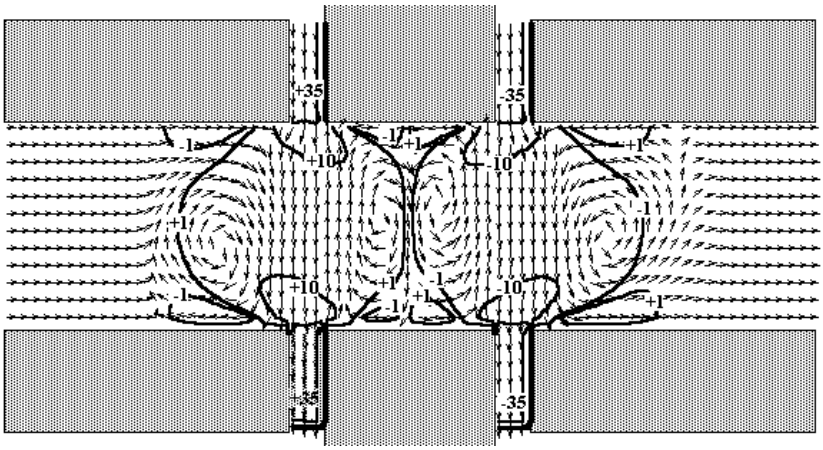

FIGURE 5.10. Isolines of the flow vorticity ($\Omega_z \cdot 10^{-3}$, s^{-1}) in the RPA working zone at $\mu = 1.0$ Pa·s and $\Delta p = 0$.

With increasing fluid viscosity, the degree of flow vorticity decreases. At $\mu = 1.0$ Pa·s, its values in the gaps decrease to $\Omega_Z = \pm 35000$ 1/s, and in the slot of the rotor $-\Omega_Z = \pm 1000$ 1/s.

5.4. Pressure fields in the working area of RPA

Important factors affecting the processes of deformation and fracture of dispersed particles in heterogeneous media processed in RPA are pressure pulsations, as well as normal and shear stresses arising in the flow during its passage through the working area of the apparatus [5.8, 5.9]. The pressure distribution over the volume of the working zone is characterized by a significant degree of unevenness, and the character of its distribution is rapidly changing over time. The pressure gradients arising in the flow contribute to the deformation of the particles, and its pulsations in time can cause high-frequency vibrations of their shells, which leads to a rupture of the interphase boundaries. In addition, the pulsating nature of the pressure change can cause adiabatic boiling of the treated medium and subsequent cavitation effects in the working area of the apparatus, which also contributes to the destruction of particles of the dispersible substance.

In figure 5.11 shows the pressure fields in the RPA working zone obtained by the method of numerical simulation of a fluid flow with a viscosity of $\mu = 0.01$ Pa·s at a zero differential pressure ($\Delta p = 0$). Since the process under consideration is periodic in time, it is assumed that the moment of coincidence of the slots of the rotor with the slots of the stator corresponds to the time $\tau = 0$. As can be seen from figure 5.11 a, at this moment the pressure field is relatively uniform. Positive overpressure (up to +26 kPa) is observed near the right inner corner of the slot of

the external stator. The negative pressure region (up to -14 kPa) is located in the gap between the rotor and the inner stator near the right outer corner of the inner stator and at the entrance to the rotor slot.

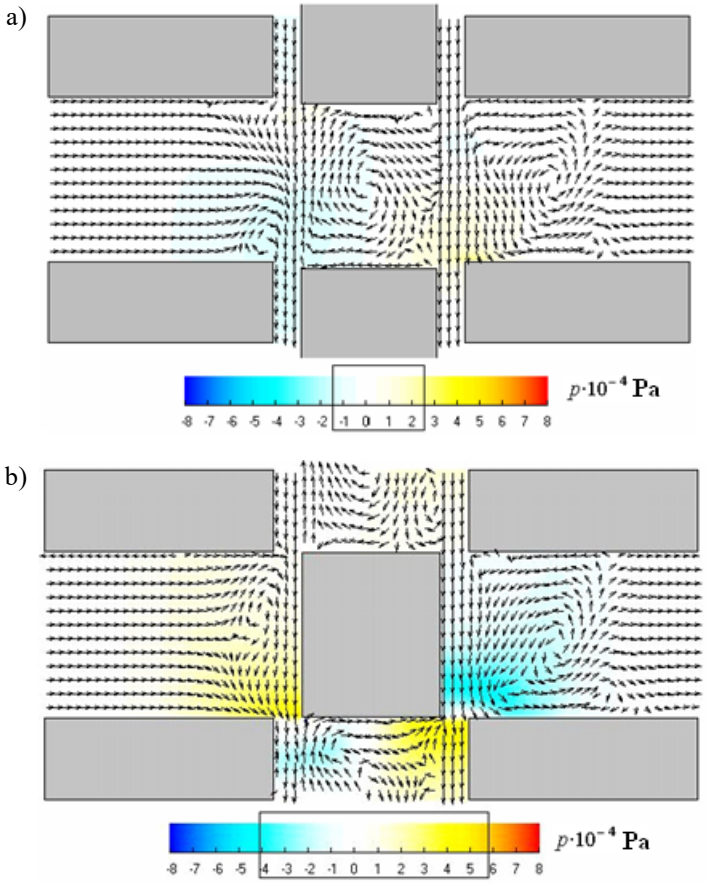

FIGURE 5.11. The pressure fields in the working space of the RPA at $\mu = 0.01$ Pa·s and $\Delta p = 0$ at time instants $\tau/\Delta\tau = 0$ (a) and $\tau/\Delta\tau = 1/2$ (b).

As the stator slots gradually overlap by the rotor wall, the pressure begins to increase at the right inner corner of the slots of the external stator. An increase in pressure is also observed near the inner left corner of the rotor slot. Near the right outer corner of the inner stator, the pressure decreases. A negative pressure region also begins to form in the central and left parts of the input section of the slot of the external stator. With a further increase of the degree of mutual overlapping of the slots, the pressure in the flow near the inner wall of the rotor (from the side of slot of the inner stator) begins to increase, and near the outer surface of the rotor (from the side of slot of the external stator) it decreases.

By the time of complete mutual overlapping the stator slots by the rotor wall, the negative pressure region near the right outer corner of the inner stator moves downstream and occupies the region in the gap between the rotor and the inner stator, and at this place already is formed the zone of excess positive pressure. The greatest positive pressure in this zone is achieved in the gap between the outer right corner of the slot of the inner stator and the left inner corner of the slot of the rotor (fig. 5.11b).

The opposite picture takes place in the gap between the right inner corner of the slot of the outer stator and the left outer corner of the slot of the rotor. Since the slot of the external stator is practically blocked by the wall of the rotor, a rarefaction region (up to –40 kPa) forms at the entrance to the slot of the external stator. At the same time, at the entrance to the gap between the rotor and the external stator, the pressure increases to +59 kPa. As can be seen from figure 5.11b, which is corresponding to the time instant $\tau/\Delta\tau = 1/2$, in the areas of space adjacent to the corners of the slots, the pressure drop reaches 99 kPa. At the same time, the distance between the maximum and minimum pressure points is ~1 mm. However, the described pattern of pressure distribution in the RPA working area takes place over a very short period of time. After the moment of complete mutual overlapping of the slots, the pressure in the flow begins to gradually equalize.

To study the effect of the viscosity of the medium on the pressure field, we also consider the results of solving a similar problem for the case $\mu = 0.3$ Pa·s. In the case of more viscous liquids, the nature of the pressure change over time in the slots of the rotor and stators is qualitatively the same as for a liquid with a low viscosity. However, since approximate symmetry of the velocity field with respect to the midline of the rotor is characteristic for the flow of highly viscous fluids, the pressure field also turns out to be close to symmetric with increasing viscosity of the medium. As the slots of the rotor and stators overlap, an increase in pressure is also observed near their converging corners, but more significant than with the flow of liquids with low viscosity. At this period of time for flows with highly viscous media, a pressure drop (up to -45 kPa) in the gaps between the rotor and the stators is characteristic.

At the moment of complete overlapping of the stator slots by the rotor wall, the excess positive pressure near their converging corners reaches +95 kPa, which exceeds the similar value obtained for a fluid with a viscosity of $\mu = 0.01$ Pa·s. In this case, in the region of the entrance to the slot of the external stator, the vacuum becomes -35 kPa (not as significant as in the case of a medium with a low viscosity).

At a time interval of $0.5 < \tau/\Delta\tau < 1$ for the flow of highly viscous fluids, a characteristic is increase in pressure in the gaps, especially in the gap between the rotor and the external stator. If for low-viscous media this time interval was characterized by a gradual equalization of pressure, then in this case a high value of excess pressure (+95 kPa) in the external gap remains almost until the slots of the

rotor and stators coincide, after which, as already mentioned, the pressure in the gaps begins fall rapidly. Thus, for flows of highly viscous media, more significant pressure drops in the gaps are characteristic.

The above results relate to cases of zero pressure drops. As shown by the results of numerical simulation of the flow of media in RPA at a positive difference in external pressure (Δp = +10 kPa), the range of changes in overpressure in the working area is wider than in the case of Δp = 0. As in the case of Δp = 0, the largest range of pressure changes in the working zone at Δp = +10 kPa is observed when the stator slots are completely blocked by the walls of the rotor. At this moment, in the region of the flow inlet into the slot of the external stator, a maximum pressure drop is observed (up to -50...-60 kPa relative to the fluid pressure at the inlet to the working area). At a given moment in time, conditions may arise for adiabatic boiling of the medium with subsequent cavitation.

As follows from the presented results, during operation of the rotary-pulsating apparatus, the pressure changes most intensively near the right edge of the output section of the slot of the inner stator, the right edge of the input section of the slot of the outer stator, in the areas of both edges of the left wall of the slot of the rotor, as well as on the inner and the outer cylindrical surfaces of the rotor. In order to more closely consider the change in time of pressure in the indicated zones of the working space, we consider the time dependences of static pressure at four characteristic points of the flow region. These points are located in the middle of the exit section of the slot of the inner stator (a), in the middle of the entrance section into the slot of the outer stator (b), in the middle of the entrance section into the gap between the rotor and the inner stator (c), and in the middle of the entrance section into the gap between the rotor and external stator (d). Presented on figures 5.12-5.15 the results relate to the case Δp = 0 for liquids with viscosity coefficients μ = 0.01; 0.1 and 0.3 Pa·s.

In the first half-cycle ($0 < \tau/\Delta\tau < 0.5$), the cross-section for the radial fluid flow is reduced as a gradual mutual overlap of the slots of the stators and rotor occurs. Due to the braking of the radial directed flow, there is an increase in excess pressure at the outlet from the internal slot of the stator (fig. 5.12) from negative values (-12... -8 kPa) to positive (+8...+18 kPa). Moreover, the higher of these pressure values relate to the case of low (μ = 0.01 Pa·s) viscosity of the medium. However, this growth is not monotonous. Curves $p(\tau)$ except for the moment $\tau/\Delta\tau \approx 0.5$ (complete mutual overlapping of the slots of the rotor and stators) also have maxima at $\tau/\Delta\tau \approx$ (0.23...0.25), which corresponds to the moment of approach of the lower edge of rotor slot to point (a). The fluid flowrate in the radial direction at this moment is maximum.

The value of this first pressure maximum (~ +12 kPa) weakly depends on the viscosity of the liquid, while the second maximum as the greater as lower the

viscosity. The minima of the considered curves are located between the above maxima and correspond to $\tau/\Delta\tau \approx 0.36$.

The reason for a certain decrease in pressure at point (a) is associated with a change in the direction of flow from radial to tangential in this point. This pressure drop is more significant for liquids with high viscosities. Thus, the pressure at point (a) for the first half-cycle is generally higher for liquids with lower viscosity. This is because the maximum pressure corresponding to $\tau/\Delta\tau \approx 0.5$ is associated with the braking process of the radial fluid flow, and higher values of radial velocities falling to a minimum at $\tau/\Delta\tau \approx 0.58$ correspond to liquids with lower viscosities.

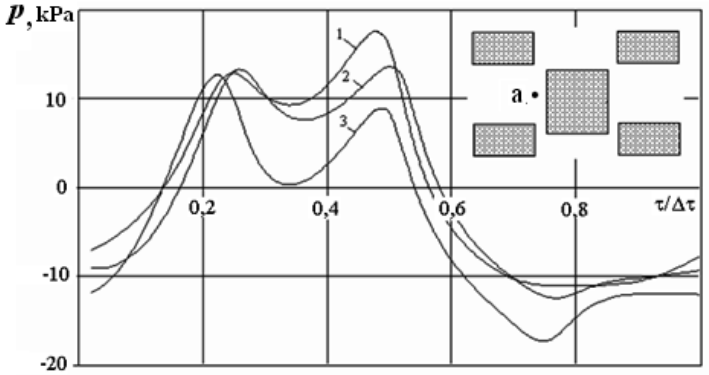

FIGURE 5.12. The influence of the viscosity of the medium on the character of time change of pressure at point (a), located in the middle of the output section of the slot of the inner stator: 1 – μ = 0,01 Pa·s; 2 – 0.1 Pa·s; 3 – 0.3 Pa·s.

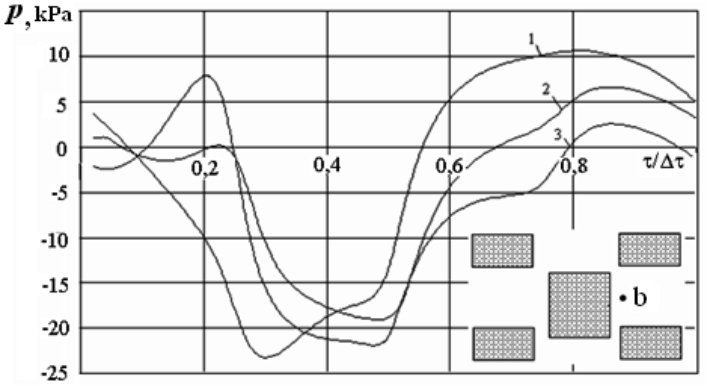

FIGURE 5.13. The influence of the viscosity of the medium on the character of time change of pressure at point (b), located in the middle of the inlet section of the slot of the external stator: 1 – μ = 0.01 Pa·s; 2 – 0.1 Pa·s; 3 – 0.3 Pa·s.

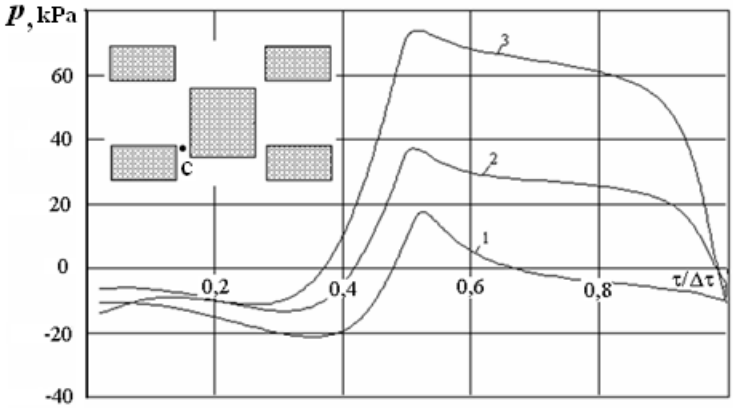

FIGURE 5.14. The influence of the viscosity of the medium on the character of the change in pressure over time at point (c) located on the middle of the inlet section into the gap between the rotor and the internal stator 1 – μ = 0.01 Pa·s; 2 – 0.1 Pa·s; 3 – 0.3 Pa·s.

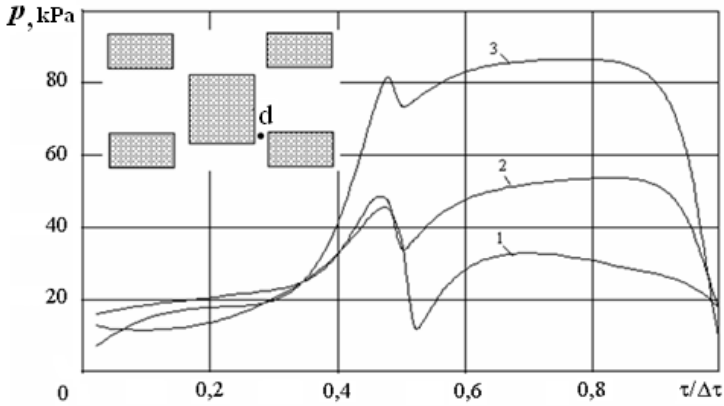

FIGURE. 5.15. The influence of the viscosity of the medium on the character of the change in pressure over time at point (d) located in the middle of the inlet section into the gap between the rotor and the external stator: 1 – μ = 0.01 Pa·s; 2 – 0.1 Pa·s; 3 – 0.3 Pa·s.

At point (b), located in the middle of the inlet section of the slot of the external stator, the character of the function of the pressure change over time is different for media with different viscosities (fig. 5.13). For a fluid flow with a low viscosity (μ = 0.01 Pa·s), the pressure in the time interval $0 < \tau/\Delta\tau < 0.3$ decreases to -23 kPa, and for fluids with a high viscosity (μ = 0.3 Pa·s) the pressure initially rises to +7.5 kPa, and then drops to -23 kPa. This sharp decrease in pressure (by about 30 kPa) occurs in a very short period of time (in 0.3 $\Delta\tau$ or in 10^{-4} s). The reason for the pressure drop at point (b) during the period of gradual mutual overlapping of the

slots of the rotor and stators is the same as the reason for the pressure increase at point (a). If at point (a) the pressure increases due to flow inhibition, then at point (b) it drops due to a significant decrease in the flowrate of liquid entering the slot of the external stator.

The pressure at points (c) and (d) located in the space between two stators and not yet separated in the first half-cycle by the rotor wall, up to the moment $\tau/\Delta\tau \approx 0.32$ weakly depends on time and does not significantly depend on viscosity. At point (c), located closer to the internal stator, the pressure is negative (-10...-20 kPa), and at point (d) it is positive (+15...+20 kPa).

In the second half-cycle ($\Delta\tau/2 < \tau < \Delta\tau$), the rotor wall enters the space between the stators, displacing fluid from there, and the slots of the rotor and stators gradually begin to fit together. The resistance to fluid flow in the radial direction decreases, and the pressure at point (a) begins to fall and the flowrate increases. A minimum pressure (-11 kPa for $\mu = 0.01$ Pa·s and -18 kPa for $\mu = 0.3$ Pa·s) is reached at this point with $\tau/\Delta\tau \approx 0.75\ldots0.85$, when the edge of the wall of the rotor slot moves away from points (a) and slots are half fit together. At point (b), the character of the pressure change in the second half-cycle is the opposite. In the time interval $0.5 < \tau/\Delta\tau < 0.8\ldots0.85$, the pressure at this point increases. At that, the maximum pressure is higher when the viscosity of fluid is lower. For $\mu = 0.3$ Pa·s at point (b), the maximum is 2.5 kPa, and for $\mu = 0.01$ Pa·s, respectively, 10.6 kPa.

The second half-period is characterized by a sharp increase in pressure at points (c) and (d). At point (c) (fig. 5.14), its maximum is reached immediately after the entrance of the wall of the rotor slot into the space between the walls of the stators (when points (c) and (d) appear in the gaps between these walls). By the time moment $\tau/\Delta\tau \approx 0.52$, the pressure at point (c) increases to +17 kPa for $\mu = 0.01$ Pa·s and to +72 kPa for $\mu = 0.3$ Pa·s. Thus, in contrast to the situation observed at points (a) and (b), the pressure in the gap between the internal stator and the rotor in the second half-cycle is higher, the higher the viscosity of the liquid. After $\tau/\Delta\tau \approx 0.9$, the pressure at point (c) begins to drop sharply and again becomes negative by the end of the full period. At point (d), the pressure in the second half-cycle is also higher than in the first (fig. 5.15). However, the law of its change in time is more complex than at point (c). The function $p(\tau)$ at point (*d*) has two maxima and one local minimum. A sharp increase in pressure towards the end of the first half-period is followed by a slight decrease (in a short period of time), and then again an increase, but smoother. For $\mu = 0.3$ Pa·s, the pressure increases to +86 kPa, and for $\mu = 0.01$ Pa·s – only to +33 kPa. Thus, the pressure in the gap between the rotor and the external stator in the second half-cycle is higher, the higher the viscosity of the liquid.

Comparing the time dependences of pressure at the four marked points of the working space of the apparatus, it can be noted that for liquids with high viscosity, the amplitude of pressure fluctuations is much higher in the gaps than in the inlet

and outlet sections of the stators. At μ = 0.3 Pa·s at point (c), the pressure for the period $\Delta\tau$ changes by 87.7 kPa, while at point (a) it changes only by 29.7 kPa. At lower viscosities (for example, μ = 0.01 Pa·s), the amplitude of the pressure fluctuation at point (a) is approximately the same as at μ = 0.3 Pa·s, and at point (c) amplitude of the pressure fluctuation is only 38.6 kPa. Nevertheless, in flows of media with both low and high viscosity, the highest pressure pulsations are observed precisely in the gaps between the stators and the rotor. Apparently, the most favorable conditions in the flow of the carrier medium for the deformation and destruction of particles of the dispersible substance are creating in these areas of RPA. This is also confirmed by the time dependences of a number of dynamic characteristics of the flow (pressure, normal and tangential stresses, acceleration) at three characteristic points of the region located near the right inner edge of the slot of the external stator (fig. 5.16-5.18).

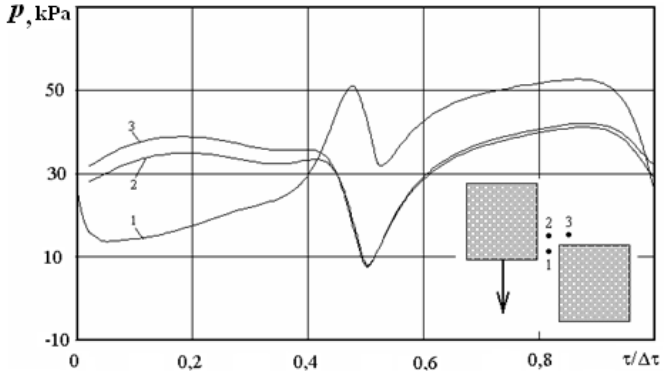

FIGURE 5.16. The time variation of the pressure at points located near the entrance to the gap between the rotor and the external stator Δp = 0, μ = 0.1 Pa·s.

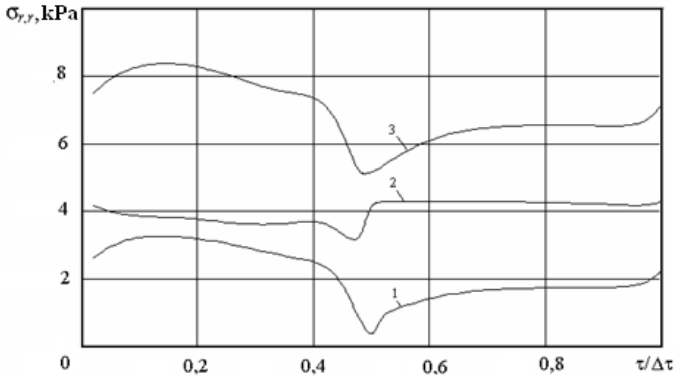

FIGURE 5.17. The change in time of the normal stress at the points located at the entrance to the gap between the rotor and the external stator Δp = 0, μ = 0.1 Pa·s.

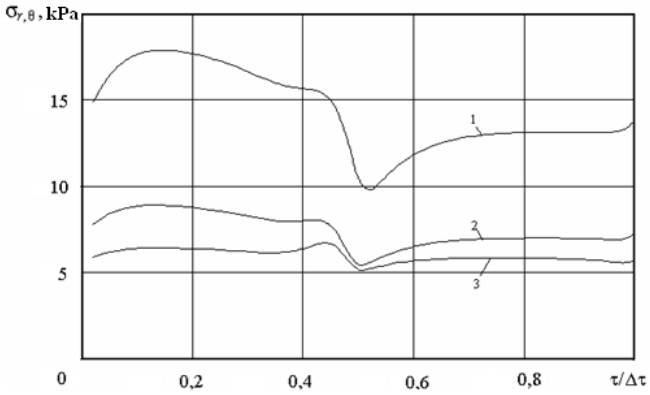

FIGURE 5.18. The change in time of the shear stress at the points located at the entrance to the gap between the rotor and the external stator $\Delta p = 0$, $\mu = 0.1$ Pa·s.

These results relate to the case $\Delta p = 0$ and $\mu = 0.1$ Pa·s. As can be seen from the figures, at the moment of complete mutual overlapping of the slots of the rotor and stators, the pressure at the entrance to the external gap increases sharply, while at the points adjacent to the gap it drops. At this moment, the normal and tangential stresses at the points reach their minimum values, and then they begin to increase sharply (impulsively). At point 1 (the entrance to the gap), normal stresses are lower, and tangential are higher than similar values at neighboring points. At the moment of complete mutual overlapping of the slots of rotor and stator, the modules of accelerations at all points sharply increase. Before entering the gap (point 2), the flow acceleration, determined as $\left|\frac{D\vec{V}}{D\tau}\right| = \sqrt{\left(\frac{Dv_r}{D\tau}\right)^2 + \left(\frac{Dv_\theta}{D\tau}\right)^2}$, reaches 10^5 m/s^2 (fig. 5.19), which is the manifestation of effect of discrete impulse energy input in the RPA working area.

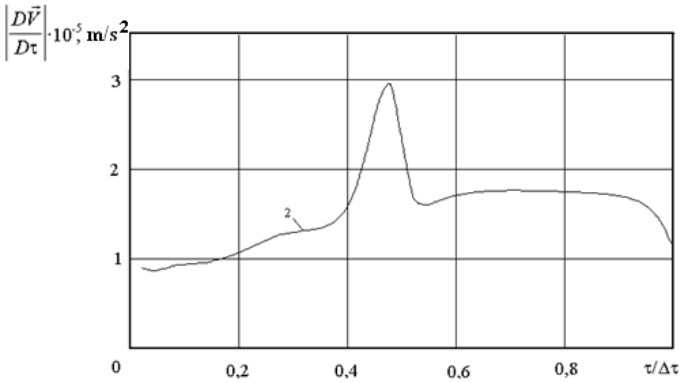

FIGURE 5.19. Dependence on the time of acceleration of the flow in front of entrance entering the gap between the rotor and the external stator (point 2), $\Delta p = 0$, $\mu = 0.1$ Pa·s.

5.5. The moment of hydrodynamic drag forces acting on the rotor from the side of a viscous fluid

When the rotary-pulsation apparatus is operating, the forces of hydrodynamic resistance from the side of a viscous fluid flow act on the surface of its working elements. The greatest power impact is experienced by a rotor rotating with a high angular velocity. The hydrodynamic resistance forces acting on the rotor are due to the presence in the flow of a pressure that varies in time, and also of normal and tangential stresses. These forces create a moment M_h relative to the axis of rotation of the rotor. The forces creating a moment relative to the axis of rotation include the forces created by the tangential stresses $\sigma_{r,\theta}$, acting on the outer and inner cylindrical surfaces of the rotor, as well as the forces due to the pressure and normal stresses $\sigma_{\theta,\theta}$, acting on the side surfaces of the rotor which are the walls of its slots. In this case, the pressure and normal stress acting on the cylindrical surface of the rotor (external and internal), as well as the shear stresses acting on the walls of its slots, do not contribute to the resulting moment of forces. Thus, if a certain part of the rotor wall is within the angular $\theta_r \le \theta \le \theta_r + \Delta\theta/2$ and radial $r_{r,in} \le r \le r_{r,ex}$ coordinates, the value of M_h can be calculated as:

$$M_h = zh\left\{\int_{r_{r,in}}^{r_{r,ex}}\left[\left(p-\sigma_{\theta\theta}\right)_{|\theta_r+\Delta\theta/2}-\left(p-\sigma_{\theta\theta}\right)_{|\theta_r}\right]rdr+\int_{\theta_r}^{\theta_r+\Delta\theta/2}\left[\left(r^2\sigma_{r\theta}\right)_{|r_{r,in}}-\left(r^2\sigma_{r\theta}\right)_{|r_{r,ex}}\right]d\theta\right\} \tag{5.2}$$

Taking into account the fact that the radial velocity v_r on the walls of the rotor is zero, the stress values $\sigma_{\theta,\theta}$ and $\sigma_{r,\theta}$, can be found from the expressions:

$$\sigma_{\theta,\theta} = 2\mu\frac{\partial\omega}{\partial\theta};\quad \sigma_{r,\theta} = \mu\cdot r\frac{\partial\omega}{\partial r}$$

Using the results of numerical simulation presented above, namely, the calculated velocity and pressure fields in the flow, it is possible to find on the basis of expression (5.2) the values of the moments of the hydrodynamic drag forces M_h acting on the rotor from the side of a viscous flow. The time dependences of the relative moment of resistance forces $M_h / \bar{M}$ for one period $\Delta\tau$ obtained for the case $\Delta p = 0$ and various viscosities of the liquid are shown in figure 5.20. Values $\bar{M}$ are averaged over a time period $\Delta\tau$ moments M_h:

$$\bar{M} = \frac{1}{\Delta\tau}\int_0^{\Delta\tau} M_h(\tau)d\tau$$

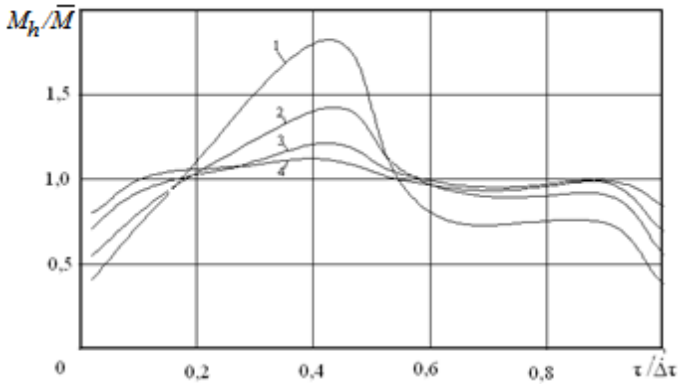

FIGURE 5.20. The time dependence of the relative moment of hydrodynamic resistance forces: 1 – μ = 0.01 Pa·s; 2 – 0.03 Pa·s; 3 – 0.1 Pa·s; 4 – 0.3 Pa·s.

As can be seen from figure 5.20, the values of M_h depend substantially on the time τ. However, this dependence decreases with increasing of viscosity of the liquid, i.e. at high viscosities of the medium, the $M_h(\tau)$ values are more uniformly distributed in time.

The dependence of $\overline{M}$ on viscosity is shown in figure 5.21.

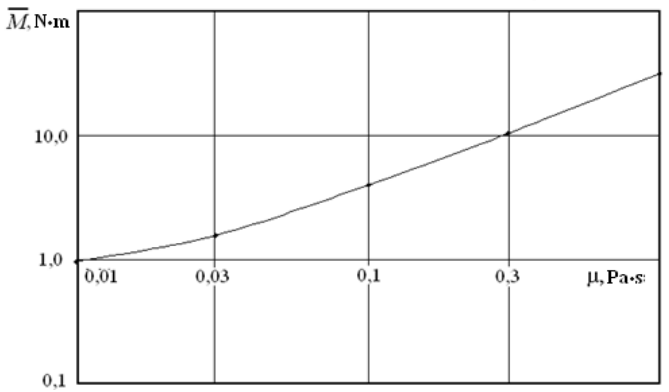

FIGURE 5.21. Dependence of the average moment of hydrodynamic resistance forces on the viscosity of a liquid.

As one would expect, with an increase in the viscosity of the liquid, the averaged in time moment of the resistance forces increases (fig. 5.21), however, the dimensionless quantity $\overline{M}/\left(\mu\omega_0 r_0^3\right)$ decreases with an increase in viscosity (fig. 5.22). The reason for this is that with an increase in viscosity, both the flowrate of the liquid through the apparatus and the shear rate of the flow near the side surfaces

of the rotor slots decrease. It should be noted that the minimum electric motor power N, which is necessary for the rotor to rotate at a constant angular velocity ω_r, overcoming the force of hydrodynamic resistance, can be found from the expression $N = \omega_r \bar{M}$.

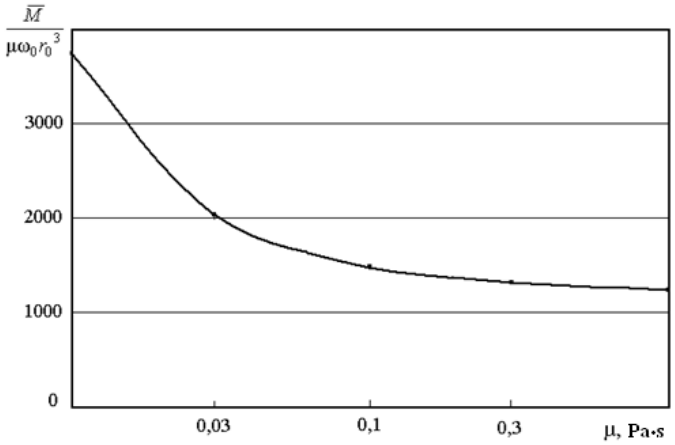

FIGURE 5.22. Dependence on fluid viscosity of the dimensionless average moment of hydrodynamic resistance forces.

5.6. Fluid flow in a rotary pulsation apparatus at the stage of its acceleration

A condition for solving the problems considered in the previous subsections is the constancy in time of the angular velocity of rotation of the rotor ω_0. Since previously only periodic modes of operation of the apparatus were investigated, the problems were solved as non-stationary, but without concrete initial conditions. It was assumed that at the initial moment of time, the liquid is at rest, and the rotor already has a constant angular velocity of rotation ω_0, given by the condition of the problem. Such a statement is characteristic of the so-called problems without initial conditions. When solving them, it is assumed that after a certain period of time, the process acquires a character determined only by boundary conditions, regardless of what conditions were in the beginning. If the features of the process during the transition period are not of interest, then for such problems the initial conditions can be, as in the case under consideration, arbitrary.

The angular velocity of rotation of the rotor, which is set as a known parameter, acquires, strictly speaking, a stable value only after the completion of the transition process associated with the exit of the rotor from the rest state. Theoretically, this period of time is equal to infinity, practically – a few seconds.

Consider the results of solving the problem of fluid flow in a rotary-pulsating apparatus at the stage of acceleration of the rotor from a state of rest at a time-varying angular velocity of its rotation. The difference between this formulation of the problem and the formulation of the problem considered earlier is that instead of the condition $\omega_0 = \text{const}$, the condition $\omega_0 = \omega_0(\tau)$, is set on the surfaces of the rotor, moreover, $\tau = 0$: $\omega_0 = 0$, and for $\tau \to \infty$: $\omega_0(\tau) \to \text{const}$. For such a problem, specific initial conditions will already be necessary. It is most natural to accept at each point of the computational domain for $\tau = 0$ the conditions $v = 0$; $\omega = 0$, which corresponds to the initial state of rest of the entire system [5.6].

At the moment of time $\tau = 0$, the process of acceleration of the rotor begins. The law of change in time of the angular velocity $\omega_0(\tau)$ must either be specified or calculated taking into account a number of additional conditions. The rotational motion of the rotor in the general case is described by a differential equation of the form:

$$I \frac{\partial \omega_0}{\partial \tau} = M_e - M_h \tag{5.3}$$

where: I – the moment of inertia of the system consisting of the rotor of the apparatus and the rotor of the electric motor; M_e – the moment of forces of the electromagnetic field of the engine.

For known values of I and M_e, equation (5.3) together with expression (5.2) could be used to find the time dependence $\omega_0(\tau)$. Thus, the system of equations of fluid dynamics in RPA at the stage of acceleration of the rotor becomes closed. If I and M_e are unknown, the function $\omega_0(\tau)$ can be approximately described by an expression of the form $\omega_0(\tau) = \omega_{0,\infty}[1 - \exp(-k \cdot \tau)]$, in which $\omega_{0,\infty}$ is the rotor velocity after the RPA exits to a steady-state operation mode, k is a parameter that determines the rate at which the apparatus reaches the indicated mode.

The finite-difference scheme for solving the problem considered in chapter 4 for the case $\omega_0(\tau) = \text{const}$ assumes that during the one step of dimensionless time δH, the rotor moves one step $\delta\theta_j$ in the angular coordinate. Obviously, in this case, the equality $\delta H = \delta\theta_j$, holds, and in the case $\delta\theta_j = \text{const}$, the step in the dimensionless time δH is also constant. With $\omega_p(\tau) = \text{var}$, this condition will no longer be satisfied. In this case, in one time step (if it is constant), the rotor can only move for some part of the step in the angular coordinate (at $\delta\theta_j = \text{const}$), or, if it is still required that the rotor moves one step $\delta\theta_j$ along the angular coordinate in one time step, this time step δH should be variable. For the finite-difference solution of the fluid flow problem in a rotary-pulsating apparatus at the stage of its

acceleration, just this approach was chosen. The step in dimensional time $\delta\tau$ is considered time-dependent and is determined from the condition

$$\delta\theta = \int_{\tau}^{\tau+\delta\tau} \omega_p(\tau)d\tau$$

In the case of using the law of the change in the angular velocity with time presented above, this condition, converted to a dimensionless form, is reduced to the transcendental equation

$$\delta H = \delta\theta - \frac{\omega_{0,\infty}}{k}\left\{\exp\left[-\frac{k}{\omega_{0,\infty}}(H+\delta H)\right] - \exp\left[-\frac{k}{\omega_{0,\infty}}H\right]\right\}$$

which at each time step is solved by the iteration method. The average value of angular velocity of rotor for the time interval $H \ldots H + \delta H$ is taken in the calculations as

$$\bar{\omega}_0 = \omega_{0,\infty} \cdot \frac{\delta\theta}{\delta H}$$

Using the specified refinements to the algorithm presented in chapter 4, a finite-difference solution of the problem of fluid flow in the working space of a rotary-pulsating apparatus with a variable rotor velocity is made. The initial conditions for this problem will be: at $H = 0$: $V = 0$; $\Omega = 0$; $\Omega_0 = 0$.

The results of calculating the dependence on the dimensionless time of the averaged velocity $V_r(H)$ of the radial fluid flow in the inlet section of the internal stator for cases of a constant over time differential pressure Δp = 0 and a time-varying differential pressure $\Delta p = \Delta p(\tau)$ are presented in figure 5.23 and figure 5.24. The viscosity of the medium in both cases is the same and is μ = 0.1 Pa·s. In figure 5.25, the change of the moment of hydrodynamic drag forces $M_h(H)$ in time for the condition Δp = 0 is presented. For the case of a pressure difference varying in time, the function $\Delta p(\tau)$ is adopted in a form similar to the form of the function $\omega_0(\tau)$, i.e. $\Delta p(\tau) = \Delta p_0[1 - \exp(-k \cdot \tau)]$, where Δp_0 = 10 kPa. The parameters in the function of changing of the angular velocity with time are taken equal to: $k = 80 \cdot \pi\ \mathrm{s}^{-1}$; $\omega_{0,\infty} = 100 \cdot \pi\ \mathrm{s}^{-1}$. With these parameters, the angular velocity $\omega_{0,\infty}$ will differ by 99% from $\omega_{0,\infty}$ after approximately 0.02 s.

As can be seen from figures 5.23, 5.24, with an increase of $\omega_0(\tau)$ and a corresponding reduction in the intervals between the moments of alignment and mutual overlap of the slots of the rotor and stators, the values of minima and maxima of average velocity $V_r(H)$ of the radial fluid flow are increasing. The

figures also show the previously considered dependences $V_r(H)$, which are obtained from the solutions of the problems under the condition that the angular velocity is constant $\omega_0 = \text{const}$. It can be seen from the figures that as values $\omega_0(\tau)$ tends to $\omega_{0,\infty}$, the graphical dependences $V_r(H)$ also gradually transform to the form corresponding to the case $\omega_0 = \text{const}$. The same can be said about the dependence $M_h(H)$ for the case $\Delta p = 0$ (fig. 5.25).

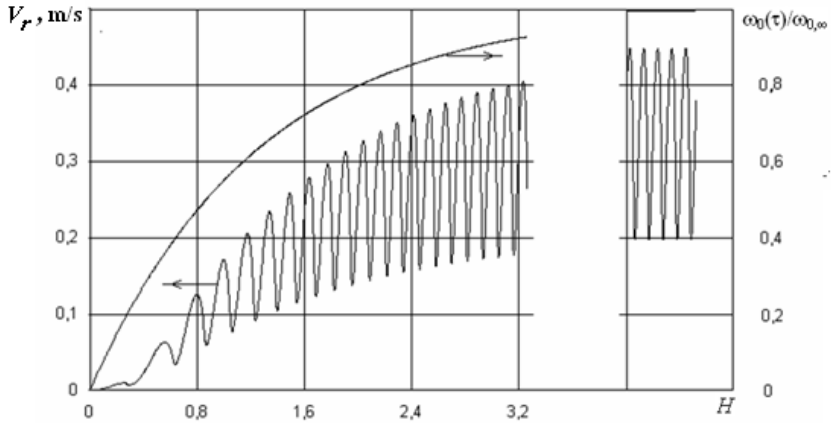

FIGURE 5.23. The time dependence of the average radial velocity $V_r(H)$ for a variable angular velocity of the rotor for the case $\Delta p = 0$, $\mu = 0.1$ Pa·s.

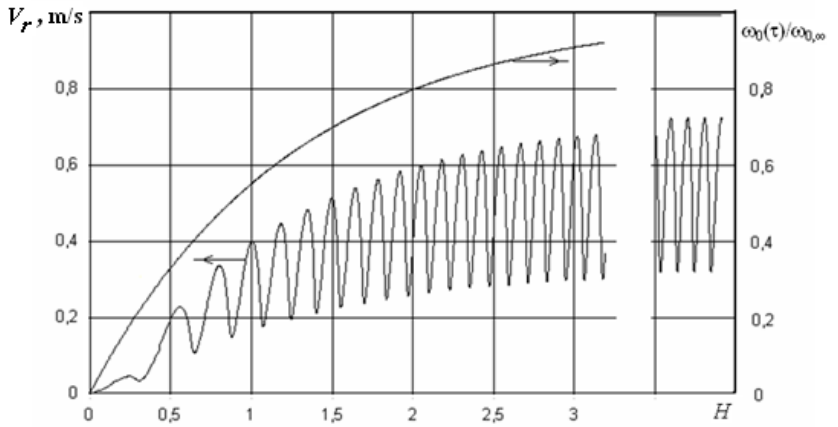

FIGURE 5.24. The time dependence of the average radial velocity $V_r(H)$ for a variable angular velocity of the rotor for the case $\Delta p = \Delta p(H)$, $\mu = 0.1$ Pa·s.

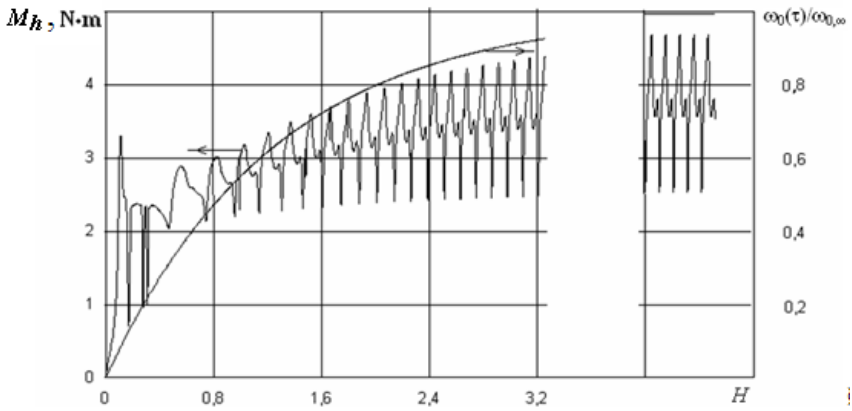

FIGURE 5.25. The time dependence of the moment of hydrodynamic drag forces at a variable angular velocity of the rotor for $\Delta p = 0$, $\mu = 0.1$ Pa·s.

From the presented results it follows that both statements of the unsteady problem of fluid flow in the working space of the RPA (i.e., with specific given initial conditions, or to some extent arbitrary, as was considered earlier), lead to the same solutions for $\tau \to \infty$. The rate at which dynamic processes in RPA reach the steady-state periodic mode depends on parameter k in the law of variation of $\omega_0(\tau)$. For those considered in figures 5.23-5.25 cases, it can be seen that practically the RPA operation mode becomes steady periodic at $H > 4...5$.

5.7. The structure of the fluid flow in a vertical section of RPA

The results presented above were found from solving two-dimensional problems of fluid flow in horizontal sections of the RPA working zone. These solutions were obtained under the assumption that the distribution functions of velocity and pressure weakly depend on the vertical coordinate z. For the problems considered, the determining parameter was the pressure drop Δp between the input and output sections of the working area. In general, it was set arbitrarily, although in reality its value depends both on the nature of the pressure change in the area before the inlet section into the working area, and on the law of pressure change in the fluid flow after it leaves the working zone. The difference between the heights of the liquid levels in the loading channel of the apparatus and in the branch pipe has a significant effect on the Δp value. If this difference is positive, then, most likely, $\Delta p > 0$. In the case of equal liquid levels, the pressure drop Δp will depend on the difference in hydraulic pressure losses in the areas of fluid supply to the inlet section of the working area and drainage of liquid through the outlet section. To estimate the magnitude of this difference, we consider an approximate solution of the fluid flow problem in a vertical section of the apparatus, from which it will be possible to evaluate the above hydraulic pressure losses with a certain degree of accuracy.

Strictly speaking, the fluid flow in the working space of the RPA is three-dimensional. If, when solving the two-dimensional problem of fluid dynamics in the horizontal section of the apparatus, the change in velocity and pressure in the direction of the vertical coordinate could be neglected under certain requirements for the accuracy of the solution, then neglect the change in these functions in the angular coordinate θ in the presence of a periodic geometry of the working bodies of the apparatus, strictly speaking, is impossible. Finding the numerical solution of the three-dimensional problem with such a rather complicated geometry of the computational domain is quite problematic. A compromise can be found by somewhat simplifying the geometry of the working area, which would nevertheless make it possible to reduce the problem under consideration to two-dimensional. For this purpose, we replace the system of radial slots in the rotor and stator with a system of horizontal slots that section the rotor and stators into a series of cylindrical bodies located one above the other. For a given (to some extent arbitrary) number of these slots, their width (the same for all) is chosen so that the equivalent diameter of the horizontal slot system is the same as that of the radial slot system. This makes it possible to achieve at least an approximate coincidence of the values of the static pressure drops in this equivalent system of horizontal slots and in the system of actually existing radial slots of RPA working elements.

The three-dimensional character of the fluid flow problem in the apparatus is also manifested in the fact that the processed fluid is discharged from it through a single fitting located near the bottom of the apparatus. A discharge hose is connected to the fitting, through which the liquid is sent to the receiving tank or fed back to the loading tank if it is necessary to repeatedly process the liquid. To comply with the model problem of equivalence of static pressure losses in the nozzle and hose, the external surface of the apparatus body ("cup") is considered the inner wall of the annular channel through which (instead of the nozzle and hose) liquid is removed from the apparatus. Of course, the width of this channel is chosen so that its equivalent diameter is the same as the diameters of the fitting and the hose. A scheme of the equivalent computational domain is shown in figure 5.26.

The peculiarity of the considered equivalent geometry of the computational domain is that now it allows one to consider all three components of the velocity vector v_z; v_r and $v_\theta = \omega \cdot r,$ as well as the pressure p – independent of the angular coordinate θ. Moreover, the initial system of equations of fluid dynamics (4.1)-(4.4) can be represented as:

$$\frac{\partial (v_r r)}{\partial r} + r \frac{\partial v_z}{\partial z} = 0 \tag{5.4}$$

$$\frac{\partial v_r}{\partial \tau} + v_r \frac{\partial v_r}{\partial r} - \omega^2 r + v_z \frac{\partial v_r}{\partial z} = -\frac{1}{\rho}\frac{\partial p}{\partial r} + \nu\left(\frac{\partial^2 v_r}{\partial r^2} + \frac{1}{r}\frac{\partial v_r}{\partial r} - \frac{v_r}{r^2} + \frac{\partial^2 v_r}{\partial z^2}\right) \tag{5.5}$$

$$\frac{\partial v_z}{\partial \tau} + v_r \frac{\partial v_z}{\partial r} + v_z \frac{\partial v_z}{\partial z} = -g - \frac{1}{\rho}\frac{\partial p}{\partial z} + \nu\left(\frac{\partial^2 v_z}{\partial r^2} + \frac{1}{r}\frac{\partial v_z}{\partial r} + \frac{\partial^2 v_z}{\partial z^2}\right) \tag{5.6}$$

$$\frac{\partial \omega}{\partial \tau} + \frac{v_r}{r^2}\frac{\partial\left(r^2\omega\right)}{\partial r} + v_z \frac{\partial \omega}{\partial z} = \nu\left(\frac{1}{r^3}\frac{\partial}{\partial r}\left(r^3 \frac{\partial \omega}{\partial r}\right) + \frac{\partial^2 \omega}{\partial z^2}\right) \tag{5.7}$$

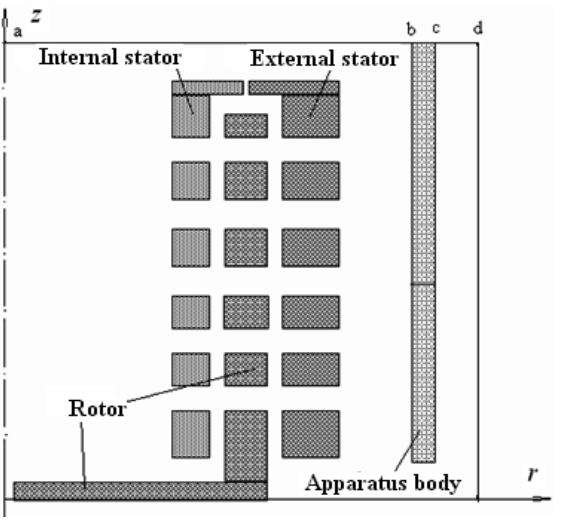

FIGURE 5.26. Equivalent computational scheme of the RPA working space.

Since the problem is considered symmetric about the vertical axis, the boundary conditions for it will have the form:

at $r = 0$: $\quad \dfrac{\partial v_z}{\partial r} = 0; \quad \dfrac{\partial \omega}{\partial r} = 0; \quad v_r = 0$

at $r = r_{\max}$: $\quad v_z = 0; \quad \omega = 0; \quad v_r = 0$

at $z = 0$: $\quad v_z = 0; \quad \omega = 0; \quad v_r = 0$

at $z = z_{\max}$: $\quad p = 0; \quad \dfrac{\partial \omega}{\partial z} = 0; \quad v_r = 0$

stator, apparatus body: $v_z = 0; \quad \omega = 0; \quad v_r = 0$

rotor: $v_z = 0; \quad \omega = \omega_0; \quad v_r = 0$

It is believed that the liquid levels in the loading capacity of the apparatus and at the outlet of the discharge hose are the same, which is typical for RPA operation in recirculation mode.

After the standard linearization procedure, the finite-difference analogue of equation (5.7) will contain only unknown grid functions for ω. Therefore, the method for solving the system of difference equations obtained on the basis of differential equation (5.7) will be similar to the method for solving the energy equation considered in chapter 4. In equation (5.5), the unknown function ω occurs only once in the form of the term on the left side of this equation. This term can be found from the solution of equation (5.7) and taken for (5.5) as a known quantity. The function ω is not included in the system of equations (5.4)-(5.6). Therefore, to solve the indicated system of two-dimensional equations, the tridiagonal matrix algorithm mentioned in chapter 4 can be used.

Calculation starts from $z = z_{\max}$ and is performed in the direction opposite to the direction of the O*Z* axis. As a result of the numerical solution of this problem, the fields of the velocity functions $v_z(z,r), v_r(z,r), \omega(z,r),$ and also the pressure fields $p(z,r)$ are determined. The fluid flow rate through the outlet section of the annular channel with radii r_c and r_d (fig. 5.26) simulating a discharge pipe is also calculated. The results of calculation by the presented algorithm of the velocity and pressure fields in the RPA working volume are shown in figure 5.27.

The calculation results relate to a rotary pulsation apparatus with the following geometric characteristics: apparatus height 43.8 mm; the radii of the inner stator r_i = 26.5 mm; r_0 = 29.9 mm; the radius of the rotor r_i = 30.15 mm; r_0 = 33.8 mm; the radii of the external stator r_i = 34.0 mm; r_0 = 39.0 mm; the radii of the "cup" r_i = 53.0 mm; r_0 = 55.0 mm; the radius of the outer pipe of the annular channel r_c = 61.8 mm. The rotor velocity is 48 r/s. Fluid viscosity μ = 0.1 Pa·s. The radial cuts of the working elements of the apparatus are replaced by five slots, the total passage area of which is equal to the total area of the radial cuts of the RPA working elements.

As can be seen from figure 5.27, the movement of fluid in the central part of the vessel's capacity is predominantly downward, and near the inner surface of the stator the direction of flow becomes radial. The movement of fluid in the radial direction through the slots of the rotor and stators occurs due to the action of centrifugal forces created by the rotating rotor. The fluid flow rate through the cross section of the loading tank is $0.75 \cdot 10^{-3}$ m^3/s. Very remarkable is the distribution function of the relative pressure $p_{rel} = p - 0.5\rho g z_{\max}$ along the radius of the apparatus in its average horizontal section (fig. 5.28).

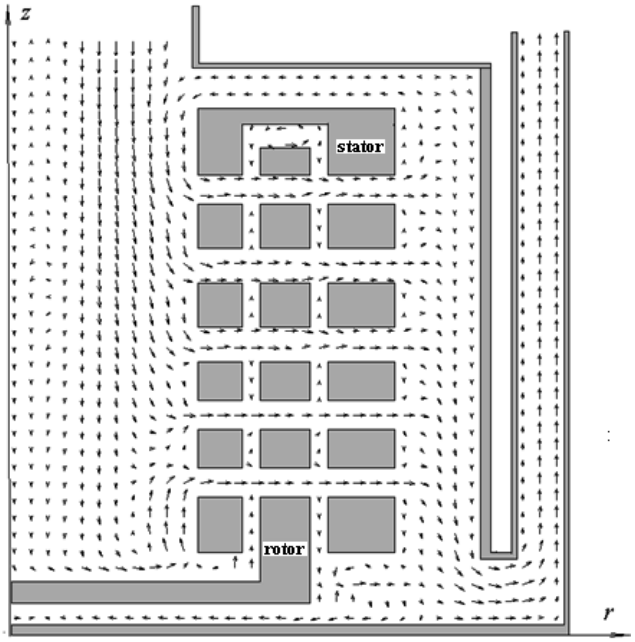

FIGURE 5.27. The velocity field in the vertical section of the RPA.

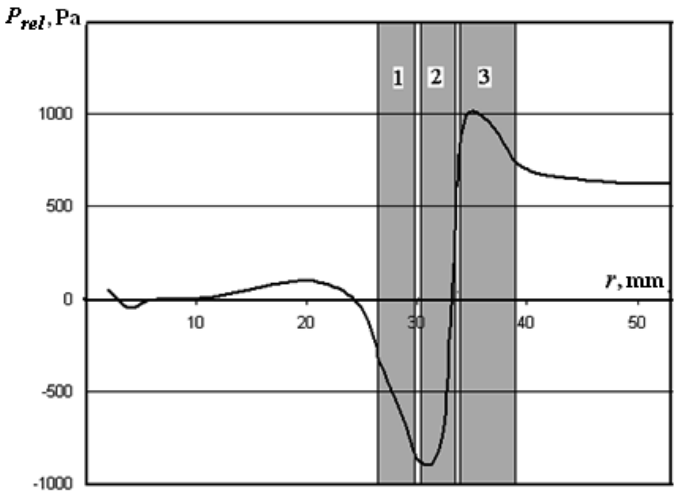

FIGURE 5.28. Distribution of the relative pressure of the liquid along the radius at the level of the average horizontal section of the RPA: 1 – internal stator; 2 – rotor; 3 – external stator.

As can be seen from the figure 5.28, in the inlet section of the slot of the internal stator, the relative pressure is negative ($p_{rel,in}$ = -295 Pa). Along the radius of the

slot of the internal stator, the pressure, due to hydraulic friction losses, drops to -845 Pa. In the rotor, due to the action of centrifugal force, the pressure increases and in the inlet section of the slot of the external stator reaches +842 Pa. Along the radius of the slot of the external stator, the pressure, as in the internal stator, drops to the value of $p_{rel,out}$ = +740 Pa. In general, it turns out that the working area is under the influence of a negative pressure drop: $\Delta p = p_{rel,in} - p_{rel,out}$ = -1037 Pa.

A number of important conclusions follow from the presented results. At the same liquid levels (relative to the O*Z* axis) in the inlet section of the loading vessel and in the outlet pipe, the liquid pressure in the inlet section of the slot of the internal stator is less than in the outlet section of the slot of the external stator. The movement of fluid through the working area occurs only due to the action of centrifugal force (pumping effect) and, in general, against pressure forces.

From the analysis of the velocity field presented in figure 5.27 also follows that in the region of the flow occupied by the RPA working bodies, the vertical fluid velocity v_z is much lower than the radial velocity v_r, and they can be neglected. Consequently, the two-dimensional formulation of the problem of fluid flow in the horizontal plane, the results of which were considered earlier, can be considered sufficiently satisfactory for determining the basic dynamic characteristics of RPA. In this case, the pressure drop Δp, as the initial parameter of the problem, can be estimated by the method considered above.

The indicated pressure drop Δp can also be determined by an approximate estimate of the total hydrodynamic pressure losses due to friction and at local resistances along the fluid flow path before and after the working zone. In this case, one should take into account the difference in liquid levels in the loading tank and in the section of the outlet fitting. It should also be borne in mind that, strictly speaking, the Δp values are not constant in time and depend on the time-varying average mass flow rate.

5.8. RPA dynamic characteristics at turbulent flow

The presented results of numerical simulation of fluid dynamics in the RPA working zone were obtained under the assumption of a laminar flow regime of the medium being treated. This flow pattern may be characteristic of high viscosity media. In cases of relatively low viscosity of the media, a transition to a turbulent flow regime is possible [5.7]. The cause of the turbulent flow in the RPA working volume may be a loss of flow stability. According to [5.10], in the gap between two coaxial cylinders, of which the inner rotates and the outer is stationary, the transition to the turbulent regime is possible at $\mathrm{Re} = \omega_0 r_p \delta / \nu > 3960$ (Ta > 1715). As for RPA, due to the more complex

structure of the flow in its working zone, a transition to a turbulent regime is possible even with lower values of these criteria. However, reliable experimental data on the conditions for the emergence of a turbulent flow regime in RPA, as well as on the values of Reynolds numbers corresponding to these conditions, are absent. Therefore, we conditionally assume that for media for which $\mu < 0.01$ Pa·s, the flow regime in the RPA working area with the considered structural parameters is most likely to be transient or turbulent. The indicated boundary value of viscosity is also taken because, as experience shows, that if the laminar model of fluid flow in RPA for $\mu < 0.01$ Pa·s is used, stable periodic mode of fluid flow in the working area is not installs. This also indicates the instability of the numerical laminar flow models under the indicated conditions. Of course, the character of the flow regime in the RPA is determined not only by the viscosity of the medium, but also by the geometric parameters of the working zone and the rotor velocity. It follows from the foregoing that, in connection with the possibility of the emergence of a turbulent regime of the medium flow in the working zone of the RPA, it is also advisable to study the dynamic characteristics of the RPA under the indicated regime.

The results of solving the problem of turbulent fluid flow in the RPA working area are presented in the form of fields of velocity, pressure, kinetic energy of turbulence, and its dissipation. As an example, a turbulent flow of a medium with a molecular viscosity of $\mu = 0.001$ Pa·s and a density of $\rho = 1000$ kg/m^3 (water) in an RPA of TFG type is considered [5.11]. The working elements of this apparatus contain 60 radial slots. The rotor velocity is $\omega_0 = 96\pi$ s^{-1}. The solution to the problem is made for a positive difference in external pressure ($\Delta p = +10$ kPa). As a turbulence model, the RNG model [5.12], considered in chapter 4, is used.

The velocity and pressure distributions in the RPA working zone during turbulent flow of the indicated medium are shown in figure 5.29. As can be seen from the figure, the structure of the fluid flow has a very complex vortex-like character. Vortex formation is observed in the rotor slot (two asymmetric multidirectional vortices), as well as at the exit from the slot of the internal stator and at the entrance to the slot of the external stator. In this case, the flow turns out to be almost radial in the initial section of the slot of the internal stator.

At the moment of mutual overlapping of the slots of the rotor and stators, an area of increased pressure arises in front of the rotor wall (up to +60 kPa). In this case, the pressure in the region of the edges of the walls of the rotor and of the external stator sharply increases up to +85 kPa. At the same time, a vacuum region (up to -60 kPa) arises in the area behind the rotor wall (at the entrance to the slot of the external stator).

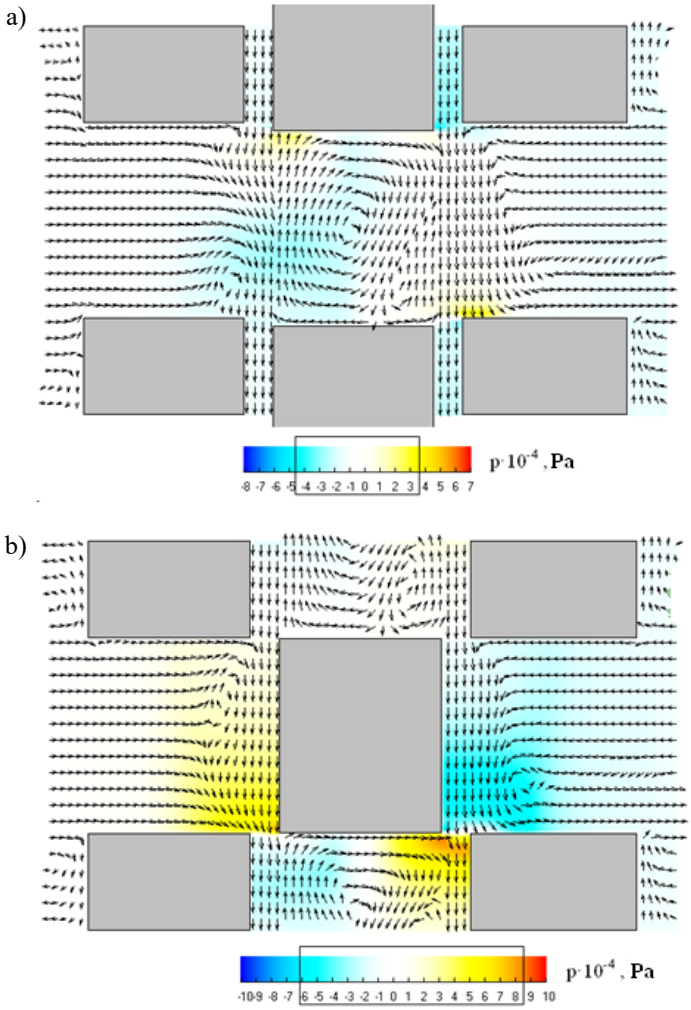

FIGURE 5.29. The velocity and pressure fields in the RPA working zone with turbulent flow (μ = 0.001 Pa·s; Δp = 10 kPa): a) $\tau/\Delta\tau = 0$; b) $\tau/\Delta\tau = 1/2$.

Due to the high degree of flow swirl, in the areas of the output section of the slot of the inner stator, the input section of the slot of the outer stator, as well as in the region of the rotor slot, turbulence is generated most intensively. In figure 5.30 shows the distributions of the kinetic energy of turbulence k in the flow region. As can be seen from the figure, at the inlet of the flow into the working area of the RPA, the values of k are of the order of 10^{-2} m^2/s^2. However, already in the middle part of the slot of the internal stator, where the flow is almost radial, the kinetic energy of turbulence decreases significantly (to $k \sim 10^{-4}...10^{-5}$ m^2/s^2). As the flow approaches the outlet cross section of the slot of the internal stator, the kinetic energy of turbulence begins to increase rapidly and in the region of the internal gap

it already reaches $k \sim 1...10$ m^2/s^2. The same orders of magnitude k has in the region of the external gap, as well as at the entrance to the slot of the external stator. In the middle part of the slots of the rotor and the external stator, the kinetic energy is slightly lower ($k \sim 0.1$ m^2/s^2).

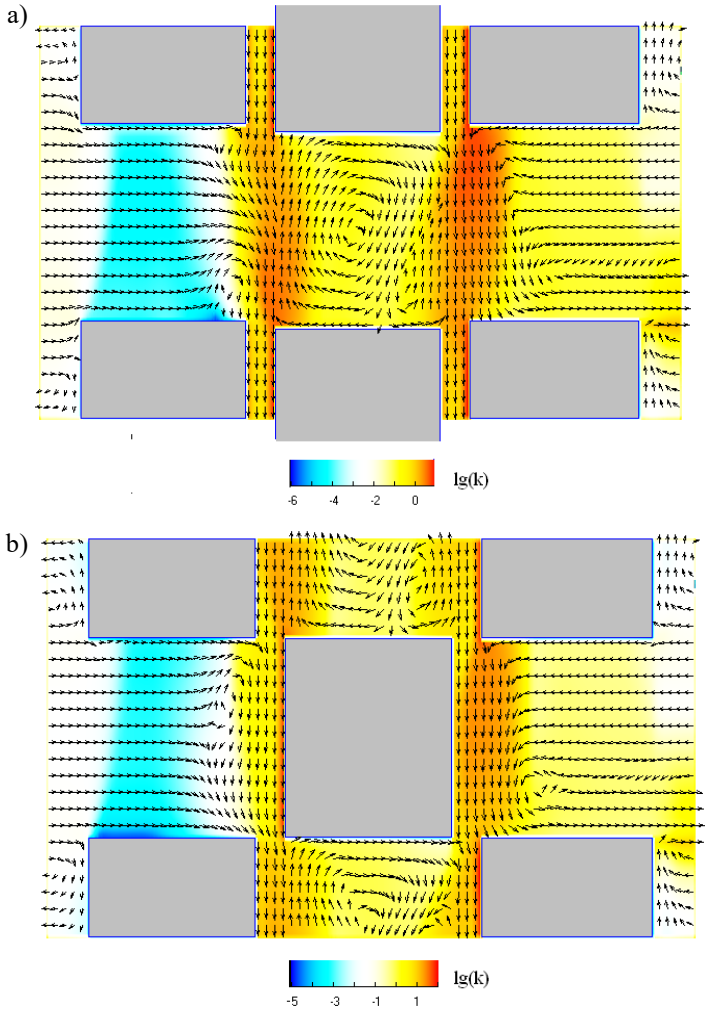

FIGURE 5.30. The field of kinetic energy of turbulence in the RPA working area ($\mu = 0.001$ Pa·s; $\Delta p = 10$ kPa): a) $\tau/\Delta\tau = 0$; b) $\tau/\Delta\tau = 1/2$.

Qualitatively similarly are distributed in the flow region the values of the dissipation of the kinetic energy of turbulence ε (fig. 5.31). The highest values ($\varepsilon \sim 10^{+5}$ m^2/s^3) of the dissipation rate ε have in the region of gaps between the working elements. The lowest values ($\varepsilon \sim 10^{-4}...10^{-5}$ m^2/s^3) have the dissipation rate in the middle part of the slot of the internal stator.

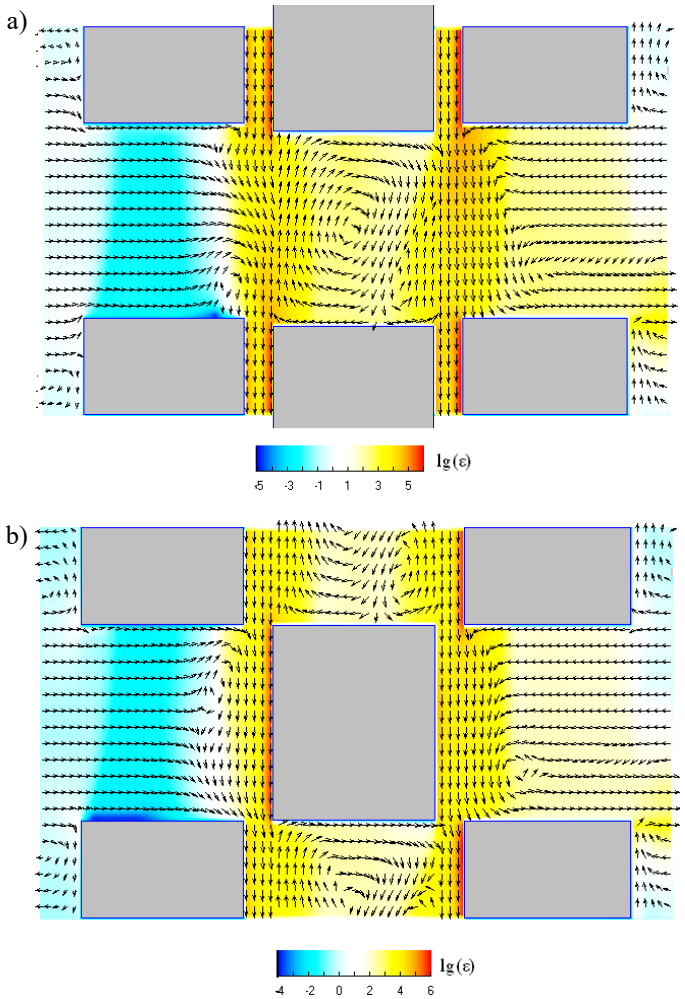

FIGURE 5.31. Turbulence energy dissipation rate field in the RPA working area (μ = 0.001 Pa·s; Δp = 10 kPa): a) $\tau/\Delta\tau = 0 = 0$; b) $\tau/\Delta\tau = 0 = 1/2$.

Correspondingly, turbulent viscosity coefficients $\mu_t = \rho C_\mu \frac{k^2}{\varepsilon}$ are distributed in the flow region. It follows from the results of solving the considered problem that the ratios μ_t / μ have the greatest values (~10) in the region of the internal and external gaps between the rotor and the stators. The smallest (~0.1) ratios μ_t / μ turn out to be in the middle part of the slot of the internal stator. In this region, the fluid flow has a predominantly radial direction and is close to laminar.

As already indicated, the most important technical characteristics of RPA include: the mass-average radial velocity of the medium flow, characterizing the productivity of the apparatus, the moment of hydrodynamic resistance forces acting

on the rotor, and the heating of the working area of apparatus due to dissipation of energy. The time variation of the average radial flow velocity at the entrance to the working zone is shown in figure 5.32. As can be seen from the figure, the curve $V_r(\tau)$ in shape turns out to be similar to the curves shown in figure 5.2, which correspond to the laminar flow of liquids with high viscosity.

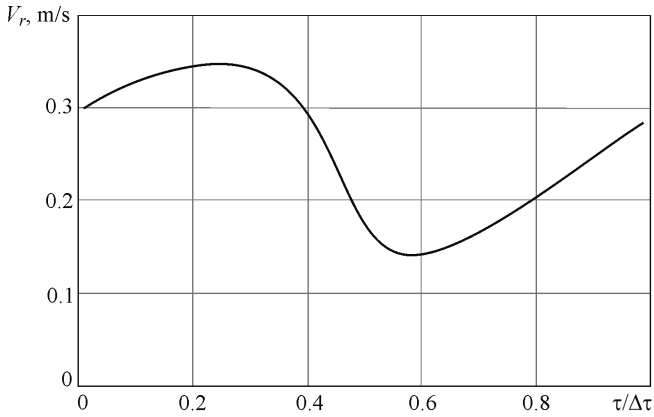

FIGURE 5.32. The time variation of the average fluid velocity in the inlet section of the slot of the internal stator in a turbulent flow (Δp = +10 kPa).

The time dependence of the moment of hydrodynamic drag forces M_h acting on the rotor under the turbulent regime of the medium flow is shown in figure 5.33.

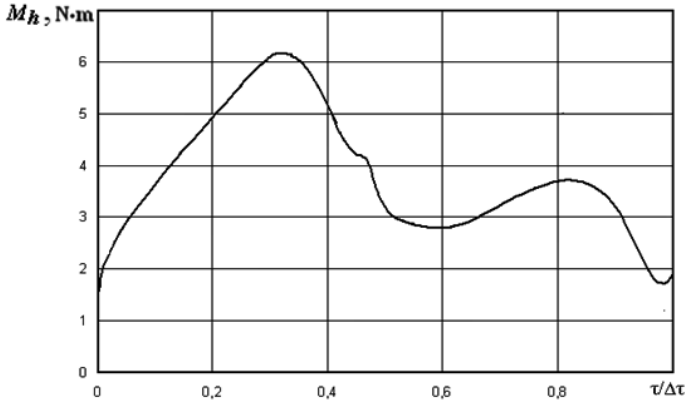

FIGURE 5.33. Change in time of the moment of resistance forces acting on the rotor during turbulent fluid flow (Δp = +10 kPa).

As can be seen from the figure, the value of the moment of forces M_h varies significantly over the period $\Delta\tau$. The minimum value (1.8 N·m) is achives at

$\tau/\Delta\tau$ = 0; 1, when the slots of the rotor and stators coincide, and the maximum value (6.2 N·m) – at $\tau/\Delta\tau$ = 0.32, i.e. after reaching the maximum values of the average radial velocity V_r over the cross section (fig. 5.32). On the whole, the nature of the change in time of the moment of forces M_h is qualitatively similar to that obtained for the laminar flow model (fig. 5.20). The mean value of the moment $\overline{M} \approx 4$ N·m for the turbulent regime over the period $\Delta\tau$ approximately corresponds to the value $\overline{M}$ for the laminar regime of fluid flow with a viscosity coefficient μ = 0.05 Pa·s (fig. 5.21).

The moment of hydrodynamic resistance forces is formed by tangential stresses on its cylindrical surfaces, as well as by pressure and normal stresses on opposite walls of the rotor slots. It follows that the values of M_h are significantly affected by the shape and slope of the tangential velocity profile near the surfaces of the rotor walls. To clarify the nature of the influence of these factors on the moment of hydrodynamic drag forces in the turbulent flow regime, we consider the distribution of tangential velocity rotor V_θ in the gap width between the internal stator and rotor the at the moment of coincidence of the slots of rotor with the slots of stator. In figure 5.34 shows the profiles of the tangential velocity in the indicated gap, constructed from the results of numerical simulation of the turbulent flow (curve 1), as well as those found from the solution of the problem for the laminar regime of fluid flow with a viscosity coefficient μ = 0.05 Pa·s (curve 2). Here, a curve of V_θ velocity variation is plotted, obtained from a well-known analytical solution to the problem of fluid flow between two coaxial cylinders (curve 3).

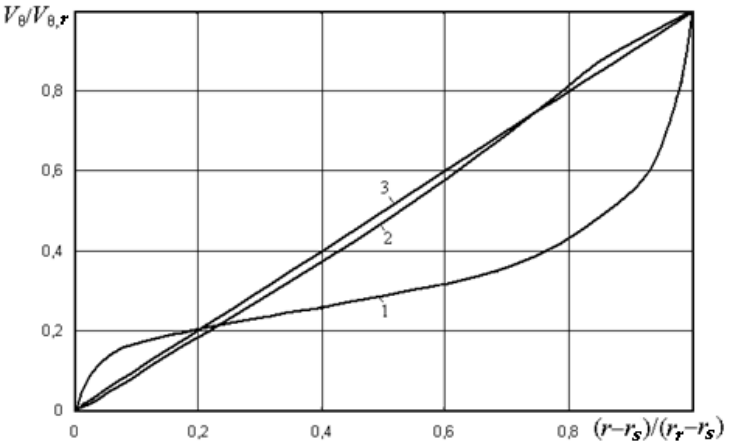

FIGURE 5.34. Changes in the tangential velocity in the gap between the internal stator and the rotor: 1 – turbulent flow; 2 – laminar flow; 3 – analytical solution of the problem of fluid flow in the gap.

As can be seen from the figure, curves 2 and 3 practically coincide, which indicates the similarity of the fluid flow in the gap between the RPA working elements to the flow between two coaxial cylinders. Curve 1 differs significantly from them. The rate of flow shear at the walls of the stator and rotor at turbulent flow is much higher than at laminar flow, which is the main reason for the increase in the moment of hydrodynamic resistance forces in the turbulent flow mode compared to similar values characteristic for the laminar regime.

Summing up the considered results of numerical simulation of fluid dynamics in the working volume of RPA, we can draw the following conclusions:

- as shown by the analysis of the flow structure in the working area of the RPA, in the slots of the rotor and stators there are areas of circulation flow. In this case, the vorticity in the flow reaches $\Omega_Z \sim 50 \cdot 10^3$ s^{-1}. The consequence of this is high flow deformation rates, high pressure gradients, significant normal and shear stresses in the slots of the working elements, as well as in the gaps between them. As will be shown below, the noted dynamic characteristics of the fluid flow in the working volume of the RPA significantly contribute to the destruction of dispersed structures of a heterogeneous medium;
- at times corresponding to the mutual overlap of the slots of the rotor and stators, an intensive change in the indicated dynamic characteristics of the flow is observed. These changes are similar to pulsation. Pressure drops at local points in the workspace can exceed 100 kPa. In this case, the acceleration of the flow increases to ~10^5 m/s^2. With an increase in the viscosity of the medium, as well as with an increase in the difference in external pressure, these trends intensify;
- noted characteristics of fluid dynamics in the RPA working space indicate the implementation of the process of discrete-pulse energy input into the flow. This effect contributes to the destruction of particles of the dispersed component of a multiphase medium processed in RPA;
- the areas of the working space that have the highest potential for the destruction of dispersed inclusions should most likely include sections of the edges of the slots of the stators adjacent to the gaps, as well as the gaps themselves. At the moments of time corresponding to the mutual overlapping of the slots of the rotor and stators, a significant increase in the flow acceleration, rates of flow deformation, as well as pressure gradients, normal and tangential stresses is observed in these areas;
- the fluid flow through the working elements in the radial direction periodically varies in time. The maximum values of the radial flow velocity are observed with half mutual overlapping of the slots of the rotor and stators. This flow rate increases both with an increase in the difference in external pressure, and with a decrease in the viscosity of the medium;

- the ratio between the radial and tangential flowrates of a fluid varies depending on the viscosity of the medium and the differential pressure. For media with low viscosity values, the radial flowrate usually exceeds the fluid flowrate through the gaps;
- the moment of hydrodynamic resistance forces acting on the rotor during a laminar flow of the medium increases with increasing viscosity, but the specified increase is not proportional to viscosity;
- in the case of turbulent fluid flow in the RPA working volume, the kinetic energy of turbulence has the highest values in the region of gaps between the working elements, as well as in the areas with the greatest vorticity of the flow;
- in the case of turbulent flow of the medium being processed in RPA, the moment of hydrodynamic resistance forces acting on the rotor increases in comparison with the laminar regime mainly due to an increase in the shear rate of the flow in the gaps between the working elements.

References

[5.1] Basok B.I., Davydenko B.V., Kravchenko Y.S., Pirozhenko I.A., Issledovanie mikrostruktury potoka zhidkosti v rotorno-pul'satsionnom apparate [Investigation of the microstructure of the liquid flow in the rotary pulsation apparatus]. *Reports of the National Academy of Sciences of Ukraine.* No. 11, 2003, pp. 71-76 (rus.)

[5.2] Basok B.I., Davydenko B.V., Kravchenko Y.S., Pirozhenko I.A., Model′ dynamiky ridyny u rotornomu aparati tsylindrychnoho typu [Model of fluid dynamics in a rotary apparatus of cylindrical type] *Vìsnik Nacìonal'nogo unìversitetu "L'vìvs'ka polìtehnìka" [Bulletin of Lviv Polytechnic National University]*. No. 506, 2004, pp. 163-167 (ukr.).

[5.3] Kravchenko Y.S., Basok B.I., Davydenko B.V., Pirozhenko I.A., Vliyaniye vyazkosti obrabatyvayemoy sredy na dinamicheskiye kharakteristiki rotorno-pul'satsionnogo apparata [Influence of the viscosity of a treated medium on the dynamic characteristics of a rotary-pulsatory apparatus]. *Industrial heat engineering.* Vol. 26, No. 1, 2004, pp. 7-11 (rus.).

[5.4] Basok B.I., Davydenko B.V., Obodovich A.N., Vliyaniye komponovki rabochikh organov na tekhnicheskiye kharakteristiki rotorno-pul'satsionnykh apparatov [Influence of the configuration of working bodies on the technical characteristics of rotor-pulsating devices]. *Industrial heat engineering.* Vol. 30, No. 3, 2008, pp. 5-11 (rus.).

[5.5] Basok B.I., Davydenko B.V., Avramenko A.A., Pirozhenko I.A., Gidrodinamika, teploobmen i effekty drobleniya vo vrashchatel'no-pul'siruyushchikh potokakh [Hydrodynamics, heat transfer and effects of crushing in rotational-pulsating flows]. Kiev: Express. 2012, 296 p. (rus.).

[5.6] Kravchenko Y.S., Davydenko B.V., Basok B.I., Teslya A.I., Techeniye zhidkosti v rotorno-pul'satsionnom apparate na stadii yego razgona [Fluid flow in a rotary pulsation apparatus at the stage of its acceleration]. *Industrial heat engineering.* Vol. 26, No. 2, 2004, pp. 31-36 (rus.).

[5.7] Davydenko B.V., Dinamicheskiye kharakteristiki rotorno-pul'satsionnogo apparata pri turbulentnom techenii zhidkosti [Dynamic characteristics of a rotary pulsation apparatus in turbulent fluid flow]. *Industrial heat engineering.* Vol. 31, No. 7, 2009, pp. 131-136 (rus.).

[5.8] Pavlenko A.M., Basok B.I., Strukturoobrazovaniye i dezintegratsiya emul'siy v vikhrevykh apparatakh [Structuring and disintegration of emulsions in vortex devices]. Dneprodzerzhinsk, DSTU publishing house. 2009, 205 p. (rus.).

[5.9] Dolinsky A.A., Pavlenko A.M., Basok B.I., Teplofizicheskiye protsessy v emul'siyakh [Thermophysical processes in emulsions]. Kiev: Nauk. Dumka. 2005, 264 p. (rus.).

[5.10] Shlihting G., Teoriya pogranichnogo sloya [The boundary layer theory]. M.: Nauka, 1974, 712 p. (rus.).

[5.11] Basok B.I., Gartvig A.P., Koba A.R. Goryachev O.A., Oborudovaniye dlya polucheniya i obrabotki vysokovyazkikh dispersnykh sred [Equipment for obtaining and processing highly viscous dispersed media]. *Industrial heat engineering.* Vol. 18, No. 1, 1996, pp. 50-56 (rus.).

[5.12] Avramenko A.A., Basok B.I., Kuznetsov A.V, Gruppovyie metodyi v teplofizike [Group methods in thermophysics]. Kiev: Nauk. Dumka, 2003, 484 p. (rus.).

Chapter 6

ENERGY DISSIPATION AND HEAT TRANSFER IN THE WORKING AREA OF A RPA

It is known that the fluid flow through the RPA working zone is accompanied by its heating. Often this phenomenon is considered undesirable, since in some cases an increase in the temperature of a liquid can cause a change in its physical characteristics, as is the case, for example, when protein-containing solutions are processed in an apparatus. In addition, a significant overheating of the nodes and parts of the apparatus can lead to its failure. It follows from this that when designing apparatuses of this type and choosing the modes of their operation, this phenomenon must be taken into account.

Liquid heating in RPA is a consequence of the dissipation of the mechanical energy of the flow, i.e. conversion of mechanical energy into heat energy. A number of scientific publications have been devoted to the study of this question in relation to cylindrical RPA, of which the works [6.1, 6.2] should be noted. In these works, when calculating the degree of fluid heating in the inter-cylinder gaps, where the energy dissipation proceeds most intensively, the assumption of the linearity of distribution function of the tangential velocity in the gap was used. In this case, the space of the apparatus in which dissipative phenomena were considered was actually limited by the gaps. The theoretical results obtained in [6.1, 6.2] turned out to be generally close to the results of experimental studies, although it is obvious that the picture of the phenomenon under study would be more complete when considering the dissipation of mechanical energy in the entire RPA working space, including both gaps and radial slots in rotors and stators of the apparatus.

The study of fluid heating in the RPA working area is carried out on the basis of a numerical solution of the energy equation (4.10) with boundary conditions (4.11)-(4.18), chapter 4. Recall that the distribution function of the liquid temperature over the working volume of the RPA is periodic in the angular coordinate, same as velocity and pressure fields. The temperature of the liquid at the entrance to the working area is assumed to be set, and at the exit from the working area, the radial derivative from temperature is taken equal to zero. A detailed statement of this problem and a method for solving it are presented in [6.3].

Assuming that the physical properties of the liquid are weakly dependent on temperature, the velocity field in the working area of the RPA can be considered

known from the solution of the dynamic problem. In the case of a significant effect of temperature on the results of its solution, as is the case, for example, for flows of non-Newtonian fluids, it is necessary to simultaneously solve the entire system of equations (4.7)-(4.10), using the method of successive approximations.

6.1. The effect of the viscosity of processed medium on the level of heat dissipation in the working volume and on the degree of heating of processed medium

Calculations of the fields of excess temperature ($T - T_0$) for the laminar flow of Newtonian fluids with different viscosity coefficients were performed for the case $\Delta p = 0$, provided that the surfaces of the working elements are thermally insulated and that for all considered fluids $C_p = 1600$ J/(kg·K); $\lambda = 0.11$ W/(m·K) and $\rho = 1000$ kg/m^3. For a fluid with a viscosity $\mu = 1.0$ Pa·s, the results of calculating the temperature field are presented in figure 6.1.

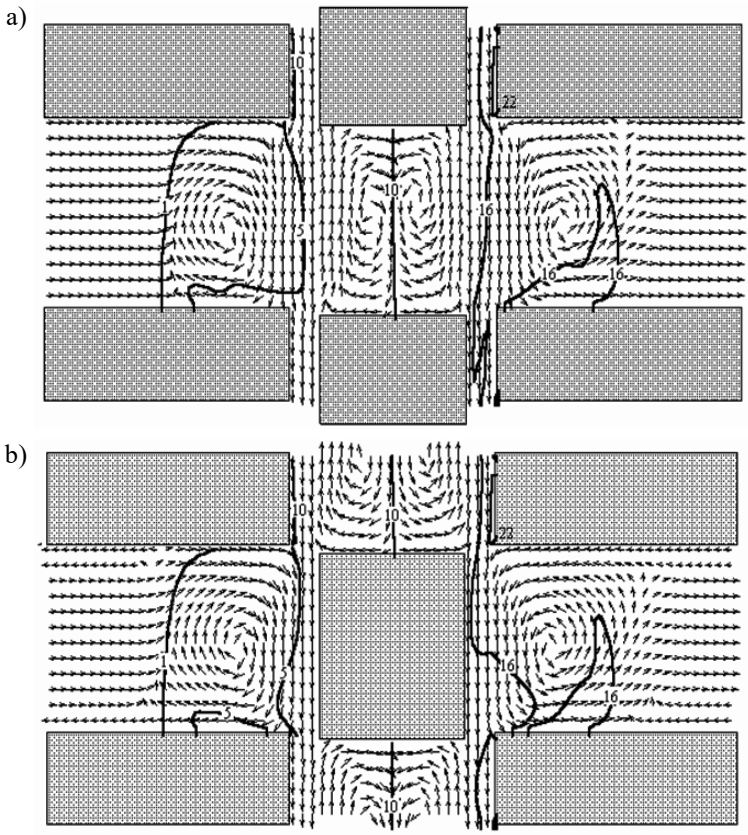

FIGURE 6.1. The field of excess temperature (°C) in the RPA working area during fluid flow with a viscosity coefficient $\mu = 1.0$ Pa·s at $\Delta p = 0$: a) $\tau/\Delta\tau = 0$; b) $\tau/\Delta\tau = 1/2$.

The calculation results showed that in the working space of the RPA, the liquid is most significantly heated in the gaps between the rotor and the stators, where, due to the high values of the flow strain rate, energy dissipation proceeds most intensively. So, for example, for the case $\mu = 0.3$ Pa·s, near the internal edges of the slots of the external stator (from the gaps), the density of heat sources due to dissipation reaches values exceeding $q_v = 6 \cdot 10^9$ W/m^3. Here, the maximum overheating of the processed fluid is also observed.

The distribution of the density of sources q_v over the space of the working zone, obtained for the case $\mu = 0.1$ Pa·s, is presented in figure 6.2. The figure shows that the areas of the most intense heat generation are located near the cylindrical surfaces of the RPA working elements. In the rest of the space, the values of the source densities q_v are much lower.

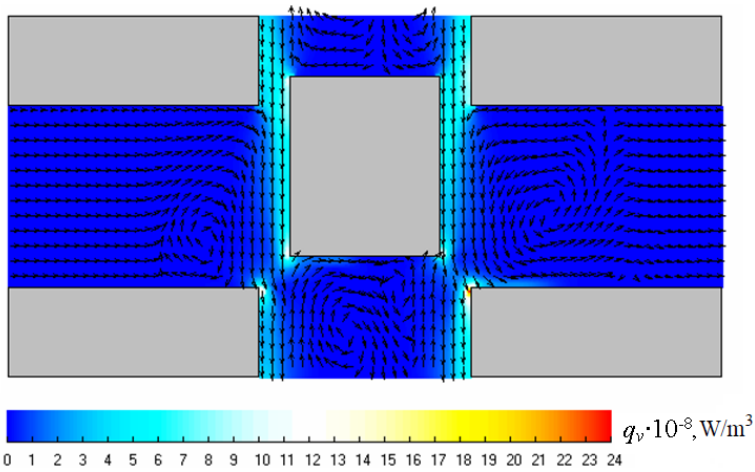

FIGURE 6.2. The distribution of the density of heat generation sources over the space of the RPA working area for the case $\mu = 0.1$ Pa·s, $\Delta p = 0$.

As was shown in chapter 5, the fields of velocity, pressure, as well as the flow rate of the liquid through the apparatus, periodically change in time. Moreover, over one period, their values can change quite significantly. At the same time, the temperature field, that has a higher inertia in comparison with the velocity and pressure fields, changes slightly over one period. This is explained by a slight change in one period of the total power of heat generation sources Q in the stream, the value of which can be found by integrating value q_v over the volume of the working space. Another reason for the comparative stability over time of the temperature field is the high values of the Prandtl numbers for fluids under consideration.

The source term in the energy equation is represented as the product of viscosity μ and the dissipative function, which depends on the structure of the fluid flow. It is

obvious that with increasing fluid viscosity μ, the power of heat generation sources should increase. At the same time, speaking about the dependence of the degree of dissipation of mechanical energy in the flow on viscosity, attention should also be paid to the dependence on viscosity of the dissipative function itself. Characteristic in this sense is the dependence on viscosity of a dimensionless quantity $F = Q / \left(\mu \omega_0^2 r_0^3 \right)$ (fig. 6.3).

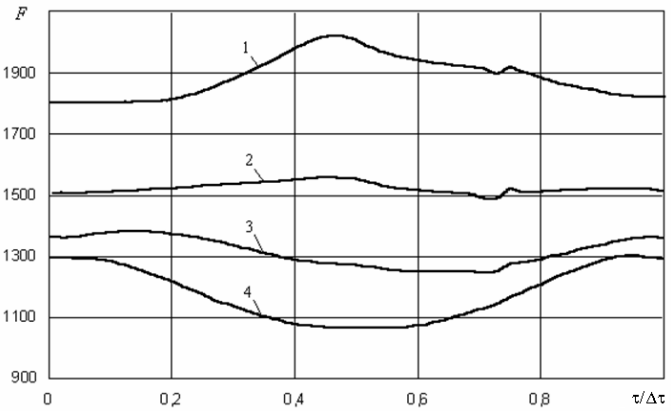

FIGURE 6.3. The dependence of the dimensionless total heat generation power in the apparatus volume on time at $\Delta p = 0$: 1 – $\mu = 0.01$ Pa·s; 2 – $\mu = 0.03$ Pa·s; 3 – $\mu = 0.1$ Pa·s; 4 – $\mu = 1.0$ Pa·s.

As can be seen from the figure, with an increase in the viscosity of the liquid, the dimensionless total power of the sources of dissipative of heat generation F decreases. This is due to a decrease in the strain rate of flow S with increasing viscosity μ. In addition, as the viscosity changes, the nature of the dependence F on time also changes. If, at a low viscosity of the liquid, the maximum of the total heat generation power occur at the moment of mutual overlapping of the slots of the rotor and stators, then at high values of μ minimum of this value corresponds to this moment. The maximum value F in this case corresponds to the moment of coincidence of the slots of the rotor and stators, at which the effective length of all the gaps is maximum. Dependence from viscosity of the dimensionless powers of heat generation sources F_{ev} averaged over the period $\Delta\tau$, is shown in figure 6.4. It can be seen from this figure that with an increase μ, the values F_{ev} monotonically decrease.

As shown above, an increase in viscosity leads to an increase in the total heat generation Q due to energy dissipation in the working zone. On the other hand, with an increase in viscosity, the total hydraulic resistance to friction in the entire volume of the working zone increases, this leads to a decrease in the radial fluid flow G_r through the apparatus. Therefore, it is quite natural that the average liquid

temperature difference between the inlet and outlet sections of the working zone, which is determined from the expression, $\Delta T = \overline{T}_{out} - T_0 = Q / \left(G_r C_p \rho \right)$, will increase with increasing viscosity of the liquid. It will be possible to answer the question of how intensely the value of μ affects a given temperature difference by considering the dependence on the viscosity of the dimensionless temperature difference $\Delta \vartheta = \Delta T \cdot C_p \rho / \left(\omega_0 \mu \right) = Q / \left(G_r \omega_0 \mu \right)$.

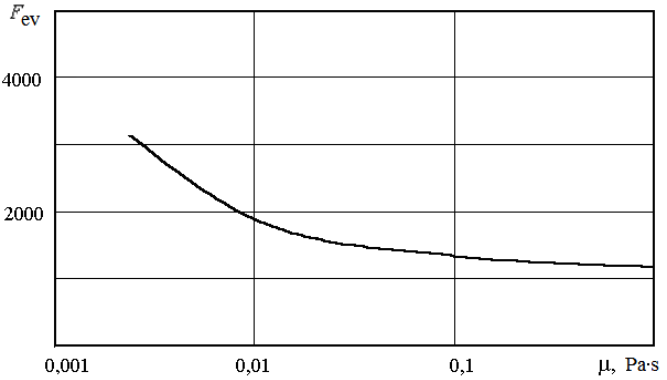

FIGURE 6.4. Dependence on viscosity of the time-average dimensionless total heat generation power in the apparatus volume at $\Delta p = 0$.

For liquids with the same values of heat capacities and densities, this dependence is presented in (fig. 6.5).

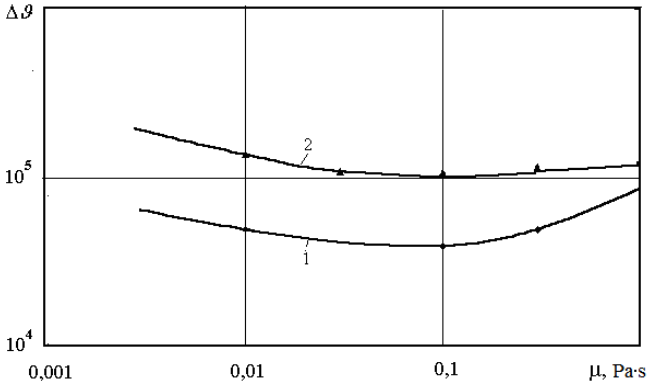

FIGURE 6.5. Dependence on viscosity of dimensionless temperature difference in RPA working area: 1 – $\Delta \vartheta$; 2 – $\Delta \vartheta_{\max}$.

As can be seen from the figure 6.5, the dependence $\Delta \vartheta$ on viscosity is complex. With an increase in μ, the value $\Delta \vartheta$ in the viscosity range 0.004 Pa·s < μ < 0.065

Pa·s initially decreases, and then begins to increase. The dimensionless temperature $\Delta\vartheta_{\max}$, constructed from the values of the maximum temperature $T_{\max}$ in the working zone, changes similarly with viscosity. The maximum temperature of the fluid, as can be seen from figure 6.1, it appears at the leading edges of the input section of the slot of the external stator.

The effect of viscosity on the temperature regime in the working area of the rotary pulsation apparatus is also reflected in table 6.1.

TABLE 6.1. The effect of the viscosity of processed fluid on time-averaged dynamic and temperature characteristics of its flow in RPA at $\Delta p = 0$.

μ, Pa·s	$\overline{V}_r$, m/s	$\overline{G}_r\ 10^3$ m^3/s	$\overline{Q}$, W	$\Delta\overline{T}$, °C
0.01	0.3631	0.9869	151.67	0.097
0.1	0.3233	0.8787	1075.69	0.74
1.0	0.1310	0.3560	9426.58	16.5

The table 6.1 shows that with fluid viscosities above 1.0 Pa·s, heating of the fluid being processed due to dissipation can be quite significant, which necessitates the creation of a special cooling system of the apparatus.

If in one pass through the working space of the RPA the heterogeneous medium has not reached the required quality indicators for the size of the dispersed particles, it is again sent to the loading capacity of the apparatus and processed again. In this regime, the medium can be processed multiple times. This not only achieves a reduction in the size of the dispersed particles, but also ensures uniformity of the emulsion by the dispersed composition. At the same time, with multiple processing of the medium, its temperature increases.

The change in the mass-average temperature of the liquid over time can be obtained from the solution of the heat balance equation

$$\left(C_p\rho B + C_{con}m_{con}\right)\frac{\partial T}{\partial \tau} = Q - \alpha\left(T - T_\infty\right)f \qquad (6.1)$$

in which B is the total volume of liquid loaded into the apparatus, C_{con}, m_{con} is the specific heat of the material and the mass of the RPA construction, the outer surface area of which is f, α is the heat transfer coefficient from the outer surface of the apparatus to the external environment, which temperature is T_∞. This heat balance equation is made under the assumption that the temperature of the outer walls of the RPA case differs little from the temperature of the liquid.

6.2. Statement and results of solving of conjugate heat transfer problem in the RPA working area

In the previous subsection, the heat transfer problem in the RPA working space was considered under the condition that the surfaces of the cylindrical working elements are thermally insulated. Such a statement of the problem allows us to determine the maximum possible temperature values of the medium being treated, since heat removal outside the flow region is not provided in this statement. Under real conditions of RPA operation, both conductive heat transfers through the working elements and heat removal from the walls of the apparatus body to the surrounding space take place.

A more accurate estimate of the temperature values of the medium being treated, as well as the temperature of the working elements, can be obtained by solving the heat transfer problem as conjugate. Conjugate statement of the problem involves solving the heat transfer equation for a liquid together with the heat conductivity equation for the elements of the working bodies, as well as setting the conditions of heat transfer to the surrounding space. In this case, the previously considered system of equations (4.7)-(4.10), which describes the dynamics of the liquid and heat transfer in the working space of the RPA, is supplemented by the heat conductivity equations for fixed stators

$$\frac{\partial T}{\partial \tau} = a_{con}\left[\frac{1}{r}\frac{\partial}{\partial r}\left(r\frac{\partial T}{\partial r}\right)+\frac{1}{r^2}\frac{\partial^2 T}{\partial \theta^2}\right] \tag{6.2}$$

and rotating rotor

$$\frac{\partial T}{\partial \tau}+\omega_0\frac{\partial T}{\partial \theta} = a_{con}\left[\frac{1}{r}\frac{\partial}{\partial r}\left(r\frac{\partial T}{\partial r}\right)+\frac{1}{r^2}\frac{\partial^2 T}{\partial \theta^2}\right] \tag{6.3}$$

where a_{con} is the thermal diffusivity coefficient of RPA construction elements.

In this case, the temperature boundary conditions on the surfaces of the working elements are modified. To solve the conjugate problem, instead of thermal insulation conditions on the surfaces of the rotor and stators, conditions of the fourth kind are set:

$$-\lambda_{con}\left.\frac{\partial T(r,\theta)}{\partial n}\right|_{n-0} = -\lambda_f\left.\frac{\partial T(r,\theta)}{\partial n}\right|_{n+0}; \quad T\big|_{n-0} = T\big|_{n+0}$$

On the outer surface of the RPA case wall, conditions of the third kind are set, which provide for heat transfer by natural convection to the surrounding space:

$$-\lambda_{con}\left.\frac{\partial T}{\partial r}\right|_{r=r_{con}} = \alpha\left(T-T_\infty\right)$$

where: α – the heat transfer coefficient calculated by the well-known similarity equation for natural convection on a cylindrical surface [6.4, 6.5]; T_∞ – the temperature of the external environment.

Equations (6.2), (6.3), as well as boundary conditions, are dimensionless and solved numerically together with the energy equation for a liquid. The conjugation conditions on the surfaces of the working elements are also written in the form of finite differences.

It is convenient to trace the features of the results of solving the heat transfer problem in the conjugate formulation by comparing them with the results of solving a similar problem without taking into account the conjugation conditions, i.e. under conditions of adiabaticity of the surfaces of the working elements. In contrast to the solutions considered earlier in this case, the computational domain additionally includes a part of the flow region in front of the internal stator, the flow region between the external stator and the RPA case wall and the case wall itself.

The results of solving the heat transfer problem without taking into account the heat conductivity of the working elements are presented in figure 6.6, and the results of solving the problem in the conjugate formulation are shown in figure 6.7. A fluid flow is considered with a viscosity coefficient $\mu = 0.1$ Pa·s at a differential pressure $\Delta p = +10$ kPa between the input and output sections of the working zone.

Since when solving the conjugate problem, heat transfer from the outer surface of the RPA case to the environment is taken into account, the statement of the problem involves setting its temperature. In this case, it is assumed that this temperature is 5°C lower than the temperature of the liquid at the entrance to the working area. In addition, it is necessary to set the thermophysical properties of the material of the working elements and RPA case. In this case, it is assumed that stainless steel is used as the material.

Comparison of the results presented in figure 6.6 and figure 6.7, shows that in this case under consideration, taking into account the heat conductivity of the working elements and the RPA case wall does not significantly affect the results of calculating the temperature field of the liquid. The increase in the mass average temperature of the liquid due to energy dissipation turns out to be approximately the same in both cases (0.51°C).

In both versions of the calculation, the maximum excess temperature is observed in the external gap near the flow inlet into the slot of the external stator, where the maximum density of heat sources occurs. Its values are $\Delta T_{\max} = 1.7$°C for solving the conjugate problem, and $\Delta T_{\max} = 1.9$°C under the condition of thermal insulation of the surfaces of the working elements. It follows that when solving the problem in the conjugate setting, the maximum values of the flow temperature decrease, which is a consequence of taking into account the conductive heat transfer through the

working bodies, as well as taking into account the heat transfer to the external space. Since the excess temperature of the outer wall of the casing is 0.2°C (fig. 6.7), the temperature difference between the outer surface of the RPA casing and the surrounding space is only 5.2°C. In this case, the heat transfer coefficient by natural convection from the outer surface of the casing to the air is α = 3.8 W/(m^2·K), and the heat flow density from the casing surface is q = 20.9 W/m^2.

A characteristic feature of temperature fields obtained from solutions of the conjugate problem is that the isotherms around the surfaces of the working elements suffer a significant kink. This kink is due to a significant difference values of the heat conductivity coefficients of the substance being processed, for which the accepted value λ_f is 0.11 W/(m·K), and of the wall material, for which λ_{con} = 18.0 W/(m·K).

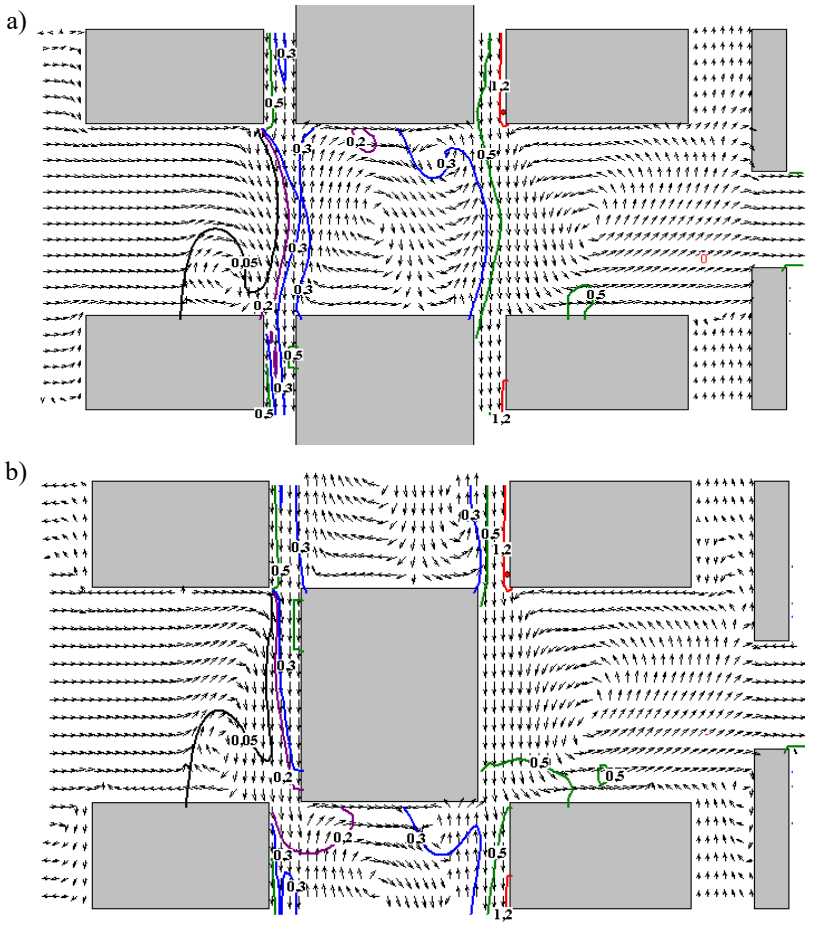

FIGURE 6.6. The temperature field in the working area of the RPA during a fluid flow with viscosity μ = 0.1 Pa·s at Δp = 10 kPa (the surfaces of the working elements are thermally insulated): a) $\tau/\Delta\tau = 0$; b) $\tau/\Delta\tau = 1/2$.

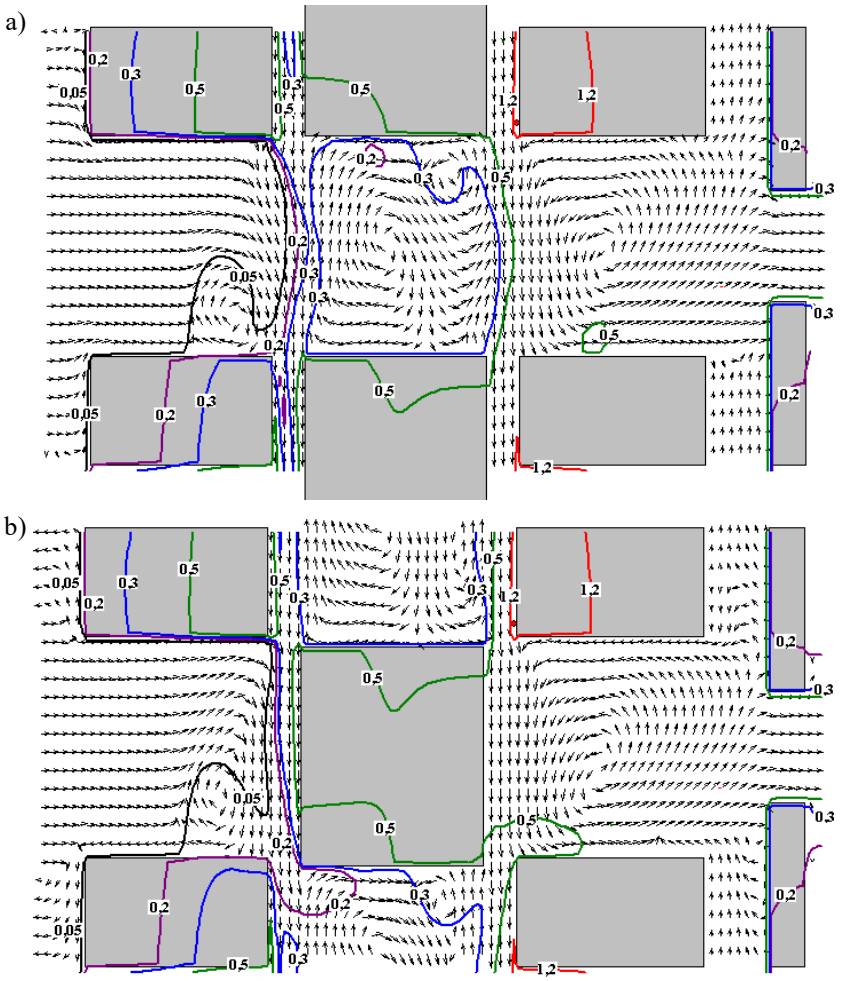

FIGURE 6.7. The temperature field in the RPA working area during a fluid flow with viscosity $\mu = 0.1$ Pa·s at $\Delta p = 10$ kPa (conjugate setting): a) $\tau/\Delta\tau = 0$; b) $\tau/\Delta\tau = 1/2$.

More significantly, taking into account the mutual influence of heat transfer processes in a liquid and a solid affects the calculation of the temperature state of the RPA working zone during the flow of a liquid with a higher viscosity. In figures 6.8, 6.9 present the results of solving heat transfer problems in conjugate and non-conjugate formulations for the case $\mu = 1.0$ Pa·s. The remaining parameters of the process under consideration remain the same as in the case considered earlier. Since the mass-average overheating of a liquid with a viscosity of $\mu = 1.0$ Pa·s is already about 10°C, the temperature difference between the wall of the RPA case and the environment will be 15°C. As a result of this, heat transfer from the surface of the casing has a more significant effect on the temperature state in the working area. At the same time, as can be seen from a comparison of figures 6.8 and 6.9, this effect is

expressed mainly in a decrease in the temperature of the liquid in the slot of the external stator, as well as in the area located near the surface of the casing.

At the same time, the maximum excess temperature of the liquid observed in the same part of the working space as in the case considered earlier decreases due to taking into account the conjugated boundary conditions from 20.3°C to 18.8°C. At the same time, taking into account the heat transfer to the surrounding space from the surface of the casing leads to a decrease in the temperature of the liquid at the outlet of the working area from only 9.95°C to 9.75°C. The heat transfer coefficient from the outer surface of the casing is $\alpha = 4.89$ W/(m^2·K), and the heat flux density is $q = 73$ W/m^2.

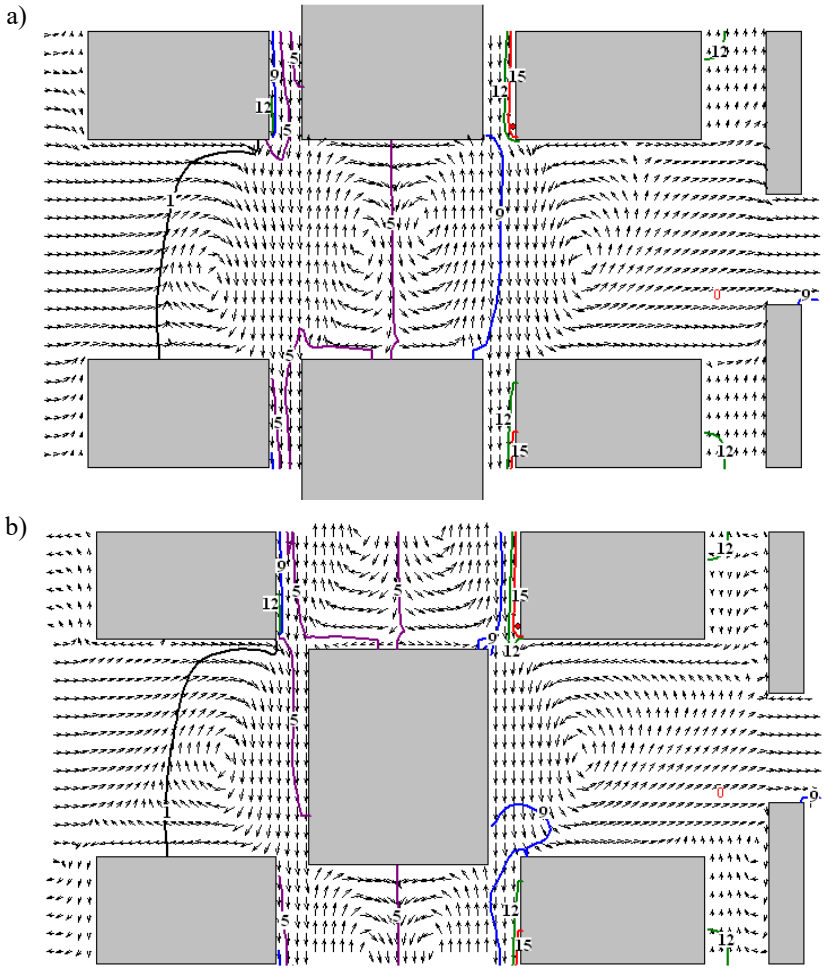

FIGURE 6.8. The temperature field in the working area of the RPA during a fluid flow with a viscosity of $\mu = 1.0$ Pa·s at $\Delta p = 10$ kPa (the surfaces of the working elements are thermally insulated): a) $\tau/\Delta\tau = 0$; b) $\tau/\Delta\tau = 1/2$.

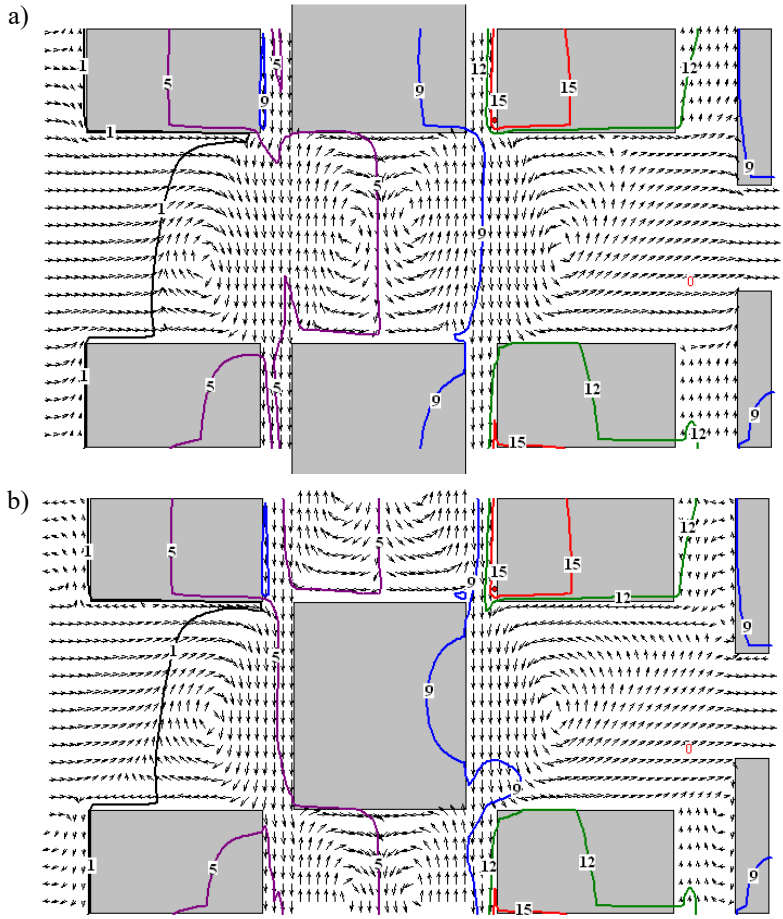

FIGURE 6.9. The temperature field in the RPA working area during a fluid flow with a viscosity $\mu = 1.0$ Pa·s at $\Delta p = 10$ kPa (conjugate setting): a) $\tau/\Delta\tau = 0$; b) $\tau/\Delta\tau = 1/2$.

Analyzing the considered results of solving heat transfer problems in conjugate and non-conjugate formulations, it should be noted that the heat conductivity of the working elements in the tangential direction as a whole does not significantly affect the calculation of the temperature field of the fluid flow. This is explained by the low values of the heat transfer potentials in the tangential direction due to the boundary conditions of the problem periodic in the angle θ.

6.3. The results of solving the conjugate heat transfer problem in the RPA working area at turbulent flow of the fluid

The above results of solving the conjugate heat transfer problem in the RPA working area relate to the case of laminar fluid flow. Let us further consider the results of solving the conjugate heat transfer problem in the RPA working volume

for turbulent water flow using the RNG turbulence model. The results of calculating the velocity field, pressures, and other characteristics of the turbulent flow for this case are presented in chapter 5 in figures 5.29-5.31.

The temperature field in the RPA working zone for two characteristic time instants is shown in figure 6.10.

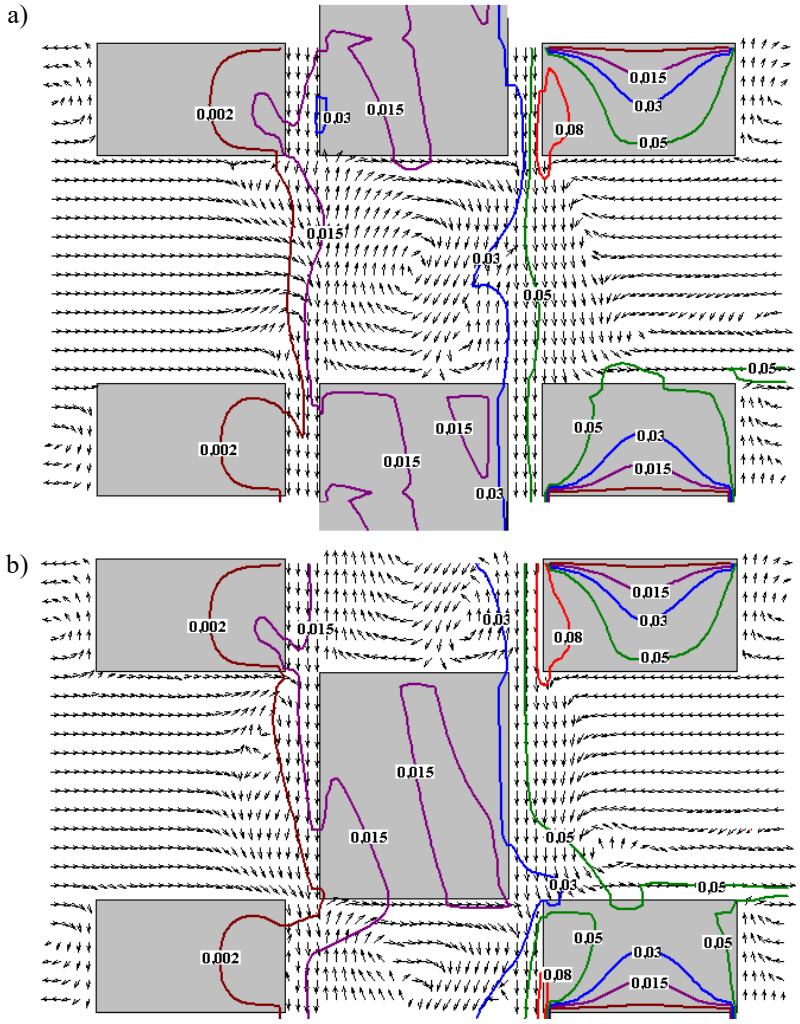

FIGURE 6.10. The temperature field in the RPA working zone at turbulent water flow ($\mu = 0.001$ Pa·s; $\Delta p = 10^4$ Pa): a) $\tau/\Delta\tau = 0$; b) $\tau/\Delta\tau = 1/2$.

As can be seen from the figures, the maximum temperatures in the flow (~0.1°C) are observed near the inner cylindrical surfaces of the outer stator, where the dissipation of mechanical energy is maximum. Near the walls of the working

elements the isotherm, as in the case of a laminar flow, have a kink. However, in the case of a turbulent flow, it is less pronounced than in the case of a laminar flow.

Comparing the results of solving heat transfer problems at the laminar and turbulent regimes of the fluid flow, it should be noted that the degree of liquid overheating at the turbulent regime is higher than at the laminar one. This is due both to higher values of the coefficients of effective viscosity in a turbulent flow and to higher values of flow strain rates, which generally leads to an increase in the total dissipative heat release power Q in the RPA working zone. In figure 6.11 shows the time dependences of the Q values obtained from the considered solution of the problem for a turbulent water flow (curve 1).

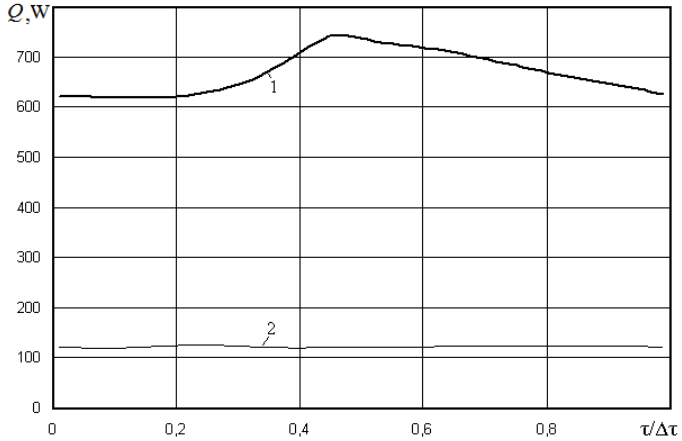

FIGURE 6.11. Comparison of values of the total dissipative heat releases during turbulent water flow (1) and laminar flow of the fluid with a viscosity coefficient $\mu = 0.005$ Pa·s (2).

As can be seen from the figure, at $\tau/\Delta\tau \approx 0.45$ this value reaches a maximum, which is 750 Watts. For comparison, in figure 6.11 also shows the dependence $Q(\tau)$, obtained under the assumption of a laminar regime of fluid flow with a viscosity coefficient $\mu = 0.005$ Pa·s (curve 2). From a comparison of these dependences, it follows that at the turbulent regime, the total power of the dissipative heat sources is 6 times higher than the power calculated using the laminar flow model.

6.4. Features of heat transfer in the working zone of RPA when processing non-Newtonian fluids

Previously, the dynamic and temperature characteristics of the flows of model Newtonian fluids in the RPA working zone were considered. It was assumed that their physical properties are constant. We now consider the case of the flow of a non-Newtonian fluid, for which the dependence of the effective viscosity on the strain rate has the form:

$$\mu_{ef} = \left(\frac{\sigma_0}{S} + A \cdot S^{k-1} \right) \tag{6.4}$$

This dependence can be considered as a special case of the generalized rheological model (4.6), chapter 4, if we accept $n = 1$; $m = 1/k$; $\mu = A^m$. As showed by the results of experimental studies presented in [6.6, 6.7], dependence (6.4) satisfactorily describes the rheological characteristics of soybean paste. The values included in expression (6.4) obtained for different concentrations C of water in soybean paste at a temperature of 40°C are given in table 6.2. The dependences μ_{ef} on the strain rate S for various water concentrations are presented in figure 6.12.

TABLE 6.2. The values of parameters σ_0, A, k of the rheological model (6.4) depending on the concentration of water in soybean paste at a temperature of 40°C.

Concentration of water C	σ_0, Pa	A, Pa·s^k	k
0	1753	1507	0.361
0.3	1649	1389	0.312
0.6	883	560	0.381

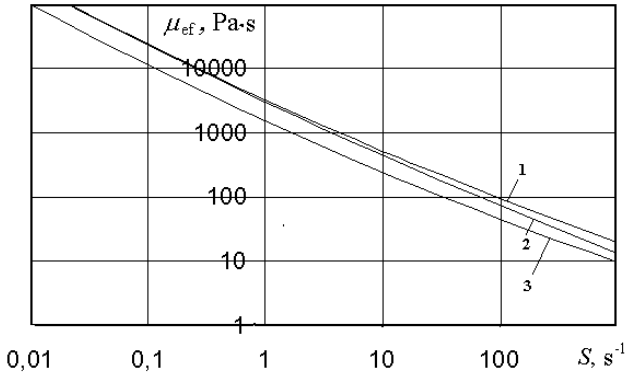

FIGURE 6.12. Dependences of value μ_{eff} on the strain rate S for various concentrations of water in soybean paste: 1 – pure soybean; 2 – water content $C = 0.3$; 3 – water content $C = 0.6$.

For the case of a non-Newtonian fluid flow, the algorithm for numerically solving of the flow and heat transfer problem presented in chapter 4 is somewhat modified. A characteristic feature of the numerical simulation method used to solve the problem in the case of a rheological medium is the need to use the iteration method. So for the current time step, the law of the distribution of the strain rate intensity S is used obtained for the previous time step. Then, for the current time

step, this value is refined. In addition, local values of the coefficients of the rheological model are refined depending on the distribution of the temperature of the fluid at a given time [6.8].

Consider the results of solving the problems of dynamics and heat transfer for flows of diluted and concentrated soybean paste through the working zone of RPA at a differential pressure between input and output sections Δp = +50 kPa. The main feature of the flows of non-Newtonian liquids is the strong dependence of the local value of the effective viscosity μ_{ef} on the strain rate of the flow S at a given point of the flow region. The distribution of value μ_{ef} (Pa·s) in the RPA working zone during the flow of a solution of soybean paste in water (water concentration C = 0.6) is shown in figure 6.13. As can be seen from this figure, in the slot of the rotor, as well as in the gaps between the working elements, i.e. in those areas of the working zone where the flow strain rates S are maximum, values μ_{ef} are minimal. The lowest values of the flow strain rate are observed at the entrance to the slot of the internal stator and at the exit from the slot of the external stator. The directions of the velocity vectors in these regions are almost radial. Therefore, in these areas, the values μ_{ef} reach maximum values of 836 Pa·s. In the gaps between the working elements, where the flow strain rate is maximum, values μ_{ef} are reduced to 0.287 Pa·s.

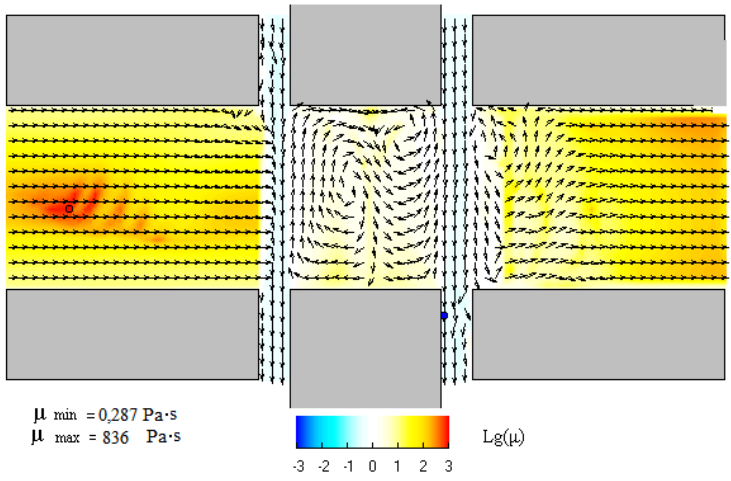

FIGURE 6.13. The distribution of value μ_{ef} (Pa·s) in the flow field of a solution of soybean paste in water (water concentration C = 0.6).

As follows from the dependence (6.4) and table 6.2, with a decrease in the concentration of water in soybean paste, μ_{ef} values generally increase. The consequence of this is a significant decrease in the mass-average radial flow velocity

of the paste V_r with a decrease in its water concentration. The dependences of these values on time for cases of different concentrations of water in soybean paste are presented in figure 6.14. As can be seen from this figure, the character of the change in time of the average by sectional velocity of the radial flow of soybean paste with a water content of $C = 0.6$ is similar to that obtained for Newtonian fluids (fig. 5.2). With a decrease in the percentage of water this character changes somewhat. At $\tau = 0.65\Delta\tau$, the functions $V_r(\tau)$ have an additional maximum. In addition, with a decrease in water concentration, the absolute values of V_r significantly decrease. This is also seen from the graph of the dependence of the time-averaged value $\overline{V_r}$ on the volume concentration of water C in soybean paste (fig. 6.15).

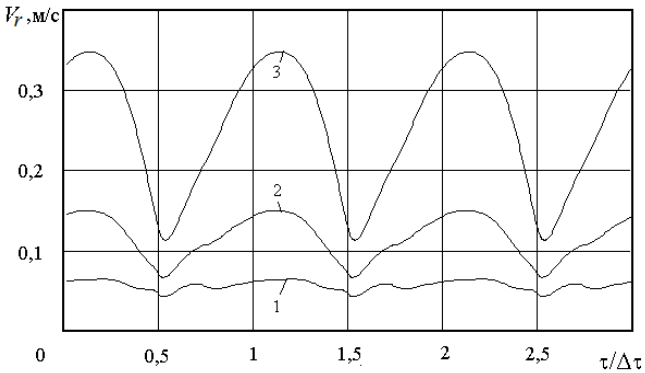

FIGURE 6.14. Change in time of the average velocity flow of soybean paste in the inlet section of the internal stator slot at $\Delta p = +50$ kPa: 1 – pure soybean ($C = 0$); 2 – $C = 0.3$; 3 – $C = 0.6$.

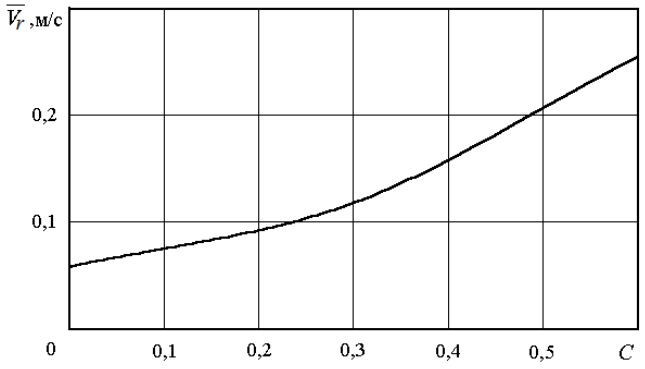

FIGURE 6.15. Dependence on water concentration C the mass-average velocity flow of soybean paste in the inlet section of an internal stator slot at $\Delta p = +50$ kPa.

The high viscosity of soybean paste and strong dependence of the parameter μ_{eff} in the rheological law on the flow strain rate, are the main factors determining the

character of heat transfer in RPA. The results of calculating the temperature field in the RPA working zone for two characteristic time points obtained for the case of the water content in soybean paste $C = 0.6$ are presented in figure 6.16 (the problem is solved as non-conjugate). As can be seen from this figure, the heating of the paste proceeds most intensively near the inner surface of the outer stator, adjacent to the left inner edge of its slot. In this area, the excess temperature reaches a maximum value of 10°C. The excess temperature of the liquid at the exit from the working zone is 8°C, and time-averaged total power of heat sources is $\overline{Q} = 9620$ W.

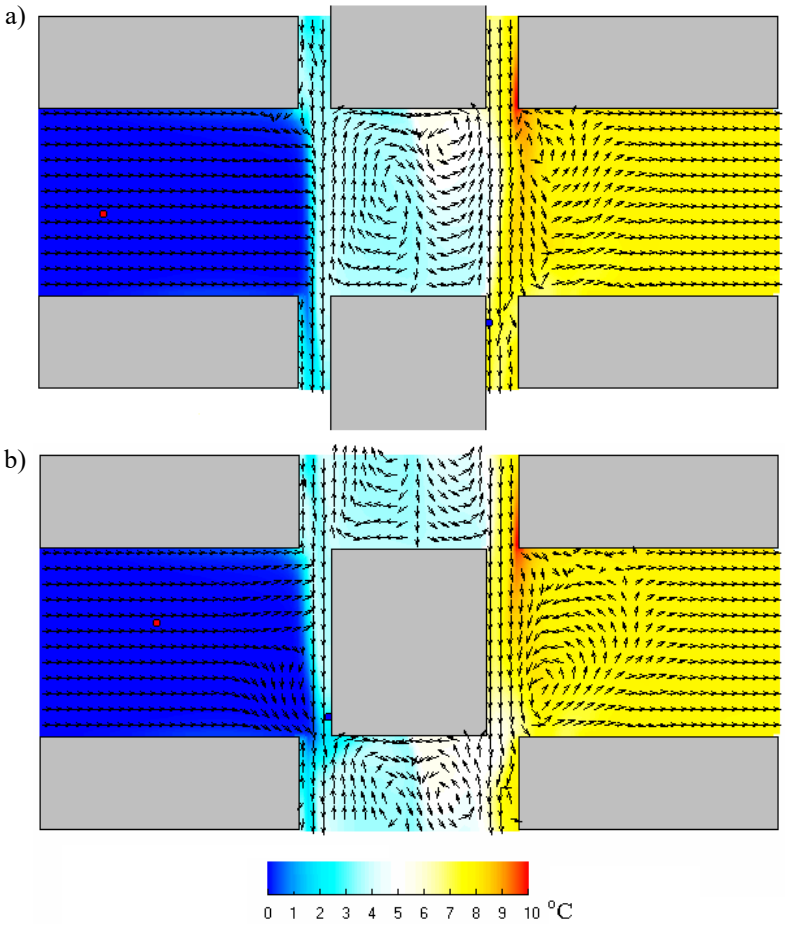

FIGURE 6.16. The excess temperature field in the soybean paste stream with a water concentration of $C = 0.6$ at $\Delta p = +50$ kPa: a) $\tau/\Delta\tau = 0$; b) $\tau/\Delta\tau = 1/2$.

With a decrease in the concentration of water in soybean paste, the effective viscosity coefficients generally increase. Due to this, at a fixed value of Δp, the mass-average fluid velocity in the radial direction decreases (fig. 6.15). In this case,

the values of flow deformation rates S also decrease. In this connection, with a decrease in the concentration of water in the paste, the average total heat release in the flow $\overline{Q}$ generally increases slightly. Their appreciable growth begins at water concentrations below $C = 0.3$ (fig. 6.17). However, due to a significant decrease in the mass-average velocity $\overline{V}_r$, the degree of overheating of soybean paste in the working zone of RPA increases with decreasing C (fig. 6.18). So, for example, in the case of $C = 0.3$, the average total power of heat sources in the working zone increases slightly compared to the case of $C = 0.6$ (up to $\overline{Q} = 9900$ W). However, at the same time, the flowrate of the processed fluid is almost 2 times reduced. As a result of this, its overheating in the working zone increases to $\Delta T = 19$°C.

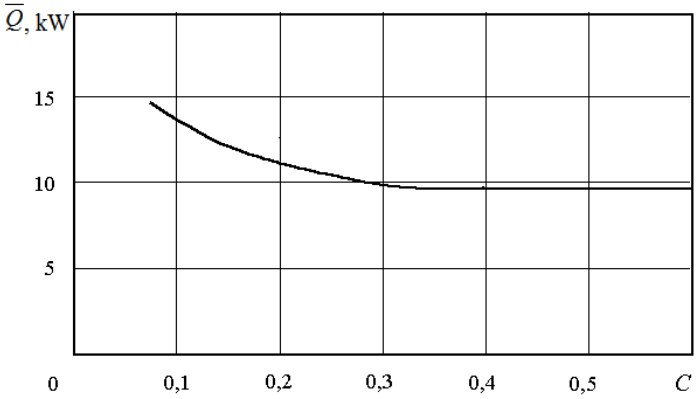

FIGURE 6.17. Dependence of the total heat release in the RPA working zone on the water concentration in soybean paste (Δp = +50 kPa).

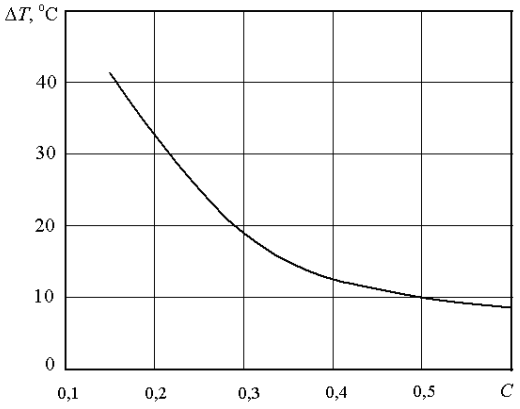

FIGURE 6.18. Dependence of the degree of overheating of water-containing soybean paste processed in RPA on the concentration of water (Δp = +50 kPa).

Thus, with an increase in the concentration of dry matters in soybean paste, its overheating in the RPA working zone can be quite significant. As a result of overheating, its quality characteristics may change. In addition, with a significant increase in the temperature of the RPA working elements, due to temperature deformations, the width of the gaps between their cylindrical surfaces can decrease, which can cause damage to the working elements.

From submitted results of the numerical simulation of the dissipation of mechanical energy in the working volume of the RPA, it follows that:

- the maximum heat release in the working zone of the RPA occurs in the area of the external gap, as well as at the edge surface between the external gap and the entrance to the slot of the external stator. In these areas, there is a maximum overheating of the processed substance;
- the total power of the sources of dissipative heat release increases with increasing viscosity of the processed fluid, however, this increase is not proportional to the increase in viscosity;
- in the turbulent regime of flow of fluids with low viscosity, the total power of heat sources is significantly higher than in cases of laminar flow of fluids with the same viscosity;
- on the example of solving the problem of the flow of soybean paste diluted with water, data were obtained on the effect of water concentration on the mass-average radial velocity, heat release levels and the degree of paste overheating. Since soya paste belongs to non-Newtonian fluids, a characteristic feature of the process under study is a change by 3...4 orders of values of the effective viscosity coefficients of the fluid in the studied flow region. With a decrease in the percentage of water in the paste, the degree of its overheating in the RPA working zone significantly increases. The consequence of this can be both deterioration in the quality characteristics of the processed product, and damage to the working elements of the apparatus due to their overheating. Therefore, when used RPA in the considered regimes, it is necessary to provide conditions for the efficient removal of excess heat releases from the working zone of the apparatus.

6.5. Numerical simulation of the mixing process of highly viscous fluids in a rotary pulsation apparatus

Rotary pulsation apparatus are widely used not only as dispersants, but also as devices for creating homogeneous mixtures of highly viscous liquids. An example of the successful use of RPA in the food industry as a mixer is the sucrose hydrolysis technology to produce glucose and fructose. As experience shows, the inclusion of a rotor-type apparatus in the sucrose hydrolysis

technological scheme leads to a significant acceleration of this process [6.9]. One of the reasons for this phenomenon is associated with the creation of conditions for intensive mixing in the rotary apparatus of the components involved in the physicochemical process under consideration. The components in this case are sugar syrup and concentrated aqueous citric acid solution. In relation to the mass of sugar syrup, the amount of acid is from one to several percent. Due to the fact that both liquids are highly viscous fluids, the creation of a homogeneous mixture from considered components in order to provide conditions for an intensive hydrolysis reaction is quite difficult. When using traditional mixing devices for this purpose, the time spent on the hydrolysis process is about two hours. Usually, an apparatus with a propeller stirrer is used as such a device [6.10]. In contrast to the mentioned devices, RPA provide rather fast and high-quality mixing of the components. This is facilitated by high-frequency pulsations of velocity, acceleration and pressure in the fluid flow flowing through the working bodies of the apparatus.

To clarify the issue of the quantitative work characteristics of the RPA as a mixing device, we consider the model problem of mass transfer of one of the components of the mixture in the flow of another component during their joint movement through the working space of this apparatus. The case of the apparatus, the working zone of which includes two stators and one rotor located between the stators, is considered. The flow of viscous fluids is assumed to be two-dimensional, laminar and is considered in a horizontal section of the apparatus perpendicular to the common axis of the cylindrical working elements.

The problem of the flow of viscous mutually mixing liquids is described by a system of differential equations of hydrodynamics and mass transfer, compiled for medium with variable density. In this regard, the indicated system will slightly differ from the system of equations (4.1)-(4.10) presented in chapter 4. In polar coordinates, the system of these equations has the form:

– continuity equation:

$$\frac{\partial \rho}{\partial \tau}+\frac{1}{r}\frac{\partial\left(\rho r v_r\right)}{\partial r}+\frac{\partial(\rho\omega)}{\partial\theta}=0 \tag{6.5}$$

– impulse conservation equations:

$$\begin{aligned}&\frac{\partial\left(\rho v_r\right)}{\partial\tau}+\frac{1}{r}\frac{\partial\left(\rho r v_r^2\right)}{\partial r}+\frac{\partial\left(\rho v_r\omega\right)}{\partial\theta}-\rho\omega^2 r=-\frac{\partial p}{\partial r}+\frac{2}{r}\frac{\partial}{\partial r}\left(r\mu\frac{\partial v_r}{\partial r}\right)-\\&-\frac{2\mu}{r}\left(\frac{\partial\omega}{\partial\theta}+\frac{v_r}{r}\right)+\frac{\partial}{\partial\theta}\left[\mu\left(\frac{1}{r^2}\frac{\partial v_r}{\partial\theta}+\frac{\partial\omega}{\partial r}\right)\right]\end{aligned} \tag{6.6}$$

$$\frac{\partial(\rho\omega)}{\partial\tau}+\frac{1}{r^2}\frac{\partial\left(\rho r^2\omega v_r\right)}{\partial r}+\frac{\partial\left(\rho\omega^2\right)}{\partial\theta}+\frac{\rho v_r\omega}{r}=-\frac{1}{r^2}\frac{\partial p}{\partial\theta}+$$
$$+\frac{2}{r^2}\frac{\partial}{\partial\theta}\left[\mu\left(\frac{\partial\omega}{\partial\theta}+\frac{v_r}{r}\right)\right]+\frac{1}{r^3}\frac{\partial}{\partial r}\left[r\mu\left(r^2\frac{\partial\omega}{\partial r}+\frac{\partial v_r}{\partial\theta}\right)\right] \quad (6.7)$$

– mass transfer equation:

$$\frac{\partial\left(\rho C_1\right)}{\partial\tau}+\frac{1}{r}\frac{\partial\left(rv_r\rho C_1\right)}{\partial r}+\frac{\partial\left(\omega\rho C_1\right)}{\partial\theta}=\frac{1}{r}\frac{\partial}{\partial r}\left(r\rho D\frac{\partial C_1}{\partial r}\right)+\frac{1}{r^2}\frac{\partial}{\partial\theta}\left(\rho D\frac{\partial C_1}{\partial\theta}\right) \quad (6.8)$$

where: ρ – the density of the mixture, C_1 – the local concentration of one of the components of the solution in the mixture, D – the coefficient of mutual diffusion of the components.

The value C_1 is set as the ratio of the mass of one of the components m_1 to the mass of the mixture m_1+m_2 concentrated in an elementary volume. Obviously, the concentration of the second component is $C_2=1-C_1$, and the density of the mixture can be obtained from the expression

$$\rho=\frac{\rho_1\rho_2}{\rho_2C_1+\rho_1\left(1-C_1\right)}$$

where ρ_1 and ρ_2 are the densities of individual solution components. Thus, $\rho=\rho(C_1)$. The coefficients $\mu=\mu(C_1)$ and $D=D(C_1)$ also depend on the local concentration values C_1. Their temperature dependencies are not taken into account in this problem.

The solution to the problem is performed in the calculation area, which includes the working space of the apparatus occupied by the stators, the rotor and the gaps between them, as well as small additional areas of space adjacent to the inner surface of the inner stator and to the outer surface of the outer stator. Since the working elements are thin cylindrical bodies with periodically repeating slots, only one periodically repeating segment with an opening angle $\Delta\theta$, including one slot and two halves of the adjacent walls separating this slot from the neighboring ones, will be considered, as before [6.11].

The boundary conditions for the dynamic problem (6.5)-(6.7) will be: the pressure difference $\Delta p=p_{in}-p_{out}$ between the input and output sections of the computational area, which are characterized by the minimum ($r_{\min}$) and maximum ($r_{\max}$) radial coordinates (in these sections the tangential velocity component is taken equal to zero); angular velocity ω_0 of rotor rotation; angle periodicity

conditions $\Delta\theta$ for all unknown quantities included in the original system of equations. The method and results of the numerical solution of the system of hydrodynamic equations (6.5)-(6.7) are presented in chapters 4 and 5.

To solve the mass transfer equation (6.8), we formulate the boundary conditions for the concentration of the first component C_1. In this case, we will assume that in the resulting mixture the mass fraction of the second component significantly prevails over the mass fraction of the first. Based on this, we will take the following expressions as a condition at the entrance to the working zone ($r = r_{\min}$):

$$\begin{aligned} &\text{at} \quad 0 < \theta < \theta^*: && C_1 = 0 \left(C_2 = 1\right) \\ &\text{at} \quad \theta^* < \theta < \theta^* + \delta\theta^*: && C_1 = 1 \left(C_2 = 0\right) \\ &\text{at} \quad \theta^* + \delta\theta^* < \theta < \Delta\theta: && C_1 = 0 \left(C_2 = 1\right) \end{aligned} \tag{6.9}$$

which means that the first component is introduced into the flow of the second component in the section on $\theta^* < \theta < \theta^* + \delta\theta^*$, θ^* is the value of the angular coordinate ($0 < \theta^* < \Delta\theta$) related to the calculation area, $\delta\theta^* << \Delta\theta$.

As can be seen from condition (6.9), it is assumed that the concentration of the first component abruptly changes from 0 to 1 in a sufficiently small site $\delta\theta^*$ of the input section of the working zone. Strictly speaking, condition (6.9) only approximately models the real picture of the process taking place in the RPA. In fact, the loading of various components into the apparatus is done through a special loading tank or through fittings located on its case. Naturally, the two-component flow on the way to the working zone of the apparatus is to some extent it turns out already mixed. The condition in the form of (6.9) will in this sense be more "stringent" than the real one. Its use will make it possible to better assess the contribution of the working elements of the apparatus to the mixing process.

At the exit from the working zone, the conditions can be formulated as:

$$\text{for } r = r_{\max}; \quad 0 < \theta < \Delta\theta: \quad \frac{\partial C_1}{\partial r} = 0 \tag{6.10}$$

As an example, we consider the process of mixing two highly viscous fluids in RPA with the following geometric characteristics: internal stator: $r_{1in} = 55.0$ mm; $r_{1out} = 58.9$ mm; rotor: $r_{2in} = 59.1$ mm; $r_{2out} = 62.9$ mm; external stator: $r_{3in} = 63.1$ mm; $r_{3out} = 67.0$ mm. While the dimensions of the calculation area are determined by the values $r_{\min} = 54.0$ mm and $r_{\max} = 68.0$ mm. Each cylindrical element has 60 slots. The rotor velocity is 48 revolutions per second. Differential pressure Δp = 50 kPa.

The solution of the model problem of mixing two highly viscous liquids is performed provided that their densities are the same: $\rho_1 = \rho_2 = 1135$ kg/m^3, and the transfer coefficients are constant: $\mu = 5.0$ Pa·s; $D = 0.63 \cdot 10^{-6}$ m^2/s.

The numerical solution of problem (6.5)-(6.8) with the indicated boundary conditions (6.9), (6.10) was performed on a difference grid with the number of steps $N = 48$ in the angular coordinate, and $M = 155$ in the radial coordinate. The radial steps of the difference grid thickened near the surfaces of the working elements, and the steps along the angular coordinate were constant: $d\theta = \Delta\theta/N$. The time step $d\tau$ was chosen so that during the interval $d\tau$ the rotor rotates by an angle $d\theta$, i.e. $d\tau = d\theta / \omega_0$.

The results of numerical simulation of the dynamics and mass transfer in RPA are considered in the time interval $0 < \tau < \Delta\tau$ ($\Delta\tau = \Delta\theta / \omega_0$), during which the rotor moves by an angle $\Delta\theta$ equal to the period. Fields of velocity and concentration obtained for the case $\theta^* = \Delta\theta / 2$; $\delta\theta^* = d\theta$, are presented in figure 6.19.

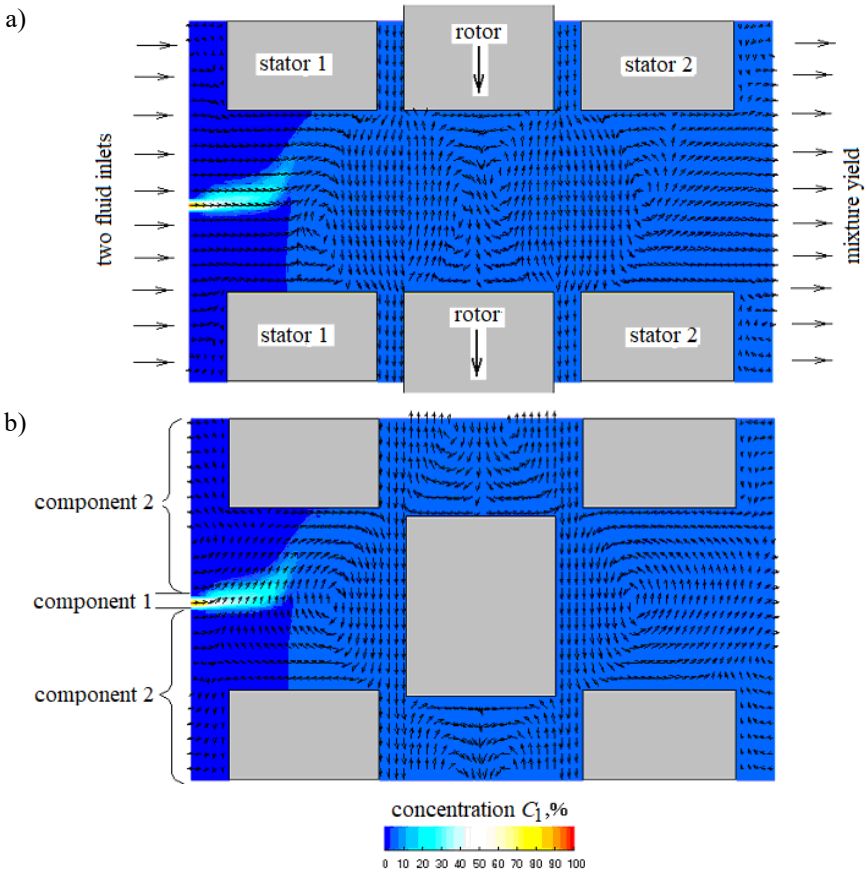

FIGURE 6.19. Fields of velocity and concentration in the working space of RPA at two positions of the rotor: a) full opening of slots ($\tau = 0$); b) total mutual overlap ($\tau = \Delta\tau/2$).

Two characteristic moments of time are considered: the moment of coincidence of the slots of the rotor and the stators (τ = 0; $\Delta\tau$) and the moment of their complete mutual overlap ($\tau = \Delta\tau/2$). As can be seen from figure 6.19, intensive mixing of the solution components begins in the second half of the slot section of the internal stator, in which the circulation zone of the flow is located, which contributes to the mixing process. Further along the path of the working space of the apparatus, the concentration of C_1 varies slightly and is within $C_1 = 0.0541...0.0545$.

The change in the radial component of the velocity v_r in the input section of the computational zone ($r = r_{\min}$) in the interval $0 < \theta < \Delta\theta$ for the above characteristic time instants is shown in figure 6.20.

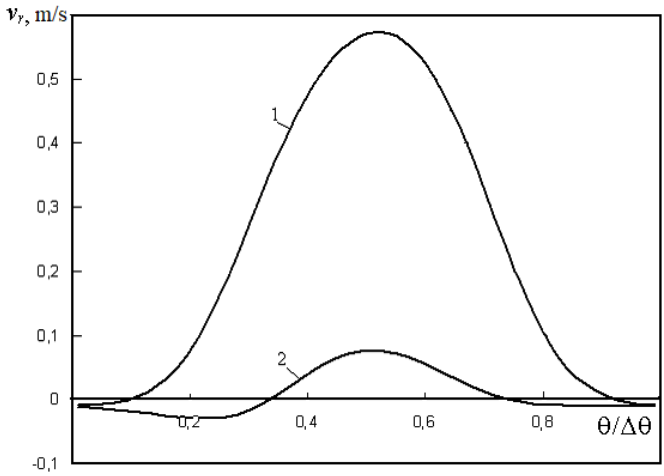

FIGURE 6.20. Changing the radial velocity v_r along the inlet section ($r = r_{min}$) of the RPA working space at two positions of the rotor: 1) complete opening of slots; 2) complete mutual overlapping of the slots.

As can be seen from the figure, the shape of the velocity profile undergoes significant changes over the specified period of time. This is due to a change in the passage section area for the fluid flow due to periodic mutual overlapping of the slots in the rotor and in the stators. In addition, the profiles of the radial velocity $v_r(\tau, r_0, \theta)$ are uneven in the angle θ. At $\theta = \Delta\theta/2$ the value of the indicated function is maximum, and in the vicinity of the points $\theta = 0$ and $\theta = \Delta\theta$ it has negative values. In the case under consideration, the region of the inlet cross section on which the radial velocity v_r is maximum coincides with the site of the feed to the solution of the first (smaller in number) component. This explains the fact that the concentration of this component in the mixture $C_1(\tau, r_1, \theta)$ at the exit from the working zone of the apparatus ($r = r_{\max}$) is greater than value

$\delta\theta^*/\Delta\theta = 1/N = 0.0208$, which characterizes part of the input section square of the working zone on which this component is introduced into the solution.

To assess the quality indicators of the operation of the rotor apparatus as a mixing device, we first determine the value mass-average concentration of the component in the mixture by the formula

$$\overline{C}_1(\tau,r) = \frac{\int_0^{\Delta\theta} v_r(\tau,r,\theta)C_1(\tau,r,\theta)r\rho\, d\theta}{\int_0^{\Delta\theta} v_r(\tau,r,\theta)r\rho\, d\theta} \tag{6.11}$$

this expresses the ratio of the mass flow rate of the first component to the mass flow rate of the entire mixture through the considered element of the apparatus. It follows from the continuity equation (6.5) that the value $\Delta G = \int_0^{\Delta\theta} v_r(\tau,r,\theta)r\rho\, d\theta$ does not depend on the radius.

At the same time, as can be seen from figure 6.20, during the period $\Delta\tau$, the flow value ΔG varies with time. The numerator of expression (6.11) varies both along the radial coordinate and in time. This is due to the fact that the mass of the first component is introduced into the working zone in time-varying portions. Since it takes a certain amount of time to advance the specified mass along the entire tract of the working zone, the flowrate of the first component in the input and output sections of the working zone, in contrast to the total mass flow ΔG, do not coincide in time. Therefore, the value $\overline{C}_1(\tau,r)$ depends both on time and on the radial coordinate. The character of its change over the period $\Delta\tau$ in the input and output sections of the working zone is shown in figure 6.21. As can be seen from the figure, the average cross-sectional concentration $\overline{C}_1(\tau,r)$ varies significantly in time in the inlet section (curve 1) and varies slightly in time in the outlet section (curve 2).

Assessing the operation of RPA as a mixing device, it is advisable to exclude the influence of time τ on its dynamic and mass transfer characteristics. For this, it is advisable, in addition to the value $\overline{C}_1(\tau,r)$ to consider the value of the concentration averaged both over the cross-section and over the time period $\Delta\tau$, namely, the expression:

$$\overline{\overline{C}}_1 = \frac{\int_0^{\Delta\tau}\int_0^{\Delta\theta} v_r(\tau,r,\theta)C_1(\tau,r,\theta)r\rho\, d\theta d\tau}{\int_0^{\Delta\tau}\int_0^{\Delta\theta} v_r(\tau,r,\theta)r\rho\, d\theta d\tau}$$

It should be noted that the value $\overline{\overline{C}}_1$ is independent of the radius *r*. This is due to the fact that with the steady-state periodic operation of the apparatus, the entire mass of the first component, which entered with the radial fluid flow into the working zone, is removed from this zone over a period of time $\Delta\tau$ (if this did not happen, the process would not be periodic). Therefore, the first component flowrates averaged over the cross section and time will be the same in both the input and output sections of the working zone. As the results of calculations showed, in the case under consideration $\overline{\overline{C}}_1 = 0.054$.

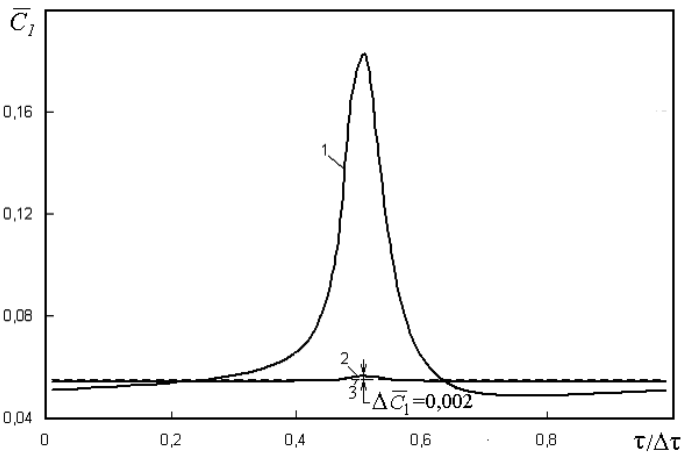

FIGURE 6.21. Change in time of average concentration $\overline{C}_1$ in the working space of RPA: 1 – input section; 2 – output section; 3 – $\overline{\overline{C}}_1$

The degrees of heterogeneity $\varepsilon_{C_1}(r)$ of the mixture of two liquids in the inlet and outlet sections of the RPA working zone can be estimated by the averaged over the period $\Delta\tau$ the mean-square deviation of the local concentrations $C_1(\tau, r, \theta)$ in the considered sections from the average concentration $\overline{\overline{C}}_1$. This value will depend both on the quality of work of the mixing device and on the mass ratio of the mutually soluble components. Therefore, evaluating the performance of RPA as a mixer, it is advisable to divide this value into the average concentration $\overline{\overline{C}}_1$. As a result, we get the expression:

$$\varepsilon_{C_1}(r) = \frac{\int_0^{\Delta\tau} \left\{ \frac{1}{\Delta\theta} \int_0^{\Delta\theta} \left[C_1(\tau, r, \theta) - \overline{\overline{C}}_1 \right]^2 d\theta \right\}^{0.5} d\tau}{\overline{\overline{C}}_1 \Delta\tau}$$

The degree of heterogeneity of the mixture, calculated by the above formula, at the entrance to the working zone ($r = r_{\min}$) is $\varepsilon_{C_1}(r_{\min}) \approx 2.71,$ and at the exit from it $\varepsilon_{C_1}(r_{\max}) \approx 0.032.$

As follows from the results of solving the hydrodynamic problem (6.5)-(6.7), in the working zone of the apparatus, the mass-average fluid velocity in the radial direction is approximately 0.128 m/s. At the same time the length of the working zone along the radius is $\Delta r = r_{\max} - r_{\min} = 0.014$ m. Therefore, the mixture processed in the apparatus is under the influence of the working bodies for about 0.11 seconds. During this time, the degree of heterogeneity of the solution in the working zone decreases by 84.7 times. This indicator of the rotary apparatus work can be considered quite high. It should also be noted that this decrease in the degree of heterogeneity of the mixture is achieved in a single passage of fluid through the working zone. In case if, according to technical conditions, the required degree of heterogeneity of the mixture is not achieved in one pass, the mixture can be repeatedly passed through the working bodies of the apparatus until the required quantitative indicators are achieved.

The influence of the viscosity of the initial components of the mixture on the degree of its homogeneity after processing in RPA was considered in [6.12].

References

[6.1] Dolinsky A.A., Basok B.I., Rotary impulse apparatus. 2. Local pulse heating of the liquid. *Industrial heat engineering*. Vol. 21, No. 1, 1999, pp. 3-5 (rus.).

[6.2] Nakorchevsky A.I., Basok B.I., Hydrodynamics and heat and mass transfer in heterogeneous systems and pulsating flows. K.: *Naukova Dumka*, 2001, 348 p. (rus.).

[6.3] Basok B.I., Davydenko B.V., Obodovich A.N., Pirozhenko I.A., Energy dissipation in the active zone of a rotor-pulsation apparatus. *Reports of NAS of Ukraine*. No. 12, 2006, pp. 81-87 (rus.).

[6.4] Isachenko V.P., Osipova V.A., Sukomel A.S., Heat Transfer. M.: Energy, 1981, 416 p.

[6.5] Mikheev M.A., Mikheeva I.M., Fundamentals of heat transfer. M.: Energy, 1973, 320 p. (rus.).

[6.6] Pirozhenko I.A., Hydrodynamics and thermal effects in a cylindrical rotary-pulsating device: Abstract. dis. candidate techn. Sciences. Institute of Engineering Thermophysics of NAS of Ukraine. K., 2005, 22 p. (rus.).

[6.7] Basok B.I., Pirozhenko I.A., Davydenko B.V., Obodovich A.N., Structural and mechanical properties of soybean paste obtained by processing in a rotary pulsation apparatus. *Industrial heat engineering*. Vol. 31, No. 2, 2009, pp. 31-36. (rus.).

[6.8] Basok B.I., Davydenko B.V., Obodovich A.N., The temperature regime of the rotor-pulsation apparatus during the processing of highly viscous rheological media. *East European Journal of Advanced Technologies*. No. 1/7 (37), 2009, pp. 44-47 (rus.).

[6.9] Obodovich A.N., Khibina M.A., Boryak L.A., Obodovich A.A., Teslya A.I., Intensification of glucose-fructose syrup production due to mechanochemical destruction. *Industrial heat engineering*. Vol. 28, No. 3, 2006, pp. 44-49 (rus.).

[6.10] Maltsev P.M., Fermentation technology. M.: Food Industry, 1980, 560 p. (rus.).

[6.11] Basok B.I., Davydenko B.V., Obodovich A.N., Pirozhenko I.A., Numerical modeling of the process of mixing mutually soluble liquids in a rotary pulsation apparatus. *Reports of NAS of Ukraine.* No. 7, 2007, pp. 79-86 (rus.).

[6.12] Obodovich A.N., Davydenko B.V., Nedbaylo A.N., Influence of fluids viscosities on the intensity of their mixing process in a rotary pulsation apparatus. East European Journal of Advanced Technologies. No. 6/7 (36), 2008, pp. 10-13 (rus.).

Chapter 7

EFFECTS OF CRUSHING DISPERSED PARTICLES OF HETEROGENEOUS FLOWS IN RPA

The most important indicator of the operation of a rotary pulsation apparatus is the size of the dispersed particles in the emulsion, which is obtained from a mechanical mixture of mutually insoluble liquids after its processing in the apparatus. As already indicated, high values of local velocities, accelerations, pressure gradients, normal and tangential stresses, the change of which in time has the character of pulsations, are characteristic of the fluid flow in the RPA working zone. These factors can be considered determining when considering the mechanism of crushing of dispersed particles in a stream. These factors can also include turbulent pulsations, cavitation and acoustic effects, if these physical phenomena are observed in the working area of the RPA.

This section discusses the methods and some results of evaluating the dispersed composition of a heterogeneous medium that has been processed in a rotary pulsation apparatus. The dispersed composition should be understood as the average size of the dispersed particles in the emulsion, and the ratio of the total mass of particles of a certain size to the mass of all dispersed particles.

7.1. Deformation and fracture mechanisms of dispersed phase particles in a heterogeneous flow

A dispersed particle in the process of its movement is subjected to force from the carrier dispersion medium. If, for example, sufficiently high pressure gradients are present in the fluid flow, individual sections of the droplet are loaded differently. Such a situation causes not only its forward movement, but also deformation, that is, the displacement of one part of it relative to another. This process can also be caused by the presence of high rates of deformation of the carrier flow, the result of which is the unevenness of tensile (normal) or crushing drop (tangential) stresses. The process of deformation of a particle is hindered by surface tension forces that tend to give it its original spherical shape. The surface tension forces are distributed unevenly on the surface of the drop. They are higher where the radius of curvature of its surface is smaller. In addition, the magnitude of these forces depends on the value of the coefficient of surface tension α at the interface between two liquid media. If the external forces acting

on the particle exceed the surface tension forces, the surface of the particle will be deformed until the drop of integrity drops, that is, until its surface ruptures.

Currently, semi-empirical models of particle crushing in a heterogeneous medium are widespread, according to which particle crushing occurs when some complexes calculated from the parameters of a moving particle reach certain critical values. Of course, these complexes should characterize the ratio of deforming forces and surface tension forces.

7.1.1. The influence of inertial effects in a heterogeneous flow on the process of particle crushing

A characteristic feature of the velocity field in a heterogeneous flow in which the carrier medium and dispersed inclusions have different densities is its local inhomogeneity. If, for example, identical pressure drops act on the same elementary volumes of dispersion and dispersed fluids, the accelerations of these two volumes will be different, which ultimately leads to the appearance of local minima or maxima in the velocity distribution functions over space. Schematically, this can be interpreted as the imposition of certain perturbations on the homogeneous field of a homogeneous flow of a dispersion medium, or as the relative motion of dispersed particles in a homogeneous flow. In reality, the heterogeneous flow velocity field is continuous. Therefore, such an interpretation can only be used to create approximate models describing some features of heterogeneous flows.

If we assume that the particle has a certain velocity different from the velocity of the dispersion medium at a given point in space, then a certain velocity head will act on the particle, contributing to its deformation and, possibly, crushing. In addition, if in a certain region of space (or at some point in time) the flow of the dispersion medium changes its velocity sharply, the particles of the dispersed component of the flow will be affected by inertia forces in their relative motion, which can also deform and destroy the particle. These phenomena are called inertial effects of deformation and crushing of particles.

The simplest way to assess the stable size of dispersed particles in a heterogeneous flow, in which the main mechanism of particle crushing is associated with inertial effects, is based on a comparative analysis of the levels of physical loads on a particle's surface, which tend to deform its surface, and the forces that prevent this deformation. The former usually include pressure drops and high-pressure heads on the front and aft surface areas. The second – surface tension forces. Such an assessment performed in [7.1], leads to relations for the critical radius of a spherical particle, which should be fragmented if its own radius is above the critical. In this case, the particle crushing conditions look like $r_1 > 2\sqrt{2}\,\dfrac{\alpha}{\rho_0 w^2}$.

This ratio is obtained for flows in which there are no turbulent pulsations. A close to this result of estimating the critical radius of a drop is presented in [7.2]:

$$r_1 > \sqrt[3]{\frac{6}{C}} \frac{\alpha}{\rho_0 w^2}$$

where: $C \approx 0.5$ – empirical constant; $w = \left|\overrightarrow{w_1} - \overrightarrow{w_0}\right|$, w_1 and w_0 – the velocity of dispersed and continuous (dispersive) media relative to a fixed reference system.

The process of crushing dispersed liquid particles in a heterogeneous flow is often associated with the phenomenon of hydrodynamic instability of the interface. The analysis of stability conditions presented in [7.3], leads to relations between some determining similarity numbers characterizing the relative motion of a particle in a dispersion medium and their critical values. The determining similarity numbers in these cases are the Weber number

$$\mathrm{We} = D \frac{\rho_0 \rho_1 w^2}{\alpha(\rho_0 + \rho_1)} \tag{7.1}$$

which characterizes the ratio of the pressure head acting on the particle in its relative motion, and surface tension forces, and the Bond number $\mathrm{Bo} = D^2 \frac{|\rho_1 - \rho_0|}{\alpha} \frac{dw}{d\tau}$, which expresses the ratio of the sum of deforming forces, the magnitude of which is proportional to the relative acceleration of the particle $\frac{dw}{d\tau}$ and surface tension forces. In the above expressions, the initial diameter of the spherical particle is used $D = 2r_1$.

Under the condition $\mathrm{We} > \mathrm{We}_{cr}$, the so-called Kelvin-Helmholtz instability, and at $\mathrm{Bo} > \mathrm{Bo}_{cr}$ – instability of the interface between two media, or Rayleigh-Taylor instability. Thus, the fragmentation of dispersed particles should be expected in cases where the values of numbers We or Bo numbers calculated from the parameters of a moving particle exceed certain critical values.

Theoretical estimates of the critical values of the numbers Bo_{cr} and We_{cr} can be performed only approximately, therefore their values are usually determined from experiment. For an approximate estimation of the possibility of crushing of dispersed particles in a flow, $\mathrm{We}_{cr} \sim 10\ldots12$ and $\mathrm{Bo}_{cr} \sim 40$ are often used as critical values.

The above relations are obtained on the basis of an analysis of the equations of fluid dynamics, in which the terms characterizing the presence of viscous stresses are not taken into account. In this regard, it should be expected that these conditions can satisfactorily describe the process of crushing of liquid particles in

dispersion media with a relatively low viscosity (for example, in gas flows [7.4, 7.5]). To some extent, the influence of the viscosity of the dispersion medium can be taken into account by setting some additional conditions. So in [7.1] an additional condition is $r_1 > 10\dfrac{\mu_0}{\rho_0 w}$, which reflects the fact that particle fragmentation can occur if the Reynolds numbers for the particle are at least 10.

In [7.3], it is proposed to take into account the effect of the viscosity of a dispersion medium on the process of crushing particles in a gas stream by setting the dependence of the critical Weber number on the Laplace number $\mathrm{Lp}_i = \dfrac{D\rho_i\alpha}{\mu_i^2}$ (i = 0; 1), expressing the ratio of surface tension forces and viscosity forces. The form of this dependence is determined by the particle crushing mechanism.

In a number of published sources, the number $\mathrm{Oh} = \dfrac{\mu_1}{\sqrt{D\rho_1\alpha}} = \dfrac{1}{\sqrt{\mathrm{Lp}}}$ is used. So in [7.6] the critical value of the Weber number is proposed to be calculated by the formula $\mathrm{We}_{cr} = 12(1 + 1.077\ \mathrm{Oh}^{1.6})$.

It is also necessary to take into account that the crushing of a particle after it reaches the indicated critical parameters does not occur instantly, but after a certain period of time, during which the particle has time to deform. The necessary period of time during which the similarity numbers considered must exceed critical values depends both on the particle motion parameters and on how substantially the indicated similarity numbers exceed critical values. The greater the corresponding similarity number exceeds the critical value, the usually less time is required for a particle to deform and collapse under these conditions. According to the results of work [7.6], the time required for the process of deformation, leading to the destruction of the particle, is calculated from the expression, $\tau_b = T\left(\dfrac{\rho_1}{\rho_0}\right)^{1/2}\dfrac{D}{w}$, in which the dimensionless coefficient T calculated according to the value of the number We, characterizing the mode or nature of the crushing process. So, for example, if 12 < We < 18, then $T = 6\cdot(\mathrm{We}-12)^{-0.25}$, and if 18 < We < 45, then $T = 2.45\cdot(\mathrm{We}-12)^{+0.25}$ etc. In the same work, a formula is proposed for calculating the diameter D_s stable particles, that is, the diameter smaller than which at given dynamic loads the particle will no longer be able to split:

$$D_s = \mathrm{We}_c\frac{\alpha}{\rho_0 w^2}\left[1-\left(\frac{\rho_0}{\rho_1}\right)^{1/2}\left(0.375\cdot T + 0.2274\cdot T^2\right)\right]^{-2}$$

In work [7.7] it is assumed that particle crushing is possible with We > 12, and the characteristic time of its destruction can be calculated by the formula

$$\tau_b = \frac{5}{\left[1 - \mathrm{Oh}/7\right]}\left(\frac{\rho_1}{\rho_0}\right)^{1/2}\frac{D}{w} \tag{7.2}$$

The diameter of a stable particle, in turn, is determined from the expression

$$D_s = 6.2 \cdot D\left(\frac{\rho_1}{\rho_0}\right)^{1/4}\sqrt{\frac{\mu_1}{\rho_1 D w}}$$

When deriving these relations, an approximate model of a heterogeneous flow was used, in which it is assumed that dispersed inclusions can move at velocities different from the velocity of the dispersion (carrier) medium at a given point in space.

7.1.2. The effect of viscous stresses on the particle crushing process

The above conditions for crushing particles take into account the influence of inertial effects in the flow, leading to deformation and destruction of particles of the dispersed phase. These effects usually occur in the stream during its sharp braking (acceleration) in certain areas of the working space of the dispersing device. These crushing models are based on the assumption that disperse inclusions move with velocities different from the velocity of the dispersion (carrier) medium at a given point in space, which, strictly speaking, does not correspond to the model of viscous fluid flow, according to which the "sticking condition" must be carried out. In this regard, the above relations for critical We numbers, particle destruction time and stable particle diameters is more expedient to use for the cases of dispersion media with low viscosity.

Another area of research into the processes of particle crushing in dispersing devices is based on the assumption that viscous stresses play the main role in the processes of deformation and fracture of particles. Longitudinal stresses tend to stretch or compress a particle in the direction of its motion. Stretching or compression takes place depending on the sign of the derivative of the longitudinal velocity component u_0 along the longitudinal coordinate x_0. The longitudinal in this case is the coordinate that coincides in direction with the velocity vector of the center of mass of the particle. Transverse (shear) stresses tend to rotate the particle at a certain angle relative to the direction of motion of its center of mass, as well as to stretch and bend its surface. As a result of the action of shear stresses alone (as, for example, in the case of the Couette flow), the particle takes the form of an extended thin cylinder or an ellipsoid with ends bending in opposite directions [7.8]. In real dispersing devices,

in which the flow of the carrier medium has a rather complicated structure, dispersed particles are exposed to both longitudinal and shear stresses.

The indicated mechanisms of particle deformation and crushing were studied both theoretically and experimentally. The basis of most theoretical studies is the assumption of a weak effect of inertia forces on these processes. This makes it possible to describe the fluid flow of a particle by the quasi-stationary Stokes equation. In contrast to the formulation of the problem of the deforming effect of inertial effects, the formulation of the problem of viscous deformation assumes the continuity of the velocity field and tangential stresses at the interface. Normal stresses at the boundary experience a jump by the value of capillary pressure. The velocity field of the carrier (dispersion) medium is usually considered given. If this field is two-dimensional, then for describing the tensor of viscous stresses at some point of the carrier medium, it suffices to specify two quantities: $\sigma_{x_0x_0} = 2\mu_0 \dfrac{\partial u_0}{\partial x_0}$ (longitudinal stress) and $\sigma_{x_0y_0} = \mu_0 \left(\dfrac{\partial u_0}{\partial y_0} + \dfrac{\partial v_0}{\partial x_0} \right)$ (shear stress), as $\sigma_{y_0y_0} = -\sigma_{x_0x_0}$ due to the continuity equation, and $\sigma_{x_0y_0} = \sigma_{y_0x_0}$. The last expressions are made taking into account that the direction of the axis $0X_0$ coincides with the direction of motion of the particle at the current time. Given the small particle size, it is assumed that $\sigma_{x_0y_0}$ and $\sigma_{x_0x_0}$ slightly changes along its surface. Thus, the influence of the structure of the external flow on the process of viscous deformation of a particle is characterized by two quantities: $\sum = \sigma_{x_0y_0} + \sigma_{x_0x_0}$ and

$$\mathrm{A} = \frac{\sigma_{x_0x_0}}{\sigma_{x_0x_0} + \sigma_{x_0y_0}} \tag{7.3}$$

When solving the problem of viscous deformation of a particle in a dimensionless formulation, instead of Σ its dimensionless analogue is used:

$$\mathrm{Ca} = r_1 \Sigma / \alpha \tag{7.4}$$

dubbed the “capillary number”. In addition to the quantities Ca and A, the third necessary parameter for solving the particle deformation problem is the ratio of the viscosities of two media $\Lambda = \mu_1 / \mu_0$. The character of the deformation of the particle and the possibility of its crushing depend on the values of these three parameters. To predict the probability of crushing of a particle under the action of viscous stresses, the concept of a critical capillary number is introduced $\mathrm{Ca}_{cr}(\Lambda,\ \mathrm{A})$. It is believed that a particle is destroyed if $\mathrm{Ca} > \mathrm{Ca}_{cr}$.

In order to establish the character and patterns of changes in particle shape under the action of viscous stresses, numerous theoretical and experimental studies were carried out. Brief reviews of the results of early work carried out in this direction are presented in [7.1, 7.9].

Of the early works, the most famous is the work of Taylor [7.10], in which the author presented an analytical solution to the problem of weak deformation of a drop. According to this result, a drop in the process of deformation takes the form of an ellipsoid. In [7.8] the problem of particle deformation in a flow with shear stress was also solved by an approximate analytical method. The so-called the approximation of a thin body, according to which the particle is considered elongated into a curved thread, the cross sections of which are in the form of a circle.

The indicated analytical solutions only qualitatively describe the real process of particle deformation in a viscous flow and cannot reliably predict the conditions for its destruction. More suitable for this purpose were numerical solutions to the problem of changing the shape of a particle under the action of viscous stresses. In a number of studies, numerical solutions of the integral equation for the velocity of a liquid on the surface of a particle are used to study the processes of deformation and crushing of a drop. The indicated integral equation obtained in [7.11] by transforming the system of differential equations of viscous fluid dynamics, it contains the Green functions corresponding to the Stokes problem. In dimensionless form, it also contains quantities Ca, A and Λ as the initial parameters of the problem [7.12].

In [7.13-7.15] this approach was used to study the deformation and crushing of drops under the condition of a constant value of dimensionless viscous stress in time. In [7.16, 7.17] problems were solved under unsteady conditions, which include cases of sudden braking of the external flow or an abrupt change in value Ca. The effect of surfactants on particle deformation and crushing was investigated in [7.18].

In the mentioned works, the capillary number Ca was set as an independent parameter of the problem. More realistic conditions under which viscous stresses change in the region of the external flow were studied in [7.17, 7.19]. In these works, the method of boundary integrals was used to study the deformation and crushing of a particle moving in the gap between rotating cylinders with displaced axes and in the gap between moving flat surfaces.

Currently, in addition to the integral method considered, for the numerical simulation of particle behavior in a viscous flow, the finite element method is widely used, VOF (Volume of fluid) – method, CVLGA (Continuous-velocity lattice gas cellular automata) – method, as well as other modern methods and algorithms that allow to obtain results with high accuracy [7.20-7.26].

From the results of numerical simulation of deformation and crushing of particles that are in satisfactory agreement with experiments [7.10, 7.16, 7.17, 7.24, 7.27-7.35], it follows that in flows in which predominantly longitudinal viscous stresses exist (A = 1), the particle of the dispersed component initially takes an ellipsoidal shape. Further, if longitudinal stresses continue to affect its surface, an isthmus forms in the middle of the ellipsoid, which becomes thinner over time. As a result, the ellipsoid is transformed into a thin thread with thickened rounded edges. In the case of rupture of this thread, two large "daughter" drops are formed, and, possibly, one or more small drops.

More complicated is the process of droplet deformation when $0 < A < 1$, and when longitudinal and shear stresses act together. In these cases, the extension of the surface of the particle is accompanied by the rotation of its longitudinal axis around the center of mass. At A = 0, when only shear (tangential) stresses are present in the external flow, the fragmentation of the particle is preceded by a complex process of changing its shape. Deformation of the droplet surface at near critical values Ca investigated in [7.36].

As already mentioned, the features of the process of deformation of a particle at a fixed A depend both on the ratio of viscous and capillary forces Ca, and on the ratio of viscosities of media Λ. Destruction of the particle surface with the formation of daughter droplets occurs when the number Ca exceeds the critical value characteristic of these quantities A and Λ. If $Ca < Ca_{cr}$, then at any of the indicated stages of deformation, a drop can acquire an equilibrium shape and destruction of its surface will not occur. With a decrease in the values of viscous stresses, the surface of the particle usually relaxes to its original form [7.27], if before this the length of the stretched particle does not exceed the so-called "Critical length" [7.37]. To assess the possibility of a particle reaching critical parameters leading to its crushing, the dependences are used $Ca_{cr}(\Lambda, A)$, which are built both according to the results of numerical modeling and according to experiments. Received in [7.29, 7.30] function $Ca_{cr}(\Lambda, A)$ presented in figure 7.1 in the form of dependencies Ca_{cr} on Λ at various values A. It can be seen from the figure that if shear stresses prevail in the flow (A = 0.2; curve 5), article crushing can occur only in a narrow range of changes in the ratio of viscosity coefficients Λ. At $A > 0.6$ dependence Ca_{cr} on A becomes less significant, and dependence Ca_{cr} on Λ at $A > 0.6$; $\Lambda > 1$ almost disappears. In general, with the increase A critical numbers Ca_{cr} are decreasing.

In a slightly different form, graphic dependence $Ca_{cr}(\Lambda, A)$ presented in [7.19] (fig. 7.2). As an argument, the quantity A, and the graphs correspond to various ratios of viscosity coefficients of the media.

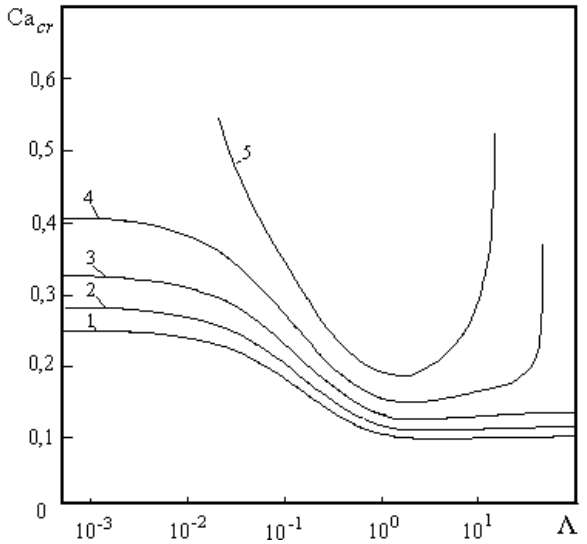

FIGURE 7.1. The dependence of the critical capillary number on the parameter Λ at various parameter values A (according to [7.30]): 1 – A = 1; 2 – A = 0.8; 3 – A = 0.6; 4 – A = 0.4; 5 – A = 0.

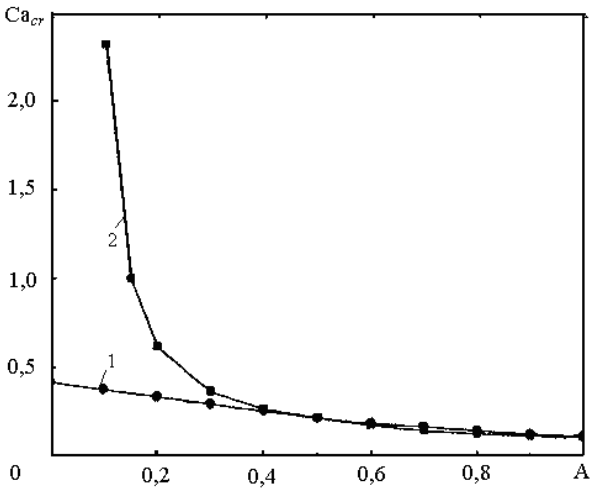

FIGURE 7.2. The dependence of the critical capillary number on the parameter A at various values of parameter Λ (according to [7.19]): 1 – Λ = 1; 2 – Λ = 5.

From an analysis of the results shown in figures 7.1 and 7.2, follows that:

– minimum critical capillary numbers Ca_{cr} are provided in those cases when the viscosities of the dispersed and dispersive media are of the same order;

- for flows in which only tangential stresses are present, the destruction of particles occurs only at $\Lambda < 4$; this is explained by the fact that, due to the equality of the tangential stresses at the interface, the strain rate of the external flow at $\mu_0 << \mu_1$ will not correspond to the deformation rate of the fluid of the particle, in which it turns out to be much less;
- more efficiently, the process of particle crushing occurs in the presence of longitudinal stresses in the external flow (A = 1), than shear stresses (A = 0). So, for example, when $\Lambda = 1$ critical capillary number is $\mathrm{Ca}_{cr} = 0.12$ for A = 1 and $\mathrm{Ca}_{cr} = 0.42$ for A = 0. However, a slight increase A compared with A = 0 can lead to a significant decrease Ca_{cr} and weakening his dependence on Λ.

It should be noted, however, that these conclusions follow from solutions to problems of droplet deformation in the "creeping flow" approximation for a dispersed medium, which means neglecting inertial effects ($\mathrm{Re} \to 0$) in the statement of the problem. The consideration of inertial effects in solving these problems can lead to a significant decrease in the values Ca_{cr} for a given Λ compared with the critical capillary numbers found from solutions of the Stokes problem for the same Λ [7.38, 7.39]. In figure 7.3, given in [7.40], dependences $\mathrm{Ca}_{cr}(\Lambda)$ obtained by numerical simulation are shown for A = 0 at various Reynolds numbers. The Reynolds number in this case is written as $\mathrm{Re} = D^2 \dfrac{\rho_0 \sigma_{x_0 y_0}}{4\mu_0^2}$, based on the fact that for flows with predominant shear stresses, the characteristic velocity is $U_m = \dfrac{\sigma_{x_0 y_0} D}{2\mu_0}$.

As can be seen from figure 7.3, for fixed Λ with increasing number Re values Ca_{cr} decrease, which means an increase in the probability of particle crushing with an increase in the influence of inertial effects.

In [7.40] the concept of critical viscosity ratio is introduced Λ_{cr}, as a value above which particle fragmentation cannot occur ($\mathrm{Ca}_{cr} \to \infty$). For creeping external flow ($\mathrm{Re} \to 0$ due to $\mu_0 \to \infty$) this value is estimated as $\Lambda_{cr} = 3.1$, and when Re = 1 it already makes up $\Lambda_{cr} = 6.5$. As already mentioned, in the presence of only tangential stresses (A = 0) minimum values Ca_{cr} for the "creeping flow" correspond $\Lambda = 0.6$. Taking into account inertial effects leads to the fact that for Re = 10 the minimum Ca_{cr} will be at $\Lambda = 3.0$, and in case Re = 50 – at $\Lambda > 5.0$. The influence of inertial effects on the process of crushing particles in a viscous flow is also considered in [7.20].

The combined influence of viscosity forces and inertial effects during particle crushing or in the decay of jets into droplets can also be estimated using the criterion Oh considered above [7.41].

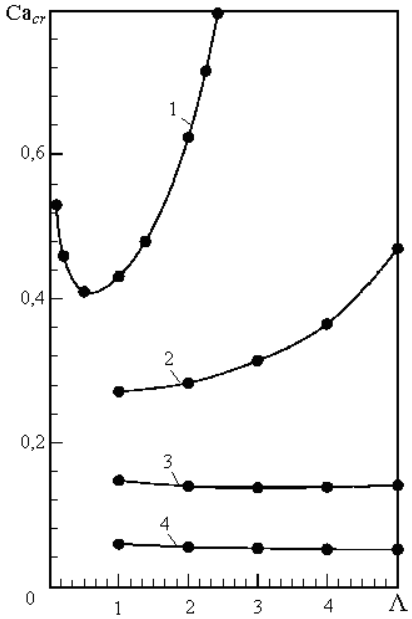

FIGURE 7.3. The dependence of the critical capillary number Ca_{cr} on parameter Λ for A = 0 at various numbers Re (according to [7.40]): 1 – creeping flow (Re → 0); 2 – Re = 1; 3 – Re = 10; 4 – Re = 50.

The presence of surfactants (SAS) in the flow has a certain effect on the process of deformation and crushing of particles by viscous stresses [7.18, 7.42, 7.43]. Since the presence SAS can change both capillary pressure at the interface, and the values of normal and shear stresses, the effect SAS in principle, it can be estimated through a change in the defining criteria Ca, Λ and A considered above. However, since particle crushing is preceded by a complex process of changing its shape (for example, the formation of two spherical drops at the ends of a particle elongated into a thread [7.30, 7.31]), the effect of a particular effect from the presence of SAS at different stages of deformation has its own specifics, which can affect both the acceleration and deceleration of the processes of deformation and destruction of particles.

7.1.3. Crushing of dispersed particles in a turbulent flow of a carrier medium

In a turbulent flow of a dispersion medium, the main mechanism for the destruction of dispersed particles is associated with the presence in the flow of turbulent

pulsations of velocity and pressure. It is believed that the cause of crushing is the interaction of a particle with a turbulent vortex, the size of which should be less than the particle size. The indicated interaction leads to a pulsed increase in dynamic pressure on its surface, which is the reason for the destruction of the particle if the external pressure on the surface of the particle is higher than capillary. If the size of the vortex exceeds the particle size, the latter will be completely carried away by turbulent formation of a large scale and its fragmentation will not occur.

In [7.1] fragmentation of a particle colliding with a turbulent vortex is considered as a result of the transition of the kinetic energy of the pulsation of the velocity of the carrier flow into the potential energy of the particle surface. If the amount of energy received exceeds a certain threshold value for a given drop, the drop will collapse. In order for a liquid particle to split in two after colliding with a turbulent vortex, it is necessary to fulfill the conditions under which the increment of the energy of surface tension forces $\Delta E_{\Pi} = \pi D^2 \alpha \left(2^{1/3} - 1\right)$ would be less kinetic energy of the droplet oscillation $E_K = \rho_1 \pi D^3 \Delta u^2(D) / 2,$ where $\Delta u^2(D)$ – squared velocity difference of diametrically opposite points of the particle surface. The latter value can be considered as the average square of the relative velocity between two points of the external turbulent flow located at a distance *D*. This value, according to the theory of locally isotropic turbulence Kolmogorov [7.44], estimated as $\overline{\Delta u^2(D)} \sim (\varepsilon D)^{2/3}$, where ε – kinetic energy dissipation rate of turbulence.

Based on the presented relations and the considered qualitative models of particle crushing in [7.45] dependency $D_s = C\left(\alpha / \rho_1\right)^{0.6} \varepsilon^{-0.4}$ is obtained to calculate the stable size of dispersed inclusions in a turbulent heterogeneous flow. The theoretical value of the coefficient *C* included in it is close to one. In real conditions of operation of specific dispersing devices, the value *C* may vary significantly from unity and should be determined from experiment [7.46].

The presented expression for the diameter of stable particles is most often used to estimate the dispersed composition of emulsions obtained in those devices in which a turbulent flow regime of a medium is realized [7.47-7.53].

By analogy with the Weber number considered earlier, which characterizes the ratio of inertia forces to surface tension forces, a Weber number is also introduced for a turbulent flow in the form $\mathrm{We}_t = \dfrac{\rho_0 D^{5/3} \varepsilon^{2/3}}{\alpha}$, for which instead of the squared velocity of the relative motion of the media, the above expression is used $\overline{\Delta u^2(D)} \sim (\varepsilon D)^{2/3}$. Of course, the values of critical numbers We_t for turbulent flows will be different from the values We, previously considered for the inertial

mechanism of particle crushing. Critical values We_t determined experimentally depending on the type of dispersing device. In [7.48], for example, the values of the critical Weber numbers in the case of crushing of particles in the extraction columns are estimated at $\mathrm{We}_{t,cr} = 0.05...0.09$.

To determine the average diameter of dispersed particles in emulsifiers, which are characterized by a turbulent flow of the medium, empirical dependences of the form $D_{32} / D = c\mathrm{We}_t^{-0.6}$ are often used, in which the coefficient c depends on the type of equipment and on the concentration of the dispersed component in the stream [7.51, 7.52]. Magnitude D_{32}, called the average "Sauter diameter" is determined according to [7.54], as

$$D_{32} = \frac{\Sigma n_i D_i^3}{\Sigma n_i D_i^2} \tag{7.5}$$

where: D_i – particle diameter of the i-th fraction, n_i – the number of particles of this fraction.

As already indicated, for crushing dispersed inclusions by turbulent pulsations, it is necessary that the particle diameters exceed the characteristic scales of the turbulent formations. However, in [7.49] it is noted that in a number of experimental studies on the dispersion of heterogeneous media in rotary-type apparatuses, the effect of droplet crushing was discovered, the sizes of which are smaller than the Kolmogorov scale of turbulence. This effect is explained both by the difference in the initial diameters of the dispersed particles, and by the combination of crushing mechanisms present in devices of this type. Droplets of large diameter can be crushed as a result of turbulent pulsations, and droplets of smaller sizes are destroyed by viscous stresses.

This idea was developed in the work [7.55], in which, depending on the ratios of the initial particle size and the turbulence scale, two crushing modes are considered: inertial turbulent and viscous turbulent. If the initial particle diameter exceeds the characteristic size of the turbulent formations in the flow, the crushing mode is treated as inertial. In this mode, the quantity that determines the possibility of particle crushing is the critical Weber number calculated by the formula $\mathrm{We}_{t,cr} = f_1 \dfrac{\rho_0 D^{5/3} \varepsilon^{2/3}}{2\alpha}$, which has an empirical coefficient f_1 that is close to unity and practically does not depend on the ratio of viscosities and densities of the dispersed and dispersion phases. If the initial particle sizes are less than the characteristic scale of the turbulent formation, the particle crushing mode is considered as viscous. In this case, the critical turbulent capillary number

$\mathrm{Ca}_{t,cr} = f_2(\Lambda, \mathrm{A})\dfrac{\mu_0 \gamma_t D}{2\alpha}$, constructed by analogy with the capillary number considered above, turns out to be a criterion for the possibility of particle destruction. In this case, the shear rate of the flow under the turbulent flow of the carrier medium is considered as $\gamma_t = \sqrt{\varepsilon / \nu}$, and the coefficient f_2 depends on viscosity ratio Λ and on the relationship between longitudinal and shear stresses A. The time required for crushing a particle is estimated as

$$T_b = 6.8\Lambda^{0.35}\frac{\mu_0 D}{2\alpha} \tag{7.6}$$

An expression close to this for estimating the time of droplet crushing is presented in [7.28], in which the mechanism of crushing particles by viscous stresses was considered.

In parallel with the effect of fragmentation of particles in a heterogeneous system, there is also the effect of their coalescence [7.56-7.59], which, strictly speaking, should be taken into account when calculating the dispersion composition of an emulsion after processing it in a dispersing device. However, the influence of coalescence can be neglected to a first approximation in cases where surfactants are present in the medium, or if the concentration of the dispersed component in the stream is relatively small.

Based on the foregoing, we propose the following approach to solving the problem of crushing dispersed particles in the working volume of RPA:

1. The calculation of the velocity and pressure fields in the fluid flow passing through the RPA working area is performed. If the flow is turbulent, the local values of the dissipation of turbulence energy in the flow are also calculated.
2. Based on the obtained data on the flow structure, the trajectories of individual particles are calculated depending on their initial location in the input section of the RPA working area. In this case, the current values of the relative velocity $w = \left|\overrightarrow{w_1} - \overrightarrow{w_0}\right|$, vectors of the direction of motion of the particle, as well as components of the stress tensor $\sigma_{x_0 y_0}$ and $\sigma_{x_0 x_0}$ in the coordinate system associated with the center of mass of the particle are recorded.
3. Estimated by formulas (7.1) and (7.4) current numbers We and Ca for particles at every moment in time. In the case of a turbulent flow regime, the maximum stable particle diameter is also estimated D_s according to the local value of the turbulence energy dissipation rate.
4. In the case of a laminar flow, the current values of the crushing criteria are compared with their critical values. The critical value of the number We_{cr},

accepted according [7.7], equal 12. Critical capillary number Ca_{cr} calculated for a given Λ and current A by linear interpolation of the functions presented in the form of graphs in figures 7.1, 7.2. If at least one of the above criteria exceeds a critical value, the particle is considered to be in a critical state. In a turbulent flow of a medium, the state of a drop is considered critical if the maximum possible particle diameter D_s it turns out to be less than the actual particle diameter at a given point in space.

5. The time spent by the particles in the state at which $\mathrm{We} > \mathrm{We}_{cr}$ or $\mathrm{Ca} > \mathrm{Ca}_{cr}$, or $D > D_s$ (in turbulent mode) is estimated. At the same time according to the formulas (7.2) or (7.6) time required for particle destruction is calculated.
6. If the residence time of a particle in a critical state is sufficient for its deformation and destruction, the particle is considered to be split into two equal parts.
7. Two identical particles obtained from the initial fragmented particle continue to move in the RPA working area along the same paths and can be crushed again. The study of the dynamics of daughter particles and the possibility of their subsequent crushing is carried out in accordance with paragraphs 2-7.

With this approach, the possible coalescence of particles is not taken into account.

7.2. Calculation of the trajectories of dispersed particles in the working area of RPA

At the first stage of solving the problem of particle crushing in the RPA working area, it is necessary to calculate the velocity and pressure fields in the carrier (dispersion) medium flowing through the working area of the apparatus. The results of such calculations are discussed in detail in chapter 5. Recall that these flow characteristics periodically change in time and space. The geometric period of the working space is considered to be its part, which includes the slots of the stators and the halves of the walls of these slots adjacent to them on the left and on the right. The time period will be the time interval between two consecutive alignments of the slots of the rotor with the slots of the stators. The calculation of the velocity and pressure fields is carried out under the assumption that dispersed particles do not have a noticeable effect on these fields. Naturally, this assumption is one of the approximate assumptions in the statement of the problem.

Strictly speaking, the problem of motion, deformation, and crushing of a particle could, in principle, be solved in an exact formulation. For this, it would be necessary to write down the system of Navier-Stokes equations for each component of the heterogeneous flow, set the initial configuration of the regions occupied by dispersed particles, write down the conditions for the equality of normal (taking into account the pressure jump at the interface due to surface tension) and shear stresses, and solve the problem about the flow of a two-phase

medium. However, the implementation of such an approach for the case of fluid motion in the working space of RPA with time-varying geometry is very difficult, even if one single dispersed particle is considered.

A simpler, albeit less stringent, is the other way. It consists in the fact that the motion of a dispersed particle is considered autonomously. It is believed that mass forces (for example, gravity) and surface forces (pressure and hydrodynamic drag forces) act on this particle from the side of the carrier flow. Under the action of these forces, the particle moves with acceleration, acquiring a velocity different from the velocity of the carrier flow at a given point. This model of motion of dispersed particles is called the Lagrange model [7.60].

Thus, at the second stage of solving the problem of crushing dispersed particles, it is necessary to solve the problem of the motion of an individual particle based on the Lagrange model, for which the initial location, shape (it is believed to be spherical) and physical properties (density, viscosity, surface tension coefficient on the boundary of the particle and the carrier medium) are known. In addition, as already mentioned, the velocity and pressure fields of the carrier dispersion medium, which vary with time, as well as its physical properties, are known.

A similar formulation of the problem for studying the motion, deformation, and crushing of liquid droplets in laminar and turbulent flows of a carrier medium was used in the works [7.19, 7.50, 7.61-7.63]. In [7.19, 7.61] the laminar flow in the gap between the rotating and fixed cylinders was considered, and in [7.50] – turbulent flow between the rotating and fixed disks equipped with protrusions. In [7.62] crushing of liquid particles in a turbulent air flow was considered.

According to the accepted model, the vector equation of motion of a dispersed particle has the form:

$$B_1\rho_1\frac{d\overrightarrow{w_1}}{d\tau}=-0.5C_D\rho_0 S_1\left|\overrightarrow{w_1}-\overrightarrow{w_0}\right|\cdot(\overrightarrow{w_1}-\overrightarrow{w_0})-B_1\cdot\overrightarrow{grad}(p)-0.5\rho_0 B_1\frac{d(\overrightarrow{w_1}-\overrightarrow{w_0})}{d\tau}$$

where: $B_1=\pi D^3/6$ – volume of a spherical particle; $S_1=\pi D^2/4$ – particle mid-sectional area; C_D – coefficient of its hydrodynamic resistance.

On the left side of the equation of motion is the product of the mass of a particle and its acceleration relative to a fixed frame of reference. The terms on the right side of this equation express the forces acting on the particle. Among them (sequentially): the hydrodynamic drag force from the carrier medium, the pressure force, as well as the force associated with the so-called the effect of the attached mass. The derivation of this equation and the physical meaning of the added mass effect are described in sufficient detail in the literature on dispersed flows (for example, in [7.3, 7.46, 7.64]). In this case, it should be noted that the effects of

gravity and buoyancy are not reflected in this equation, because the problem is considered in the plane to which the acceleration vector of gravity is perpendicular. It is also assumed that the densities of the carrier and dispersed media are approximately the same. The influence of other mass forces (for example, Bosset forces), which are mentioned in the works [7.65-7.67], not taken into account.

In the presented equation, the terms expressing the influence of the resistance force and the force associated with the added mass effect contain the velocity differences of the particle and the dispersion medium at a given point in space. Therefore, it is convenient to rewrite this equation in a reference frame associated with a moving dispersion medium. In addition, it is advisable to present the equation written in vector form in projections on the coordinate axis and in dimensionless form. Since these equations include the projection of the velocity of a continuous medium moving in the RPA working area, it is advisable to use the same variables as dimensionless variables as in the problem of fluid flow in the working area (chapter 4). After dimensionlessness and some transformations, the system of equations of particle motion in projections on the coordinate axis takes the form:

$$\frac{dW_x}{dH} = -\eta_d \frac{dW_{0,x}}{dH} - \frac{3}{4\bar{D}} \eta_c C_D W_x \cdot |W| - \eta_c \frac{\partial P}{\partial X}$$

$$\frac{dW_y}{dH} = -\eta_d \frac{dW_{0,y}}{dH} - \frac{3}{4\bar{D}} \eta_c C_D W_y \cdot |W| - \eta_c \frac{\partial P}{\partial Y}$$

where: $X = x / r_0$; $Y = y / r_0$; $W_x = \left(w_{1,x} - w_{0,x}\right) / u_\infty$; $W_y = \left(w_{1,y} - w_{0,y}\right) / u_\infty$; $|W| = \sqrt{W_x^2 + W_y^2}$; $W_{0,x} = w_{0,x} / u_\infty$; $W_{0,y} = w_{0,y} / u_\infty$; $\bar{D} = D / r_0$; $\eta_d = \rho_1 / (\rho_1 + 0.5\rho_0)$; $\eta_c = \rho_0 / (\rho_1 + 0.5\rho_0)$; $u_\infty = \omega_0 r_0$; ω_0 – rotor velocity; r_0 – inner stator radius.

The presented equations are written in a non-inertial reference frame associated with a moving carrier medium. They explicitly contain projections of the acceleration of the carrier flow at a given point in space and pressure gradients in the flow. Functions $W_{0,x}(\tau, x, y)$; $W_{0,y}(\tau, x, y)$; $P(\tau, x, y)$, as already mentioned, are considered known from solving the problem of the flow of a viscous medium in the working space of RPA. Since this problem was solved in polar coordinates: $R = \sqrt{X^2 + Y^2}$; $\theta = arctg\ (Y / X)$, the system of equations of particle motion is also advisable to represent in the polar coordinate system. Using expressions:

$$W_x = V_R \cos(\theta) - U_\theta \sin(\theta); \quad W_y = V_R \sin(\theta) + U_\theta \cos(\theta); \quad U_\theta = \Omega R$$

we get

$$\frac{dV_R}{dH} - \Omega^2 R = -\eta_d \frac{dV_{0,R}}{dH} - \frac{3}{4\overline{D}}\eta_c C_D \cdot |W| \cdot V_R - \eta_c \frac{\partial P}{\partial R} \tag{7.7}$$

$$\frac{d\Omega}{dH} + \frac{V_R \Omega}{R} = -\eta_d \frac{d\Omega_0}{dH} - \frac{3}{4\overline{D}}\eta_c C_D \cdot |W| \cdot \Omega - \frac{\eta_c}{R^2}\frac{\partial P}{\partial \theta} \tag{7.8}$$

where $|W| = \sqrt{V_R^2 + (\Omega R)^2} = w / u_\infty$.

Thus, in the system of equations (7.7), (7.8) dimensionless radial V_R and angular Ω particle velocities are considered relative to a moving dispersion medium, the dimensionless radial and angular velocity of which at a given point in space are equal $V_{0,R}$ and Ω_0 respectively. Drag coefficient C_D for a liquid spherical particle, it can be calculated from known experimental or theoretical relationships. In this case, for C_D, the expression given in [7.68] is used

$$C_D = \left(\frac{24}{\mathrm{Re}_D} + \frac{3.3}{\mathrm{Re}_D^{0.5}} + 0.48 \right) \cdot \frac{1 + 2/3 \cdot \sigma}{1 + \sigma}$$

where: $\mathrm{Re}_D = \frac{wD\rho_0}{\mu_0} = \frac{\omega_0 r_0^2 \rho_0}{\mu_0} |W| \cdot \overline{D} = \mathrm{Re}|W| \cdot \overline{D}$; $\mathrm{Re} = \frac{\omega_0 r_0^2 \rho_0}{\mu_0}$; $\sigma = \mu_0 / \mu_1 = 1/\Lambda$.

Included in the equation (7.7), (7.8) composition $C_D \cdot |W|$ has the form

$$C_D |W| = \left(\frac{24}{\mathrm{Re}\overline{D}} + \frac{3.3}{(\mathrm{Re}\overline{D})^{0.5}} \cdot |W|^{0.5} + 0.48 \cdot |W| \right) \cdot \frac{1 + 2/3 \cdot \sigma}{1 + \sigma}$$

It is more convenient to use it in the calculations, since when $|W| = 0$ the presented expression has no singularity.

Included in the equations (7.7) and (7.8) projections of the carrier acceleration vector are calculated by the formulas

$$\frac{dV_{0,R}}{dH} = \frac{\partial V_{0,R}}{\partial H} + \frac{1}{R}\frac{\partial \left(R \cdot V_{0,R}^2 \right)}{\partial R} + \frac{\partial \left(V_{0,R} \cdot \Omega_0 \right)}{\partial \theta} - \Omega_0^2 R$$

$$\frac{d\Omega_0}{dH} = \frac{\partial \Omega_0}{\partial H} + \frac{1}{R^2}\frac{\partial \left(R^2 \Omega_0 V_{0,R} \right)}{\partial R} + \frac{\partial \Omega_0^2}{\partial \theta} + \frac{\Omega_0 V_{0,R}}{R}$$

Functions $V_{0,R}$, Ω_0, as well as the components of the pressure gradient $\frac{\partial P}{\partial R}$ and $\frac{\partial P}{\partial \theta}$ in a carrier medium, are considered to be known from solving the problem of fluid flow in the RPA working space.

Solving the system of equations (7.7) and (7.8) after linearization numerically, using the implicit Euler scheme, we obtain the values of the radial and angular velocities of the particle at each moment of its stay in the working space of the RPA.

The coordinates of the particle at the *k*-th time step are determined from the expressions:

$$R_k = R_{k-1} + \left[V_R\left(H, R_{k-1}, \theta_{k-1}\right) + V_{0,R}\left(H, R_{k-1}, \theta_{k-1}\right) \right] \cdot \delta H \tag{7.9}$$

$$\theta_k = \theta_{k-1} + \left[\Omega\left(H, R_{k-1}, \theta_{k-1}\right) + \Omega_0\left(H, R_{k-1}, \theta_{k-1}\right) \right] \cdot \delta H \tag{7.10}$$

where δH – dimensionless time step, the same as in the problem of the flow of a carrier dispersion medium.

Obviously, this approach to solving the problem of the motion of a dispersed particle has an error associated with the fact that the particle is considered spherical in the process of its movement. This incorrect statement of the problem is overcome in the work [7.68], in which the problem of the motion of a single particle is considered together with the problem of its deformation. It is assumed that the particle shape is ellipsoidal, and the deformation of the particle consists in changing the ratio of the axial lengths of the ellipsoid. Thus, in this work, in addition to the velocity and location of the particle, its shape was also calculated. It was also assumed in the work that a particle, being deformed into an ellipsoid, collapses when its thickness decreases to 20% on the value of the initial radius of a spherical drop.

7.3. Evaluation of the dispersed composition of the emulsion after processing in RPA

Using the above approach to solving the problem of motion and crushing of dispersed particles in the working volume of RPA, we consider as an example the case of laminar fluid flow in the working space of RPA type TF-2, provided that the pressure drop between its inlet and outlet sections is zero. The dynamics of the dispersion medium flow for an apparatus of the indicated type was considered in subsections 5.2-5.4, chapter 5. Dispersion medium is a fluid with a viscosity $\mu_0 = 0.01$ Pa·s and density $\rho_0 = 1000$ kg/m^3, and dispersed – vegetable oil ($\mu_1 = 0.06$ Pa·s, $\rho_1 = 880$ kg /m^3). Surface tension at the interface α = 0.02 H/m.

It is assumed that the particles of the dispersed component of the initial mixture are distributed uniformly throughout the liquid volume. Therefore, the entry of particles into the working area of the apparatus occurs throughout the input section of the channel of the internal stator. To study the question of the influence of the initial position of the particle in the input section of the working zone on the character of its trajectory, the solution of the considered problem is m various options for the initial position of the particle, i.e. $j = 1 \ldots m$ values of the initial angular coordinate of the particle, calculated as $\theta_j = (j - 0.5)\delta\theta$. It is also assumed that all particles approaching the input section of the working area in a sector with an opening angle $(j-1)\delta\theta < \theta < j\delta\theta$, are in the same conditions and move in the RPA working area along the same paths.

In figure 7.4 presents the results of calculating the trajectory of dispersed particles for four cases of their initial position in the input section of the channel of the internal stator. It is believed that in the initial state the diameters of all particles are the same and equal D = 100 μm. As can be seen from this figure, depending on the place where the particle enters the working area, its trajectory, indicated by colored circles, can vary significantly.

If the parameters We and Ca for a particle at some point of its trajectory do not exceed critical values, the particles in the figure are indicated in green. For comparison, in these figures, the trajectories of the markers are represented in black, i.e. particles of a dispersion medium that are at the initial time in the same positions as dispersed particles. Marker trajectories are constructed according to the known velocity field of the carrier medium. As can be seen from the figures, the trajectories of dispersed particles and markers are close only in the initial section of motion. Then they diverge.

Plots of trajectories in which particles are characterized by numbers We, exceeding critical value (We > 12), marked in blue in the figure. From the point in time at which the number We becomes above critical, the countdown of time τ of the particle staying at critical condition begins. If τ exceeds value τ_b, characterizing the time required for the destruction of the particle (dependence (7.2)), it is considered split into two equal parts. In the picture, this moment is marked by a blue circle of large diameter.

At the same time as the number We, the capillary number Ca (7.4) and parameter A (7.3) for the particle are also fixed. Starting from the moment at which $\mathrm{Ca} > \mathrm{Ca}_{cr}$ the time spent by the particle in a given critical state is recorded.

Further, as in the case $\mathrm{We} > \mathrm{We}_{cr}$, the possibility of crushing particles by viscous stresses is estimated. Trajectory points at which $\mathrm{Ca} > \mathrm{Ca}_{cr}$, marked in figure 7.4 in red. The moment of particle crushing by viscous stresses is fixed in the figure by a red circle of large diameter.

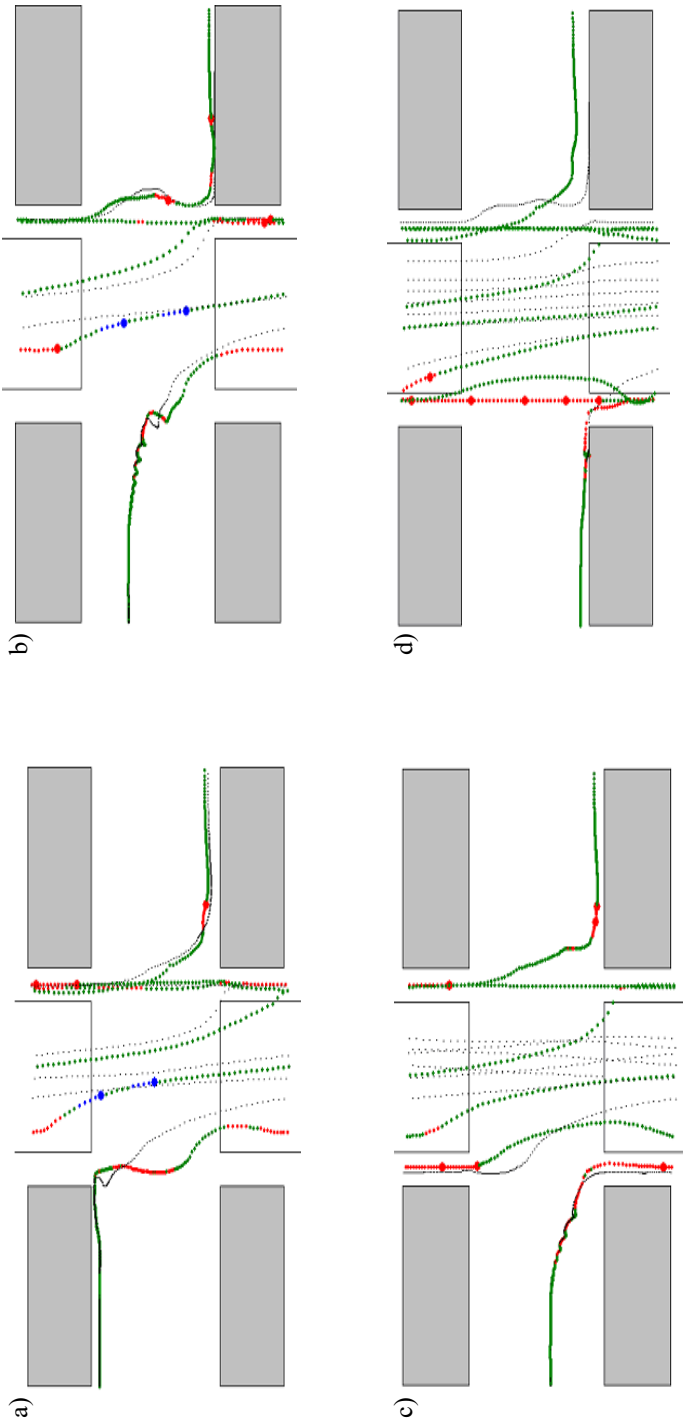

FIGURE 7.4. The dependence of the particle trajectory on its initial location in the input section of the working area.

Analyzing the results presented in figure 7.4, it should be noted that the particle, being in the working area of the RPA, can be crushed repeatedly. The number of crushing particles in one pass through the working area is the greater, the larger its initial diameter. As can be seen from figure, particle crushing due to viscous stresses (red circles) occurs mainly in the region of gaps between work elements, where the values of viscous stresses are maximum, and particle crushing due to inertial effects occurs in the rotor slot. In some parts of the trajectories, there is a situation in which a particle in a critical state does not subsequently crush. This occurs in cases where the duration of a particle in this state is less than the time required for its deformation and destruction.

According to the accepted model, after each crushing event, the total number of daughter particles doubles, and their diameters decrease in $\sqrt[3]{2}$ time. If there was a n_j crushing events (they can be counted by the total number of red and blue circles of large diameter in figure 7.4), then the number of particles formed from one initial particle will be $k_j = 2^{n_j}$, and their final diameters at the exit from the working area will be equal $D_{n_j} = D_0 / \sqrt[3]{2^{n_j}}$. For all *m* considered options for the initial position of particles with an initial diameter D_0 the total number of crushed particles will be $K = \sum_{j=1}^{m} 2^{n_j}$.

To each of *m* different variants of the initial position of the particle corresponds to a certain number n_j crushing events in the working area. However, for some of the considered $j = 1 \ldots m$ value options n_j may be the same. Therefore, you can calculate how many particles of a certain diameter $D_{n_j} = D_0 / \sqrt[3]{2^{n_j}}$ formed in the working area from *m* initial particles with a diameter D_0. You can also calculate the total mass of all particles $\Delta M\left(D_{n_j}\right)$, having a diameter after processing the dispersed medium D_{n_j}, and based on the results obtained, construct a histogram of the distribution of particle diameter. For the case considered in figure 7.4, such a histogram is shown in figure 7.5. The ordinate is the relation $\Delta M\left(D_{n_j}\right) / M$, in which value $M = m\pi D_0^3 / 6$ reflects the mass of all *m* initial particles in the input section of the working area. The number of initial positions of particles for this case is taken equal $m = 24$.

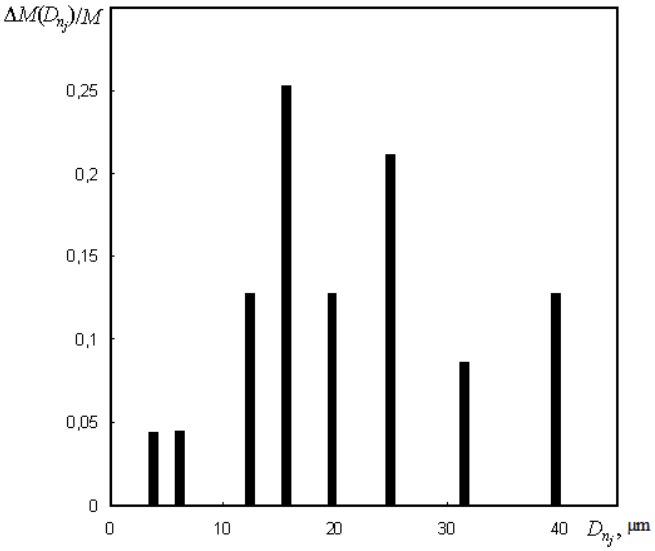

FIGURE 7.5. Dependence of the mass ratio of particles of diameter D_{n_j} to the total mass of all particles on their diameter.

Unlike propeller mixers [7.53, 7.54], rotary pulsation apparatuses are characterized in that the mass of the medium being processed is constantly removed from the working volume of the apparatus. In this regard, in one passage of the medium through the working volume, not all particles of the dispersed phase are in the conditions most favorable for crushing. Therefore, in some cases, in order to achieve a given or minimum possible average particle size in the emulsion, the processed mixture must be passed through the apparatus repeatedly. The calculation model of the process of multiple processing of the medium can be represented as follows. After the first passage of the mixture through the working zone, at which the first stage of particle crushing occurs, their average diameter D_{32} according to the formula (7.5) is calculated based on the obtained data on the distribution of particles by diameter (or mass).

Then the calculation is repeated again, however, the initial diameter of all particles at the entrance to the working area at the second processing stage is taken to be equal to D_{32}, that is, the average particle diameter obtained after the initial treatment. In the same order, the third and subsequent stages of processing the medium are calculated.

With each new stage, the average particle diameters at the entrance to the working area are reduced. In this regard, at each subsequent stage, the number of particle crushing events is also reduced in comparison with the previous stage. In figure 7.6 shows the dependence of the value of D_{32} on the number of processing stages i for

the case shown in figures 7.4 and 7.5. As can be seen from the figure, with each new processing cycle, a decrease of D_{32} become less significant. After i = 4 further decrease of D_{32} almost no longer observed.

Histogram of the distribution of the relative mass of particles of diameter D_{n_j} of the value of this diameter after the fourth cycle of processing the medium is presented in figure 7.7.

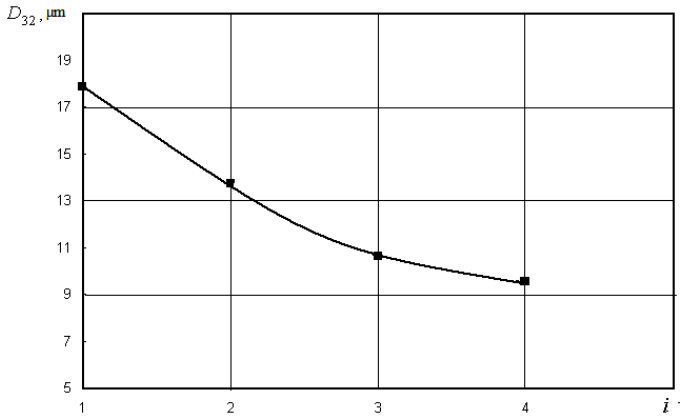

FIGURE 7.6. The dependence of the average particle diameter D_{32} from processing cycle number.

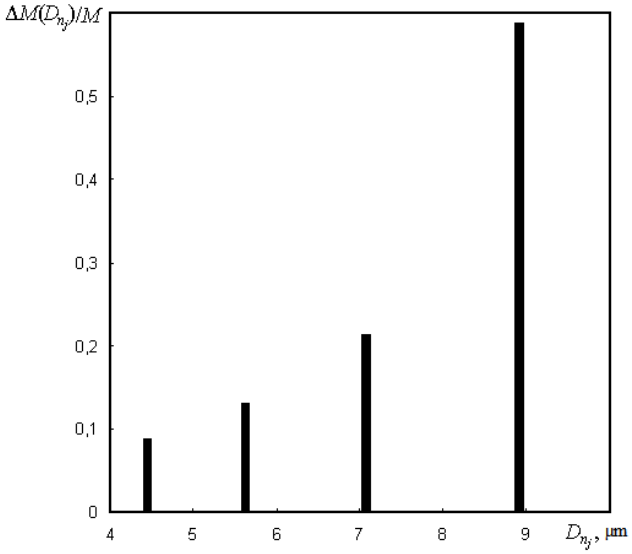

FIGURE 7.7. Dependence of the mass ratio of particles of diameter D_{n_j} to the total mass of all particles on their diameter after the fourth medium treatment cycle.

As an example of particle crushing in a turbulent flow, we consider the case of a turbulent water flow (dispersion phase) in the working volume of an RPA of the TFG type, which was considered in the subsection 5.8. The dispersed phase, as in the first example, is vegetable oil.

The trajectories of dispersed particles are calculated based on those found using RNG models of turbulence of velocity and pressure fields in the flow for the case Δp = 10 kPa (fig. 5.29). To find the maximum possible diameter of the dispersed particle D_s in a turbulent flow, the obtained distribution of the turbulence energy dissipation rates ε in the working zone is used (fig. 5.31, chapter 5).

Particle trajectories with an initial diameter D_0 = 100 μm for various cases of their initial location, as well as the points at which the particle crushing act is expected under the influence of turbulent pulsations (blue circles), are presented in figure 7.8.

From a comparison of figure 7.8 and figure 7.4 it is seen that, in contrast to the case of a laminar flow of a medium, particles in a turbulent flow are crushed mainly in the region of gaps between cylindrical elements. This is explained by the fact that, in the region of gaps, the dissipation rates of turbulent energy are maximum. Moreover, in most cases, cascade fragmentation of particles is observed, i.e. after the first act of crushing particles into two equal parts (according to the accepted model), the second and subsequent acts of crushing immediately occur. This is due to the fact that in the gap region due to the high dissipation rates of turbulence energy, the maximum possible stable particle diameters D_s turn out to be several times smaller than the diameters of non-fragmented particles approaching the most active RPA zone. In the areas of the slits, where values are much smaller, there are practically no crushing events. From figure 7.8 it is also seen that most particles are crushed in the internal gap, since the diameters of the particles approaching the external gap are already smaller than the values D_s, corresponding to the dissipation rate of turbulence energy in the external gap.

A histogram of the particle diameter distribution for the considered case of turbulent flow is shown in figure 7.9. As can be seen from the figure, the total mass of particles with a diameter of 9.9 μm is about 33% of the mass of all dispersed particles of the emulsion. About 21% of the total masses are particles with diameters of 7.87 microns and 6.95 microns. The percentage of other fractions (both larger and smaller) does not exceed 4%.

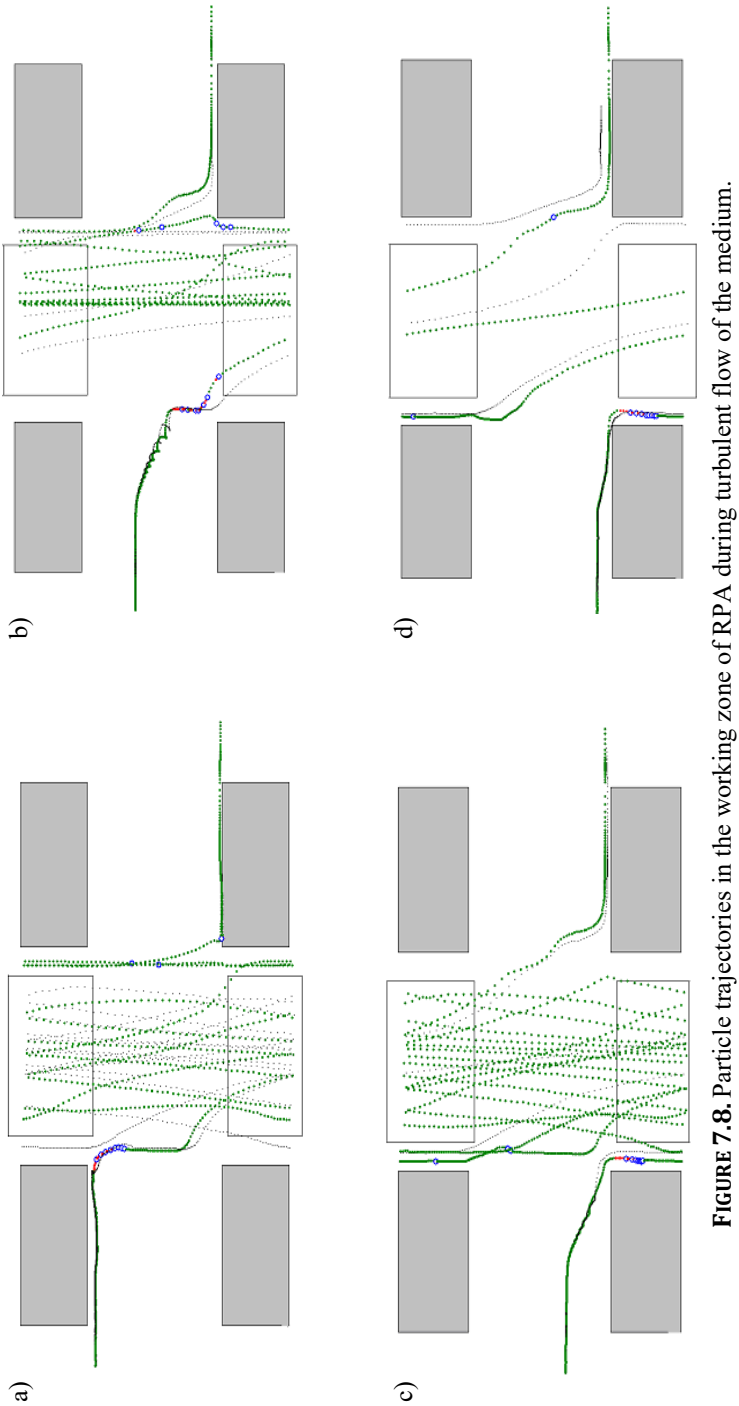

FIGURE 7.8. Particle trajectories in the working zone of RPA during turbulent flow of the medium.

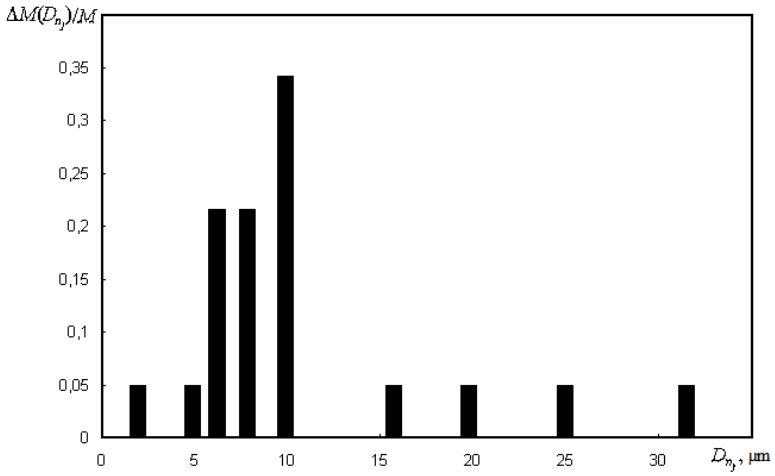

FIGURE 7.9. Dependence of the mass ratio of particles of diameter D_{n_j} to the total mass of all particles on their diameter for turbulent flow.

The results shown in figure 7.9 in the form of a histogram are also presented in figure 7.10 in the form of a graph (curve 1) for a narrower range of changes in the diameters of dispersed particles (from 2 μm to 16 μm). Similar results obtained according to an experimental study of the processing process in RPA of a mixture of vegetable oil with water are shown in figure 7.10 of curve 2.

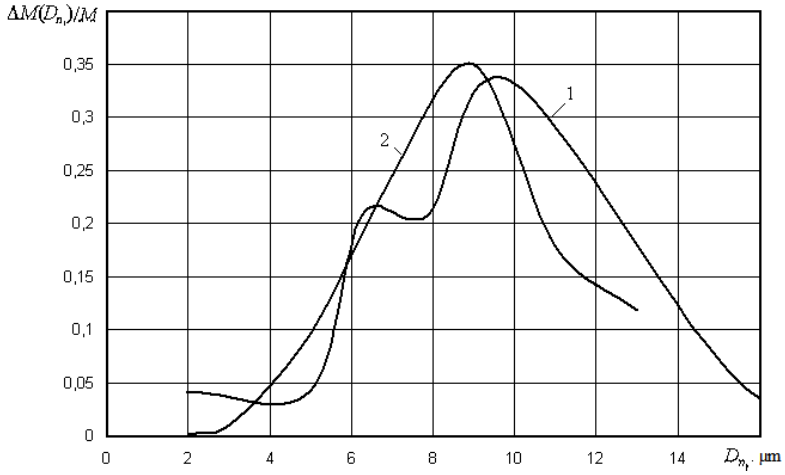

FIGURE 7.10. Comparison of calculated (1) and experimental (2) data on the dispersed composition of a heterogeneous mixture after its processing in RPA.

As can be seen from the figure, the data of theoretical and experimental studies are in satisfactory agreement. At the same time, it can be noted that the maximum of

the experimental curve 2 in figure 7.10 is somewhat shifted relative to theoretical curve 1 towards smaller fractions. This is explained by the fact that, when obtaining the theoretical curve, only the turbulent mechanism of particle crushing was taken into account, while in real conditions all the mechanisms discussed above take place in the RPA working zone.

As follows from the above results, the indices of the dispersed composition of the heterogeneous mixture obtained after treatment in RPA under a turbulent flow regime exceed the similar indices in figure 7.5 for laminar mode. The average diameter of the particles obtained after a single treatment of the medium in RPA is $D_{32} =$ 7.65 μm. From this it follows that the turbulent flow of fluid in the working volume of the RPA contributes to the crushing of particles of the dispersed phase.

7.4. The influence of structural and operational parameters of RPA on the average size of dispersed particles

Method for determining the average size of dispersed particles of a heterogeneous mixture D_{32} in case of its laminar flow through the RPA working zone; it is considered using an apparatus of the type TF-2. Characteristic for it are the number of slots z = 36 for all work items, the width of both gaps between work items δ = 0.2 mm, rotor angular velocity $\omega_0 = 96\pi$ s^1. Determination results D_{32} by the indicated method are presented in figures 7.4-7.7.

It is now advisable to consider the effect of various variants of the indicated structural and operational parameters of the RPA on the dispersed composition of the emulsion during the laminar flow of a heterogeneous mixture, the components of which have the same physical properties as in the case considered above. Consider the option of changing the number of slots z from 24 to 48; gap width δ from 0.1 mm to 0.3 mm and rotor velocity ω_0 from 72π s^{-1} to 120π s^{-1} (from 36 to 60 turn/s). Other geometric parameters, as well as differential pressure (Δp = 0), remain unchanged.

In this case, the velocity and pressure distributions obtained earlier (chapter 5) in the RPA working volume are used to determine, using the method described above, the average size of dispersed particles of a heterogeneous medium for the above options of geometric and operating parameters.

The results of the calculation of the average particle diameter D_{32} for various z and δ at $\omega_0 = 96\pi$ s^{-1} in the case of one treatment cycle of the substances are presented in table 7.1 and in figure 7.11.

TABLE 7.1. The dependence of the average diameter of the dispersed particles on the width of the gap and the number of slots in a single treatment cycle of a substance.

D_{32}, μm	δ = 0.1 mm	δ = 0.2 mm	δ = 0.3 mm
z = 24	8.55	12.17	13.06
z = 36	7.37	10.05	10.9
z = 48	6.37	8.05	9.91

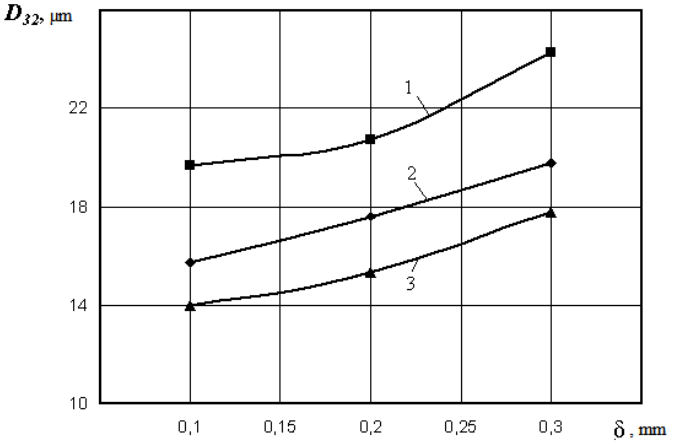

FIGURE 7.11. The effect of the width of the gap and the number of slots on the average diameter of the dispersed particles during a single treatment of the substance: 1 – z = 24; 2 – z = 36; 3 – z = 48.

Similar results obtained after a four-fold passage of the processed medium through the working area are presented in table 7.2 and in figure 7.12. Effect of rotor velocity on values D_{32} at constant δ = 0.2 mm and z = 36 presented in the table 7.3 and in figure 7.13.

TABLE 7.2. The dependence of the average diameter of the dispersed particles on the width of the gap and the number of slots after four processing cycles.

D_{32}, μm	δ = 0.1 mm	δ = 0.2 mm	δ = 0.3 mm
z = 24	19.66	20.72	24.25
z = 36	15.74	17.6	19.76
z = 48	14	15.35	17.78

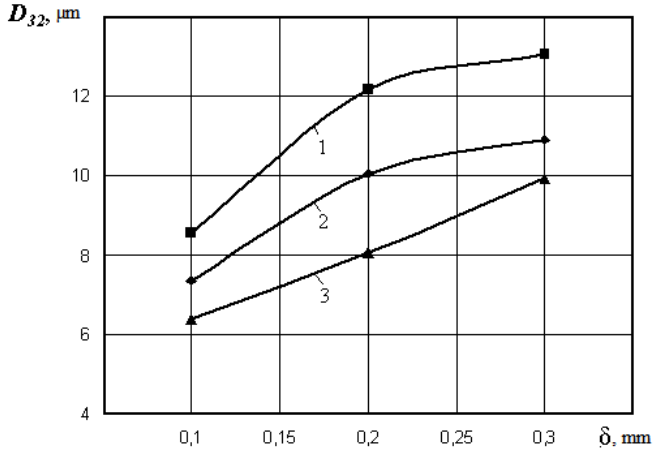

FIGURE 7.12. The influence of the gap width and the number of slots on the average diameter of the dispersed particles after four cycles of treatment of the substance: 1 – $z = 24$; 2 – $z = 24$; 3 – $z = 48$.

TABLE 7.3. The dependence of the average diameter of the dispersed particles on the rotor velocity.

D_{32}, μm	$\omega_0 = 72\pi$ s^{-1}	$\omega_0 = 96\pi$ s^{-1}	$\omega_0 = 120\pi$ s^{-1}
One cycle	26.73	17.6	14.9
Four cycles	15.58	10.55	8.85

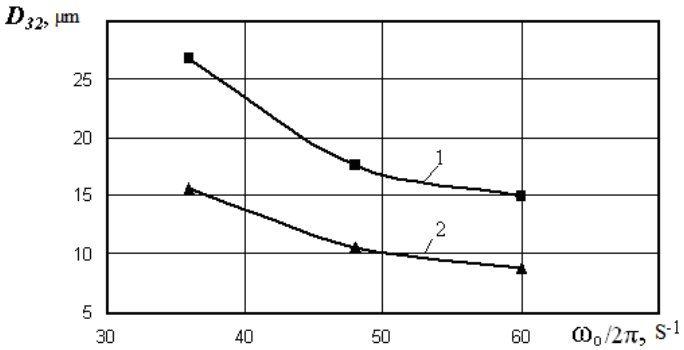

FIGURE 7.13. The effect of rotor velocity on the average diameter of dispersed particles: 1 – one cycle; 2 – four cycles.

The calculation results show that the average particle diameter decreases with decreasing gap width δ. This, on the one hand, is explained by the fact that a decrease in the width of the gap leads to an increase in shear stresses between rotating and

stationary work elements. However, it should be noted that not only the increase in shear stresses in the gaps intensifies the process of particle crushing with decreasing δ. With a decrease in the gap width δ, the amplitudes of pressure pulsations and the acceleration of the flow near the edges of the working elements also increase at the moment of mutual overlapping of the slots of the rotor and stators. Longitudinal viscous stresses also increase in these areas. These effects, which can be considered as the implementation of discrete-pulse energy input into the flow, were considered in detail in chapter 5. As follows from the equations (7.7) and (7.8), the pulsed change in the pressure gradients and the acceleration of the carrier flow leads to increases in the relative velocities and accelerations of dispersed particles, which intensifies the inertial mechanism of their fragmentation. At the same time, an increase in longitudinal stresses intensifies the viscosity mechanism of particle crushing (subsection 7.1.2), because critical capillary numbers when exposed to a particle of longitudinal viscous stresses are for any Λ rather low values (fig. 7.1).

An increase in the number of slots in the working elements also leads to reducing of the average particle diameter. Although with an increase in the number of slots, the levels of pressure pulsations and acceleration of the flow decrease somewhat, however, in proportion to the number of slots, the pulsation frequency of the indicated values increases (at a constant rotor speed). As a result of this, the probability of finding a dispersed particle in the most active (from the point of view of the crushing process) area of the working zone of the apparatus increases.

Such mechanisms lead to a decrease in the average particle diameter of the heterogeneous substance being processed with an increase in the number of rotor revolutions (table 7.3, fig. 7.13).

From the foregoing, it can be concluded that to reduce the size of dispersed particles, it is necessary to increase the number of slots, increase the rotor velocity and reduce the gap between the working elements. Naturally, it is possible to change these values only up to certain limit values, which are limited by the technological capabilities of manufacturing RPA, as well as operational requirements.

The dependences of the average diameter of the dispersed particles of the processed substance on the width of the gaps, the number of slots and the rotor velocity, shown in figures 7.11-7.13, can be represented as a quadratic polynomial

$$D_{32} = \sum_{k=0}^{k=2} \sum_{i=0}^{i=2} \sum_{j=0}^{j=2} a_{k,i,j}^{D} \delta^k z^i \omega_0^j \qquad (7.11)$$

for which the coefficients $a_{k,i,j}^{D}$ can be found on the basis of the data given in table 7.1-7.3.

7.5. The energy spent on crushing particles in RPA

It is known that the surface energy of a spherical particle of radius r_0 is calculated by the formula $E = 4\pi r_0^2 \alpha$. The minimum work that needs to be done so that by crushing out M_0 particles of radius r_0 receive $M_1 = M_0 \left(r_0 / r_1 \right)^3$ particles of radius r_1, calculated as $A = M_0 4\pi r_0^2 \alpha \left(r_0 / r_1 - 1 \right)$.

If the flow rate of the mixture entering the RPA working area is $G = \pi r_{st} h \overline{V}$, and the volume concentration of the dispersed phase – φ, then the number of dispersed particles of radius r_0, arriving every second in the working area will be equal $M_0 = \dfrac{3 r_{st} h \overline{V} \varphi}{4 r_0^3}$. Thus, the minimum power spent on crushing particles in the apparatus is $N_{dis} = \varphi \dfrac{3\pi r_{st} h \overline{V} \alpha}{r_0} \left(r_0 / r_1 - 1 \right)$.

Using data on average particle diameter D_{32}, presented in figure 7.11, as well as the results of calculating the mass average velocity $\overline{V}_r$, it is possible to calculate what minimum power is spent in the RPA on the process of crushing particles depending on the width of the gap δ and the number of slots z in the working elements. The results of this calculation are presented in the table 7.4.

TABLE 7.4. The dependence of the power spent on crushing particles in RPA, on the width of the gap and the number of slots.

N_{dis}, W	z = 24	z = 36	z = 48
δ = 0.1 mm	0.846	1.086	1.508
δ = 0.2 mm	0.910	1.052	1.372
δ = 0.3 mm	0.852	1.184	1.292

It should be borne in mind that the results presented in the table reflect only the minimum required power spent on crushing particles, since these values were calculated based on the initial and final sizes of spherical droplets. With a more rigorous approach to calculating the energy required for crushing, it is also necessary to take into account the work spent on deforming the surface of the particles before their destruction.

The method of estimating the average particle diameter of a dispersed medium, considered in this section, after processing it in RPA allows one to determine the dependence of their average size on the structural and operational parameters of the

apparatus. As the results of using this method show, a decrease in the average diameter of dispersed particles can be achieved by reducing the width of the gaps between the cylindrical working elements, increasing the number of radial slots and increasing the velocity of rotation of the rotor. From a comparison of the results of calculating the average diameter of dispersed particles of a heterogeneous medium under the laminar and turbulent regimes of its flow in the working volume of RPA, it follows that the turbulent flow regime of the medium contributes to a more intense fragmentation of particles.

7.6. The effect of crushing the dispersed phase of a highly viscous medium

As previously emphasized, rotary pulsation apparatuses can be effectively used to implement various technologies for the treatment of liquid heterogeneous low and high viscosity media, mainly with the aim of intensifying the processes of mixing, emulsification, mixing and homogenization of heterogeneous systems, as well as the processes of dissolution or dispersion of the solid phase in liquids. The RPA simultaneously implements the principles of operation of rotary mixers, disintegrators and dismembrators, centrifugal and vortex pumps, colloid mills and liquid sirens of the radial type. In the process, RPA converts the initial mixture of mutually insoluble liquids into a finely divided homogeneous stable emulsion. RPA was most widely used precisely in technologies that combine the processes of dispersion and mixing: to obtain medical emulsions; for the preparation of emulsion thickeners and printing inks; in the pulp and paper industry for bleaching pulp and crushing paper medium; for chemical industries in the process of mixing several mutually insoluble liquids, in the food industry for the production of mayonnaise, mixtures for ice cream, emulsions, protein caviar, sauces, desserts, mashed potatoes, as well as for the processing of beans and the production of new types of meat, curd and sour-milk products, etc.

The determination of dispersion as an important quality characteristic of the final product is of great interest, since according to these data it is possible to evaluate the effectiveness of the homogenizing equipment used. In this regard, a theoretical and experimental assessment of the degree of dispersion in the processing of emulsions and biological media was carried out.

We emphasize that the implementation of the effects of crushing of dispersed particles in rotationally pulsating flows is due to the manifestation in RPA of a wide variety of physical phenomena. As a result of numerical simulation of the fluid flow in the working elements of the rotary pulsation apparatus, it was established that this flow is periodic in time. The average fluid velocity in the radial direction depends on its viscosity and on the pressure drop. Due to the action of centrifugal force, this speed can be positive even with certain negative values of

this difference. Pressure pulsations periodically occur in the flow caused by the overlapping of the stator slots by the walls of the rotor slots. The amplitude of the pulsations also depends on the viscosity of the medium and the pressure difference between the inlet and outlet sections of the slots of the stators. In the flow there are simultaneously regions of positive and negative (with respect to the inlet section) pressures located close to each other. This is the reason for the occurrence of significant spatial pressure gradients, as well as normal and shear stresses that can deform and destroy particles of a dispersed substance.

Let us consider the results of experimental studies of the dispersed composition of some heterogeneous media that have undergone processing in rotary pulsation devices.

Homogenization of mayonnaise emulsion

The results of experimental studies of the crushing of particles of an immiscible component during the processing of a highly viscous emulsion are presented in figure 7.14a. As an object of research, a water-fat emulsion of mayonnaise with a concentration of vegetable oil in 65%. The average particle size of fat was 4.4 μm with error 1.1 μm and the normal nature of the distribution. For comparison in figure 7.14b a histogram of the distribution of particles of a similar mayonnaise emulsion obtained on a valve homogenizer at nominal pressure 100 atmospheres. The size of the inclusions of oil is 7.9 μm, almost in 2 times more than with rotary pulsation homogenization technology, which confirms the high efficiency of the latter.

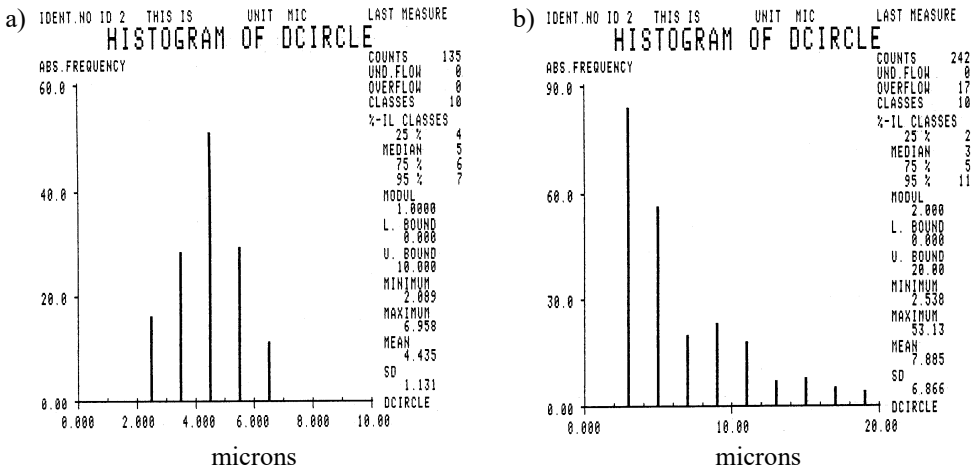

FIGURE 7.14. A histogram of the size distribution of fat particles of a mayonnaise emulsion obtained in: a) RPA type TF-2M; b) valve homogenizer type A1-OGM-5.

Crushing of biological systems during rotary pulsation treatment. Soya paste

Note that rotor-pulsation homogenization is one of the effective and widespread methods of dispersing complex biological systems. The paper presents the results of structural and dispersed analysis [7.69-7.71] of the original soya beans and homogenized soybean paste obtained by sequentially carrying out thermal-humid, and then rotary-pulsating treatment of soybeans. Based on rheological analysis, systems of this type are usually called viscoplastic. Modeling the processes of hydrodynamic crushing of such media in RPA is complex and little studied, therefore, we briefly dwell on some experimental results on the dispersion of highly viscous media.

The physical properties of the product obtained as a result of rotary-pulsation homogenization – soybean paste mainly depend on the structural characteristics of soybean. In this regard, the microstructure of untreated and thermo-moistened soybean was studied in this work. The need for heat-moisture treatment is explained by the rather rigid structure of the bean, which, without pre-treatment, requires large shearing forces in the process of further homogenization and is the reason for the violation of the uniformity of the final product – soybean paste.

The determination of dispersion as an important characteristic of the quality of soybean paste is of great interest, since according to these data it is possible to evaluate the effectiveness of the homogenizing equipment used.

Optical and electron microscopic examination of soybean samples was carried out according to standard microscopy techniques for the study of biological systems [7.72] using an optical microscope type “Opton”, automatic image analysis system “IBAS” and electron microscope EM-400T.

In figure 7.15 microphotographs of a longitudinal section of the uncured soybean cotyledon are shown. As you can see, the soybean cotyledon consists of oblong cells (fig. 7.15a), and the width of the intercellular space is 50÷70 nm (fig. 7.15b). A detailed analysis of the distribution of cotyledon cells by characteristic sizes showed that the maximum cell size does not exceed 100 μm, and the minimum size – 40 μm. Soy cells contain lipid inclusions and are filled with a large amount of fat vacuoles, the average size of which is 0.2÷0.5 μm.

The quality of the paste, as well as products based on it, largely depends on the degree of dispersion, uniformity and uniformity of the distribution of particles of the dispersed phase. Therefore, to determine the effectiveness of rotor-pulsation treatment and evaluate the effect of homogenization, a dispersed analysis of soybean paste was carried out. As an experimental sample, soybean paste with a moisture content of 65 weight % and density 1115 kg/m^3 obtained under industrial conditions using RPA type BGT was used.

Presented in figure 7.15c micrograph of particles of soybean paste indicates the destruction of the soybean structure during processing to the cellular level. This means that rotary pulsation treatment of soybeans leads to the destruction of intercellular connections and the formation of systems consisting of isolated cells.

A micrograph of a particle of soybean paste is shown in figure 7.15d. As can be seen, the particle has an oblong shape. This is a single soybean plant cell surrounded by oily inclusions. The internal structure of the cell is a loose structure enclosed in a shell (fig. 7.15d), which indicates the denaturation of the protein that occurred during the thermo-humid and rotor-pulsation treatment, which led to its coagulation and disruption of the bonds between globular proteins. The presence of fat droplets allows us to note that as a result of processing, not only the destruction of the intercellular structure occurs, but also the destruction of some cells. This entails the release of all components of the cell, including soybean oil, that is, the processing of protein molecules by enzymes is accelerated.

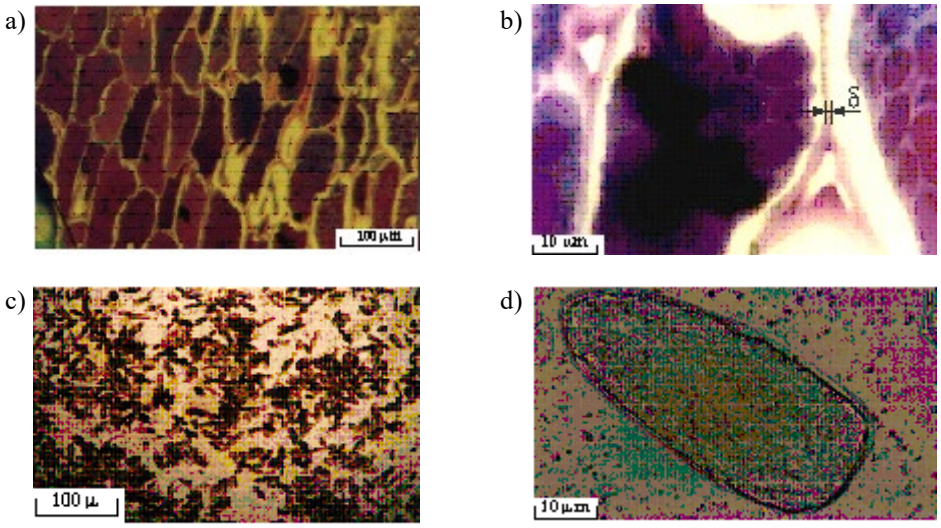

FIGURE 7.15. The micro structure of the soybean portion to (a – microscope magnification ×200, b – ×2000) and after (c – single soybean cells, d – single bean cell, points outside the particle – fatty inclusions) rotary pulsation treatment. The size $\delta \approx 50\ldots70$ nm.

Note that soybean paste processed in RPA is a mixture of a suspension (particles of solid denatured protein in an aqueous medium) and emulsion (particles of soybean oil in an aqueous medium). The histograms of the size distribution of both classes of particles are presented in figure 7.16. Dispersion studies showed that the average size of protein particles of soybean paste (fig. 7.16a) is about 40 μm, and the values of the most characteristic sizes are given in table 7.5.

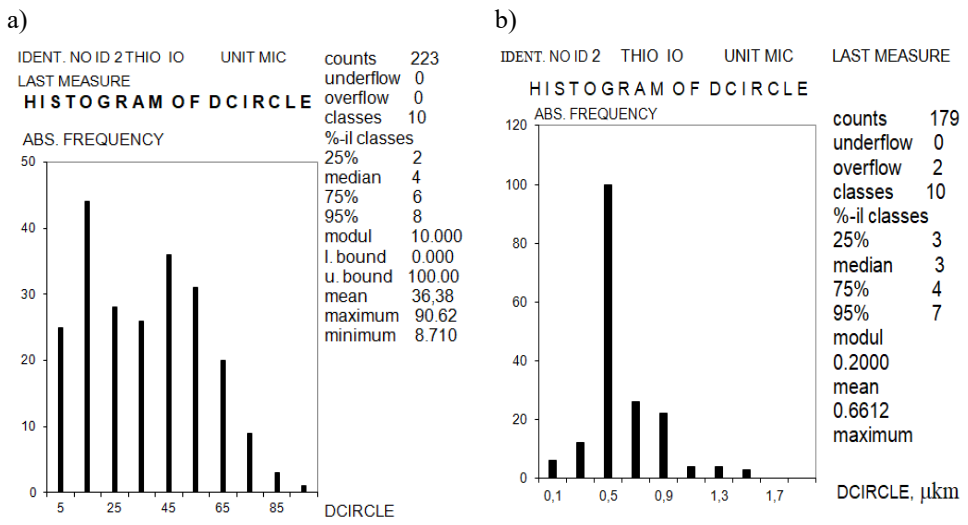

FIGURE 7.16. Histograms of distribution in a sample of soybean paste: a) protein particles; b) fat drops.

TABLE 7.5. Dispersion parameters of protein particles of soybean paste.

	The average value	Maximum value	Minimum value	Dimension module	By area
D_c, µm	36.38	90.62	8.71	10	21.08
S, µm^2	1387	6450	59.58	1000	1343
$D_{\max}$, µm	70.21	222.9	12.31	20	43.37
$D_{\min}$, µm	30.84	93.41	4.659	5	18.83

The data of statistical processing of the results of the distribution of protein particles of the paste by characteristic geometric sizes are presented in the form of histograms in figure 7.17.

The results of studies of the distribution of particles by maximum size allow us to note that the bulk of the sample are particles of size 30 µm (20% from the total number of particles), 15% make up particle size 70 µm and 16% – 90 µm. In the distribution of particles over $D_{\min}$ the largest number of particles (18%) have size 7.5 µm, and the maximum size $D_{\min}$ particles does not exceed 93.4 µm. For distribution by D_c predominant particle size 15 µm and 45 µm, what is 20% and 16% respectively. Analysis of the histogram of the distribution of particles by their area (fig. 7.17b) shows that it is proportional to the increase in area (up to

6450 μm^2) occupied by particles, there is a decrease in the proportion of the number of particles of this size to 1%.

To determine the size of the fat droplets in the soybean paste, pasta samples were analyzed, including only drops of soybean oil. As can be seen from figure 7.16b, in the studied sample of 179 particles there are no particles larger than 1.6 μm. The largest amount of fat particles of soybean paste (55.8%) has a size of 0.4 μm to 0.6 μm, and particles of a minimum size (up to 0.2 μm) make up 3.35% of the sample.

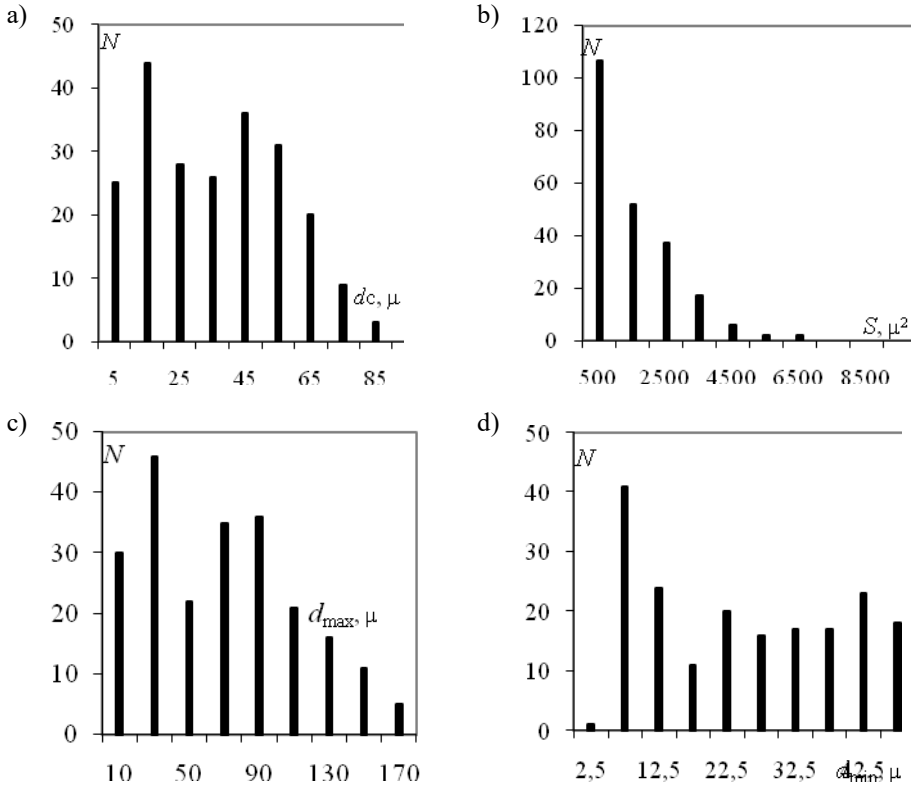

FIGURE 7.17. Histograms of the distribution of protein particles of soybean paste: a) by the average size, b) by the occupied cross-sectional area, c) by the maximum, d) by the minimum size.

When comparing the degree of dispersion of fat droplets before and after rotary-pulsation treatment, a significant decrease in the average size of drops of soybean oil is clearly visible (by 80%).

A set of studies on microstructural and disperse analysis suggests that the selected processing mode of durable biosystems such as soybeans leads to dispersion to a cell size. Obviously, in order to disperse the system into individual cells, it is

necessary to break the bonds in the area of their connection. As shown by our electron microscopy data, the thickness of the cell binding region is up to 70 nm. Therefore, the rotor-pulsation effect allows you to destroy the nanoscale region of the specified size, and this type of technological impact can be attributed to nanotechnology processing biological systems.

Sunflower seed paste

The production of sunflower paste was first carried out by crushing them in a screw extruder, followed by dispersion of the resulting mixture in a TF-2 type RPA.

The data of statistical processing of the results of optical studies of the distribution of paste particles by average size and occupied area are shown in the form of histograms in figure 7.18, where the abscissa in figure 7.18a the diameter of a circle is plotted, the area of which is equivalent to the area of the particle, (D_c) in microns, and in figure 7.18b – particle area (S) in μm^2. The ordinate shows the absolute value of the number of particles analyzed.

The results of studies of the distribution of particle size by average size indicate that the predominant number of particles has a size of from 35 μm to 55 μm.

Analysis of the histogram of the distribution of particles over their area (fig. 7.18b) shows that it is proportional to the increase in the area occupied by the particles (up to 4500 μm^2), a decrease in the proportion of the number of particles of this size to 5%. Thus, the resulting sunflower paste has a fairly high degree of dispersion, which fully meets the technological requirements for its further use.

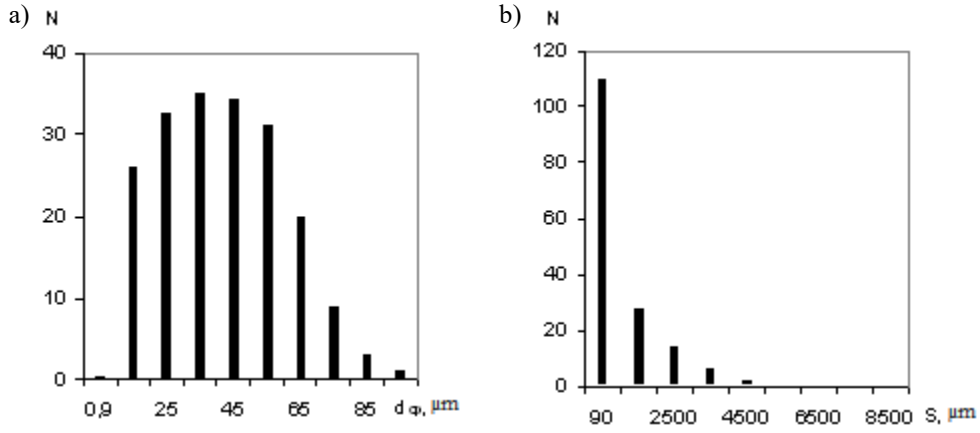

FIGURE 7.18. Histograms of the distribution of particles of paste from sunflower seeds: a) by average size, b) by occupied area.

Homogenization of tomato paste

Obtaining tomato paste was carried out by dispersing tomatoes using RPA type TF-2. In figure 7.19 presents the results of statistical processing of a sample of 172 particles of tomato paste.

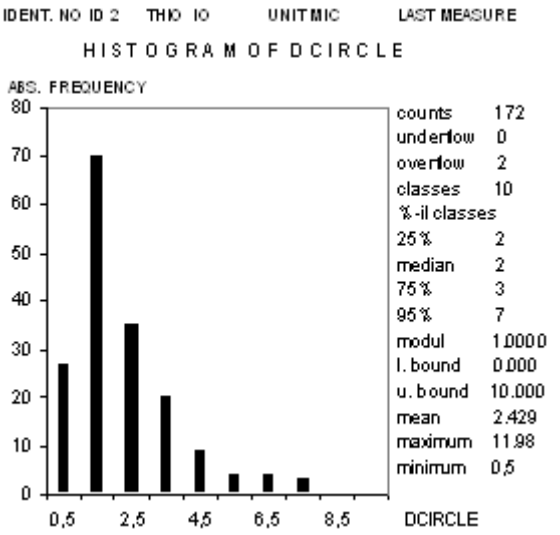

FIGURE 7.19. A histogram of the average particle size distribution of tomato paste particles.

As can be seen from the histogram of the distribution of paste particles by average size, the maximum number of particles (40.7%) has a size of 1 μm to 2 μm. Particles of the largest size of 5-8 microns make up about 2%, and particles with a size of up to 1 micron are about 16%.

The high degree of dispersion of emulsions and dispersion of biological media to the cell size confirms the effectiveness of the rotary pulsation equipment used.

References

[7.1] Protodyakonov I.O., Ulyanov S.V., Hydrodynamics and mass transfer in dispersed liquid-liquid systems. Leningrad: Science, 1986, 272 p. (rus.).

[7.2] Koval V.P., Zhigula V.A., Introduction to aerohydromechanics of multiphase media. Dnepropetrovsk 1975, 90 p. (rus.).

[7.3] Nigmatulin R.I., The dynamics of multiphase media. M.: Science, Part 1, 1987, 464 p. (rus.).

[7.4] Sternin L.E., Schreiber A.A., Multiphase gas flows with particles. M.: Mechanical engineering, 1994, 320 p. (rus.).

[7.5] Dubrovsky V.V., Podvysotsky A.M., Schreiber A.A., An experimental study of droplet crushing by aerodynamic forces. *Applied mathematics and theoretical physics*. No. 5, 1991, pp. 87-93.

[7.6] Pilch M., Erdman C., Use of breakup time data and velocity history data to predict the maximum size of stable fragments for acceleration-induced breakup of a liquid drop. *International Journal of Multiphase Flow*. Vol. 13, No. 6, 1987, pp. 741-757.

[7.7] Hsiang L.P., Faeth G.M., Near-limit drop deformation and secondary breakup. *International Journal of Multiphase Flow*. Vol. 18, No. 5, 1992, pp. 635-652.

[7.8] Hinch E.J., Acrivos A., Long slender drops in a simple shear flow. *Journal of Fluid Mechanics.* Vol. 98, No. 2, 1980, pp. 305-328.

[7.9] Honor A.L., Rivkind V.Ya., Drop dynamics. *Results of science and technology. Mechanics of fluid and gas*. Vol. 17, 1982, pp. 86-159 (rus.).

[7.10] Taylor G.I., The formation of emulsions in definable fields of flow. *Proceedings of the Royal Society of London. Series A.* Vol. 146, 1934, pp. 501-523.

[7.11] Ladyzhenskaya O.A., Mathematical problems of viscous fluid dynamics. Moscow: Science, 1970, 288 p. (rus.).

[7.12] Pozrikidis C., Effects of surface viscosity on the finite deformation of a liquid drop and the rheology of dilute emulsions in simple shearing flow. *Journal of Non-Newtonian Fluid Mechanics.* Vol. 51, No. 2, 1994, pp. 161-178.

[7.13] Rallison J.M., Acrivos A., A numerical study of the deformation and burst of a viscous drop in an extensional flow. *Journal of Fluid Mechanics*. Vol. 89, 1978, pp. 191-200.

[7.14] Rallison J.M., A numerical study of the deformation and burst of a viscous drop in general shear flows. *Journal of Fluid Mechanics.* Vol. 109, 1981, pp. 465-482.

[7.15] Power H., On the Rallison and Acrivos solution for the deformation and burst of a viscous drop in an extensional flow. *Journal of Fluid Mechanics*. Vol. 185, 1987, pp. 547-550.

[7.16] Rallison J.M., Note on the time-dependent deformation of a viscous drop which is almost spherical. *Journal of Fluid Mechanics.* Vol. 98, No. 3, 1980, pp. 625-633.

[7.17] Stone H.A., Leal L.G., The influence of initial deformation on drop breakup in subcritical time-dependent flows at low Reynolds numbers. *Journal of Fluid Mechanics*. Vol. 206, 1989, pp. 223-263.

[7.18] Stone H.A., The effects of surfactants on drop deformation and breakup. *Journal of Fluid Mechanics.* Vol. 220, 1990, pp. 161-186.

[7.19] Feigl K., A numerical procedure for calculating droplet deformation in dispersing flows and experimental verification. Feigl K., Kaufmann S.F.M., Fischer P., Windhab E.J., *Chemical Engineering Science.* Vol. 58, 2003, pp. 2351-2363.

[7.20] Cristini V., Renardy Y., Scalings for Droplet Sizes in Shear-Driven Breakup: Non-Microfluidic Ways to Monodisperse Emulsions. *Fluid Dynamics and Materials Processing*. Vol. 2, No. 2, 2006, pp. 77-93.

[7.21] Kitakawa A., Simulation of break-up behavior of immiscible droplet under shear field by means of continuous-velocity lattice gas cellular automata. *Chemical Engineering Science.* Vol. 60, 2005, pp. 5612-5619.

[7.22] Anderson A., Zheng X., Cristini V., Adaptive unstructured volume remeshing – I: The method. *Journal of Computational Physics*. Vol. 208, 2005, pp. 616-625.

[7.23] Zheng X., Adaptive unstructured volume remeshing – II: Application to two- and three-dimensional level-set simulations of multiphase flow. Zheng X., Lowengrub J., Anderson A., Cristini V.*, Journal of Computational Physics*. Vol. 208, 2005, pp. 626-650.

[7.24] Cristini V., Guido S., Alfani A. etc, Drop breakup and fragment size distribution in shear flow. *Journal of Rheology*. Vol. 47, No. 5, 2003, pp. 1283-1298.

[7.25] Inamuro T.A., Konishi N., Ogino F., Galilean invariant model of the lattice Boltzmann method for multiphase fluid flows using free-energy approach. *Computer Physics Communications.* Vol. 129, 2000, pp. 32-45.

[7.26] Li J., Renardy Y., Renardy M., Numerical simulation of breakup of a viscous drop in simple shear flow through a volume-of-fluid method. *Physics of Fluids.* Vol. 12, No. 2, 2000, pp. 269-282.

[7.27] Stone H.A., Leal L.G., Relaxation and breakup of an initially extended drop in an otherwise quiescent fluid. *Journal of Fluid Mechanics.* Vol. 198, 1989, pp. 399-427.

[7.28] Grace H.P., Dispersion phenomena in high viscosity immiscible fluid systems and application of static mixers as dispersion devices in such systems. *Chemical Engineering Communications*. Vol. 14, 1982, pp. 225-277.

[7.29] Stegeman Y.W., Van de Vosse F.N., Meijer H.E.H., On the applicability of the Grace Curve in practical mixing operations. *The Canadian Journal of Chemical Engineering*. Vol. 80, No. 4, 2002, pp. 632-637.

[7.30] Bentley B.J., Leal L.G., An experimental investigation of drop deformation and breakup in steady, two-dimensional linear flows. *Journal of Fluid Mechanics*. Vol. 167, 1986, pp. 241-283.

[7.31] Stone H.A., Bentley B.J., Leal L.G., An experimental study of transient effects in the breakup of viscous drops. *Journal of Fluid Mechanics.* Vol. 173, 1986, pp. 31-158.

[7.32] Tjahjadi M., Ottino J.M., Stretching and breakup of droplets in chaotic flows. *Journal of Fluid Mechanics.* Vol. 232, 1991, pp. 191-219.

[7.33] Kusch H.A., Ottino J.M., Experiments on mixing in continuous chaotic flow. *Journal of Fluid Mechanics*. Vol. 236, 1992, pp. 319-348.

[7.34] Stone H.A., Dynamics of droplet deformation and breakup in viscous fluids. *Annual Review of Fluid Mechanics*. Vol. 26, 1994, pp. 65-102.

[7.35] Shear Rupturing of Complex Fluids: Application to the Preparation of Quasi-Monodisperse Water-in-Oil-in-Water Double Emulsions. Goubault C., Pays K., Olea D. etc, *Langmuir.* Vol. 17, 2001, pp. 5184-5188.

[7.36] Blawzdziewicz J., Cristini V., Loewenberg M., Critical behavior of drops in linear flows. I. Phenomenological theory for drop dynamics near critical stationary states. *Physics of Fluids.* Vol. 14, No. 8, 2002, pp. 2709-2718.

[7.37] Khakhar D.V., Ottino J.M., Deformation and breakup of slender drops in linear flows. *Journal of Fluid Mechanics.* Vol. 166, 1986, pp. 265-285.

[7.38] Eggers J., Fontelos M.A., Isolated inertialess drops cannot break up. *Journal of Fluid Mechanics.* Vol. 530, 2005, pp. 177-180.

[7.39] Brenner M.P., Breakdown of scaling in droplet fission at high Reynolds number. Brenner M.P., Eggers J., Joseph K. etc, *Physics of Fluids.* Vol. 9, No. 6, 1997, pp. 1573-1590.

[7.40] Khismatullin D.B., Renardy Y., Cristini V., Inertia-induced breakup of highly viscous drops subjected to simple shear. *Physics of Fluids.* Vol. 15, No. 5, 2003, pp. 1351-1354.

[7.41] Cramer C., Fischer P., Windhab E.J., Drop formation in a coflo-wing ambient fluid. *Chemical Engineering Science.* Vol. 59, 2004, pp. 3045-3058.

[7.42] Eggleton C.D., Stebe K.J., An adsorption–desorption-controlled surfactant on a deforming droplet. *Journal of colloid and interface science.* Vol. 208, 1998, pp. 68-80.

[7.43] Drumright-Clarke M.A., Numerical simulations that characterize the effects of surfactant on droplets in shear flow. Dissertation for the degree of Doctor of Philosophy in Mathematics, Blacksburg, Virginia, USA, 2002, 81 p. https://vtechworks.lib.vt.edu/bitstream/handle/10919/26895/Main2.pdf.

[7.44] Kolmogorov A.N., On droplet crushing in a turbulent flow. Reports of the USSR. *Academy of Sciences*. Vol. 66, No. 5, pp. 825-828 (rus.).

[7.45] Hinze J.O., Fundamentals of the hydrodynamic mechanism of splitting in dispersion processes. *American Institute of Chemical Engineers Journal.* Vol. 1, No. 3, 1955, pp. 289-295.

[7.46] Wallis G., One-dimensional two-phase flows. M.: World, 1972, 440 p. (rus.).

[7.47] Abismail B., Emulsification processes: on-line study by multiple light scattering measurements. Abismail B., Canselier J.P., Wil-helm A.M. etc, *Ultrasonic Sonochemistry*. No. 7, 2000, pp. 187-192.

[7.48] Gourdon C., Casamatta G., Angelino H., Single drop experiments with liquid test systems: a way of comparing two types of mechanically agitated extraction columns. *The Chemical Engineering Journal*. Vol. 46, 1991, pp. 137-148.

[7.49] Pacek A., Baker M., Utomo A.T., Characterization of Flow Pattern in a Rotor Stator High Shear Mixer. *Proceedings of European Congress of Chemical Engineering Copenha-gen.* 2007, 16 p.
http://folk.ntnu.no/skoge/prost/proceedings/ecce6_sep07/upload/519.pdf

[7.50] Vikhansky A., Kraft M., Modeling of a RDC using a combined CFD-population balance approach. *Chemical Engineering Science.* Vol. 59, 2004, pp. 2597-2606.

[7.51] Coulaloglou C.A., Tavlarides L.L., Droplet size distribution and coalescence frequencies of liquid-liquid dispersion in flow vessels. *American Institute of Chemical Engineers Journal*. Vol. 22, 1976, pp. 289-297.

[7.52] Calabrese R.V., Chang T.P.K., Dang P.T., Droplet breakup in turbulent stirred contactors, part I: Effect of dispersed phase viscosity. *American Institute of Chemical Engineers Journal*. Vol. 32, 1986, pp. 657-666.

[7.53] Braginsky L.N., Belevitskaya M.A., On droplet crushing with mechanical stirring in the absence of coalescence. *Theoretical foundations of chemical technology.* Vol. 24, No. 4, 1990, pp. 843-852 (rus.).

[7.54] Braginsky L.N., Begachev V.I., Barabash V.M., Mixing in liquid media. L.: Chemistry, 1984, 336 p. (rus.).

[7.55] Tjaberinga W.J., Boon A., Chesters A.K., Model experiments and numerical simulations on emulsification under turbulent conditions. *Chemical engineering science.* Vol. 48, No. 2, 1993, pp. 285-293.

[7.56] Duchemin L., Eggers J., Josserand C., Inviscid coalescence of drops. *Journal of Fluid Mechanics*. Vol. 487, 2003, pp. 167-178.

[7.57] Eggers J., Lister J.R., Stone H.A., Coalescence of liquid drops. *Journal of Fluid Mechanics.* Vol. 401, 1999, pp. 293-310.

[7.58] Eggers J., Singularities in droplet pinching with vanishing viscosity. *SIAM Journal on Applied Mathematics.* Vol. 60, No. 6, 2000, pp. 1997-2008.

[7.59] Kolev N.I., Fragmentation and Coalescence Dynamics in Multiphase Flows. *Experimental Thermal and Fluid Science.* No. 6, 1993, pp. 211-251.

[7.60] Desjonqueres P., Berlemont A., Gouesbet G.A., Lagrangian approach for the prediction of particle dispersion in turbulent flow. *Journal of Aerosol Science.* Vol. 19, No. 1, 1988, pp. 99-103.

[7.61] Megias-Alguacil D., Droplet deformation under simple shear investigated by experiment, numerical simulation and modeling. Megias-Alguacil D., Feigl K., Dressler M., Fischer P., Windhab E.J., *Journal of Non-Newtonian Fluid Mechanics.* Vol. 126, 2005, pp. 153-161.

[7.62] Apte S.V., Gorokhovski M., Moin P., LES of atomizing spray with stochastic modeling of secondary breakup. *International Journal of Multiphase Flow.* Vol. 29, 2003, pp. 1503-1522.

[7.63] Volkov K.N., Transfer of discrete inclusions by flows with concentrated vorticity. *Physics Engineering Journal.* Vol. 80, No. 2, 2007, pp. 36-45.

[7.64] Nakorchevsky A.I., Guly S.I., The transport action of the attached mass in the flow of boiling liquid. *Thermophysics of high temperatures*. Vol. 31, No. 4, 1993, pp. 596-599.

[7.65] Sow S., Hydrodynamics of multiphase media. M.: World, 1971, 536 p. (rus.).

[7.66] Schreiber A.A., Gavin L.B., Naumov V.A., Yatsenko V.P., Turbulent flows of gas suspension. K.: Scientific thought, 1987, 240 p. (rus.).

[7.67] Schreiber A.A., Milyutin V.N., Yatsenko V.P., Hydromechanics of two-component flows with solid polydisperse substance. K.: Scientific thought, 1980, 252 p. (rus.).

[7.68] Ivanitsky G.K., Modeling the processes of deformation and crushing of droplets when moving in a liquid. *Industrial heat engineering.* No. 1, 1997, pp. 8-16.

[7.69] Basok B.I., Pirozhenko I.A., Bulavka A.V., Dispersion analysis of soybean paste obtained by rotary pulsation homogenization. *Industrial heat power engineering*. Vol. 25, No. 4, 2003, pp. 88-92 (rus.).

[7.70] Basok B.I., Pirozhenko I.A., Bulavka A.V., Dispersion analysis of homogeneous biological systems. Abstracts XX scientific conference of the CIS countries "Dispersion systems". Odessa 2002, pp. 25-26 (rus.).

[7.71] Nakorchevsky A.I., Basok B.I., Features of the processing of pasty media in rotary-pulse apparatus. *Industrial heat engineering.* Vol. 23, No. 3, 2001, pp. 18-21 (rus.).

[7.72] Karupu V.Ya., Electron microscopy. K.: High school, 1984, 208 p. (rus.).

Chapter 8

EXPERIMENTAL RESEARCHES OF RPA HYDRAULIC AND THERMAL CHARACTERISTICS

8.1. Experimental stand

To confirm the reliability of the results of theoretical studies, as well as to obtain additional information about the hydrodynamic and thermal characteristics of rotary pulsation apparatuses, experimental studies of these characteristics were carried out. For experimental studies, RPA-type TF-2 was used [8.1]. The results of computational studies relating to the apparatus of this type were considered in chapter 7.

The main working body of the apparatus is the rotor-pulsation unit (RPU), which includes the internal and external stators, and the rotor located between them, connected to the motor shaft. The specified arrangement of working elements can also be supplemented by a disk with blades, which is the impeller of a centrifugal pump, and a cutting element (knife) installed in front of the internal stator. These additional elements are also connected to the motor shaft.

Experimental studies were carried out on the installation, the scheme of which is shown in figure 8.1. In the process of research, the volume liquid in the tank was determined by a measuring ruler with an error of 0.5 dm^3. The duration of filling the receiving tank (10) was measured by a stopwatch with a division value of 0.1 s, and the pressure readings were recorded with a standard gauge (6) with a division price of 200 Pa. The hydraulic characteristics of the RPA for the steady state of its operation were determined at a given speed of rotation of the motor shaft. The required speed was set using the frequency converter (5). The energy consumption of the electric motor was determined by the K-505 measuring complex with an accuracy class of 0.5, including a wattmeter with a division price of 2.5 W, a voltmeter with a division price of 2.5 V and an ammeter with a division price of 0.1 A. The engine speed was measured with a digital tachometer (4). The fluid flow through the apparatus was determined using a flow meter (11) of the Hydrometer E-TX type, as well as by the volumetric method. The temperature was measured using primary measuring transducers – thermoelectric thermometers (12-14), differential thermoelectric thermometers (16, 17) and secondary automatic devices: KSP-4 (15), millivoltmeters SC 68000 (18) and B 7-35 (19).

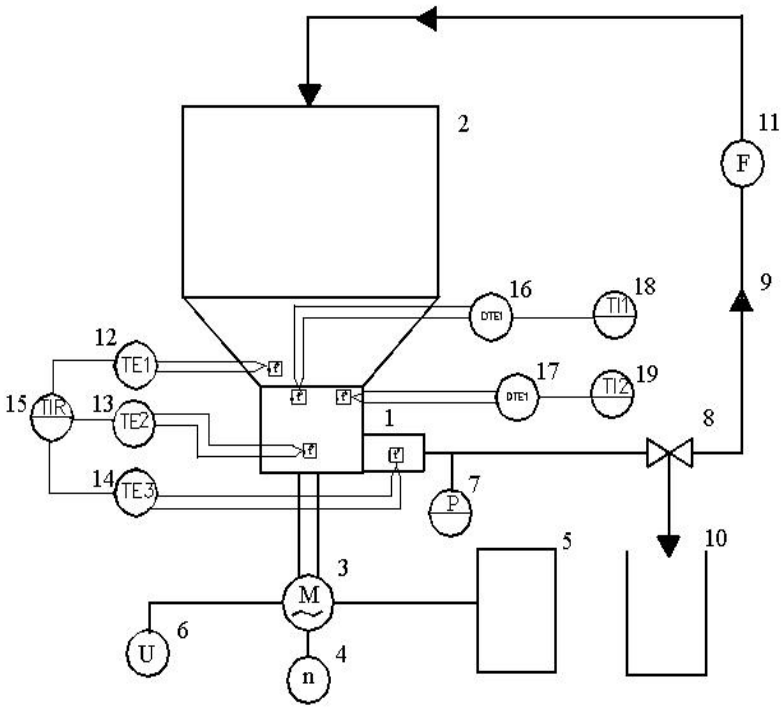

FIGURE 8.1. Schematic diagram of the experimental setup: 1 – rotor-pulsation unit, 2 – measured capacity, 3 – electric motor, 4 – tachometer, 5 – frequency converter, 6 – measuring system, 7 – pressure gauge, 8 – three-way control valve, 9 – flexible pipe, 10 – receiving tank, 11 – flow meter, 12, 13, 14 – thermoelectric thermometers, 15 – potentiometer, 16, 17 – differential thermoelectric thermometers, 18, 19 – millivoltmeters.

8.2. The methodology of experimental research

Studies of pressure and flow characteristics of RPA were carried out according to the following method. Before starting the RPA, the measuring tank (2) was filled with a working fluid, for example, industrial water. Using an additional three-way valve, the line connected to the pressure gauge was purged, which ensured both the filling of an annular tube suitable for pressure gauge (7) and the elimination of a possible pressure measurement error. The frequency converter (5) set the specified rotation speed of the motor shaft (3), as well as the RPA rotating elements fixed on it: a knife, a rotor and a disk with blades. The number of revolutions of the electric motor was determined by the readings of the tachometer (4). The working medium from the measuring tank (2) was sent to the rotor-pulsation unit (1) and passed through the elements of its design. After exiting this unit, the medium being processed through the outlet pipe through the hydrotract 9 again entered the measuring tank (2).

The pressure head characteristic of the apparatus for various layout options of the elements of the rotor-pulsating unit was determined by the indications of a reference manometer (7). The fluid flow rate was determined using a flow meter (11). In addition, the flow rate was also calculated by determining the time of filling the reservoir (10) of a known volume with the working medium. The dependence of the liquid flow rate through the apparatus on time was also established. In parallel, the following were measured: pressure, voltage, current, power and engine speed.

After all measurements related to a given rotor speed, a different speed was set using the frequency converter (5), which was recorded by a tachometer (4). For the new rotor speed, the pressure and flow characteristics of the RPA were measured in different arrangements of the elements of the rotor-pulsation unit in the same order.

In the study of the thermal characteristics of the RPA, the temperature was measured at some of its characteristic points: at the entrance to the RPU, in the RPU building, at the exit from the RPU. Temperature measurement, as already mentioned, was carried out using thermoelectric thermometers 12-14, 16-17 and instruments 15, 18, 19.

Thermoelectric thermometers consisted of two thermocouples soldered and insulated along the length. Thermoelectrode materials – chromel and kopel. Differential thermoelectric thermometers consisted of chromel-alumel thermocouples. To protect against external electromagnetic fields and mechanical influences, the thermo-electrodes were covered with bakelite.

As secondary devices working with thermoelectric thermometers, millivoltmeters were used: SC 68000 (accuracy class 0.25), 7-35 (accuracy class 0.25), as well as an automatic 12-point potentiometer KSP-4 (class accuracy 0.25), in which a bridge measuring scheme was used, providing continuous correction of the temperature of the free ends of the thermometer.

Calibration of thermoelectric thermometers 12-14 was carried out using a potentiometer KSP-4. Differential thermoelectric thermometers 16 and 17 were calibrated using millivoltmeters SC 68000 and B 7-35. As a result of calibration, appropriate calibration schedules and dependencies were built.

8.3. RPA hydraulic characteristics studies

For experimental studies, water and sunflower oil were used as model media. The studies were carried out at various values of the rotor speed, which varied from 0 to 100 rev/s.

In the previous sections, the basic three-element ("stator-rotor-stator") RPA scheme was mainly considered. In order to increase the flow rate of the treated heterogeneous medium, as well as for preliminary grinding of solid-state inclusions, the considered basic scheme of the apparatus was supplemented with such elements as a blade with blades and a "knife". The knife is similar to a rotor located in front of the inner stator, in which the slots have sharp edges. Both of these elements are connected to a rotating shaft of an electric motor.

To clarify the influence of these additional elements on the hydrodynamic characteristics of RPA type TF-2, experimental studies were carried out for the following options for the arrangement of working bodies:

a) shaft-stator-rotor-stator (basic three-element circuit);
b) a shaft disk with blades;
c) shaft-knife-stator-rotor-stator;
d) shaft-knife-stator-rotor-stator-disk with blades (complete assembly).

The results of these experimental studies are presented in figures 8.2, 8.3. Water (μ = 0.001 Pa·s) was used as a model medium for these studies. The data presented in figure 8.2, indicate a close to linear dependence of the fluid flow rate G_r on the number of revolutions n. Moreover, the slope of the curves related to different layouts of RPA working elements is also different.

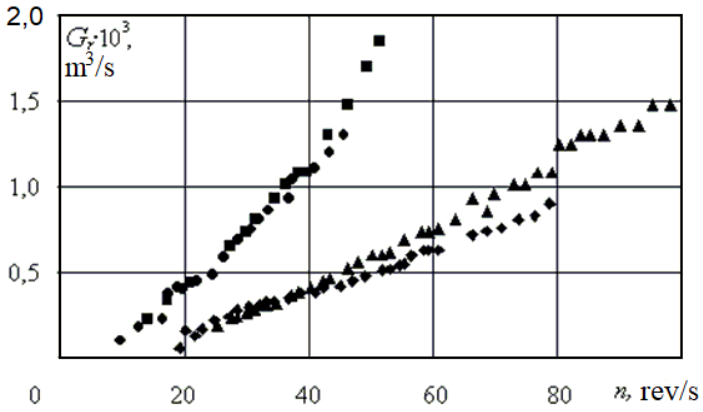

FIGURE 8.2. The dependence of the fluid flow on the RPA electric motor speed for various configurations of working elements: ♦ – shaft + RPA itself, ● – shaft + disk with blades, ▲ – shaft + RPA proper + knife, ■ – RPA in full assembly.

As can be seen from figure 8.2, the installation of a disk with blades leads to a significant increase in flow rate. So at n = 47 rev/s (the nominal value of the rotational speed of the motor shaft), the RPA itself, assembled according to the stator-rotor-stator scheme, provides a flow rate of $0.45 \cdot 10^{-3}$ m^3/s. When the "knife"

element is added to the scheme in front of the internal stator, the flow rate increases by another $0.12 \cdot 10^{-3}$ m^3/s. If there is a disk with blades, the fluid flow increases to $G = 1.35 \cdot 10^{-3}$ m^3/s. For the case of RPA in the complete assembly, the flow rate reaches a value of $1.52 \cdot 10^{-3}$ m^3/s.

From the presented results it follows that when installing additional rotating elements (a disk with blades and a knife) on the motor shaft, an increase in the flow rate of the liquid through the apparatus is observed. This is due to an increase in the pumping effect caused by centrifugal forces acting on the rotating fluid. This effect is also associated with the experimentally observed increase in pressure at the outlet of the RPA working zone. As can be seen from figure 8.3, at $n = 47$ rev/s, the pressure of the liquid at the outlet of the RPA, equipped with a rotating disk with blades, exceeds the pressure created by the apparatus itself without the indicated element by 21.3 kPa. In the case of RPA in complete assembly, the fluid pressure at the outlet of the apparatus reaches 73 kPa.

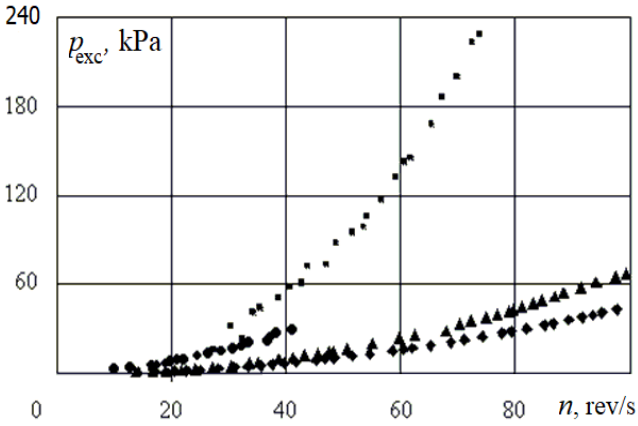

FIGURE 8.3. The dependence of the fluid pressure at the outlet of the RPA on the number of revolutions of the electric motor for various options for the arrangement of working elements: ♦ – shaft + RPA proper, ● – shaft + disk with blades, ▲ – shaft + RPA proper + knife, ■ – RPA in complete assembly.

An important energy characteristic of rotary-pulsating devices is the power consumption Q. According to the experiment, the power consumed by the RPA type TF-2 in complete assembly at a speed of 0...75 rev/s varies in the range 0...880 W (fig. 8.4).

The influence of the viscosity of the medium on the hydrodynamic characteristics of RPA was established by comparing the results of experimental studies obtained in the treatment of water and sunflower oil. The experiments were carried out in an apparatus of the TF-2 type, assembled according to the basic three-element

scheme. From the obtained results it follows that the dependences between the pressure p_{exc} at the outlet of the RPA and the engine speed both in the treatment of water and oil are close to quadratic. Moreover, the curve obtained for water is higher than the curve corresponding to vegetable oil, which is associated with a higher viscosity of the latter. The dependences of the flow rates of media processed in RPA on the number of rotor revolutions are close to linear. The curve obtained during water treatment lies above the corresponding curve for oil, which is also associated with its higher viscosity.

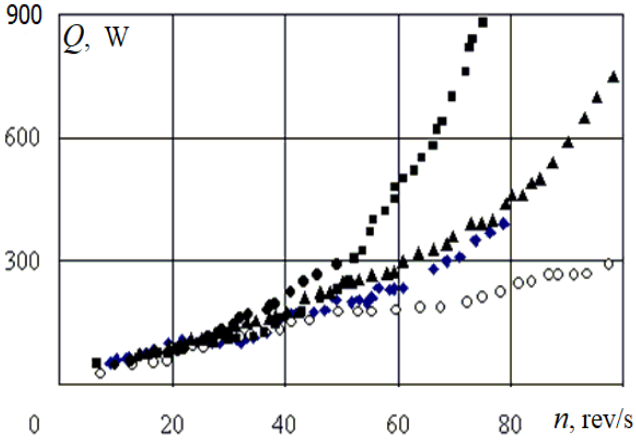

FIGURE 8.4. The power consumed by the RPA, depending on the number of revolutions for various options for the arrangement of working elements: ♦ – shaft + RPA itself, ● – shaft + disk with blades, ▲ – shaft + RPA proper + knife, ■ – RPA in full assembly, and points ○ – only RPA shaft.

Thus, in the processing of vegetable oil (highly viscous medium), the head and flow rates are lower than in the case of processing a low-viscosity medium (in this case, water). It should be noted that the flow of liquids along the hydrodynamic path in the case of the basic layout scheme was observed only when the shaft reached the threshold value of the number of revolutions. In these experiments, it corresponded to n = 38 rev/s. As a result of this, the curves reflecting the dependence of the flow rate on the number of revolutions did not pass through the origin. From this it follows that the translational motion of the liquid under conditions when the pressure at the outlet of the RPA working zone exceeds the pressure at the entrance to the working zone is observed only at $n > 38$ rev/s.

Experimental studies of the hydraulic characteristics of a rotary pulsation apparatus of the TF-2 type made it possible to establish the character of the change in pressure at the outlet of the apparatus working zone and the flow rates of the treated media with different viscosities at a variable engine speed in recirculation

mode. It was established that the rotor-pulsating apparatus included in the hydraulic scheme shown in figure 8.1, operates in a mode in which the pressure at the outlet of the RPA working area exceeds the pressure at the inlet to the working area ($\Delta p < 0$). This mode arises due to the fact that the liquid levels in the loading tank and in the outlet cross section of the outlet pipe practically coincide, and the hydrodynamic pressure loss in the outlet fitting and pipe exceeds the pressure loss during the lower flow of liquid from the loading tank into the RPA working volume. Features of this mode were considered in subsection 5.7.

With an increase in the angular velocity of rotation of the rotor associated with the shaft of the electric motor, the flow rate of the processed medium increases. With an increase in flow rate, pressure losses in pipeline 9 also increase (fig. 8.1), which results in an increase in fluid pressure at the outlet of the RPA (fig. 8.3). Each rotating element complementing the design of the RPA enhances the centrifugal effect, which leads to an increase in flow rate, an increase in pressure at the outlet of the RPA working area and, accordingly, an increase in power consumption.

The method of numerical simulation was used to obtain the dependence of the mass-average radial velocity of the fluid $\bar{V}_r$ on the angular velocity of rotation of the rotor ω_0. As the initial data for the calculations, the condition was accepted that, regardless of the number of revolutions n, the differential pressure Δp was equal to zero. A similar calculated dependence can be constructed for the hydraulic circuit considered in figure 8.1, for which an experimental dependence of Δp on the engine speed n was obtained. The dependence of water flow ($\mu = 0.001$ Pa·s) on the angular velocity ω_0, which was found by numerical simulation, taking into account the real values of Δp, is shown in figure 8.5 (solid curve). Here, the experimentally obtained dependence is plotted, reflected in figure 8.2 (bottom curve).

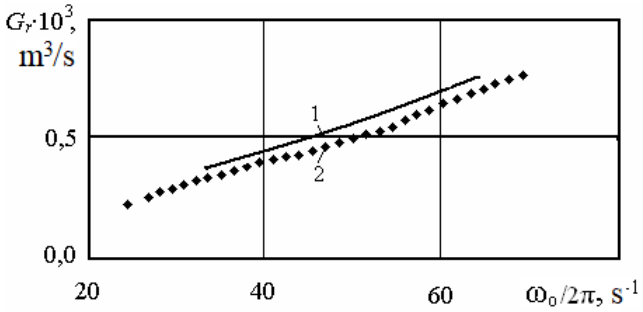

FIGURE 8.5. The dependence of the volumetric average fluid flow on the rotor speed: —— – calculation results (line 1); ♦ – experimental results (line 2).

As can be seen from figure 8.5, the results of numerical simulation are in satisfactory agreement with the experimental results.

8.4. The study of the temperature characteristics of RPA

Chapter 6 examined the results of numerical simulation of the temperature state of RPA. This section presents the results of experimental studies of the temperature conditions of these devices. Graphs of temperature dependences of liquids processed in RPA in the recirculation mode are presented in (fig. 8.6-8.8). As model media, water and vegetable oil were used.

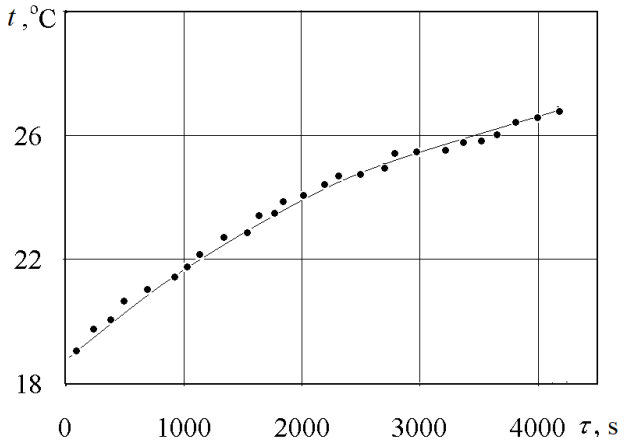

FIGURE 8.6. The change in time of the water temperature at the entrance to the RPA.

As can be seen from figure 8.6, when water was treated for $4 \cdot 10^3$ seconds, its temperature increased by 7.8°C due to energy dissipation. In this case, the temperature difference between the liquid at the inlet and outlet of the working area of the apparatus was approximately dT = 0.16...0.17°C. This value characterizes the increase in water temperature in one pass through the RPA.

The temperature dependences obtained for vegetable oil (fig. 8.7) indicate that its temperature during the treatment increases significantly more than the temperature of water. Since the viscosity of vegetable oil in the considered temperature range significantly exceeds the viscosity of water, the amount of heat released due to energy dissipation turns out to be greater than when treated with water. So for a time of $2.5 \cdot 10^3$ s, the temperature at the inlet to the apparatus increased by 12°C. The change in oil temperature between the inlet and the outlet of the apparatus exceeds the similar indicators for water by an order of magnitude and amounts to $dT \sim$ 1.5...2.5°C.

In figure 8.7, the solid line also shows the time dependence of the temperature of the sunflower oil at the outlet of the RPA, obtained by calculation using dependence (6.1). As can be seen from the figure, the calculated curve lies slightly higher than the experimental one, which, apparently, is associated with not taking

into account all real heat losses to the surrounding space. On the whole, the calculated data are in satisfactory agreement with the experimental data. Their maximum discrepancy is 1.7°C.

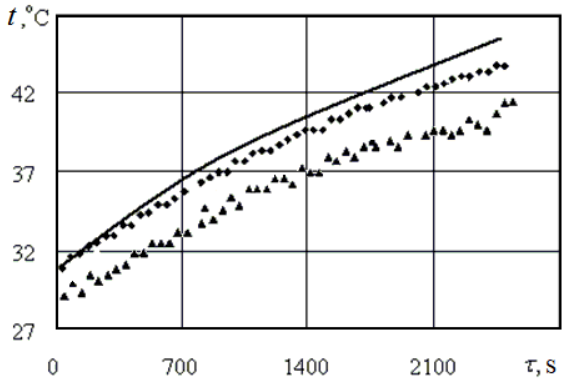

FIGURE 8.7. The change in temperature of vegetable oil over time during its processing in RPA: ▲ – at the entrance to the apparatus; ♦ – at the exit of the apparatus; ▬ – calculation results (line).

The experimental studies of the temperature characteristics of the rotary pulsation apparatus of the TF-2 type made it possible to establish that during the processing of vegetable oil a more intense increase in the temperature of the medium is observed than in the case of water treatment, which indicates a higher degree of energy dissipation for liquids with high viscosity.

An even higher degree of temperature increase during processing in RPA is observed in such a highly viscous heterogeneous medium as soybean paste. Its rheological properties, considered in chapter 6, are reflected in figure 6.15 and in table 6.2. During the flow of such a medium, the presence of internal friction leads to intense energy dissipation, which causes a significant heating of the paste during its processing (fig. 8.8).

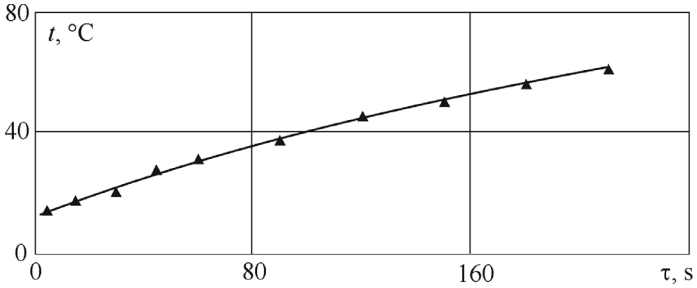

FIGURE 8.8. The change in temperature of soybean paste over time during its processing in RPA.

Thus, as a result of experimental studies, the pressure, consumable, and energy characteristics of the rotor-pulsation type TF-2 were established in the range of the engine speed 0÷100 rev/s. The thermal characteristics of RPA in the treatment of media with different viscosities were also studied. At the same number of revolutions of the electric motor, those media with a higher viscosity are heated more intensely. A comparison of the experimental data with the calculated ones shows their satisfactory agreement.

8.5. Experimental studies of the structural and mechanical characteristics of soybean paste

Chapter 6 presents the results of numerical simulation of the dynamic and temperature conditions of RPA during the processing of highly viscous non-Newtonian fluids. The characteristic features of such regimes were considered by the example of processing soybean paste in RPA. As initial data for numerical modeling, the results of experimental studies of the structural and mechanical characteristics of soybean paste (table 6.2) were used, which should be considered in more detail.

Structural and mechanical characteristics of soybean paste were measured on a Reotest-2.1 rotational viscometer using cylindrical measuring devices [8.2]. The test medium was placed in an annular gap between two coaxial cylinders. The outer cylinder in order to maintain a given temperature during the experiment was placed in a thermostat.

The rheological properties of soybean paste were determined based on the relationship between the set value of the shear rate and the measured value of shear stress. Measurements were carried out at steady state fluid flow in the gap between the cylinders at different temperatures of the product under study and various values of the concentration of water in the soybean paste.

The results of measurements of the shear stress in soybean paste with a water concentration of $C = 0.65$ are presented in figure 8.9. Studies were conducted for various ranges of shear rate changes.

As can be seen from figure 8.9, the dependence of the shear stress σ on the shear rate $\dot{\gamma}$ – is nonlinear. At low shear rates, at which the structure of soybean paste is not yet destroyed, the slope of curve $\sigma(\dot{\gamma})$ is steeper than at large $\dot{\gamma}$. As the strain rate increases, the spatial structure of the soybean paste is intensively destroyed, and the slope of the curve becomes more gentle. It should be noted that the nonlinear shape of the curve under consideration is a characteristic feature of structurally viscous media. This means that the effective viscosity for such media is not constant. With an increase in the strain rate, it decreases according to some law, which turns out to be similar to the Balkley-Herschel law [8.3]: $\sigma = \sigma_0 + A\dot{\gamma}^k$, where σ_0 is the shear stress limit value; A and k are rheological constants.

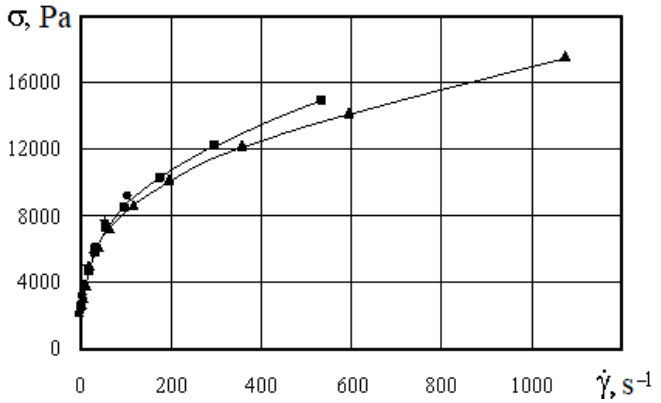

FIGURE 8.9. Dependences of shear stress on shear rate for soybean paste with water concentration C = 0.65: ▲ – 2.453...1073 s^{-1}; ■ – 1.227...536 s^{-1}; ● – 0.33...107.3 s^{-1}; + – 0.033...53.6 s^{-1}.

Using the above dependence to describe the obtained experimental results involves determining the value of the ultimate shear stress σ_0. To determine σ_0, it is advisable $\sigma = f(\dot{\gamma})$ to represent the dependence in logarithmic coordinates $\lg\sigma = f(\lg\dot{\gamma})$. The values of empirical coefficients for the above equation were established based on the dependence $\lg(\sigma - \sigma_0) = f(\lg\dot{\gamma})$ for soybean paste at different temperatures (fig. 8.10).

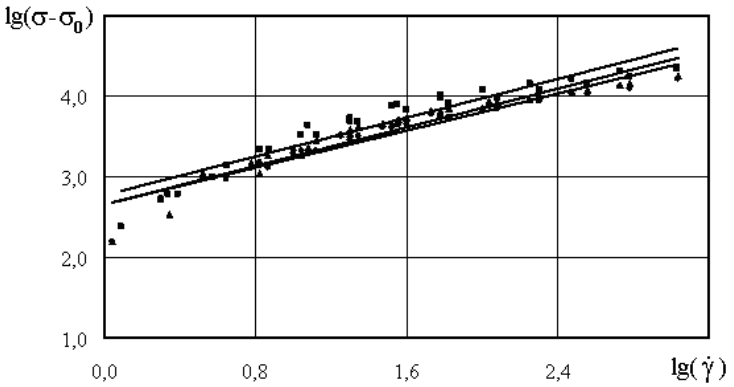

FIGURE 8.10. The dependence of the difference $(\sigma - \sigma_0)$ on the shear rate at various temperatures: ▲ – t = 40°C; ■ – t = 35°C; ● – t = 17°C.

The obtained stress values at various shear rates made it possible to calculate the effective viscosity values $\mu = d\sigma / d\dot{\gamma}$, the dependences of which on the shear rate at temperatures: 17°C, 35°C, and 40°C are presented in figure 8.11. These

dependences can be conditionally divided into three zones: in the first, the effective viscosity drops sharply, in the second, its insignificant change is observed, and the third zone is characterized by an almost constant effective viscosity, characteristic of visco-plastic media [8.4]. This rheological behavior of the paste is due to the ratio of the broken and restored bonds of the structure, depending on the magnitude of the shear stress.

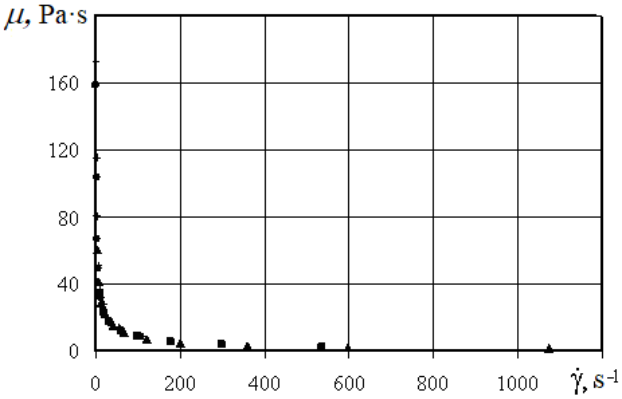

FIGURE 8.11. The dependence of the effective viscosity on shear rate: ▲ – 2.453...1073 s^{-1}; ■ – 1.227...536 s^{-1}; ● – 0.33...107.3 s^{-1}; + – 0.033... 53.6 s^{-1}.

The value of the initial viscosity μ_0 was determined from the dependence $\lg\mu = f(\lg\dot{\gamma})$ by finding the point of intersection of the approximating line with the axis $\lg\mu$ (fig. 8.12). The results obtained indicate that an increase in the concentration of the aqueous phase and temperature, respectively, leads to a decrease in the ultimate shear stress and initial viscosity.

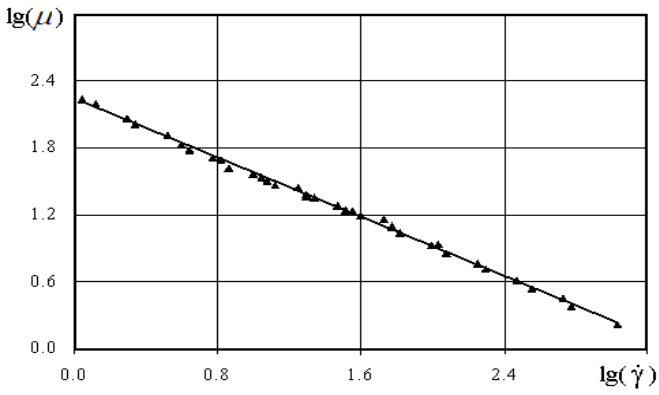

FIGRE 8.12. The dependence of the effective viscosity on shear rate.

The values of the limiting shear stresses σ_0, initial viscosities μ_0, as well as the coefficients of the approximating equation describing the dependence of viscosity on shear rate at temperatures of 17°C, 35°C, and 40°C and various concentrations of the aqueous phase added to the paste are presented in table 8.1. Using the results obtained, the values of the dynamic viscosity coefficients of soybean paste were calculated as a function of temperature for a shear rate $\dot{\gamma} = 10^4$ s^{-1}, which is characteristic of a rotary-pulsation apparatus of the BGT type. As can be seen from figure 8.13, this dependence has a linear character $\mu = -0.0088 \cdot T + 0.727$ (μ has the dimension Pa·s, and T – °C).

TABLE 8.1. Rheological characteristics of soybean paste under various initial conditions.

Trend loading	Concentration of an aqueous phase	Tempe-rature	Initial viscosity	The dependence of stress on shear rate $\sigma = \sigma_0 + A\dot{\gamma}^k$		
				Coefficient Values		
	C	T, °C	μ_0, Pa·s	σ_0, Pa	k	A
decrease	0	17	281.9	2819	0.264	3469
		34	194.5	1945	0.361	1700
		40	172.5	1753	0.361	1507
increase	0.2	15	274.7	2747	0.263	3469
		40	164.9	1649	0.323	1341
increase	0.3	15	253	2530	0.215	4236
		40	159.8	1598	0.312	1389
decrease	0.4	17	124.4	1245	0.400	1010
decrease	0.6	17	92.5	925	0.410	712
		40	88.3	883	0.381	640

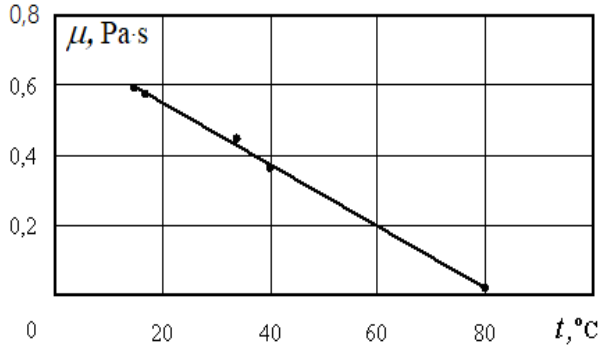

FIGURE 8.13. Dependence $\mu(t)$ for soybean paste at $\dot{\gamma} = 10^4$ s^{-1}.

In plastic disperse systems, a change in structure is observed under prolonged loading, which can lead to an irreversible change in rheological properties, as well as the manifestation of hysteresis phenomena [8.5]. In the process of studying the viscosity of soybean paste when measuring shear stresses with increasing and decreasing shear rates, it was found that the rheological properties have hysteresis.

In figure 8.14 shows the experimental data for the range of shear rate variation $\dot{\gamma}$ = 0.123...54 s^{-1} (fig. 8.14a), as well as $\dot{\gamma}$ = 0.245...1073 s^{-1} (fig. 8.14b). With a rather rapid cyclic increase, and then a decrease in the shear rate, a characteristic hysteresis curve appears on the graph, indicating a delay in structural changes compared with the change in load.

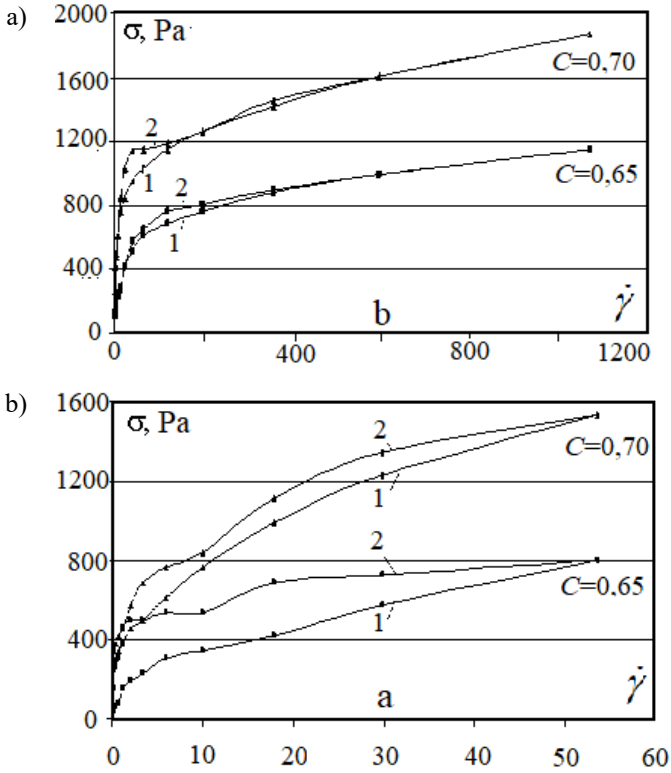

FIGURE 8.14. The hysteresis of the rheological properties of soybean paste at a temperature of 17°C in the shear rate ranges: a) 0.123...54 s^{-1}, b) 0.245...1073 s^{-1}: ■ – C = 0.65, ▲ – C = 0.7; 1 – loading; 2 – unloading.

This fact allows us to attribute the studied medium to thixotropic systems [8.5], which are characterized by intense reversible structural destruction upon deviations from mechanical equilibrium and structural restoration upon removal of the load.

This feature of structural changes in thixotropic properties under shear loads should also affect the course of other thermophysical processes.

Another characteristic feature of the rheological properties of soybean paste is the presence of relaxation phenomena in its structure. The results of experimental studies indicate that these relaxation processes proceed quite slowly. The relaxation time of undiluted soybean paste at room temperature is tens of minutes, while diluted paste is tens of seconds.

References

[8.1] Basok B.I., Hydraulic characteristics of the rotary pulsation apparatus TF-2. Basok B.I., Pirozhenko I.A., Nezhuta V.P. et al., Bulletin of the National Technical University of Ukraine "KPI", series "Mechanical Engineering". Vol. 43, 2002, pp. 160-162 (rus.).

[8.2] “Reotest 2.1” is a cylindrical and cone-plate rotational viscometer. User manual. MLW, 1981, 20 p. (rus.)

[8.3] Lykov A.V., Rheophysics and rheodynamics of fluid systems. Ed. Lykova A.V., Shulmana Z.P., Minsk: Publishing House “Science and Technology”, 1970, 172 p. (rus.).

[8.4] Belkin I.M., Rotary appliances. Measurement of viscosity and physical and mechanical characteristics of materials. M.: Mechanical Engineering, 1967, 272 p. (rus.)

[8.5] Lykov A.V., Berkovsky B.M., Transfer laws in non-Newtonian fluids. Heat and mass transfer in non-Newtonian fluids. M.: Energy, 1968, pp. 5-14 (rus.).

[8.6] Basok B.I., Davydenko B.V., Avramenko A.A., Pirozhenko I.A., Hydrodynamics, heat transfer and crushing effects in rotationally pulsating flows. Kiev 2012, 298 p. (rus.)

INFLUENCE OF RPA CONSTRUCTION AND MODE PARAMETERS ON MEDIA CHARACTERISTICS

9.1. Comparison of the hydrodynamic and thermal modes of operation of rotary-pulsating apparatuses with different arrangement of working bodies

Previously, cylindrical RPA assembled according to the "stator-rotor-stator" scheme were considered (fig. 9.1a). Such a scheme is the most common, although not the only one. For the processing of highly viscous media, apparatuses assembled according to the "rotor-stator-rotor" scheme [9.1] are also used (fig. 9.1b). In contrast to the previously considered scheme, in this case, the inner and outer cylindrical working elements rotate (rotors), and the middle element is stationary (stator). In addition, two-element working bodies are possible, consisting of an internal rotor and an external stator (fig. 9.1c), as well as an internal stator and an external rotor (fig. 9.1d).

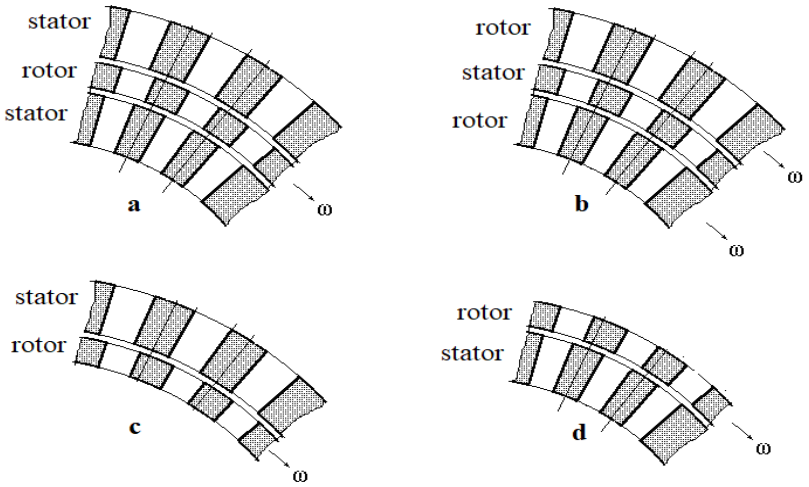

FIGURE 9.1. Different ways of arranging RPA working bodies.

Consider the features of the dynamics of fluid flows in RPA presented in figure 9.1 modifications and compare them with each other. The basic version (fig. 9.1a) has geometric dimensions: internal stator: $r_0 = 55.0$ mm; $r_1 = 58.9$ mm; rotor: $r_2 = 59.1$

mm; $r_3 = 62.9$ mm; outer stator: $r_4 = 63.1$ mm; $r_5 = 67.0$ mm. In the rotor-stator-rotor arrangement, instead of the outer and inner stators, two rotors will be present with the same geometrical dimensions, and a stator instead of the central rotor. Two-element arrangements have two working bodies, the dimensions of which correspond to the internal stator and rotor of the basic version. The number of slots in all elements is 60.

In contrast to the statement of the problem of fluid flow in the RPA working area considered earlier, in this case, the computational domain is supplemented by an upstream section of a width of 1 mm in front of the inner cylindrical working element and a section of the same width following the external working element. Boundary conditions of the form (4.11), (4.12) are now set not on the boundary surfaces of the working elements, as it was before, but on the inner and outer borders of the upstream sections. Moreover, if a fixed element (stator) is adjacent to the boundary of the computational domain, then the condition for the angular velocity at the boundary will be the same as in expressions (4.11), (4.12), namely $\Omega\left(R_{\text{bo}},\theta\right) = 0$ (R_{bo} – radius of the inner or outer borders of the upstream sections). If the rotor is adjacent to the boundary, then the condition at this boundary is represented in the form $\left.\dfrac{\partial\Omega}{\partial R}\right|_{R=R_{\text{bo}}} = 0$. For all four layout options, the pressure drop between the input and output sections of the working area was taken to be +10 kPa. The calculations were performed for a liquid with a viscosity coefficient μ = 0.1 Pa·s. The rotor speed is $\omega_0 = 100\,\pi$ s^{-1}.

In figures 9.2-9.5 presents the directions of the velocity vectors and the overpressure field for the above layout options for RPA working bodies. As before, in the slots of the stators, the velocity vectors are constructed relative to the fixed coordinate system, and in the slots of the rotors – relatively mobile.

Analysis of the results of numerical simulation showed that in the working area of the apparatus assembled according to the “rotor-stator-rotor” scheme, the fluid movement is more intense than in the case of the basic “stator-rotor-stator” scheme. This is evidenced by powerful vortex flows in all slots of the working elements. In the case of the basic scheme, in the slot of the internal stator, vortex formation is observed only at the exit from this slot. This is caused by the fact that in the “rotor-stator-rotor” scheme, the rotational motion of the liquid is initiated by the rotation of four cylindrical surfaces, and not two, as in the case of the “stator-rotor-stator” scheme. Moreover, the more intense the rotational movement of the fluid, the greater the importance of centrifugal forces, forcing the fluid to move in the radial direction.

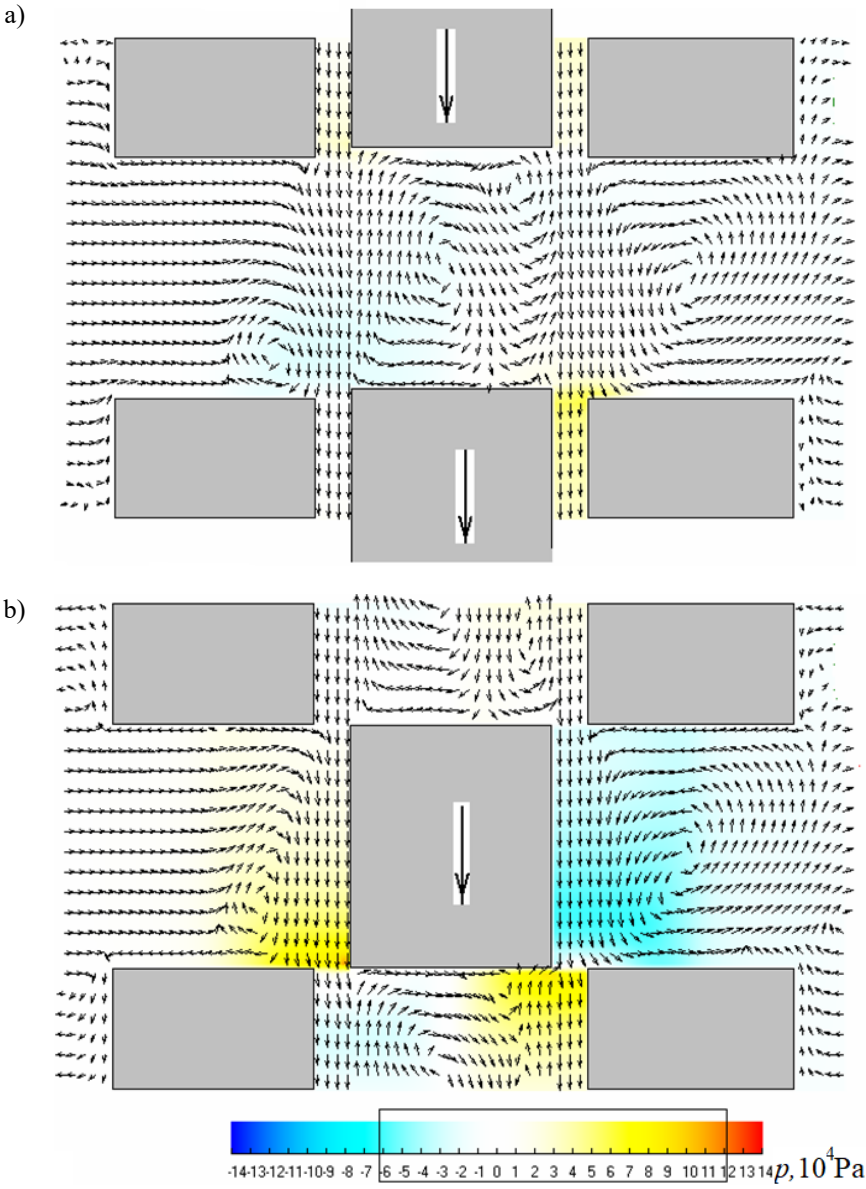

FIGURE 9.2. The picture of the fluid flow and the overpressure field in the RPA working area, assembled according to the "stator-rotor-stator" scheme: a) $\tau/\Delta\tau = 0$; b) $\tau/\Delta\tau = 1/2$.

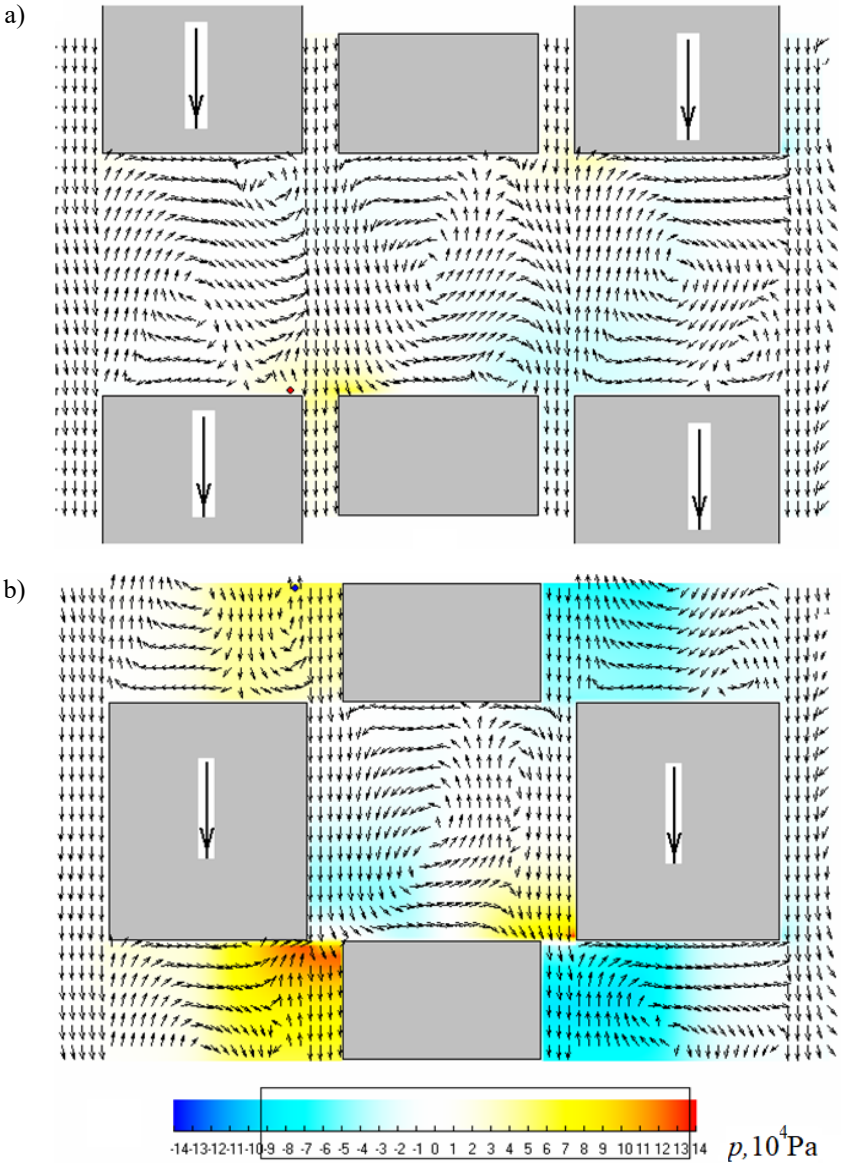

FIGURE 9.3. The picture of the fluid flow and the overpressure field in the RPA working area assembled according to the "rotor-stator-rotor" scheme: a) $\tau/\Delta\tau = 0$; b) $\tau/\Delta\tau = 1/2$.

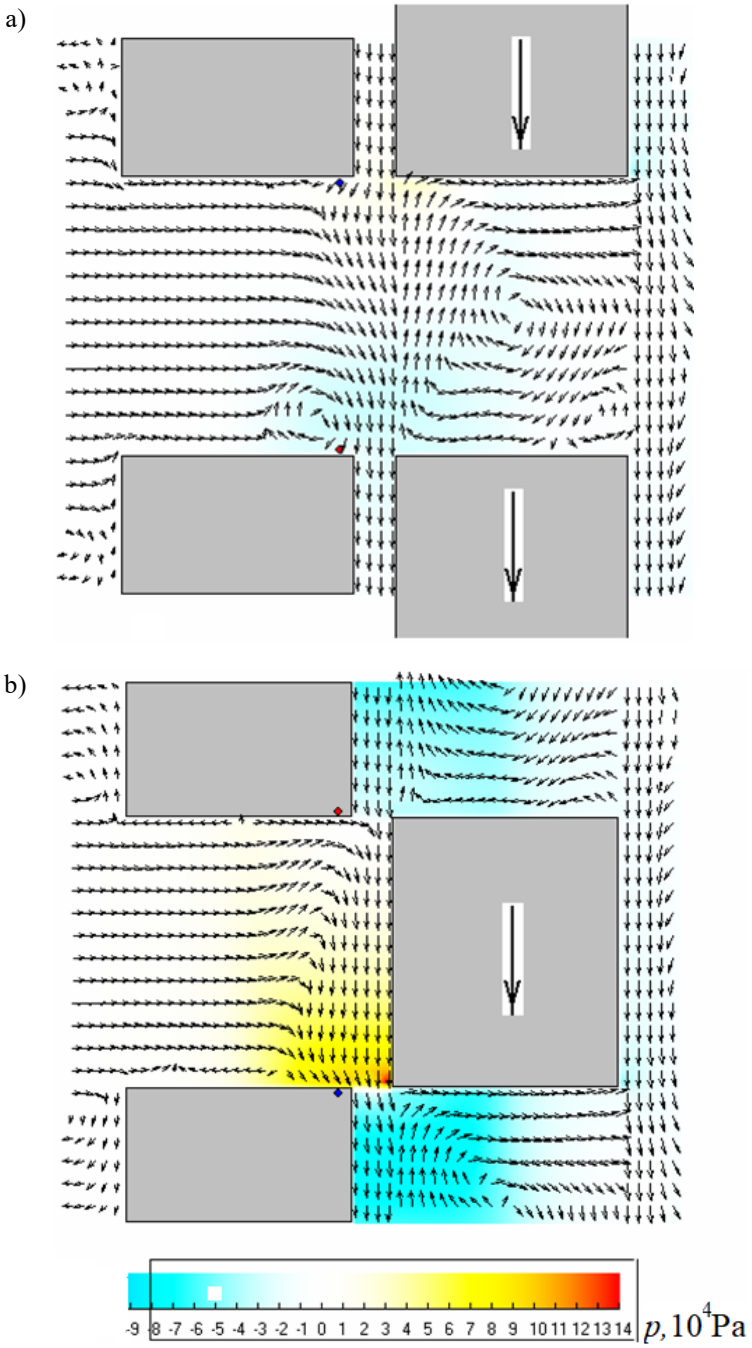

FIGURE 9.4. The picture of the fluid flow and the overpressure field in the RPA working area, assembled according to the "stator-rotor" scheme: a) $\tau/\Delta\tau = 0$; b) $\tau/\Delta\tau = 1/2$.

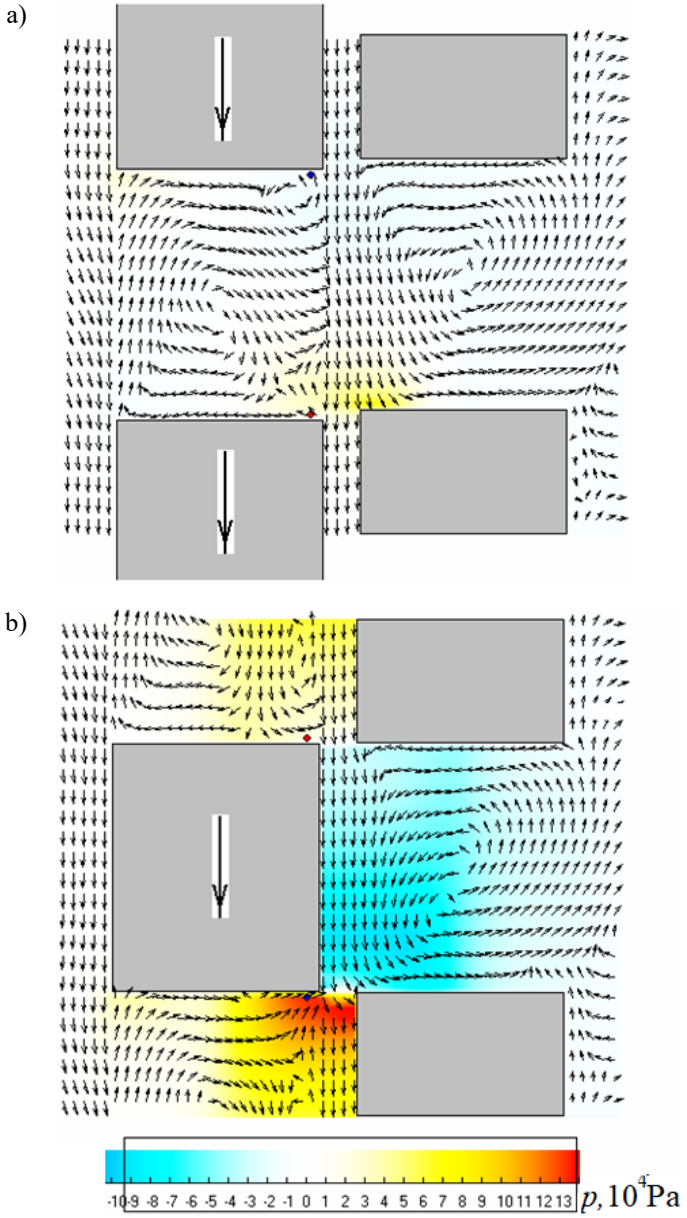

FIGURE 9.5. The picture of the fluid flow and the overpressure field in the RPA working area assembled according to the "rotor-stator" scheme: a) $\tau/\Delta\tau = 0$; b) $\tau/\Delta\tau = 1/2$.

The character of the pressure distribution in the internal gap of the apparatus with two rotors is qualitatively similar to the distribution of pressure in the external gap of the apparatus with two stators (fig. 9.2, 9.3). In the external gap of the two-rotor apparatus, the character of the pressure change is qualitatively similar to the pressure

change in the internal gap of the single-rotor apparatus. However, the range of pressure changes in the working area is significantly higher in the case of the rotor-stator-rotor scheme. A comparison of the pressure fields shows that at the moment of complete mutual overlapping of the slots of the rotating and stationary elements in the "stator-rotor-stator" scheme, the overpressure in the working zone changes from -61.5 kPa to +12.1 kPa, and in the case of the "rotor-stator-rotor" from -92.0 kPa to +13.8 kPa. Practically the same pressure change intervals at a specified point in time are observed in the cases of both schemes with two working elements.

The main reason for the pulsating increase in pressure in the gaps at the moment of mutual overlapping of the slots is associated with a significant decrease in the flow area for the radial fluid flow and its sharp braking. At this moment, a phenomenon similar to water hammer occurs. As will be shown below, the various layout schemes of the working bodies provide for the same differential pressure Δp different flow rates of the fluid in the radial direction. This explains the differences in the ranges of pressure changes in the working areas of the apparatus, assembled according to different layout schemes.

As already mentioned, the radial motion of the fluid is provided by both the differential pressure Δp and the centrifugal force caused by the rotational motion of the fluid. The rotational movement of the fluid is ensured by the frictional forces between the moving cylindrical surfaces and the adjoining layers of the medium to be treated. In the "rotor-stator-rotor" scheme there are four rotating cylindrical surfaces. In all other schemes shown in figure 9.1, two at a time. The radial movement of the fluid is prevented by friction against the walls of the slots of the movable and stationary working elements, as well as a periodic change in the flow area along the path of movement. As a result of the interaction of all these factors, a time-periodic radial velocity V_r averaged over the input section is established (fig. 9.6).

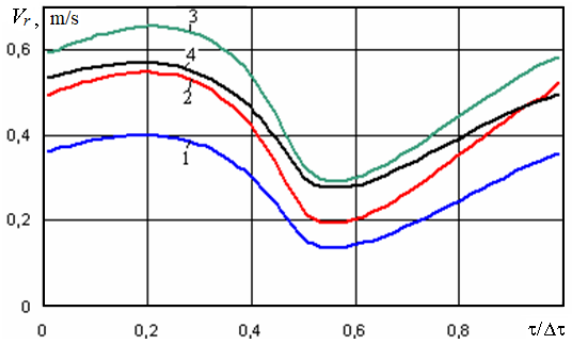

FIGURE 9.6. Time variation of the averaged radial velocity in the input section of the computational domain: 1 – "stator-rotor-stator"; 2 – "rotor-stator-rotor"; 3 – "rotor-stator"; 4 – "stator-rotor".

Comparing the curves shown in figure 9.6, it can be noted that the minimum radial flow rate is provided by the basic stator-rotor-stator circuit (curve 1). The rotor-stator-rotor scheme (curve 2) has a higher radial flow rate due to the fact that the rotational motion of the liquid in this case is more intense, and the friction losses are almost the same as the basic scheme due to the identical geometric parameters. In two-element schemes, there are fewer rotating surfaces than the rotor-stator-rotor circuit, but there are also fewer surfaces that impede radial movement. As a result of this, in schemes with two elements, the mass-average radial velocities are higher than in schemes with three elements.

Since fluid braking during mutual overlapping of the rotor and stator slots occurs more smoothly in the case of the "stator-rotor-stator" scheme (fig. 9.6), the pressure drops in the working area also turn out to be smaller at this point in time. This is evidenced by graphs of the time dependences of the overpressure at two characteristic points of the computational domain located in the input sections of the internal and external gaps. As can be seen from figure 9.7, for both three-element layout schemes, at the moment of mutual overlapping of the slots of the movable and fixed elements in the input sections of the external and internal gaps, the overpressure reaches its maximum values. Then there is a sharp drop in pressure at the entrance to the gaps located above the rotating elements (curve 1b, corresponding to the internal gap of the "rotor-stator-rotor" scheme and curve 2a, corresponding to the external gap of the "stator-rotor-stator" scheme). It is followed by a less significant increase. In the input sections of the gaps located above the fixed elements, in the period following the moment of mutual overlapping of the slots, the pressure also begins to fall, but more monotonously (curves 1a and 2b).

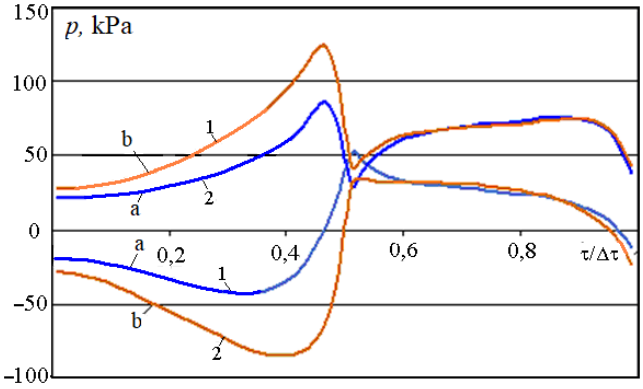

FIGURE 9.7. The time variation of the overpressure in the inlet cross sections of the gaps: a – stator-rotor-stator scheme; b – scheme "rotor-stator-rotor"; 1 – internal clearance; 2 – external clearance.

Differentiating the dependences presented in figure 9.7, over time, we find quantities called “pressure pulsations”. The time dependences of these quantities are presented in figure 9.8. As can be seen from the graphs, at the moment of mutual overlapping of the slots of the movable and fixed elements, the maximum positive pressure pulses are observed in the input section of the internal gap of the “stator-rotor-stator” scheme ($\frac{\partial p}{\partial \tau} = +4.17 \cdot 10^9$ Pa/s) and external gap of the “rotor-stator-rotor” scheme ($\frac{\partial p}{\partial \tau} = +8.91 \cdot 10^9$ Pa/s). At the same time, the maximum negative pressure pulses are observed in the external gap of the "stator-rotor-stator" scheme ($\frac{\partial p}{\partial \tau} = -5.74 \cdot 10^9$ Pa/s) and in the internal gap of the “rotor-stator-rotor” scheme ($\frac{\partial p}{\partial \tau} = -8.25 \cdot 10^9$ Pa/s). As can be seen from this figure, the “rotor-stator-rotor” scheme provides higher values of both positive and negative pressure pulsations.

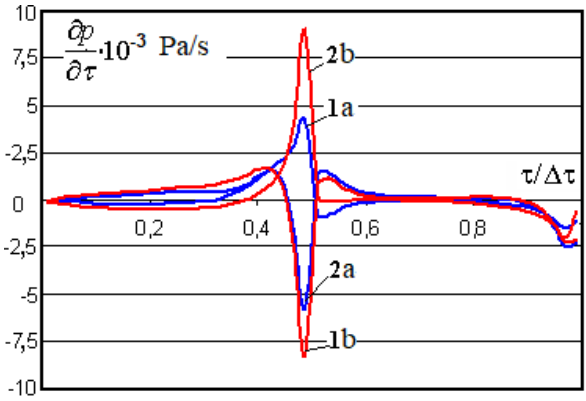

FIGURE 9.8. Change in time of pressure pulsations in the inlet cross-sections of the gaps: a – stator-rotor-stator scheme; b – scheme "rotor-stator-rotor"; 1 – internal gap; 2 – external gap.

An analysis of such dependencies constructed for schemes with two working elements showed that the time variation of the pressure at the inlet to the RPA gap, assembled according to the "stator-rotor" scheme, is similar to the dependences for the external gap of the "rotor-stator-rotor" scheme. The time variation of the pressure at the entrance to the gap for the "rotor-stator" scheme is close to the dependencies constructed for the internal gap of the "rotor-stator-rotor" scheme (fig. 9.9). Thus, the "rotor-stator-rotor" scheme, as it were, combines both schemes with two working elements.

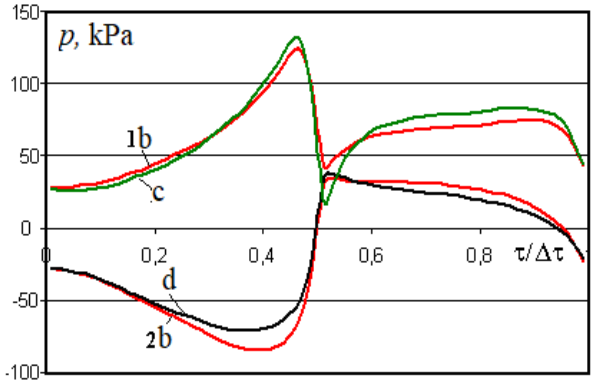

FIGURE 9.9. The time variation of the overpressure in the inlet cross sections of the gaps: b – "rotor-stator-rotor"; 1 – internal gap; 2 – external gap; c – "rotor-stator"; d – "stator-rotor".

An analysis of the velocity and pressure fields in the working area of the apparatus makes it possible to construct the dependences of the moments of hydrodynamic drag forces acting on rotating elements (rotors). The meanings of these values are important when choosing the type of motor in the RPA scheme. The calculation of the indicated moments of resistance forces, depending on time, is performed according to dependence (5.2). Recall that the moment is created by the forces of pressure and normal stress acting on the inner surfaces of the slots of the rotor, and by the forces of shear stress acting on the cylindrical surfaces. The results of calculating the moments of resistance forces for different arrangements of working bodies are presented in figure 9.10.

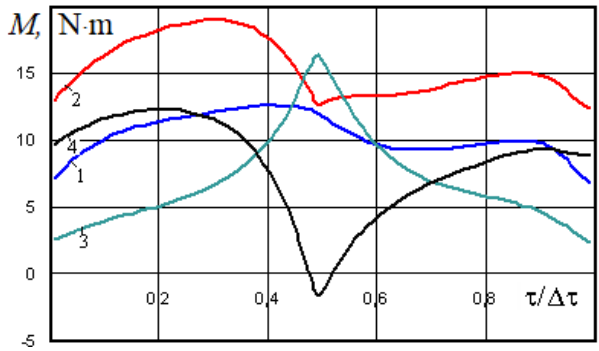

FIGURE 9.10. Change in time of the total moment of hydraulic resistance forces acting on the surface of the rotors: 1 – "stator-rotor-stator" scheme; 2 – "rotor-stator-rotor"; 3 – "rotor-stator"; 4 – "stator-rotor".

As expected, the maximum total moments are created by forces acting on the surface of two rotors of the "rotor-stator-rotor" scheme (curve 2). This is mainly due to the maximum surface area on which resistance forces act. It is interesting to note that in the case of the "stator-rotor" scheme for a short period of time, including the moment of mutual overlapping of the slots of the rotor and stator, the moment of resistance forces acting on the rotor becomes negative, i.e. this moment of forces does not prevent the rotation of the rotor, but rather contributes to it (curve 4). This can be understood from the analysis of the pressure field presented in figure 9.4b. As can be seen from the figure, at the indicated moment in time, the wall of the rotor separating two adjacent slots is exposed to a pressure difference contributing to the rotational movement of the rotor, since the pressure in front of the wall of the slot is slightly lower than the pressure behind the wall. It is also interesting to note that when summing the moments of forces found for the "stator-rotor" and "rotor-stator" schemes (curves 3 and 4), values close to those obtained for the "rotor-stator-rotor" scheme are obtained (curve 2).

An important parameter characterizing the operation of RPA is the average total power of heat sources Q due to energy dissipation in the working area. The influence of the viscosity of the medium on the indicated value was considered in chapter 6. The time dependences of the Q values for the above four configurations of working elements in the working area of the RPA are shown in figure 9.11.

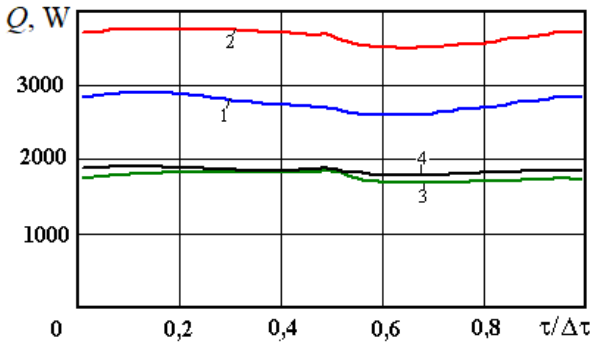

FIGURE 9.11. Change in time of the total energy dissipation in the RPA working space: 1 – "stator-rotor-stator" scheme; 2 – "rotor-stator-rotor"; 3 – "rotor-stator"; 4 – "stator-rotor".

As already indicated in the previous sections, the level of energy dissipation in the working space of RPA weakly depends on time. This is evidenced by the curves shown in figure 9.11. As expected, the maximum energy dissipation occurs when the working bodies are arranged according to the "rotor-stator-rotor" scheme (curve 2). This is a consequence of both a more intense movement of the liquid with such a scheme, and a larger surface area performing rotational motion.

For both schemes containing two working elements, the total values of heat release due to energy dissipation turn out to be almost the same (curves 3 and 4). In this case, the total dissipation levels are approximately two times lower than for the "rotor-stator-rotor" scheme. The "stator-rotor-stator" scheme occupies an intermediate position in terms of energy dissipation (curve 1).

A comparison of the time-averaged basic dynamic characteristics of the apparatuses assembled according to the four considered layout schemes is presented in table 9.1. The data relate to the conditions presented above: Δp = +10.0 kPa; μ = 0.1 Pa·s; $\omega_0 = 100 \cdot \pi$ s^{-1}.

TABLE 9.1. Basic dynamic characteristics of the apparatuses assembled according to the four considered layout schemes.

Layout scheme	Mass average radial velocity $\bar{V}_r$, m/s	Moment of resistance forces $\bar{M}$, N·m	Power of heat sources $\bar{Q}$, W
Stator-rotor-stator	0.288	10.35	2751
Rotor-stator-rotor	0.402	15.39	3650
Rotor-stator	0.501	7.02	1765
Stator-rotor	0.442	8.09	1845

From the table 9.1 it is seen that the maximum mass-average velocity of translational motion is provided by a two-element apparatus of the "rotor-stator" type, and the minimum is provided by the apparatus of the "stator-rotor-stator" type. The maximum moment of resistance forces is created in the apparatus of the “rotor-stator-rotor” type, and the minimum – in the apparatus of the “rotor-stator” type. The maximum energy dissipation takes place in the "rotor-stator-rotor" apparatus, and the minimum in the "rotor-stator" apparatus.

9.2. The influence of the width of the gaps between the working elements of RPA on the dynamic characteristics of the fluid flow and heat transfer in the working area

The operational efficiency of RPA, as a device for producing finely dispersed emulsions, depends on a number of its structural (geometric) characteristics, among which the most important role is played by the gap width δ between cylindrical working elements and the number of radial slots z in the working elements. Chapters 5, 6 studied the influence of fluid viscosity μ and the difference in external pressure Δp on the dynamic and temperature characteristics of the fluid flow in RPA at constant values of geometric parameters. To clarify the question of the dependence of the indicated characteristics of RPA on its design parameters, a

comparative analysis of the results of solving similar problems is carried out under the conditions $\Delta p = 0$ Pa; $\mu = 0.01$ Pa·s and $\omega_0 = 96 \cdot \pi$ s^{-1} for cases of different gap widths δ and different numbers of radial slots z. The apparatus assembled according to the "stator-rotor-stator" scheme is considered. It is believed that both gaps have the same width and the number of slots in each of the elements is the same. In addition to δ and z, other design parameters of the device are considered unchanged and correspond to RPA type TF-2 [9.2].

As the results of calculations showed, with a decrease in the width of the gaps, both the radial flow rate of the processed medium G_r and its flow rate G_θ in the tangential direction (through the gaps) decrease. The dependences of both characteristics on time for different values of the gap width and the same number of slots $z = 36$ are shown in figures 9.12, 9.13.

As can be seen from figure 9.12, with a decrease in the gap width δ from 0.3 mm to 0.1 mm, the radial flow rate decreases overall by 1.4 times. At the same time, the fluid flow through the gaps decreases almost in proportion to the width of the gaps (fig. 9.13).

The relations of fluid flows averaged over one-time period in the tangential and radial directions are presented in figure 9.14. As can be seen from the figure, with a gap width of $\delta = 0.3$ mm, this ratio is about 0.2%, and with $\delta = 0.1$ mm, it is only 0.08%.
As already mentioned in chapter 5, the most significantly dynamic characteristics of the fluid flow in the RPA change at the moment of mutual overlapping of the slots of the stators and rotor ($\tau/\Delta\tau = 1/2$). At this moment, due to the sharp deceleration of the flow, a phenomenon similar to water hammer is observed. Moreover, in the region of the internal edge of the slot of the external stator, the pressure, the flow acceleration, as well as the normal and tangential viscous stresses change pulsed in time. The indicated region is characterized by the fact that at $\tau/\Delta\tau = 1/2$ the maximum approach of the outer edge of the rotor slot to the inner edge of the slot of the external stator occurs. Through this "gap" between the edges of width δ, the bulk of the fluid flows from the slot of the rotor into the slot of the external stator. The smaller the gap width δ, the higher the values of the flow acceleration modulus and the pressure pulsation amplitude.

As can be seen from figure 9.15, with a decrease in the gap width from $\delta = 0.3$ mm to $\delta = 0.1$ mm, the maximum values of the flow acceleration modulus increase from $0.8 \cdot 10^5$ m/s^2 to $1.6 \cdot 10^5$ m/s^2. In this case, the maximum pressure near the inner edge of the slot of the external stator increases from $p = 36$ kPa at $\delta = 0.3$ mm to $p = 58$ kPa at $\delta = 0.1$ mm (fig. 9.16).

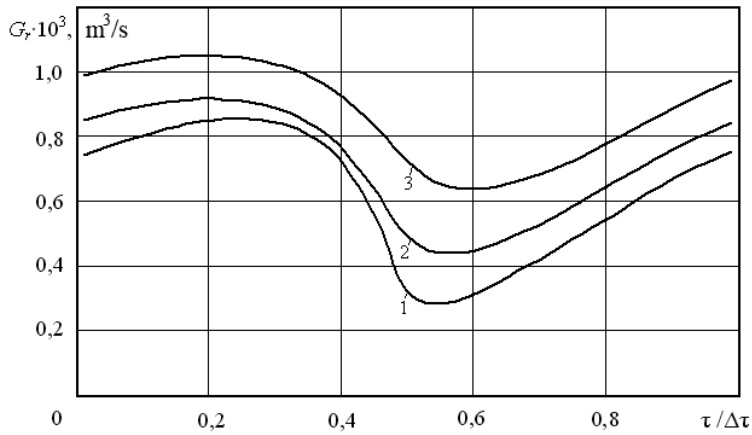

FIGURE 9.12. Time-dependent radial flow rate of a fluid with a viscosity coefficient μ = 0.01 Pa·s at Δp = 0 Pa, ω_0 = 96·π 1/s, z = 36: 1 – δ = 0.1 mm; 2 – 0.2 mm; 3 – 0.3 mm.

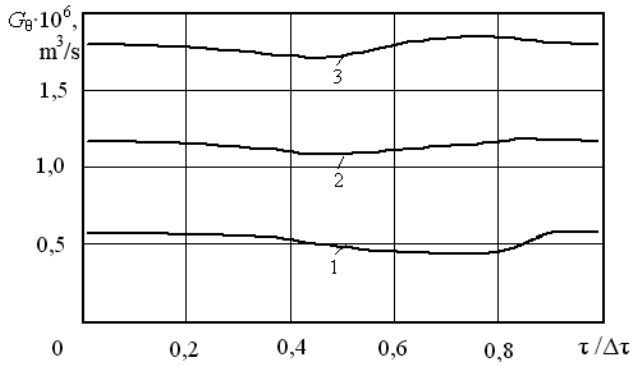

FIGURE 9.13. The dependence on the time of fluid flow through the gaps between the working elements: 1 – δ = 0.1 mm; 2 – 0.2 mm; 3 – 0.3 mm.

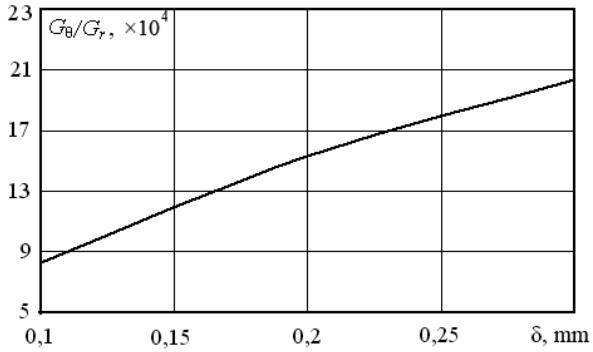

FIGURE 9.14. The influence of the width of the gap on the ratio of fluid flow in the tangential direction to flow in the radial direction.

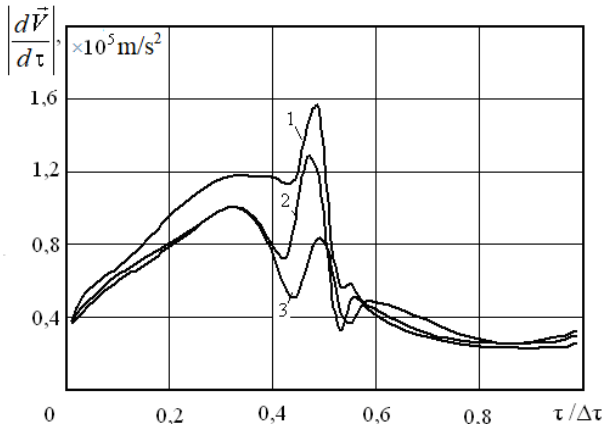

FIGURE 9.15. The time variation of the flow acceleration module near the inner edge of the slot of the external stator, depending on the width of the gap between the stator and the rotor: 1 – δ = 0.1 mm; 2 – 0.2 mm; 3 – 0.3 mm.

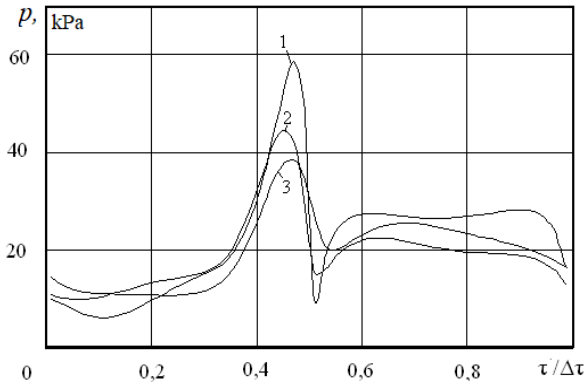

FIGURE 9.16. The time variation of the overpressure near the inner edge of the slot of the external stator, depending on the width of the gap between the stators and the rotor: 1 – δ = 0.1 mm; 2 – 0.2 mm; 3 – 0.3 mm.

The indicated pressure pulsations and flow accelerations occurring at the moment of mutual overlapping of the rotor and stator slots are an important factor in the process of crushing dispersed particles of a heterogeneous substance during its processing in RPA. Therefore, it should be expected that a decrease in the gap width δ should contribute to a decrease in the particle size of the dispersed substance. Reducing the width of the gaps also causes an increase in shear stress in the gaps, which should also contribute to the intensification of particle crushing. However, due to a significant reduction in fluid flow through gaps, in which these processes are believed to occur very intensively, the probability of

crushing for a significant number of particles decreases. In addition, a decrease in the width of the gaps causes an increase in dissipative heat and contributes to overheating of the treated medium. As can be seen from figure 9.17, with a decrease in the gap width from δ = 0.3 mm to δ = 0.1 mm, the average mass overheating of the medium with a viscosity of μ = 0.01 Pa·s at Δp = 0 Pa and $\omega_0 = 96 \cdot \pi$ s^{-1} increases almost 2 times.

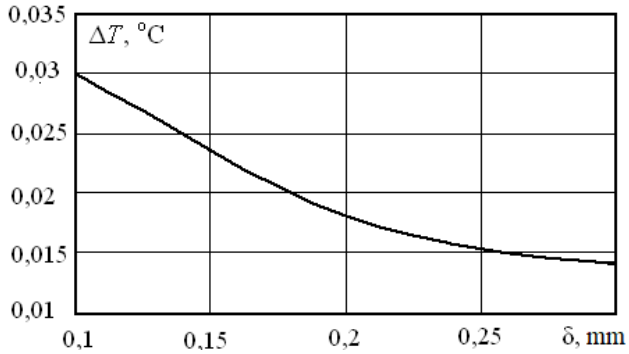

FIGURE 9.17. Dependence of the degree of overheating of the liquid processed in RPA with viscosity μ = 0.01 Pa·s, density ρ = 1000 kg/m^3 and heat capacity Cp = 4187 J/(kg·K) on the gap width.

This is due to both an increase in total heat release and a decrease in flow rate in the radial direction. At the same time, local overheating of the medium in the most heat-stressed sections of the flow also increases.

9.3. The influence of the number of slots in the RPA working elements on the dynamic characteristics of the fluid flow in the working area of the apparatus

In addition to the gap width, an important structural characteristic of the RPA is the number of slots in the cylindrical working elements. At a constant angular velocity of rotation of the rotor, an increase in the number of slots z reduces the duration of the period $\Delta\tau = 2\pi / (z\omega_0)$ between combinations of slots of the rotor and stators. This increases the frequency of pressure pulsations and other dynamic characteristics of the flow of the treated medium. For given values of the internal and external diameters of the working elements, an increase in the number of slots changes the relationship between the length and width of the slots, which leads to changes in the structure of the fluid flow. In this case, the values of the dynamic flow parameters considered above also change.

In principle, the number of slots in each of the working elements can be different, but most often their number is the same for both the stators and the rotor. To study

the effect of the number of slots on the dynamic characteristics of the flow, the velocity and pressure fields in the working zone of a TF-2 type apparatus were calculated for a medium with a viscosity μ = 0.01 Pa·s at rotor velocity of $\omega_0 = 96 \cdot \pi$ s^{-1} and at zero differential (Δp = 0) of external pressure. In addition to the previously considered RPA version with 36 slots, the cases z = 24 and z = 48 are also considered for δ = 0.1...0.3 mm. A comparison of the calculation results for different variants of combinations of z and δ will allow us to elucidate the features of the joint influence of the gap width and the number of slots on the dynamic parameters of the flow in the RPA working area. In this case, it is assumed that the width of both gaps δ is the same.

The character of the change in time over the period $\Delta\tau$ of the averaged radial velocity of the medium depending on the number of slots z at δ = 0.2 mm is seen from a comparison of the curves shown in figure 9.18.

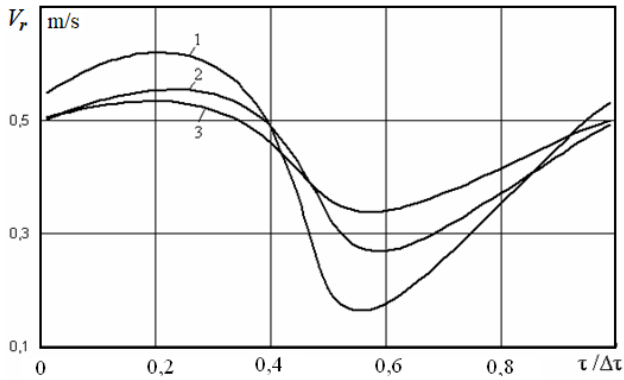

FIGURE 9.18. Effect of the number of slots z in the working elements on the time variation of the averaged radial velocity for one period (μ = 0.01 Pa·s, Δp = 0, $\omega_0 = 96 \cdot \pi$ s^{-1}, δ = 0.2 mm): 1 – z = 24; 2 – z = 36; 3 – z = 48.

As can be seen from the figure, with increasing z, the value of the maximum for a period of velocity decreases and the value of the minimum velocity of the medium in the radial direction increases. It should be noted that for each of the curves in figure 9.18, the period $\Delta\tau$ will be different, since the quantity $\Delta\tau$ itself is inversely proportional to the number of slots. The more slots z, the smaller the time interval during which the medium can freely flow from the slots of the stationary elements in the slots of the rotor. This also reduces the interval during which the slots are mutually overlapped. Thus, with an increase in the number of slots, the time intervals during which the fluid flow can be substantially rearranged decrease. This, in fact, explains the fact that with an increase in the number of slots, the oscillation amplitudes of the averaged radial velocity decrease. This, in general,

applies to other dynamic characteristics of the flow, such as, for example, pressure pulses at the moment of mutual overlapping of the slots of the rotor and stators. With an increase in the number of slots, the frequency of these pulses increases, and the amplitude decreases.

The dependences of the mass average radial velocities $\overline{V}_r$ averaged over the period $\Delta\tau$ on the number of slots z for various values of the gap width δ are shown in figure 9.19. As can be seen from the figure, the character of the change $\overline{V}_r$ on z turns out to be different for different δ. So for a variant of the apparatus in which δ = 0.2 mm, the value $\overline{V}_r$ weakly and monotonously increases with increasing z. However, for δ = 0.1 mm, the function $\overline{V}_r(z)$ has a minimum at z = 34, and for δ = 0.3 mm, a maximum at z = 37. Such features of the change $\overline{V}_r$ depending on the number of slots are explained by the complex character of the flow structure and the laws of redistribution of centrifugal forces that cause the medium to move in the radial direction. Moreover, with an increase in the gap width δ, the values $\overline{V}_r$ increase, which is consistent with the results presented in subsection 9.2.

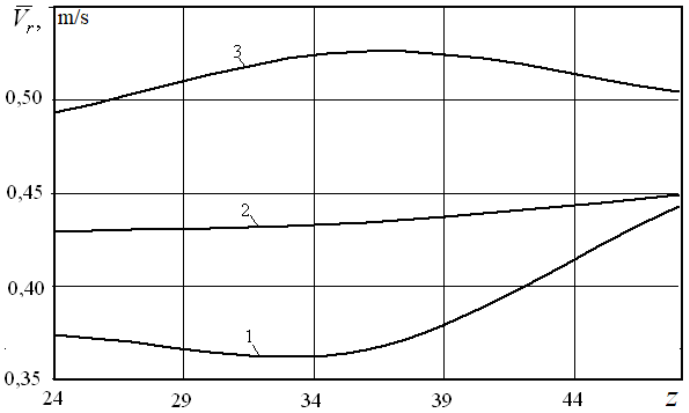

FIGURE 9.19. The influence of the number of slots z in the working elements on the mass-average radial velocity of the medium averaged over a period (μ = 0.01 Pa·s, Δp = 0, $\omega_0 = 96\cdot\pi$ 1/s): 1 – δ = 0.1 mm; 2 – 0.2 mm; 3 – 0.3 mm.

As already mentioned, an important characteristic of RPA operation is the total heat release power averaged over a period in the working area due to energy dissipation. The dependences of this quantity on the gap width δ obtained for various values of the number of slots are shown in figure 9.20. As expected, for any number of slots there is an increase in the total power of heat generation with a decrease in the width of the gaps. In the interval between 0.1 mm < δ < 0.2 mm, the increase in heat generation with a decrease in the gap width is more intense than in

the interval between 0.2 mm < δ < 0.3 mm. As for the effect of the number of slots on the level of heat release, due to an increase in the pulsation frequency of all dynamic characteristics of the flow, an increase in the number of slots also leads to an increase in the averaged power of dissipative heat releases $\overline{Q}$.

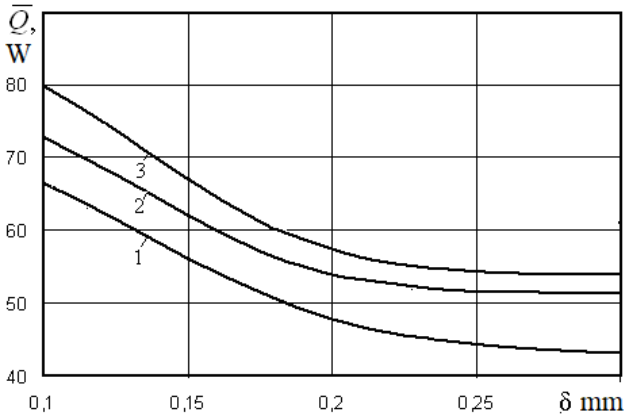

FIGURE 9.20. The dependence of the total heat dissipation power on the gap width for a different number of slots (μ = 0.01 Pa·s, Δp = 0, $\omega_0 = 96 \cdot \pi$ 1/s): 1 – z = 24; 2 – z = 36; 3 – z = 48.

9.4. The effect of the angular velocity of the rotor on the dynamic and thermal characteristics of the fluid flow in the working area of RPA

In the previous chapters, the issue of the influence of the viscosity of the medium on the dynamic characteristics of the flow and heat transfer in the working area of the RPA was discussed in detail. The previously described results of numerical simulation of the fluid flow were obtained in a dimensionless form. Moreover, the Reynolds number written in the form $\mathrm{Re} = \omega_0 r_0^2 / \mu$ was taken as the determining dimensionless parameter of the process. From this expression it follows that the influence of the rotor velocity ω_0 should be in character the inverse effect of the viscosity of the medium μ. Therefore, there is no need to dwell separately on the effect of the rotor velocity ω_0 on the dynamic characteristics of the flow. It is enough in this case to give two graphs describing the dependences on the angular velocity of rotation of the rotor averaged over one period of the mass-average radial velocity $\overline{V}_r$ (fig. 9.21) and the total averaged power of heat generation $\overline{Q}$ (fig. 9.22).

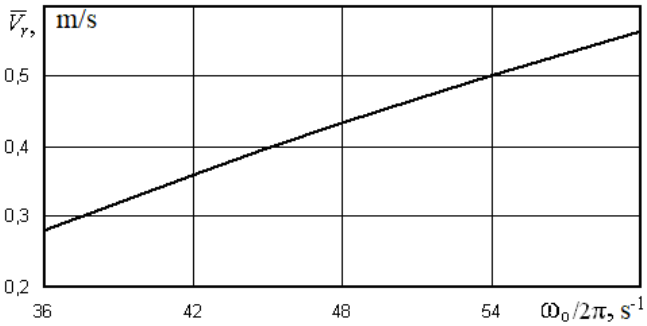

FIGURE 9.21. The influence of the angular velocity of rotation of the rotor on the mass-average radial velocity of the medium averaged over a period.

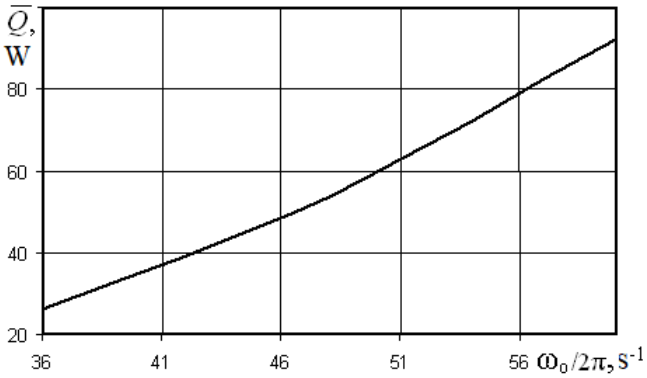

FIGURE 9.22. The influence of the angular rotor velocity on the total heat dissipation in the RPA working area.

The indicated graphical dependences were obtained for an apparatus with $z = 36$ and $\delta = 0.2$ mm at $\Delta p = 0$ for a medium with viscosity $\mu = 0.01$ Pa·s. As one would expect, with an increase in the number of revolutions of the rotor ω_0, both the mass-average radial velocity $\overline{V}_r$ and the average total power of the heat sources $\overline{Q}$ increase almost proportionally.

The data presented in figures 9.19-9.22, can be summarized in the form of polynomial dependencies:

$$\overline{Q} = \sum_{k=0}^{k=2}\sum_{i=0}^{i=2}\sum_{j=0}^{j=2} a^{Q}_{k,i,j}\delta^k z^i \omega_0^j \tag{9.1}$$

$$\overline{V}_r = \sum_{k=0}^{k=2}\sum_{i=0}^{i=2}\sum_{j=0}^{j=2} a^{V}_{k,i,j}\delta^k z^i \omega_0^j \tag{9.2}$$

Summarizing the results of numerical studies of the influence of structural and operational parameters of RPA on the dynamic characteristics of the flow of the processed medium, the following should be noted [9.3]:

- an analysis of the four layout schemes of the RPA working bodies location showed that: the "rotor-stator-rotor" scheme provides the maximum moment of hydrodynamic resistance forces and maximum total dissipative heat losses; maximum overheating of the medium being processed is typical for the "stator-rotor stator" scheme; maximum mass-average velocity is provided by the "rotor-stator" scheme;
- with a decrease in the width of the gap between the working elements, the amplitudes of pressure pulsations and flow acceleration increase; in proportion to the decrease in the width of the gap, the liquid flow through the gap decreases; with a decrease in the gap width, dissipative heat release and overheating of the medium are significantly increased;
- an increase in the number of slots in the working elements leads to an increase in the frequency of pulsations of all dynamic characteristics of the flow; the total heat in the working space of the RPA with an increase in the number of slots increase;
- with an increase in the number of rotor revolutions, both the mass-average radial flow velocity of the medium being treated and the total heat release power due to energy dissipation increase.

References

[9.1] Pat.65401 A. Ukraine. MKI 7 V01F7/02. Rotary-pulsating apparatus. Dolinsky A.A., Basok B.I., Koba A.R., Gartvig A.P., Pirozhenko I.A., Goryachov O.A., Korotich N.I., Vasiliev A. I. Claim 08/01/2003; Publ. March 15, 2004, Bull, No. 3, 3 p. (ukr.).

[9.2] Hydraulic characteristics of the rotary pulsation apparatus TF-2. Basok B.I., Pirozhenko I.A., Nezhuta V.P. [et al.]. *Bulletin of the National Technical University of Ukraine "KPI", series "Mechanical Engineering"*. Vol. 43, 2002, pp. 160-162 (rus.).

[9.3] Basok B.I., Davydenko B.V., Avramenko A.A., Pirozhenko I.A., Hydrodynamics, heat transfer and crushing effects in rotationally pulsating flows. Kiev, 2012, 298 p. (rus.).

Chapter 10

DESIGN AND TECHNICAL SOLUTIONS WHEN CREATING RPA

10.1. RPA structural and operational parameters optimization

As follows from the results of calculating the average particle diameter, presented in chapters 7 and 9, depending on the determining structural and operational parameters of the RPA, the minimum average particle diameter can be obtained at the maximum possible minimum gap width, the maximum possible number of slots and the maximum possible rotor speed. These limiting values of these parameters provide the maximum intensity of the dynamic impact of the working bodies of the apparatus on the heterogeneous medium processed in RPA. Within the considered intervals of variation of the indicated parameters, there is no local optimum (i.e., a combination of the indicated values) providing the minimum average particle size. However, in many cases, the average particle size of the dispersed particles of the emulsion D_{32} does not have to be extremely small. It can be set as a specific value that provides the required quality of the product. In this case, the optimal ratio of the determining structural and operational parameters of the RPA can be dictated by a number of other requirements, such as, for example, its maximum profitability, minimum energy consumption for the implementation of the process of crushing particles, maximum productivity of the apparatus, etc. subject to the provision of a given (although not extremely small) average particle diameter. If, for example, the average power of heat sources due to energy dissipation $\overline{Q}$, which should be minimal, is chosen as the optimization function, then the optimization problem is formulated as follows: it is necessary to find values of δ, z, and ω_0 that would ensure the average particle diameter $D_{32} = D_{32}^*$ provided that the heat release $\overline{Q} = \overline{Q}(\delta, z, \omega_0)$ is minimal. In accordance with [10.1], the mathematical formulation of this problem can be represented as:

$$x^* = \arg\min_{x \in X} \overline{Q}(x) \tag{10.1}$$

provided

$$D_{32}(x) = D_{32}^* = \text{const} \tag{10.2}$$

where x is a point of the space X with coordinates $x_1 = \delta;\ x_2 = z;\ x_3 = \omega_0$. The space X is limited by the values $\delta_{\min} \le x_1 \le \delta_{\max};\ z_{\min} \le x_2 \le z_{\max};\ \omega_{0\min} \le x_3 \le \omega_{0\max}$. It should be noted that the function $\bar{Q}(x)$ on a given set X, according to the results presented in chapter 9, has no local extrema. However, they can appear on the set Y, which is a subset of the set X and is determined by the dependence (10.2).

To solve the optimization problem (10.1), (10.2), we turn to expression (7.11), which is the quadratic dependence of the average particle diameter on the parameters of the apparatus δ, z and ω_0. For a given value of D_{32}^*, from expression (7.11), we can obtain an explicit dependence

$$\delta = \delta\left(D_{32}^*, z, \omega_0\right) \tag{10.3}$$

in which D_{32}^* will not be an argument, but a parameter. To obtain such a dependence, we represent expression (7.11) in the form

$$D_{32}^* = F_0\left(z,\omega_0\right) + F_1\left(z,\omega_0\right)\delta + F_2\left(z,\omega_0\right)\delta^2 \tag{10.4}$$

where $F_k\left(z,\omega_0\right) = \sum_{i=0}^{i=2}\sum_{j=0}^{j=2} a_{k,i,j}^D z^i \omega_0^j$, $k = 0;\ 1;\ 2$. It can be considered as an equation with respect to δ, the solution of which has the form:

$$\delta = \frac{-F_1\left(z,\omega_0\right) \pm \sqrt{F_1^2\left(z,\omega_0\right) - 4\left(F_0\left(z,\omega_0\right) - D_{32}^*\right)F_2\left(z,\omega_0\right)}}{2F_2\left(z,\omega_0\right)} \tag{10.5}$$

The sign in front of the radical is selected from the condition $\delta > 0$.

Substituting (10.5) into the expression for the power of heat sources, we obtain

$$\bar{Q}^*\left(z,\omega_0\right) = \bar{Q}\left[\delta\left(D_{32}^*, z, \omega_0\right), z, \omega_0\right] \tag{10.6}$$

To explicitly represent the function (10.6), one can use the previously obtained quadratic approximation (9.1) of the function $\bar{Q}$.

In the above way, a subset of points Y $(y_1 = z; y_2 = \omega_0)$ is distinguished from the original set X. On the subset of points Y, we can now examine the function of two variables $\bar{Q}$ for the presence of a local minimum. The optimization problem (10.1) can now be reformulated as

$$y^* = \arg\min_{y \in Y} \bar{Q}^*(y) \tag{10.7}$$

It should be noted that the arguments $y_1 = z; y_2 = \omega_0$ are now changing in narrower intervals than the arguments $x_2 = z; x_3 = \omega_0$ of the set *X*. They now turn out to be connected by an additional relation, $F_1^2(z,\omega_0) - 4\left(F_0(z,\omega_0) - D_{32}^*\right)F_2(z,\omega_0) \geq 0$, providing solvability of equation (10.4) with respect to δ.

If a solution to problem (10.7) exists, then the found value of the argument y^* will indicate the optimal values of z_{opt} and ω_{opt} that provide a minimum of heat release due to dissipation under the condition of a given average diameter D_{32}^* of dispersed particles. From the explicit expression (10.3), we can now obtain the optimal value of the gap width:

$$\delta_{opt} = \delta\left(D_{32}^*, z_{opt}, \omega_{opt}\right) \tag{10.8}$$

Similarly, it is possible to obtain a solution to the optimization problem in the case when the objective function is the maximum RPA performance for a given average particle diameter. The performance of the device is determined by the value of the mass-average radial velocity $\overline{V}_r$. Therefore, the optimization problem for the specified objective function can be formulated as

$$\begin{aligned} x^* &= \arg\max_{x \in X} \overline{V}_r(x) \\ D_{32}(x) &= D_{32}^* = \text{const} \end{aligned} \tag{10.9}$$

Since the rotor apparatus is considered the more perfect, the higher its productivity and the less thermal energy is released in it due to dissipation (which mainly affects its energy consumption), it seems most appropriate to use the ratio $\overline{Q} / \overline{V}_r$, which with optimal parameters of the apparatus should be minimal. The physical meaning of the given objective function becomes apparent from the expression $\Delta T = \dfrac{1}{C_p \rho} \dfrac{\overline{Q}}{\overline{V}_r f}$, that determines the overheating of the medium processed in RPA.

If overheating of the medium in the apparatus is taken as the objective function, then the optimization problem is formulated as follows:

$$\begin{aligned} x^* &= \arg\min_{x \in X} \Delta T(x) \\ D_{32}(x) &= D_{32}^* = \text{const} \end{aligned} \tag{10.10}$$

As an example of solving optimization problems, we consider the case of the TF-2 apparatus, for which the dependences of the average total power of the heat-release sources and the mass-average radial velocity on the determining parameters δ, *z*

and ω_0 are shown in figures 9.19-9.22 and are generalized in the form of expressions (9.1) and (9.2). The dependences of the average particle diameter D_{32} on the same parameters are presented in figures 7.11-7.13 and are generalized in the form of a polynomial (7.11). These results were obtained at constant values of all other geometric parameters. The pressure drop between the input and output sections of the working area is zero. Radial motion of the medium is caused only by the action of centrifugal forces. Recall also that the calculation results were obtained for the following physical properties of continuous (index 0) and dispersion (index 1) media: $\mu_0 = 0.01$ Pa·s; $\rho_0 =$ 1000 kg/m^3, $\mu_1 =$ 0.06 Pa·s, $\rho_1 =$ 880 kg/m^3. The surface tension at the interface is α = 0.02 N/m. The case of a single processing of the medium in RPA is considered. Given is considered the average diameter of the dispersed particles $D_{32}^* =$ 15 μm after a single treatment. The solution of equation (10.4) for this case, obtained in the form of expression (10.5), is graphically presented in figure 10.1. The numbers on the curves indicate the number of slots in the working elements. As can be seen from figure 10.1, for these conditions, a solution to equation (10.4) with respect to δ exists if the number of slots is not less than z = 30, and the number of revolutions of the rotor is not less than $\omega_0 = 47$.

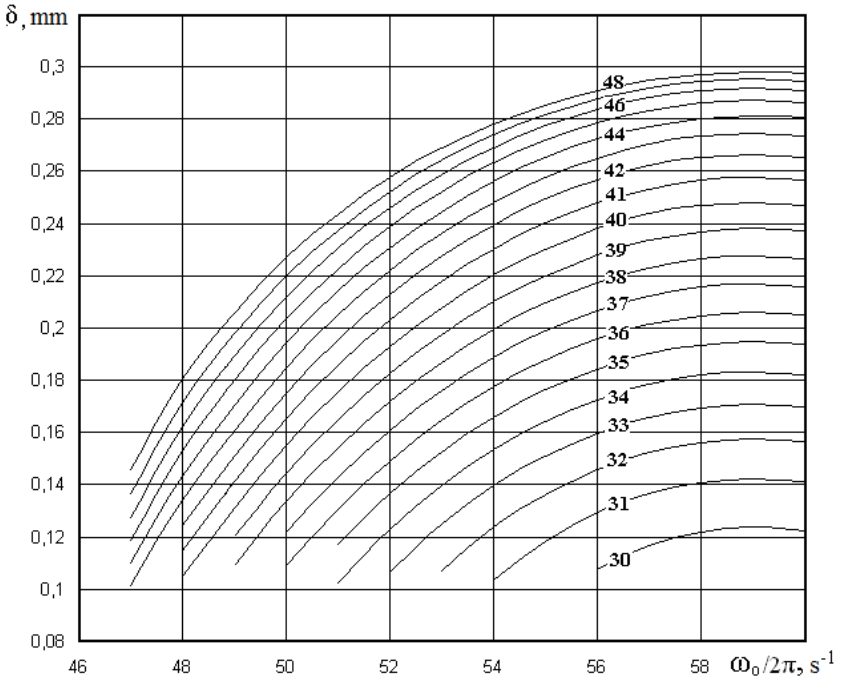

FIGURE 10.1. The dependence of the gap width δ on the rotor speed ω_0 and the number of slots z, providing an average particle diameter of D_{32} = 15 μm.

The function $\bar{Q} = \bar{Q}^*(z, \omega_0)$, obtained from expression (9.1) taking into account the found dependence $\delta = \delta(D_{32}^*, z, \omega_0)$, is shown in figure 10.2.

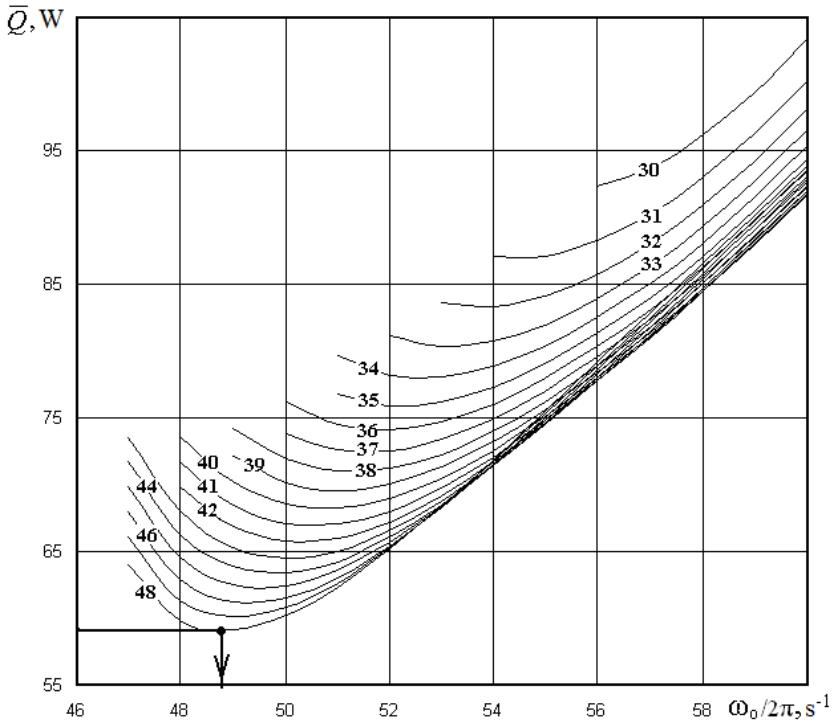

FIGURE 10.2. The dependence of the heat dissipation power on the rotor speed ω_0 and the number of slots z with an average particle diameter of D_{32} = 15 μm.

From figure 10.2 it is seen that the absolute minimum, which is $\bar{Q}$ = 59.12 W, the function $\bar{Q}^*(z, \omega_0)$ reaches at z = 48 and $\omega_0 / 2\pi = 48.8$ s^{-1}. The presented values of the number of slots and the rotational speed of the rotor are optimal from the point of view of the minimum level of heat release due to dissipation, provided that the average particle diameter in one cycle of processing the medium is D_{32} = 15 μm. Further, from the expression (10.8), the optimum gap width δ necessary for these conditions is determined, which, as can be seen from figure 10.3, will be equal to δ_{opt} = 0.204 mm. Using expression (9.2), we can now calculate the mass-average radial velocity characteristic of the obtained optimal RPA parameters, which turns out to be $\bar{V}_r$ = 0.453 m/s.

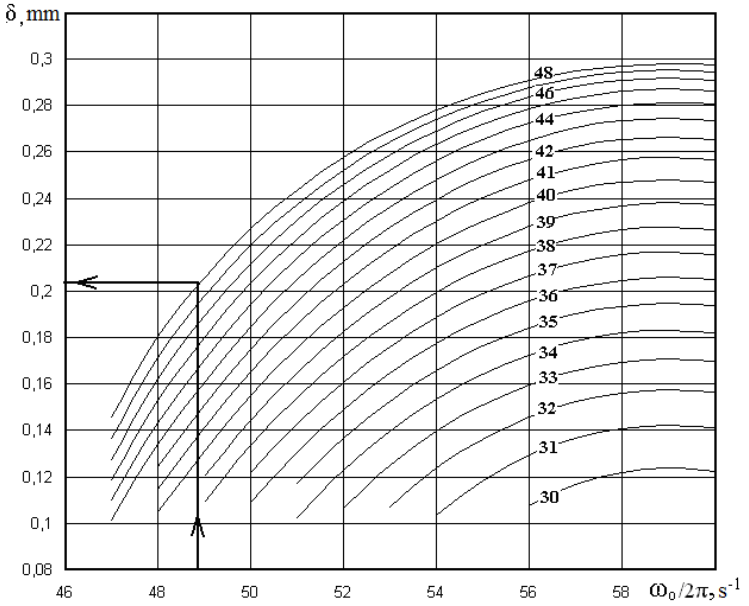

FIGURE 10.3. Determination of the optimal width of the gaps, providing a minimum level of heat dissipation.

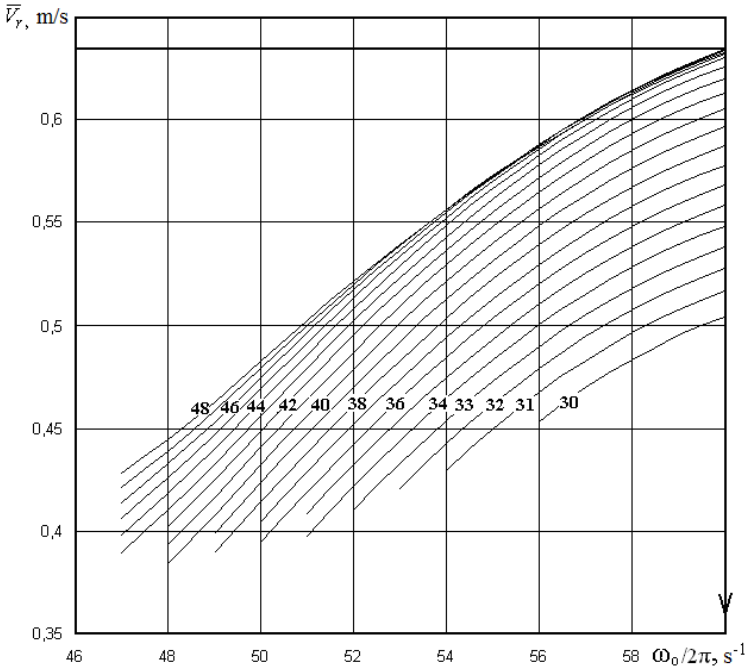

FIGURE 10.4. Dependence of the mass average velocity of the medium on the number of revolutions of the rotor ω_0 and the number of slots z at an average particle diameter of 15 μm.

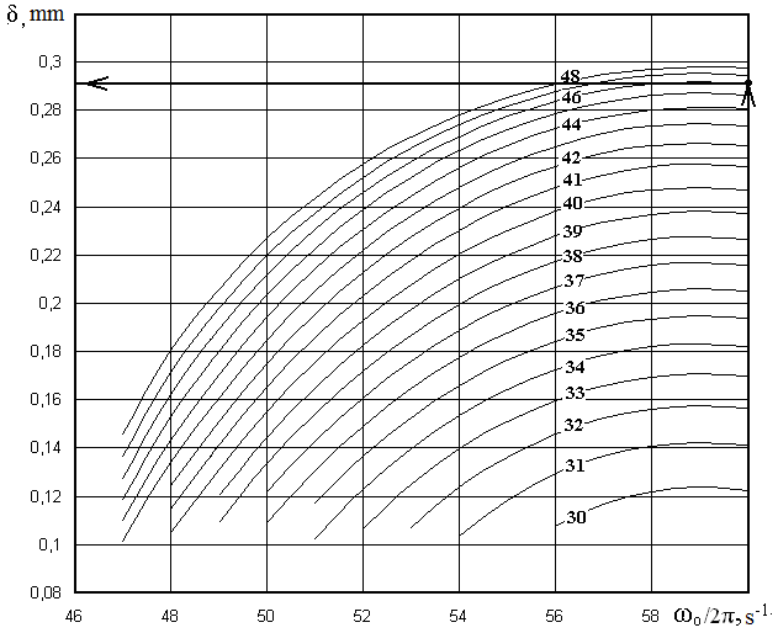

FIGURE 10.5. Determination of the optimal width of the gaps, providing the maximum mass-average speed with an average particle diameter of 15 microns.

The solution of the optimization problem (10.10) for the case when the objective function is the degree of overheating of the medium being processed in the working area is shown in figures 10.6 and 10.7.

The objective function $\Delta T(\delta, z, \omega_0)$ is constructed using expressions (9.1) and (9.2). The optimal parameters that ensure minimal overheating of the medium at D_{32} = 15 μm will be: the gap width δ_{opt} = 0.245 mm; the number of slots $z_{opt} = 48$; rotor speed $\omega_{opt} = 51$ rev/s. With the indicated average particle diameter, the above parameters provide the minimum degree of overheating of the substance ΔT = 0.016°C. In this case, the average total power of heat sources is $\overline{Q}$ = 62.34 W, and the mass-average velocity is $\overline{V}_r$ = 0.502 m/s.

Data on optimization of geometric and operational parameters of RPA type TF-2 are presented in table 10.1.

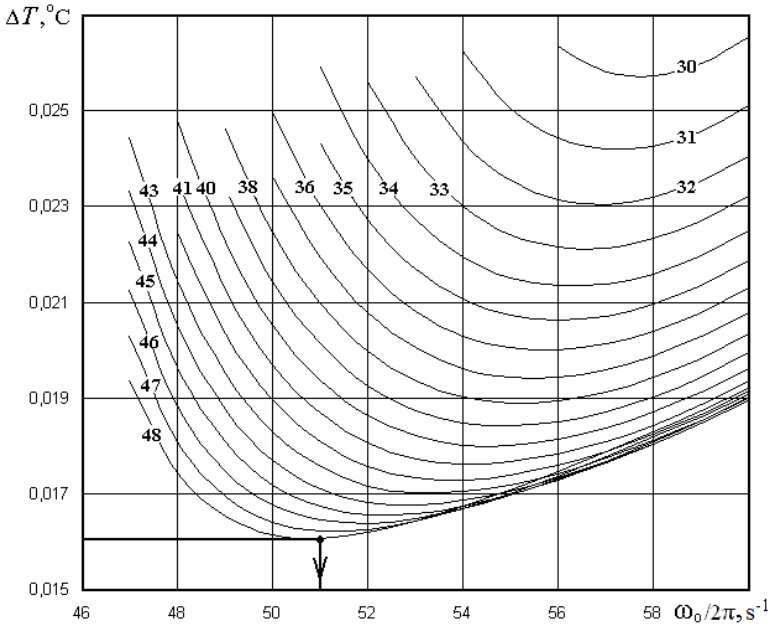

FIGURE 10.6. Dependence of the degree of medium overheating on the rotor rotation speed ω_0 and the number of slots z, providing an average particle diameter of D_{32} = 15 μm.

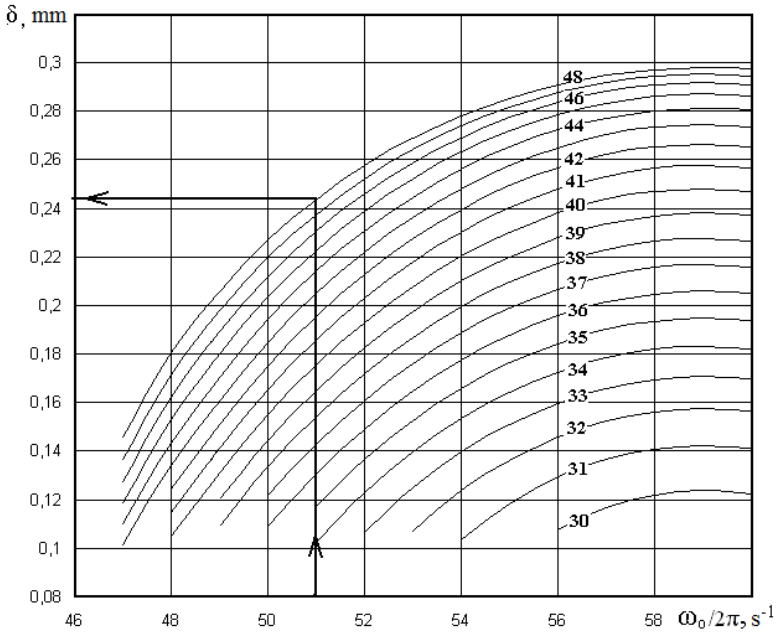

FIGURE 10.7. Determination of the optimal gap width, providing a minimum degree of overheating of the medium with an average particle diameter of 15 μm.

TABLE 10.1. RPA geometric and operational parameters optimization results.

Objective function	δ_{opt}, mm	z_{opt}	$\omega_{opt}/2\pi$, s^{-1}	$\bar{Q}$, W	$\bar{V}_r$, m/s
$\bar{Q}_{\min}$	0.204	48	48.8	59.12	0.453
$\bar{V}_{r\max}$	0.291	46	60	146.73	0.634
$\Delta T_{\min}$	0.245	48	51	62.34	0.502

Analyzing the results of solving three optimization problems, it can be noted that the geometric and operational parameters of the RPA, which ensures the minimum overheating of the medium in the working space, occupy an intermediate value in the intervals between the parameters providing the minimum dissipative heat release and the maximum productivity of the apparatus.

Thus, the considered method for optimizing the geometric and operational parameters of RPA makes it possible to create apparatuses that provide a given average diameter of dispersed particles with minimal energy dissipation in the flow, with maximum apparatus productivity and with a minimum degree of overheating of the processed medium.

10.2. Rotary pulsation equipment for the production and processing of liquid dispersed media

Due to the decrease in recent years in a number of industries, output volumes, and on the other hand, due to the expansion of the offered assortment (in order to maintain market positions), the need arose for highly efficient, versatile and small-sized compact equipment of small capacity, but easily reconfigurable in many technologies for the production of various products. Here, data are presented on a rotary-pulse type heat and mass transfer equipment complex for mixing, crushing, emulsification and homogenization processes when producing highly viscous oil-water emulsions for various purposes, as well as for their special processing [10.2, 10.3]. All installations were developed at the Institute of Engineering Thermophysics of the National Academy of Sciences of Ukraine, are produced in small batches, and are sold and operated on the markets of Ukraine and other countries. The processes of mixing, hydrodynamic crushing, or homogenization of dispersed particles of multicomponent media are based on a number of proposed physical mechanisms of the DIVE principle. The implementation of these mechanisms in the developed equipment is carried out with a pulsating effect on the substance of the field of high speeds and accelerations [10.4-10.6].

Rotor installation TF-2

This installation is intended for the preparation, emulsification and homogenization of water-oil emulsions, including highly viscous media. The plant is used for food production of mayonnaise; mixes for ice cream; caviar emulsion; sauces; pastes; mashed potatoes; desserts; for chemical production in the processes of mixing several mutually insoluble liquids, as well as for dissolving in a liquid (recovery) of powders and other bulk materials. Structurally, the installation mainly consists of a hopper with a capacity of 0.1 m^3, where the ingredients of the obtained product are preloaded, a vertical rotor assembly from a set of five coaxial cylinders with slotted holes on the side surface (two rotors and three stators, the gap between each a pair of 0.1 mm), a special mechanical seal assembly based on graphite rings, a pump assembly, an electric motor, a housing and pipelines for recirculation or output of the finished product. Schematically, the design of the apparatus is presented in figure 9.1. The installation was developed in several modifications with minor design changes for various capacities. The technical data of the installation are given in table 10.2. The TF-2 installation can be used for production with small volumes of products, in particular, in the field of food, processing industry or agriculture, and is intended for individual use, farms, small enterprises, joint ventures, joint-stock companies or cooperatives. It is possible to apply a package of new technologies, formulations and compositions of various food products, including new original ones developed at IETF NASU and implemented using the TF-2 unit [10.3].

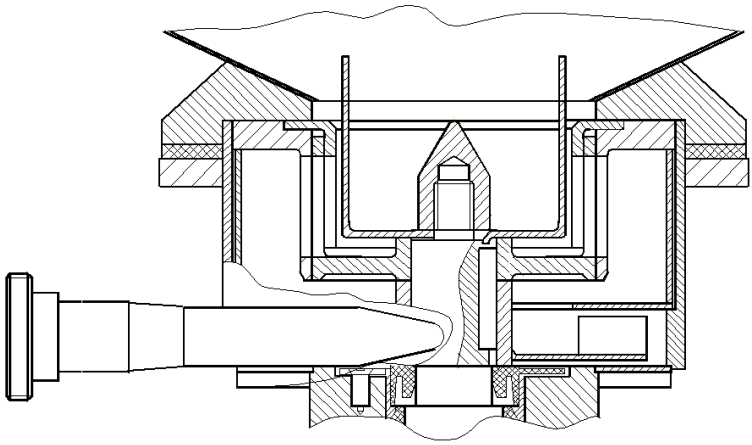

FIGURE 10.8. The scheme of the section of the working zone RPA type TF-2.

TABLE 10.2. Technical characteristics of rotary pulsation type equipment.

Name of installation	Productivity, kg/hour	Installed power, kW	Weight, kg	Dimensions, mm	Execution	Pump availability
Rotor installation TF-2	100* 500-2000**	2.2÷3.0	60	600×600×1300	***	+
Rotor installation TF-2G	150* 2000**	3.0	55	700×600×1100	***	+
BS rotary apparatus	500**	2.2	40	500×600×600	***	+
Steam (gas) – contact rotary device BSM	5000* at a steam consumption of 100 kg/h	2.2	35	400×600×600	*** ****	–
Rotary apparatus for dissolving BSR	3000**	2.2 +0.25	80	700×600×1500	*** ****	+
Rotary mixer TFM	1000**	2.2	40	300×500×300	*** **** *****	+
BGT rotary pulsation apparatus	500*-800**	11	150	650×650×1200	*** ****	+
Rotary homogenizer UPVSS-2	3000**-15000**	5.5	65	780×310×410	*** ****	+
Note. Product Type: * – high viscosity media, ** – low viscosity media. Execution: *** – food stainless steel, **** – ftoroplast, ***** – food bronze.						

Rotor installation TF-2G

Designed for grinding, emulsifying or homogenizing highly viscous dispersed media with high density components. The installation is used to obtain complex emulsions of high viscosity, in particular, for preparing the initial mixture in the production of simulation protein caviar based on fish milt, low-value fish species or other fish raw materials.

The installation constructively consists of a container for loading the initial components (including powdered or solid) and horizontally located: a screw with a special profile cutting device, rotary mixing and homogenizing unit, packing stuffing box, pump assembly, housing, electrical engine and piping kit. Technical data are given in table 10.2.

BS rotary apparatus

Designed for processes of crushing, grinding, emulsification, mixing and homogenization of dispersed media of high viscosity on a liquid basis, including emulsions, suspensions, pastes. It is used in the production technology of protein caviar, creams, sauces, pastes, mashed potatoes, ketchups, meat and dairy products. Possible application for emulsification and homogenization of mutually insoluble liquids with solid phase additives, including chemicals. The apparatus consists of a loading capacity of 0.02 m^3, a cutting device, an original rotor with specially profiled curved grooves, a reciprocal part of the stator, pump assembly, housing and pipelines. An electric motor with a belt drive unit is located in the upper part of the apparatus. Technical data are presented in table 10.2.

Steam (gas) – contact rotary device BSM

This apparatus is designed for mixing and homogenizing liquids with gas or steam. When mixed with steam, it is used as a direct contact heat exchanger. It is possible to use for technologies of steam pasteurization or sterilization of liquid dispersed systems by direct mixing. It is used in technological lines (together with other proposed equipment of vacuum equipment: a vacuum emulsifier or a vacuum homogenizer) for steam sterilization of liquid dispersed systems such as natural milk, cream, juices, mashed potatoes, baby food products and other media. The data of the BSM apparatus are given in table 10.2. Structurally, the apparatus consists of a rotor assembly in a set of five fluoroplastic disks with holes of a special profile (two – rotors, three – stators), an original mechanical seal, an electric motor, a housing, fluid and steam (or gas) inlet nozzles, and an outlet nozzle. The apparatus can also be used in aeration, saturation or flotation technologies for liquids, as well as in other technologies where the effects of direct mixing of liquids and gases are used.

Rotary apparatus for dissolving BSR

Designed for liquid dissolution (recovery) of bulk materials, including granular and lumpy. It is used in technologies for dissolving natural milk, skim milk, dried potatoes, dried juices or other powders. Structurally, it consists of a conical hopper for bulk solids with a wire screw driven by a low-speed gearbox, a grinding unit for granules or possible lumps, an input unit for a swirling fluid flow, where the product is pre-mixed and dissolved, the rotor homogenization unit of the recovered medium, compaction, pump part, electric motor, housing and system of inlet and outlet pipes.

Rotary mixer TFM

Such a mixer is designed for metered mixing, crushing and homogenization of sparingly soluble liquid media. It is used in technologies for dosed mixing of liquids, in particular, in technology for extracting biologically active liquids from seafood. It consists of an ejector mixing unit and partial recirculation of the flow and a rotary homogenizer of a dispersed medium. The latter is constructed from the rotor part in the form of a set of coaxial rotor and two stators, seals of special manufacture, pump assembly, housing, electric motor and piping system, including input and output pipes. It is made in the marine (ship) version, which provides for operation under conditions of roll, vibration, tropical climate and high humidity.

BGT rotary pulsation apparatus

The apparatus for the homogenization of BGT is intended for mixing, crushing and homogenizing the components of highly viscous pasty products in the processing, chemical, pharmaceutical, food, dairy and other industries.

Structurally, the homogenizer consists of a loading hopper, a rotor-pulsating unit, a control panel, a special seal, a frame, a casing, an electric motor. The rotor-pulsation unit consists of two cylindrical rotors with vertical slots, one stator with the same slots and a wing-chat. A knife is installed on the top of the shaft. In the lower part of the housing there is a shaft seal assembly on the drive side. The housing has a pipe for unloading the finished product, as well as pipes for supplying and draining water to the mechanical seal assembly.

The loading hopper, made in the form of a cone, is designed to load the processed raw materials and accumulate them for periodic loading. There is a lid on the top of the hopper. The working volume of the hopper is 80 liters. The housing is intended for installation and placement of the working body of the homogenizer – the drive shaft with rotors, stator and shaft seal. The working body of the rotary pulsation apparatus is designed to grind, homogenize and remove material from the working zone by creating a complex set of effects on the processed raw materials: pulsating

alternating pressure differential, high gradient flow in the gaps between rotating and stationary elements (rotors and stator), as well as large shear stress. The device operates in continuous mode and during recycling of processed raw materials.

Rotary homogenizer UPVSS-2

Used for the production of tomato juice. Tomato paste in barrels with the help of a lift enters the mixer, where it is diluted with water to a concentration of 15-20% brix. At the same time, the formulation components are added to the mixer, based on the calculation per unit mass of the finished tomato juice. After mixing in a mixer, the product enters the UPVSS-2 rotary homogenizer, where intensive mixing, grinding and homogenization of concentrated tomato juice takes place.

The process of intensive technological mixing, grinding, dispersing and homogenizing concentrated tomato juice occurs in a horizontal type rotary homogenizer UPVSS-2.

All specified in table 10.2 the rotary installations have a continuous flow regime of flow, and they are united by the general principle of rotor homogenization of a dispersed medium, which is as follows. Passing through a certain number of specially profiled openings of the rotor – stator pairs, the medium being treated falls into the zone of interaction of intense pressure pulsations and large velocity gradients, which contribute to the hydrodynamic fragmentation of the dispersed phase. In the minimum gap between the rotor and the stator, the formation of thin liquid films and their subsequent destruction, accompanied by crushing of particles. In addition, the alternating alternation of the passage openings leads to the formation of low-pressure vapor (gas) cavities and their subsequent collapse, causing cavitation effects of crushing of the immiscible component. In places of discontinuity of the liquid medium due to rarefaction (vacuum), adiabatic boiling of the dispersion component is possible. Such a complex application of various crushing mechanisms, studied in detail in [10.6, 10.7], allows one to obtain a high-quality product characterized by a low dispersion of particles in the range of 0.5-3.0 μm and the absence of separation of the resulting emulsions during standard storage and sale periods.

All RPA installations are compact, as well as easily collapsible, which allows them to be effectively washed and repaired, are easily dismantled and installed in technological lines, which determines their universal application.

References

[10.1] Sukharev A.G., Timokhov A.V., Fedorov V.V., The course of optimization methods. M.: Nauka, 1988, 328 p.

[10.2] Basok B.I., Gartvig A.P., Koba A.R., Goryachev O.A., Equipment for obtaining and processing highly viscous dispersed media. *Industrial Heat Engineering*. Vol. 18, No. 1, 1996, pp. 50-56.

[10.3] Basok B.I., Pirozhenko I.A., Nezhuta V.P., Belyaeva T.G., Goryachev O.A., Hydraulic characteristics of the rotor – pulsation apparatus TF-2. *Vestn. NTUU "KPI", series of Technical Engineering*. No. 43, 2002, pp. 160-162.

[10.4] Dolinsky A.A., Basok B.I., Rotary impulse apparatus. 1. Pulsed effects of local adiabatic boiling and cavitation of a liquid. *Industrial heat-engineering*. Vol. 20, No. 6, 1998, pp. 7-10.

[10.5] Dolinsky A.A., Basok B.I., Rotary impulse apparatus. 2. Local pulse heating of the liquid. *Industrial heat engineering*. Vol. 21, No. 1, 1999, pp. 3-5.

[10.6] Dolinsky A.A., Basok B.I., Rotary impulse apparatus. 3. Crushing inclusions of the dispersed phase. *Industrial heat engineering*. Vol. 21, No. 2-3, 1999, pp. 5-6.

[10.7] Dolinsky A.A., Basok B.I., Mechanisms of hydrodynamic crushing of inclusions during boiling of a dispersed medium flow. *Industrial Heat Engineering*. Vol. 18, No. 4, 1996, pp. 3-7.

Chapter 11

CONCLUSION

In conclusion, we dwell briefly on the main results of research in the theory of rotary pulsation apparatuses presented in this monograph.

The structure of the fluid flow in the working space of the RPA is determined, the pulsating character of the change in the dynamic parameters of the flow is established; the effect of vortex formation in the flow in separate sections at different points in time, including the presence of one or two oppositely directed vortices in the slots of the rotor elements, was detected. The dependences of the mass-average flow velocity, the moment of resistance forces acting on the rotor, the power of the dissipative heat generation sources and the degree of overheating of the treated medium on its thermophysical properties, as well as on the structural and operational parameters of the RPA, are found. Based on these data, the necessary technical characteristics of the apparatus's electrical equipment are determined, as well as the possibility of processing heat-sensitive media in RPA.

A method for determining the trajectories of dispersed particles in the working volume of RPA; the possible number of acts of their hydrodynamic fragmentation and the sizes of the formed daughter particles in cases of laminar and turbulent flow regimes of the treated medium are estimated; a phenomenological method has been constructed for estimating the average diameter of dispersed liquid particles of a heterogeneous medium processed in RPA; the dependences of the average particle diameter on the structural and operational parameters of RPA are investigated.

Based on the results of a comparative analysis of the RPA characteristics with a different arrangement of working bodies and various structural and operational parameters, the most optimal RPA design options were established in terms of their maximum performance or minimum power consumption.

A method for optimizing the geometric and operational parameters of RPA has been built. The optimal values of the width of the gaps, the number of slots in the working elements and the velocity of rotation of the rotor are found that provide, with the required average particle size, the maximum productivity or minimum energy consumption for the implementation of crushing, emulsification and homogenization processes.

The obtained research results made it possible to formulate the main characteristics of hydrodynamics and heat transfer in the working volumes of rotary pulsation apparatuses, which determine their main qualitative indicators, as dispersing and mixing devices.

The picture of the flow of the processed fluid in the slots of the rotor and stators has a periodic and mainly circulating character. Periodically occurring vortex structures in the flow contribute to the intensification of the processes of mixing, dispersion and homogenization of a heterogeneous medium. The design and layout of the working bodies of the apparatus, as well as the high rotor velocity, contribute to the occurrence of significant flow accelerations, high pressure gradients, normal and shear stresses in the slots of the working elements, as well as in the gaps between them. At the moments of mutual overlapping of the slots of the rotor and stators, a sharp (pulsation) change in the indicated dynamic characteristics of the flow is observed. With an increase in the viscosity of the medium, as well as with an increase in the difference in external pressure and rotor velocity, the considered tendencies intensify. Such phenomena can be described as discrete-pulse energy input (DIVE) into the stream. These hydrodynamic effects in the working volume of the apparatus are the main cause of the destruction of the particles of the dispersed component of the multiphase medium.

The radial flow rate of fluid through the working area in most cases prevails over the flow rate in the tangential direction. Fluid flow in the radial direction increases with an increase in the external pressure drop, an increase in the rotor velocity and with a decrease in the viscosity of the medium. An increase in the viscosity of the medium being treated leads to an increase in the moment of hydrodynamic resistance forces acting on the rotor and to an increase in heat release due to the dissipation of mechanical energy. However, this increase is not proportional to the increase in viscosity, since an increase in viscosity reduces the intensity of the flow strain rate. The maximum heat release in the working area of the RPA occurs in the area of the external gap, as well as at the edges surface between the external gap and the entrance to the slot of the external stator. In these areas, there is a maximum overheating of the medium.

In the time interval corresponding to the mutual overlap of the slots of the stators and the rotor, the maximum convergence of the edges of these slots occurs. During this time interval, the highest impulses of pressure, velocity and acceleration of the flow are observed in the region of the edges of the slots of the rotor and stators. The duration of these pulses is about 20 μs. This also indicates a discrete in space and pulsed in time mechanism for supplying energy to the working area of the rotary pulsation apparatus. Based on this, the areas of the working space that have the highest potential for the destruction of dispersed

inclusions should include sections of the edges of the slots of the stators adjacent to the gaps between the cylindrical working elements.

With a decrease in the gaps between the rotor and the stators, the strain rates of the flow increase, pressure gradients, normal and tangential stresses increase. Reducing the width of the gap also leads to an increase in the power of dissipative heat sources in the stream and an increase in the overheating of the medium being treated. An increase in the number of radial slots in the working elements, as well as an increase in the velocity of rotation of the rotor contributes to an increase in the productivity of the apparatus, but dissipative heat release also increases.

In the RPA working space, both inertial and viscous particle crushing mechanisms are realized, and in the case of turbulent flow, a turbulent crushing mechanism is realized. The implementation of these mechanisms is facilitated by the DIVE effect, which leads both to pulsed acceleration of dispersed particles and to an increase in the dynamic loads on the particle from the side of a viscous dispersion medium.

Studies of the influence of RPA geometric and operational parameters on the size of dispersed particles in a heterogeneous liquid medium showed that the average particle diameter decreases with a decrease in the gap between the working elements, an increase in the number of radial slots and an increase in the rotor velocity.

From the analysis of the layout schemes of the RPA working bodies, the "rotor-stator-rotor" scheme, in comparison with the "stator-rotor-stator" scheme, is characterized by a higher level of heat generation due to dissipation of mechanical energy and a higher moment of hydrodynamic drag forces acting on the rotors. At the same time, the highest amplitudes of pressure pulsations characteristic of the “rotor-stator-rotor” scheme should most likely contribute to the intensification of the processes of crushing of dispersed particles in the working volume of the apparatus assembled according to this scheme.

The method of optimizing the structural and operational parameters of RPA based on the results obtained makes it possible to formulate recommendations for their design and operation in the technologies of mixing, crushing and homogenization of liquid dispersed media.

Recently, the scope of rotary pulsation apparatus has expanded significantly. This explains the increased interest of researchers and practitioners in the theory of cylindrical RPA. The authors hope that this book will allow to a certain extent to satisfy him.